STRUCTURAL OPTIMIZATION OF ANTIOXIDANT COPOLYMERS FOR DRUG DELIVERY APPLICATIONS

By

Carlisle Rose DeJulius

Dissertation

Submitted to the Faculty of the

Graduate School of Vanderbilt University

in partial fulfillment of the requirements

for the degree of

DOCTOR OF PHILOSOPHY

in

Biomedical Engineering

May 10, 2024

Nasvhille, Tennessee

Approved:

Craig L. Duvall, Ph.D.

Jonathan M. Brunger, Ph.D.

Scott A. Guelcher, Ph.D.

Tonia S. Rex, Ph.D.

Leslie J. Crofford, M.D.

Karen A. Hasty, Ph.D.

Dedication

This work is dedicated to the following people: my late grandfather, Allan Ogilvie Beattie, who always inspired me to be my best. My late grandmother, Rita DeJulius, whose work ethic was bigger than anyone's I've ever seen. My late cousin, Buck Burnette, who infected everyone with his positivity and who I'll be thinking about as I move on to the University of Michigan. And to my late mother in law, Donna Beckner, who gave me the best husband in the world.

ACKNOWLEDGEMENTS

I have been so lucky to receive as much support as I have during my PhD. First, I wouldn't have been able to succeed in graduate school without my husband, Jesse Beckner. We moved to Nashville together 5.5 years ago, got engaged, made it through a pandemic, and got married, all during my PhD. His support throughout this whole process has been invaluable, I probably wouldn't have clothes to wear or food to eat without you. My family, Angela, Dennis, Sophie, and Vince, have been so incredibly supportive over the years. I'm so lucky to call you all my parents and siblings. Of course, also need to shout out the dogs, Lana and Piper. Lana also made the Nashville move with us, and we got Piper two years later. Their pure joy is infectious and makes any tough day better.

My PI, Craig Duvall, has been such an amazing mentor during my PhD. He is always available when I need advice, and I know that will continue throughout my career. His support is a major reason that I have stuck to the academic career path. Shrusti Patel has been my "ride or die" since our first day getting lost on campus as first years. She always has time for everyone, especially me. Richard D'Arcy has also been an awesome role model and friend. There's nobody I'd rather bounce ideas off. Nora Francini has also been an amazing friend and mentor.

I need to thank all my lab mates and collaborators who helped in these projects. Sarah Naguib did such amazing work on the EPO animal studies making PPSES look good. Fang Yu is a brilliant animal surgeon and friend. Thomas Dean has worked so hard as an undergrad and now research technician on my projects. Eric Dailing and Bryan Dollinger for their advice and guidance during the DMAcoTEMPO project. Megan Keech, Amelia Soltes, and Patricia Poley for their help with whatever I need. Shubham Gulati and Blake Hanan for their hard work in the lab. Sean Bedingfield for all his OA knowledge.

I also need to thank all my good friends in and out of Nashville for their support. Shrusti, Dickie, and Nora for all the great game nights. Alex, William, and Jordan for all the yoga and book clubs. The Flying Saucer crew, Ella, Kyle, Prarthana, and Jonah. Alyssa and Marianne for listening to all my stressed out phone calls. I definitely wouldn't have made it through without so much love and friendship.

I also have so much gratitude to my committee, Tonia Rex, Leslie Crofford, Jonathan Brunger, Karen Hasty, and Scott Guelcher. Dr. Rex's expertise in optic neuropathies has been so valuable during my work on the EPO particles. Shadowing Dr. Crofford in my second year was such a valuable experience. Jonathan is always so responsive when I've needed anything, and Karen's expertise and advice in OA are so appreciated. I also need to thank my funding sources, the NIH NIBIB T32-EB021937 and NSF DGE-1937963.

TABLE OF CONTENTS

TABLE OF FIGURES

TABLE OF SCHEMES

TABLE OF SUPPLEMENTARY FIGURES

TABLE OF SUPPLEMENTARY TABLES

Chapter 1: Introduction

1.1. Background & Significance

Oxidative stress is a physiological state in which levels of reactive oxygen species (ROS) overwhelm the body's innate antioxidant processes. During normal homeostasis, ROS have important roles in cellular processes including host defense and cell signaling[1,2]. However, in states of oxidative stress, excess ROS directly damage biomolecules, upregulate inflammatory processes including nuclear factor κ-light-chain-enhancer of activated B cells (NF-κB) signaling and tumor necrosis factor-α (TNFα), and promote cellular apoptosis[3-7]. Notably, excess ROS are implicated in a wide variety of chronic inflammatory and degenerative diseases, including osteoarthritis (OA) [8,9], optic neuropathies[10,11], diabetes[12], cancer[13], and atherosclerosis[14]. Therefore, therapies which reduce oxidative burden could be an innovative strategy for treating pathologies with ROS involvement.

The potential benefits of antioxidants which chemically scavenge ROS have been studied for decades, as both dietary supplements and therapeutics[15,16]. Typically, candidate drugs mimic the activity of native cellular antioxidants, including glutathione (GSH, scavenges hydrogen peroxide (H_2O_2)), superoxide dismutase (SOD, scavenges superoxide ($O_2^{\bullet-}$)), and catalase (CAT, scavenges H_2O_2). However, these therapies tend to exhibit poor pharmacokinetics and tissue distribution, necessitating repeat administration at high doses[17]. Drug delivery strategies can be used to address these shortcomings, including the use of polymer-drug conjugates, packaging in biomaterials including nano- and microparticles (NPs and MPs), and incorporation of targeting moieties.

Polymers for the application of antioxidant therapy offer many advantages, including versatility in molecular weight and composition, tunable architectures and conjugation strategies,

and formulation potential as biomaterials for countless applications. Indeed, antioxidant polymers have been pursued as therapeutic strategies for many diseases, including diabetic peripheral arterial disease[18], stroke[19], and atherosclerosis[20]. Many of these systems incorporate thioether groups for scavenging of various ROS, including H_2O_2 and hypochlorite (**Scheme 1.1**)[21]. Notably, upon oxidation, thioether-containing polymers (heretofore referred to as "polysulfides") becoming significantly more water-soluble due to the increased dipole moment of the S-O bond, which results in a solubility switch of these materials from hydrophobic to hydrophilic and dissolution in aqueous environments. In the presence of higher-reactivity species, such as hypochlorite, chain scission is another degradation mechanism[21,22]. Other notable ROS-responsive functional groups which have been used for biomaterials fabrication include thioketals[23], boronic esters[20], and stable radical scavengers[24,25].

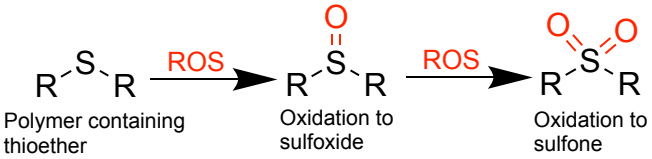

Scheme 1.1: Oxidation of thioether-containing polymers to the sulfoxide and sulfone derivatives.

Poly(propylene sulfide) (PPS) has been a leading polymer in the field since the Hubbell laboratory demonstrated formulation of oxidation-responsive vesicles using block copolymers of PPS and polyethylene glycol (PEG) [26]. Since then, PPS has been used to formulate for nanoparticle delivery of therapeutics in cancer[27], transplant rejection[28], stroke[19], and other conditions. PPS micelles and polymersomes exhibits desirable characteristics for nanoscale drug delivery, including efficient hydrophobic drug loading and high colloidal stability in non-oxidative media. To our knowledge, we are the first group to demonstrate the efficacy of PPS microparticles (MPs) for sustained local ROS scavenging and drug release[18,29,30], indicating that PPS has versatile applications in both systemic and local therapies. Notably, the PPS MPs used

by our lab exhibit a mean diameter <2 μm, meaning they are below the threshold for macrophage uptake[31]. This property can be beneficial in macrophage-driven pathologies, but could also reduce retention in tissues long-term.

As mentioned above, many small molecules exist which mimic native antioxidant mechanisms. A notable example is the stable aminoxyl radical 2,2,6,6-tetramethylpiperidine-1-oxyl (TEMPO), which mimics SOD by reducing $O_2^{\bullet-}$ to H_2O_2 (**Scheme 1.2**), which has been tested clinically to treat cardiovascular disease[32,33] and prevent radiation-induced toxicites[34,35]. However, despite its potency, TEMPO suffers from the same challenges as other small molecules, including poor circulation half-life and tissue distribution. Therefore, many groups have investigated strategies to improve TEMPO pharmacokinetics, including PEGylation[25] and core-shell NP fabrication[3638]; these preparations reduced inflammation in rodent models of ischemia-reperfusion injury. These results demonstrate the potential for SOD mimics, including TEMPO, to treat ROS-driven inflammation.

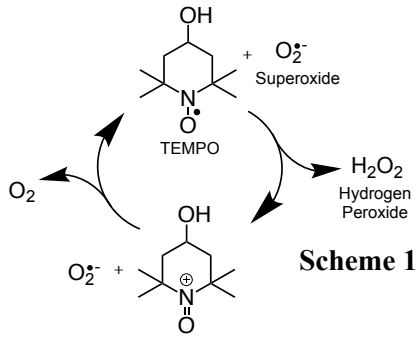

Scheme 1.2: Scavenging of superoxide by TEMPO.

Another strategy to improve drug pharmacokinetics is the fabrication of a drug-eluting depot which is implanted or injected at the disease site to provide sustained release of the therapeutic. Large depots can resist clearance from the injection site, simultaneously increasing drug concentration in the tissue of interest and reducing systemic exposure and potential off-target effects. Hydrolytically degradable polyesters, particularly poly(lactic-go-glycolic acid)

(PLGA), are the current gold standard for this application, with >20 approved clinical products, 12 of which are drug-loaded microparticles[37,38]. Because of the wide availability and clinical approval of PLGA, its tunability via lactide:glycolide ratio and molecular weight, and its biodegradability, this polymer is an attractive candidate for biomedical applications. However, there are well-documented drawbacks of PLGA, including acidic degradation products which can lower local pH[39], elicit foreign-body response[40], and activation of immune cells[41].

Controlling the pharmacokinetics and biodistribution of therapeutics via polymer and material design is essential to broadening the therapeutic landscape for difficult-to-treat diseases. Two candidate diseases which are ripe for innovation are osteoarthritis (OA) and glaucoma. Both diseases are chronic and degenerative, requiring long-term tissue protection. Additionally, the affected tissues (synovial joints and retina/optic nerve, respectively) are difficult to access systemically, but subject to rapid fluid turnover locally[42,43].

OA is a major cause of disability, which correlates strongly with age and joint injury (post-traumatic OA (PTOA)). The incidence of OA increases from 8% for patients under 44 to 30% in patients 44-65, and again to 50% in patients >65. Joint injury increases the risk of developing OA later in life 3-6x, with patients being diagnosed 10 years earlier in the case of knee PTOA compared to those with no injury history[44]. The major structural changes associated with OA include cartilage degradation, synovial inflammation, subchondral bone remodeling, and osteophyte formation, resulting in pain and loss of function of synovial joints (**Figure 1.1**). OA joints exhibit elevated levels of inflammatory cytokines, including interleukin-1β (IL-1β), IL-6, and TNFα[45]. Additionally, overproduction of proteases, particularly matrix metalloproteinases (MMPs, break down collagen[46]) and a disintigrin and metalloproteinase with thrombospondin motifs (ADAMTS, break down proteoglycans[47]) result in net catabolism of

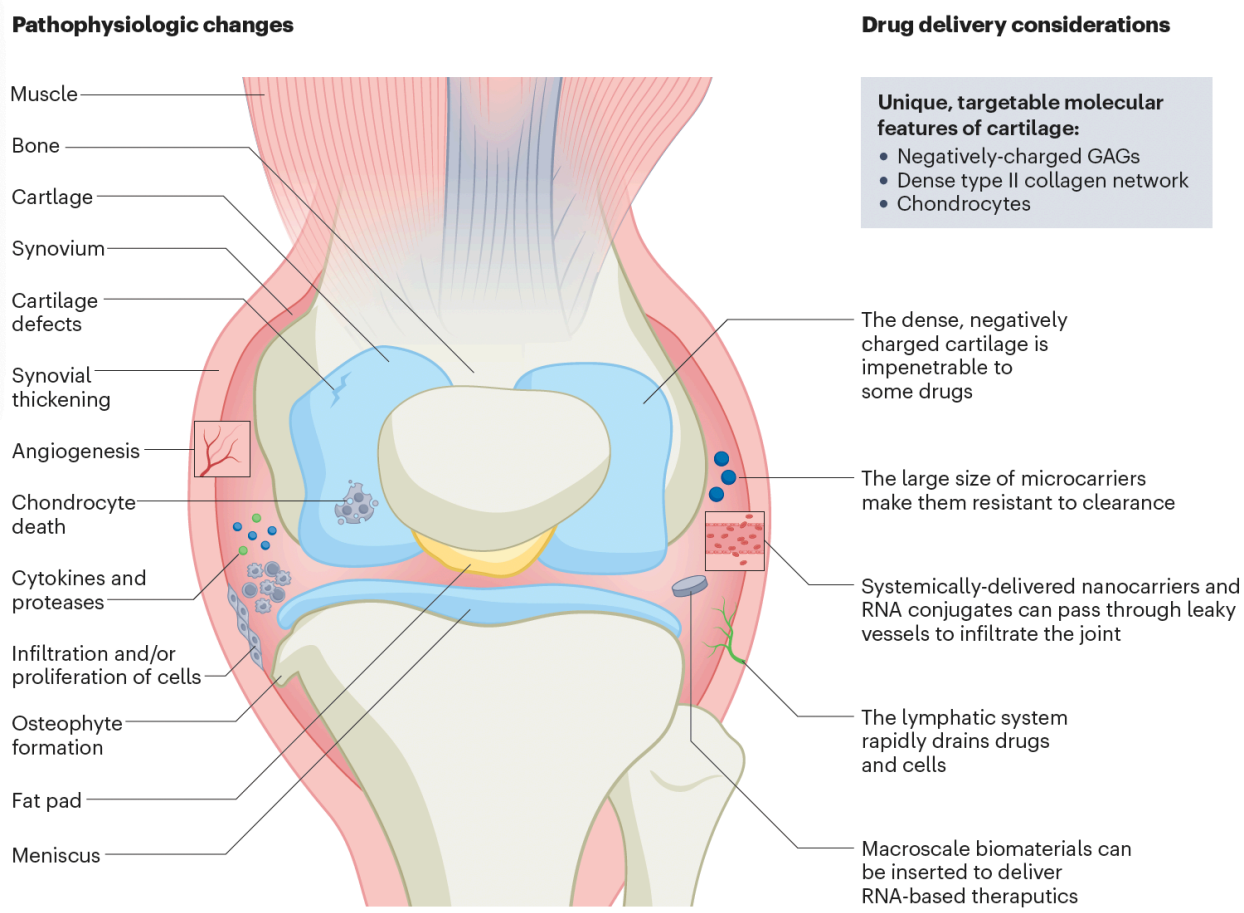

Figure 1.1: Osteoarthritis pathology.
Osteoarthritis (OA) is characterized by joint remodelling mediated by cartilage catabolism, bone spur formation and thickening of the synovium. Other features include the upregulation of pro-inflammatory cytokines and proteases, as well as blood vessel formation. Targets for disease-modifying OA drugs exploit these features through the development of size-based and charge-based carriers that localize to the arthritic joint and deploy therapeutic payloads. Intra-articular localization of therapeutics can be achieved through biomaterial encapsulation (such as the use of hydrogel or microparticle systems) or via systemic delivery through leaky vessels. GAGs: glycosaminoglycans.

cartilage and loss of matrix. In the synovium, synovial fibroblasts proliferate significantly[48]; this expansion combined with immune cell influx results in capsule thickening, particularly in PTOA. Expanded synovial fibroblasts also serve as a source of cytokines and proteases to drive pathology. Cellular senescence as a result of natural aging or injury has gained interest in recent years, with senescent cells producing senescent-associated secretory phenotype (SASP) factors to influence adjacent cells and tissues[49] and worsen OA.

Current standard of care focuses on alleviating pain, instead of halting or reversing joint tissue damage. For example, patients with mild OA often take oral non-steroidal anti-inflammatory drugs (NSAIDs) which are affordable and convenient; however, frequent use is correlated with gastrointestinal and cardiovascular risk, especially in patients with susceptibility factors[50]. Another common strategy is intra-articular injection of corticosteroids, which have been shown to prevent glycosaminoglycan (GAG) loss[51,52] and reduce MMP activity[53]. However, these benefits have not been demonstrated clinically, and the major benefit of corticosteroid injection remains pain relief (4-8 week duration[54]). Notably, repeat corticosteroid injection has been correlated to cartilage thinning in humans[55], and recent data has shown that suppression of glucocorticoid signaling in chondrocytes attenuated PTOA in mice[56]. Viscosupplementations with hyaluronic acid (HA), platelet-rich plasma (PRP) administration, or mesenchymal stem cell (MSC) injection are other intra-articular treatment strategies, but evidence for their efficacy is mixed[57-59]. End-stage disease is treated with total joint arthroplasty, a remarkably safe and effective procedure resulting in 80-90% patient satisfaction[60]. However, the economic burden is significant, with joint arthroplasty procedures representing 3.2% of total procedures and 69% of the total cost of treating OA[61].

ROS also contribute to OA pathology through a variety of mechanisms. In OA patients and animal models, OA cartilage and fluids exhibit significantly more ROS-induced DNA damage, lipid peroxidation, nitrotyrosine, and nitrated products than healthy controls[8]. Along with direct biomolecule damage, elevated ROS levels can aberrantly oxidize cysteine- and methionine-containing proteins, changing their function or rendering them inactive[62]. Through this second messenger role, ROS contribute to inhibited matrix synthesis, inhibited growth factor bioactivity, and activation of MMPs. ROS is implicated in the activation of the NFκB and mitogen activated kinase/ extracellular signal-regulated kinase (MEK/ERK) pathways, while

inhibiting the phosphatidylinositol 3-kinase (PI3)/ Akt pathway[7,63-65]. Additionally, ROS are important in activation of c-Jun n-terminal kinase (JNK) and MMP1 by IL-1 and TNFa[7]. These consequences of oxidative stress are key to propagating the cartilage destruction and inflammation driving OA.

Like OA, glaucoma is a progressively degenerative disease, resulting in optic nerve degradation and declining vision. Approximately 3.5% of the global population aged 40-80 years is affected by glaucoma, and incidence is projected to increase with an aging population[66]. The pathogenesis of glaucoma is still being elucidated; known risk factors include age, race, genetic predisposition, family history, and cardiovascular comorbidities. Along with these, the most relevant risk factor is sensitivity to elevated intraocular pressure (IOP), which causes damage to the optic nerve and leads to retinal ganglion cell (RGC) axonopathy and death (**Figure 1.2**)[67,68]. Elevated IOP increases strain on the optic nerve head, leading to posterior deformation[69]. However, increased IOP is not required for glaucoma development, and lowering IOP does not

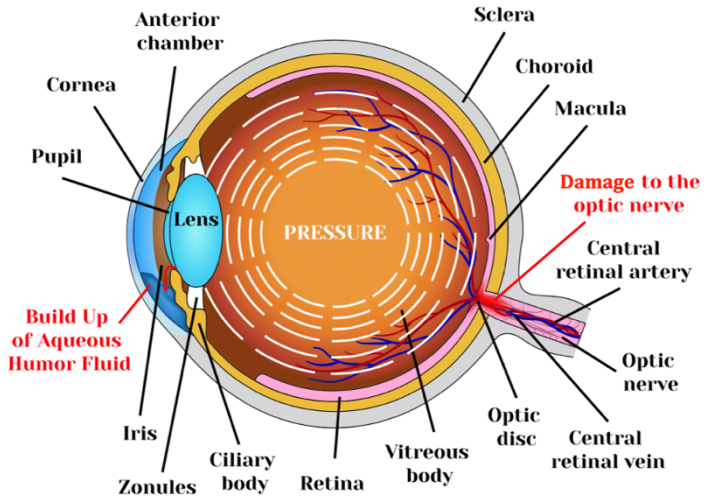

Figure 1.2: Glaucoma pathology.
In the glaucomatous eye presenting with elevated intraocular pressure (IOP), the trabecular meshwork responsible for aqueous humor turnover becomes impaired, causing buildup of fluid. The increased IOP applies strain to the optic nerve head, resulting in mechanical tissue damage, retinal ganglion cell (RGC) death, optic nerve degeneration, and vision loss. Image adapted from https://www.inmedpharma.com/learn/what-is-glaucoma/.

always prevent disease progression[70]. The two major phenotypes are primary open angle glaucoma (POAG) and primary angle-closure glaucoma (PACG). The two types represent differences in fluid blockage: in POAG, the trabecular meshwork resists aqueous humor drainage[71], while in PACG both the trabecular meshwork and uveoscleral drain are blocked[72]. Glaucoma is primarily detected clinically by examining the optic disc for changes indicating RGC loss, and visual field tests are also used to assess optic nerve function, though loss of vision typically occurs later in the disease[71].

Current treatments for glaucoma focus on lowering IOP by pharmacological or surgical methods[73]. Typically, topical prostaglandin analogues are the first-line treatment; these drugs increase aqueous humor outflow by the uveoscleral pathway[74]. If patients have poor tolerance for prostaglandin analogues, α-adrenergic agonists or β-adrenergic blockers can be used. However, these treatments, particularly β-adrenergic blockers, can present with significant systemic side effects and are contraindicated in patients with certain comorbidities including chronic pulmonary obstructive disease asthma, and bradycardia[73]. If topical treatment does not achieve the desired reduction in IOP (20-50%), laser or incisional surgery is pursued. Surgical intervention differs between POAG and PACG. POAG surgeries focus on increasing flow through the trabecular meshwork, either by inducing biological changes using laser trabeculoplasty[75] or removing part of the tissue by trabeculotomy[76]. In PACG, laser peripheral iridotomy creates a full-thickness hole in the iris to alleviate blockage. Pharmacological and surgical management of IOP has been shown to slow disease progression; however, a significant portion of patients continue to progress towards blindness[77].

Similar to OA, ROS have been shown to play a key role in glaucoma pathogenesis. In animal models, increased IOP induces retinal oxidative stress measured by upregulated ROS levels, reduced antioxidant proteins, and increased lipid peroxidation[78,79]. The trabecular

meshwork cells of glaucoma patients exhibit increased oxidative DNA damage compared to healthy controls, and both IOP increase and visual field damage are significantly related to the extent of oxidative damage to these cells[80,81]. *In vivo* perfusion of trabecular meshwork cells with H_2O_2 causes an increase in resistance to aqueous humor outflow[82]. ROS can also damage RGCs and other cells of the optic nerve; animal models have shown increased oxidative molecular damage and apoptosis in the neural tissue[78,83,84]. These pathological changes lead to axonopathy, increased IOP, optic nerve degeneration, and eventual visual field loss.

In sum, ROS represent a druggable target for many inflammatory and degenerative diseases. The versatility of polymeric systems and incorporation of ROS-scavenging chemistries make them highly adaptable to challenging pathologies. Both OA and glaucoma are demonstrably influenced by oxidative stress, and the localized, chronic nature of these diseases require therapies which are long-acting and achieve high therapeutic concentrations at the tissue of interest. The overall goal of this work is to systematically interrogate polymer composition for *in vivo* antioxidant activity and delivery of biologic therapeutics.

1.2. Specific Aims

1.2.i. Specific Aim 1: Optimize an antioxidant TEMPO copolymer for ROS scavenging and anti-inflammatory effects in vivo

Polymeric TEMPO (2,2,6,6-tetramethylpiperidine-1-oxyl) was synthesized via reversible addition-fragmentation chain transfer (RAFT) polymerization with the hydrophilic spacer monomer dimethylacrylamide (DMA). A series of polymers with varying ratios of DMA:TEMPO were generated and characterized for hydrophilicity and ROS scavenging potential. *In vitro* assays demonstrated the optimal composition for bioactive antioxidant activity at 40 mol% TEMPO/ 60 mol% DMA. This formulation was locally administered in the mouse carrageenan air pouch model of inflammation, where it was significantly retained compared to

free drug, provided superoxide scavenging, and reduced exudate TNFα levels. The optimize polymer also reduced ROS after systemic delivery in an inflammatory footpad model.

1.2.ii. Specific Aim 2: Optimize new polysulfide chemistries and formulation approaches to enable production of large, ROS scavenging microparticles with high biologic drug loading

Polypropylene sulfide (PPS) and copolymers of propylene sulfide (PS) and ethylene sulfide (ES) were synthesized via anionic ring-opening polymerization. Polymer crystallinity was characterized, and microparticles were formulated using the oil-in-water (O/W) technique. MP size and morphology were evaluated using scanning electron microscopy (SEM), and oxidation of PPSES MPs was evaluated by SEM and elemental mapping. Drug loading of proteins and small interfering RNAs (siRNAs) was optimized using water-in-oil-in water (W/O/W) and solid-in-oil-in-water (S/O/W) emulsion techniques. An optimal formulation for each cargo was selected based on size, oxidation response, and drug loading.

1.2.iii. Specific Aim 3: Test efficacy of ROS scavenging for local therapeutic delivery to reduce tissue damage in models of glaucoma and post-traumatic osteoarthritis

PPSES MPs loaded with the protein erythropoietin (EPO) were tested in a mouse model of glaucoma. Three formulations (generations 1-3) demonstrated promising results in this model, including sustained EPO release and reduction of retinal hydrogen peroxide. PPSES delivery of EPO also protected the optic nerve from degeneration and improved visual function measured by electrophysiology. The optimized formulation was tested for safety and injectability in a non-human primate model. Next, PPSES MPs were used to deliver small interfering RNA (siRNA) against either the senescence marker Cdkn2a or the protease matrix metalloproteinase-13 (MMP13). MP delivery increased target knockdown compared to free siRNA after a single injection, and MMP13 knockdown improved bone, cartilage, and synovial morphology.

Chapter 2: Optimization of a bioactive TEMPO copolymer for ROS scavenging and anti-inflammatory effects *in vivo*

2.1. Introduction

ROS encompass oxidizing compounds with oxygen as the REDOX center and include free radicals such as $O_2^{\bullet-}$ and hydroxyl radical ($OH^{\bullet}$), as well as non-radical species such as H_2O_2 and hypochlorite ion (OCl^-)[3,4,85]. Oxidative stress occurs when ROS levels overwhelm cells' ability to neutralize them through natural antioxidant mechanisms[86], and is implicated in a wide variety of chronic inflammatory diseases, including rheumatoid arthritis (RA), cancer, diabetes, and atherosclerosis[12-14,87]. A key innate defense against oxidative stress is SOD enzyme, which catalyzes the conversion of $O_2^{\bullet-}$ to the less reactive H_2O_2[88]. SOD has garnered interest as a therapeutic candidate, but suffers from short half-life *in vivo*, an inability to cross cell membranes, and the need to be produced by recombinant techniques, all of which limit its therapeutic usefulness and practicality[17].

A strategy to recapitulate SOD activity is to use small molecule mimetics of SOD for $O_2^{\bullet-}$ scavenging. These alternatives tend to be less expensive and more synthetically versatile. The small molecule TEMPO has garnered interest as a SOD mimetic due to its catalytically active, stable aminoxyl radical. Clinically, a hydroxy-functionalized TEMPO derivative (Tempol) has been tested for its ability to prevent radiation-induced toxicities[34,35] and treat cardiovascular disease[32,33]. Preclinically, targeting of TEMPO to mitochondria (MitoTEMPO[89]) has demonstrated efficacy in diabetic cardiomyopathy[90] and hypertension[91], among other conditions[92-94]. However, TEMPO presents similar circulation and tissue clearance challenges as SOD and most small molecules. Therefore, in this work, we sought a facile strategy to

polymerize TEMPO while maintaining its bioactivity, characterizing a series of copolymers for optimal TEMPO content and ROS scavenging (**Scheme 2.1**).

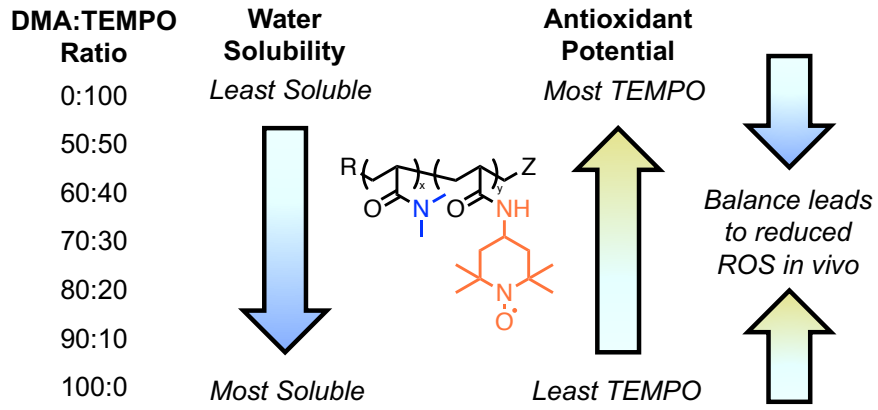

Scheme 2.1: Schematic depicting compositional tuning strategy for TEMPO copolymers. From[24].

2.2. Results and Discussion

2.2.i. Generating a series of DMA-co-TEMPO polymers with precise control of TEMPO content

To tune the water solubility of TEMPO copolymers, TEMPO was copolymerized in varying ratios with the hydrophilic spacer monomer N,N-dimethylacrylamide (DMA). A series

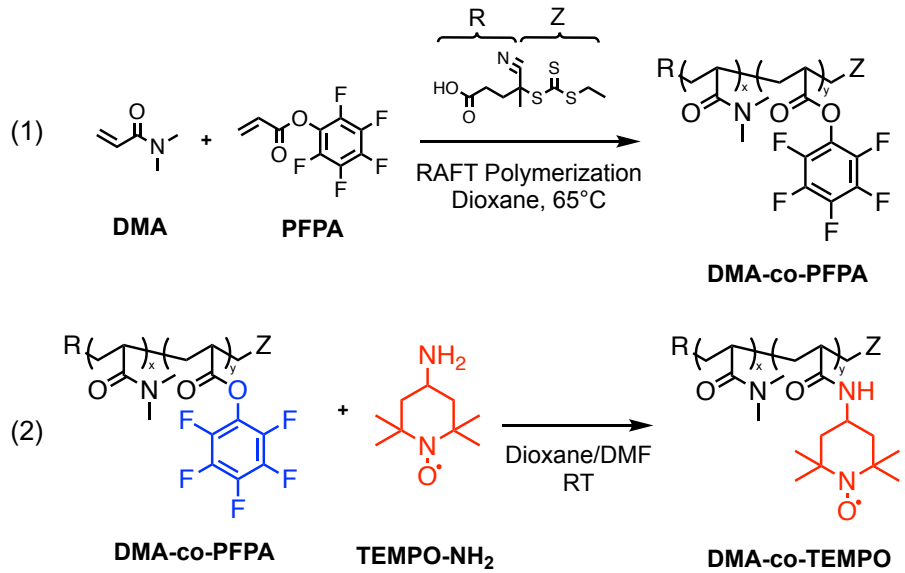

Scheme 2.2: Two-step synthesis scheme of DMA-co-TEMPO polymers.
(1) RAFT polymerization of DMA and PFPA and (2) post-polymerization substitution of TEMPO-amine for PFPA. Data from[24].

of DMA-co-TEMPO copolymers with TEMPO content ranging from 0 to 100 mol% was synthesized according to the two-step synthesis scheme shown in **Scheme 2.2**. First, DMA monomer and amine-reactive pentafluorophenylacrylate (PFPA) monomer were copolymerized via reversible addition-fragmentation chain transfer (RAFT) polymerization at varied monomer feeds (0, 50, 60, 70, 80, 90, 100 mol% DMA) to control the random copolymer composition (**Supplementary Figure A.1 -7**, **A-B**). After RAFT polymerization, amino-TEMPO was conjugated through the pentafluorophenyl (PFP) ester onto the polymer backbone. The removal of PFP was confirmed by ^{19}F NMR (**Figure 2.1** and **Supplementary Figure A.1-7, C-E**). Broad ^{19}F signal represents polymerized PFPA, with sharp shifted peaks representing a small fraction of spontaneously hydrolyzed PFP (δ= -163.75, -164.98, and -170.62 ppm) [95]. The series of polymers is henceforth defined based on TEMPO target content: 0T indicates 0 mol% TEMPO and 100 mol% DMA, 40T indicates targeting of 40 mol% TEMPO and 60 mol% DMA, etc.

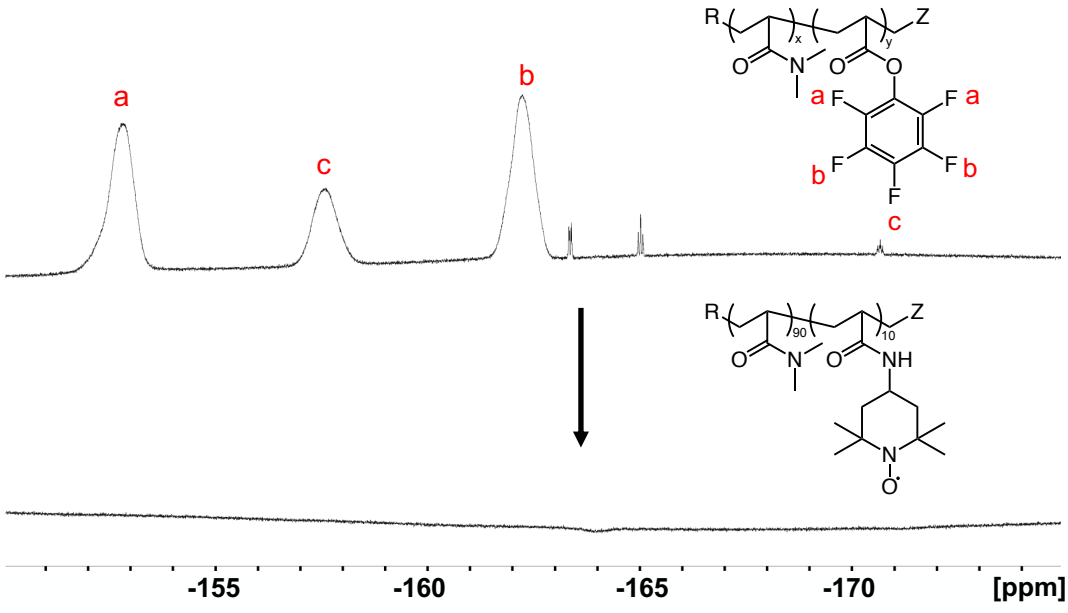

Figure 2.1: TEMPO conjugation to DMA-co-PFPA backbone.
DMA-co-TEMPO copolymers were synthesized according to **Scheme 2.2** with the sacrificial monomer pentafluorophenyl acrylate (PFPA). ^{19}F NMR confirming removal of PFPA units on the final polymer after TEMPO conjugation. Data from[24].

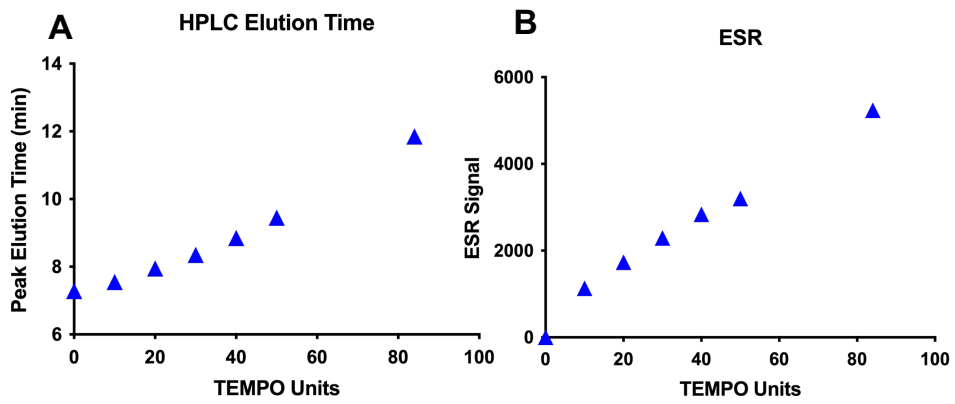

Figure 2.2: Tunability of DMA-co-TEMPO series.
(**A**) Polymers were run on high performance liquid chromatography (HPLC) with an increasingly nonpolar solvent gradient to indirectly determine relative hydrophobicity of the series. Elution time increases with TEMPO density. (**B**) Electron spin resonance (ESR) to detect stable aminoxyl radical demonstrates active TEMPO conjugated in controllable density to the polymer backbone. Data from[24].

The polymers were characterized for molecular weight (MW) and polydispersity by GPC (**Supplementary Figure A.8**). High performance liquid chromatography (HPLC) was used to determine the relative polarity of the polymers, with elution in a progressively nonpolar solvent gradient acting as an indirect measure of hydrophilicity. As TEMPO content of the series increased, elution time increased, indicating TEMPO content increases hydrophobicity of the polymers (**Figure 2.2A**). This data agreed with octanol/water partition experiments, in which the partition coefficient (logP) trended upwards as TEMPO density increased (**Supplementary Figure A.9**). These data indicate that higher TEMPO density on the polymers makes them less water soluble, in line with previous reports that TEMPO homopolymers are insoluble in water at physiological pH[96,97]. To confirm copolymer radical activity, we used electron spin resonance (ESR) to detect the aminoxyl radical of TEMPO with high sensitivity and specificity[98,99]. As expected, with increasing TEMPO content, the intensity of the ESR signal increased (**Figure 2.2B**). Additionally, the ESR spectra gradually broadened as TEMPO density on the backbone increased, due to the spin-spin interaction of the closely packed radicals[97,100] (**Supplementary Figure A.10**). These data confirm that active TEMPO was incorporated by post-polymerization

modification and that the relative TEMPO density on the polymers correlated to the monomer feed of PFPA in the RAFT reaction. Overall, a set of polymers was generated with targeted ratios of DMA:TEMPO ranging from 0:100 to 100:0, to be used to evaluate the optimal TEMPO density for biological activity.

2.2.ii.Optimizing TEMPO density for in vitro $O_2^{\bullet-}$ scavenging

After synthesizing the copolymer library, we set out to determine the effect of TEMPO backbone density on $O_2^{\bullet-}$ scavenging. We characterized both the general reducing potential via the ferric reducing antioxidant power (FRAP) assay[101] and $O_2^{\bullet-}$-specific scavenging using ferricytochrome C. By matching the dose of polymers at 20 μg, it was demonstrated that the 20T-40T polymers had the highest activity, with intermediate levels for 50T and 10T, and significantly reduced activity for 100T (**Figure 2.3A-B**). In the study of dose-matched TEMPO (170 μM), the activity of the polymers increases as TEMPO density decreases, indicating that the polymers are more active as they become more water-soluble (**Figure 2.3C-D**), correlating with HPLC polarity analysis. Notably, there was a plateau with similar $O_2^{\bullet-}$ scavenging activity between 40-10T indicating that the activity of TEMPO was not limited by polymer solubility within this composition range at the concentration tested (**Figure 2.3D**). Taken together, these data define the structure-function relationship between TEMPO density on the polymer backbone and its relative bioavailability for $O_2^{\bullet-}$ scavenging. At 100 or even 50% TEMPO, activity is suppressed due to poor water solubility. However, if DMA content is too high (20 or 10% TEMPO), the radical density is too low for optimal activity on a polymer per mass basis.

To our knowledge, only one other study has investigated the effect of TEMPO density on a polymer backbone for ROS scavenging activity[102]. Yoshitomi et al. conjugated TEMPO to a poly(chloromethylstyrene) (PCMS) backbone with Tempol at densities ranging from 22-93% and

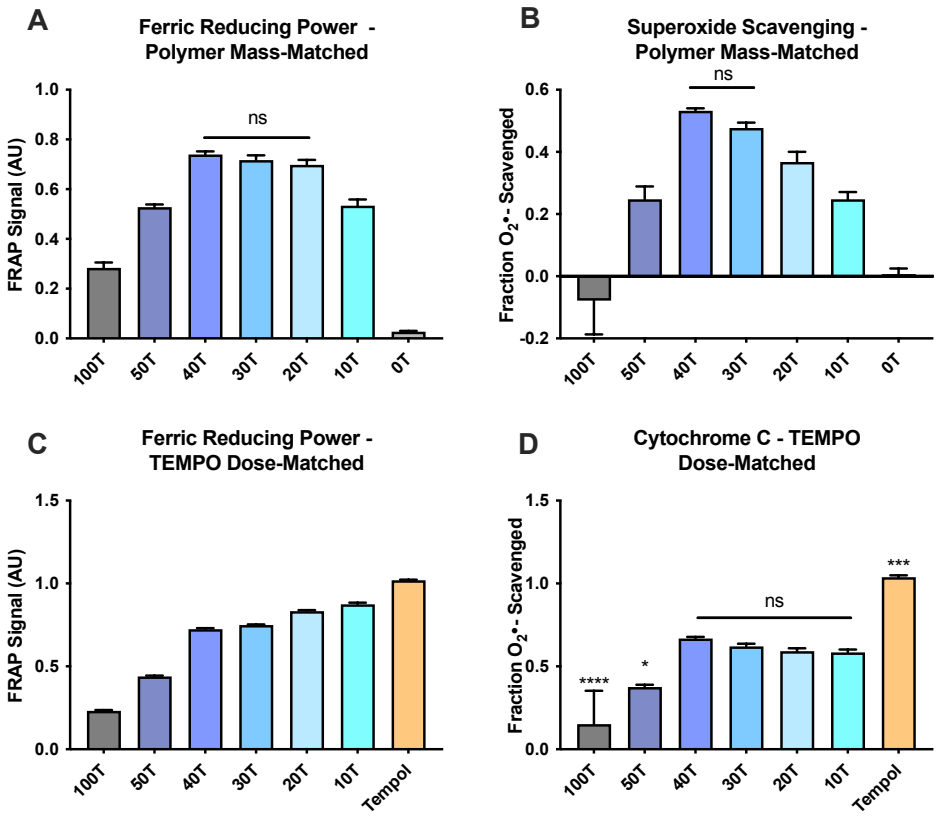

Figure 2.3: Cell-free radical activity of DMA-co-TEMPO series.
(**A** and **B**) General ferric reducing power (FRAP, **A**) and superoxide scavenging (**B**) of library for polymer mass-matched scenarios (0.2 mg/ml). (**C** and **D**) FRAP (**C**) and superoxide scavenging (**D**) for TEMPO dose-matched (170 μM) scenarios. Ns = not significantly different. * = significantly different from 10-40% TEMPO polymers. *p<0.05, ***p<0.001, ****p<0.0001. Data from[24].

coated the resulting polymer onto glass nanobeads. The authors found that increased TEMPO density increased the level of $O_2^{\bullet-}$ scavenging, in contrast to our finding that an intermediate level of TEMPO grafting is optimal. However, solubility was not a controllable parameter for their system, as the PCMS backbone rendered all polymers hydrophobic regardless of TEMPO density. Therefore, to our knowledge, this is the first demonstration of tuning TEMPO density and subsequent water solubility to optimize radical potential and $O_2^{\bullet-}$ scavenging of unimeric polymers in solution.

We further probed the activity of the polymers in cell-based assays using the ATDC5 chondrogenic cell line. All DMA-co-TEMPO copolymers were non-cytotoxic up to a dose of 5

mg/ml (**Supplementary Figure A.11)**. Additionally, confocal microscopy with Cy5-labeled polymers demonstrated increased signal at 40T compared to lower TEMPO backbone densities (**Figure 2.4A**). Cells were washed thoroughly before imaging to remove surface-associated polymer. To compare directly with small molecule Tempol, the experiment was repeated without washing, because Tempol diffuses out of cells rapidly during washes[103]. Cells were scanned by ESR, confirming the increased uptake of 40T compared to other formulations and Tempol (**Figure 2.4B**), though this method does not differentiate between surface-associated and internalized polymer. Notably, 50T and 100T polymers could not be analyzed for cell uptake due to their formation of large, insoluble aggregates in aqueous solution. These observations indicate that the balance of hydrophobic and hydrophilic character is necessary for optimal cell uptake.

The effect of hydrophobicity on cell uptake has been observed for other polymer libraries, including poly(2-oxazoline) (POx) amphiphiles[104], Pluronics[105], and alkyl-grafted anionic polymers[106]. For fully water-soluble POx polymers, Luxenhofer et al. found that more hydrophobic polymers exhibited higher levels of cell uptake in MCF7-ADR cells[104], whereas Batrakova et al. demonstrated that Pluronics with intermediate hydrophobic (poly(propylene oxide)) block lengths were best internalized by bovine brain microvessel endothelial cells[105]. Dailing et al. demonstrated that polymer cell uptake of amphiphiles with varying alkyl side chain density correlated with hydrophobicity up to a threshold point; there was monotonic increase in uptake of the polymers themselves as a function of alkyl length for all alkyl densities tested (10, 30, and 50 mol%), up until polymer solubility was lost (50 mol% density with dodecyl alkyl length) [106]. These studies support the idea that copolymers with hydrophilic and hydrophobic monomers can be tuned to modulate cell uptake. Though a detailed examination of uptake mechanism is outside the scope of this study, we speculate that the increased hydrophobic

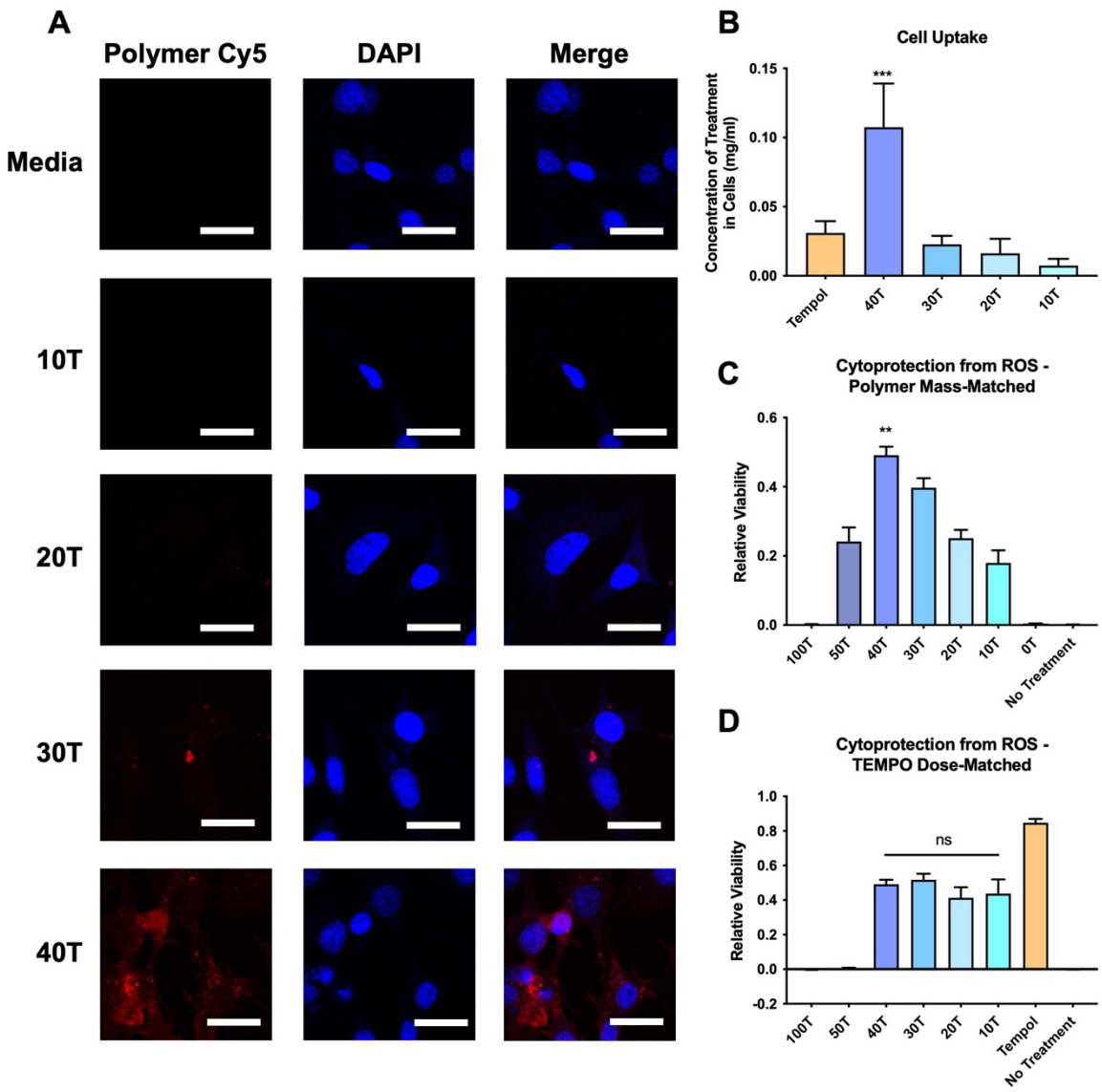

Figure 2.4: Cell uptake and protection of DMA-co-TEMPO series.
(**A**) Cell uptake of Cy5-labeled polymers observed by fluorescent microscopy after 24 hour treatment. 40T exhibits the highest Cy5 signal. (**B**) Cell uptake results were confirmed by ESR. Signal was normalized to inherent TEMPO signal to control for variable backbone density of TEMPO and allow for direct comparison between treatments. (**C** and **D**) Cytoprotection from ROS-induced cell death in polymer mass-matched (**C**, 0.2 mg/ml) and TEMPO dose-matched (**D**, 170 μM) scenarios. * = significantly different from all other groups. **p<0.005, ns = not significantly different. Data from[24].

character of the 40% TEMPO polymer allows for increased interaction with the lipids of the cell membrane (supported by the measured logP value near 0, **Supplementary Figure A.9**).

Luxenhofer et al. also showed that uptake of POx amphiphiles was significantly inhibited at

4°C[104], indicating active endocytosis is required for polymer uptake, which could explain the improved level over small molecule Tempol, which enters cells through passive diffusion[107].

One effect of excessive $O_2^{\bullet-}$ is the induction of cell apoptosis. The mechanisms for $O_2^{\bullet-}$-induced cell death include cytochrome C release from mitochondria and increased activity of caspase, NF-κB, and p38 mitogen-activated protein kinase (MAPK) [108,109]. To quantify the cell protective effect of DMA-co-TEMPO copolymers, we treated ATDC5 cells with 1 mM 3-morpholinosydnonimine (SIN-1), which can result in $O_2^{\bullet-}$, nitric oxide, and peroxynitrite in solution[110,111]. This treatment caused ~100% cell death with no scavenger present, but 20 μg 40T polymer rescued viability to ~49% of the non-ROS treated controls, with less effectiveness of other weight-matched polymers in the series (**Figure 2.4C**). In the TEMPO dose-matched scenario (**Figure 2.4D**), 170 μM TEMPO delivered in the soluble polymeric formulations (10-40T) demonstrated 41-52% cell rescue (no significant differences). These functional results demonstrate the benefit of tuning TEMPO density on the polymer backbone for cytoprotection from exogenous $O_2^{\bullet-}$.

Cellular protection from ROS-induced cell death has been demonstrated for a variety of ROS scavenging polymers. The majority of studies have utilized polymers formulated into biomaterials like hydrogels, nano/microparticles, or coatings, as opposed to solubilized unimeric polymers. A nanoparticle with TEMPO and phenylboronic acid pinacol ester (PBAP) functionalities significantly reduced RAW264.7 macrophage apoptosis in response to H_2O_2[20]. In an interesting application, Yoshitomi et al. coated a TEMPO homopolymer onto cigarette filters and measured the cytotoxicity of the resulting smoke extract, finding that ROS scavenging of the filter significantly reduced Caco-2 cell death[96]. However, these applications represent integration of the ROS-responsive polymer into a more complex system. The few studies that have

investigated free polymers in solution have focused on naturally derived antioxidants. Oligomeric and polymeric procyanidins, a type of flavonoid found in grapes, can protect HepG2 cells from *tert*-butyl hydroperoxide (TBHP)-induced cell death[112], and seaweed-derived agaro-oligosaccharides rescue liver L-02 cells from cytotoxicity of H_2O_2[113]. Our DMA-co-TEMPO system provides a simple, readily scalable, and chemically well-defined synthetic polymeric antioxidant that can be readily utilized for parenteral or intravenous (i.v.) delivery, with the 40T composition providing the best antioxidant activity *in vitro*.

2.2.iii. Anti-inflammatory effects of optimized TEMPO copolymer in vivo

To evaluate the anti-inflammatory effects of the polymer lead candidate after both local and systemic administration, we utilized the inflammatory compound carrageenan. First, we implemented the mouse air pouch model for local injection (**Figure 2.5A**) [39]. A preliminary dose-finding study identified 5 mg/animal as an appropriate dose for the 40T treatment based on tumor necrosis factor α (TNFα) levels and polymer retention in the exudate (**Supplementary Figure A.12A-B**). To evaluate our lead candidate 40T polymer, 40T, 100T, and free Tempol were co-injected with carrageenan in the air pouch. TEMPO dose was matched across treatments (8.48 μmol/animal). After 6 hours, polymer retention in the pouch was measured by ESR, demonstrating full clearance of the small molecule Tempol, ~12% retention of 40T, and ~94% retention of 100T (**Figure 2.5B**). Additionally, TNFα levels in the pouch exudate were significantly reduced with 40T compared to no treatment and Tempol (**Figure 2.5C**). After 24 hours, 40T significantly reduced ROS levels in the exudate to baseline levels, with no effect of saline, Tempol, or 100T (**Figure 2.5D**). We interpret the stronger anti-inflammatory effect of the polymeric over free small molecule Tempol to be due to the improved retention of the polymer in the air pouch, allowing for extended ROS scavenging and suppression of inflammation. It is interesting to note that the impressive retention of 100T is an effect of its insolubility and

aggregation, yielding retention in an inactive form within the air pouch. The inability of this polymer to significantly reduce TNFα or ROS levels despite its excellent retention further supports the conclusion that optimizing the density of TEMPO on the polymer backbone is crucial for anti-inflammatory activity *in vivo*.

The efficacy of antioxidant therapy in the air pouch model has been investigated by others. Drugs including 10-(6'-plastoquinonyl)decyltriphenylphosphonium bromide (SkQ1), *Cressa cretica* extract, TS-13 (a *tert*-butyl phenol thiosulfonate), and atorvastatin have shown anti-inflammatory effects in this model[114-117]. These results are promising; however, all of these treatment options required prophylactic administration 1 hour or 1-10 days (daily) before carrageenan injection to achieve therapeutic efficacy. In contrast, co-administration of our optimized TEMPO copolymer reduced both $O_2^{\bullet-}$ and TNFα levels in the air pouch by ~90 and ~83% respectively. In another example of co-administration, the novel small molecule 4b,9b-dihydroxy-6-methoxy-8-(3-oxo-but-1-enyl)-4b,9b-dihydro-5-oxa-indeno[2,1-α]inden-10-one (DMFO) reduced cell infiltration and NO levels in the air pouch. This effect was found to be due to both direct radical scavenging and activation of nuclear factor erythroid 2-related factor 2 (Nrf2) signaling[118]. These results indicate that stimulation of innate cellular antioxidant mechanisms in combination with direct scavenging could be more effective than scavenging alone.

We were also interested in the capability of our polymers to alleviate inflammation with systemic administration. Preliminary intravital microscopy (IVM) studies with Cy5-labeled polymers (200 μg, i.v.) demonstrated that the circulation half-life ($t_{1/2}$) for the water-soluble copolymers (10-40T) trended upwards from ~5.8 to ~17.5 minutes as TEMPO content increased (**Supplementary Figure A.13A**). The $t_{1/2}$ of Tempol has been found to be ~3 minutes, indicating that polymerization improves systemic circulation[119]. 40T and 30T exhibited similar $t_{1/2}$, though

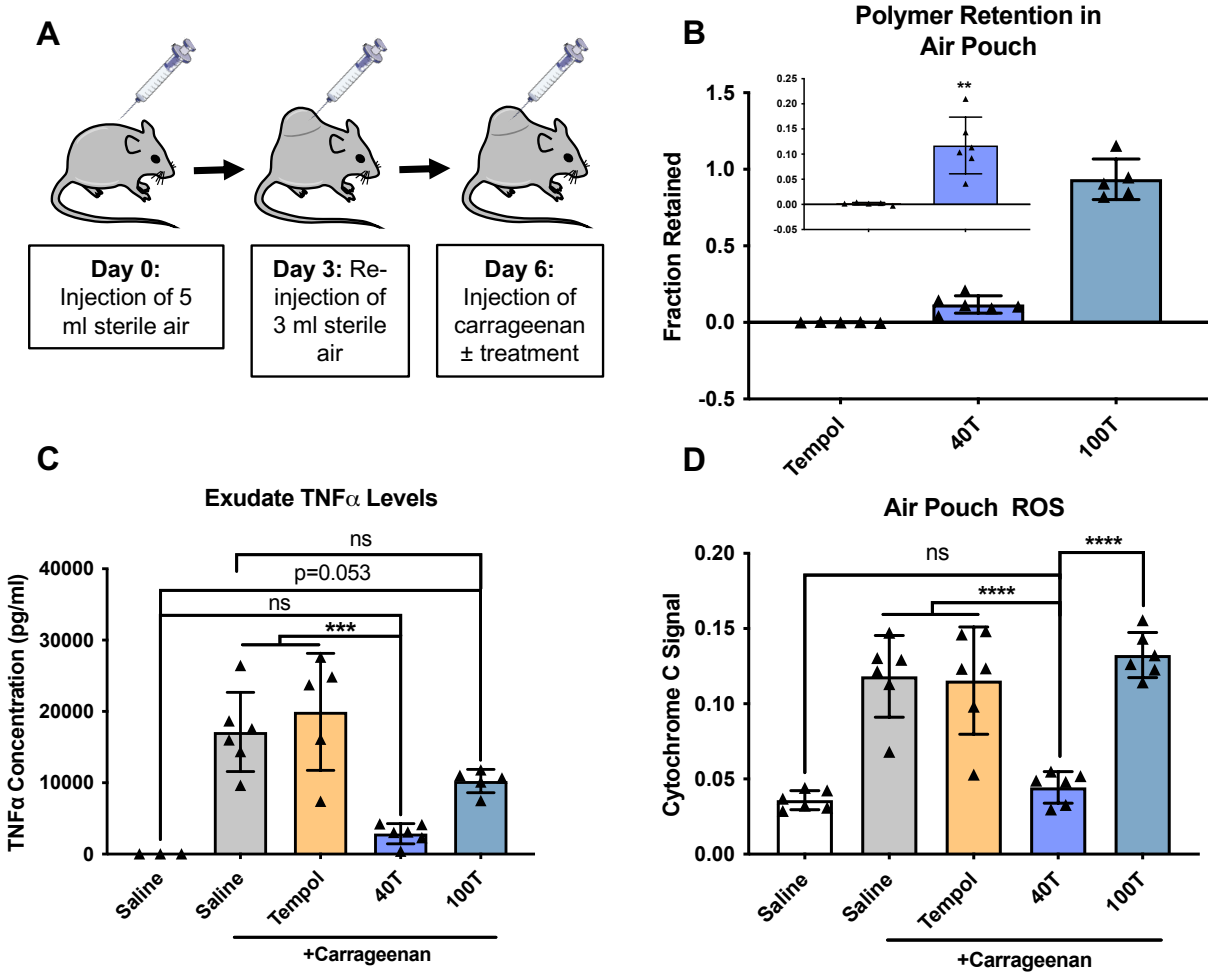

Figure 2.5: Activity of optimized TEMPO copolymer in a local inflammation model.
(**A**) Experimental set up: mice were injected with 5 ml air to establish the air pouch, which was reinjected with air 3 days later. Inflammatory carrageenan ± treatments was injected on day 6. All treatments were matched at a TEMPO dose of 8.48 µmol. (**B**) Polymer retention in exudate 6 hours after carrageenan treatment. Inset = 40T copolymer compared with Tempol. Cell-laden exudate was collected, and polymer content was measured by ESR. (**C**) TNF-a levels in exudate measured by ELISA after separation of exudate fluid from exudate cells. (**D**) ROS levels in air pouch exudate measured by cytochrome C. Fresh exudate was combined with cytochrome C, and absorbance was measured on a plate reader. **p<0.005, ***p<0.001, ****p<0.0001, ns=not significantly different. Data from[24].

30T trended toward having higher kidney and lower liver distribution relative to 40T (**Supplementary Figure A.13B**). Based on these studies, a dose of 200 µg 40T was selected for treatment in the inflammatory footpad model. Tempol and 30T were also injected at a matched TEMPO dose (377 nmol). Carrageenan was injected locally into the footpad of C57/Bl6 mice, and inflammation was allowed to develop for 6 hours before treatment. This treatment regimen

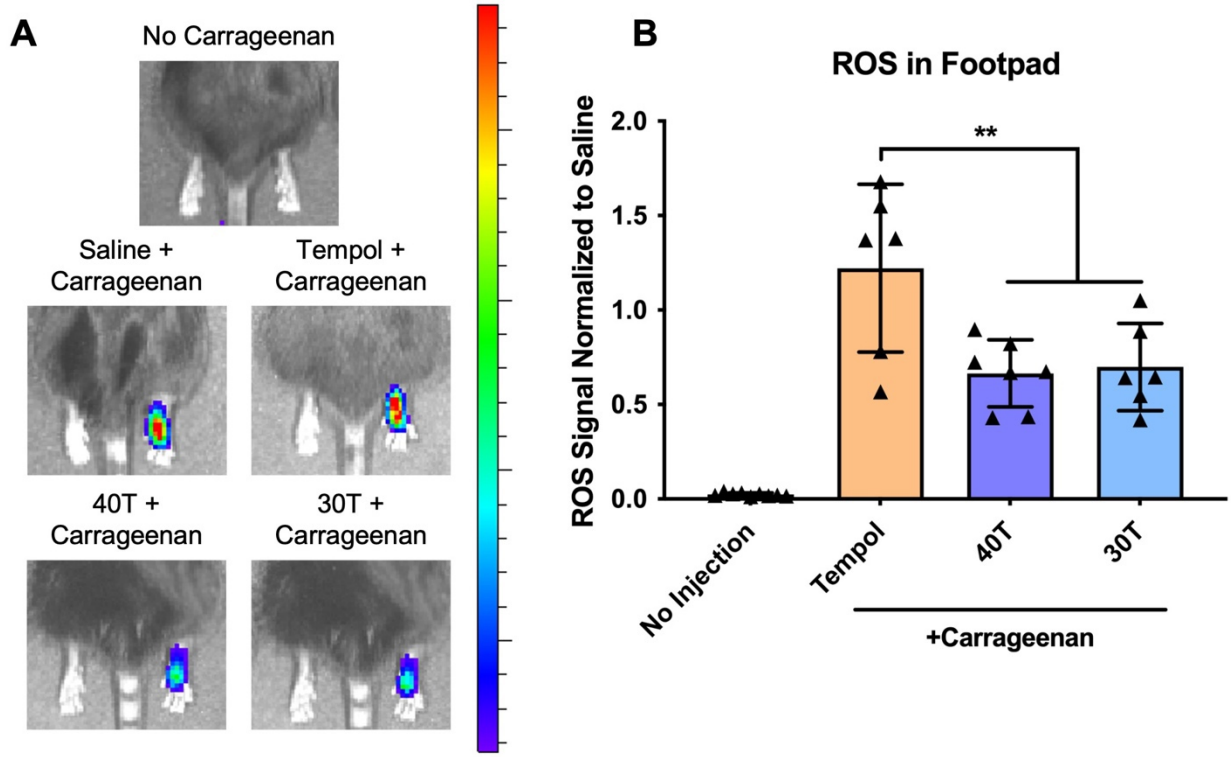

Figure 2.6: Activity of optimized TEMPO copolymer after systemic administration.
(**A**) Representative IVIS images of luminol signal in C57/Bl6 mouse paws after carrageenan injection and polymer treatment. Carrageenan inflammation was allowed to establish for 6 hours, followed by i.v. injection of treatments. All treatments were matched at a TEMPO dose of 377 nmol. (**B**) Luminol signal normalized to carrageenan + saline treated group. **p<0.005. Data from[24].

allows for cyclooxygenase-2 (COX2)-derived prostaglandins to establish high levels of ROS and other inflammatory mediators[120]. Both polymers reduced footpad ROS levels by ~33%, while Tempol had no effect **(Figure 2.6**). Notably, a larger mass dose of 30T (~260 μg vs. 200 μg) was required to achieve this effect than 40T due to its lower TEMPO density. We hypothesize that the circulation time of our polymers allows for improved accumulation and that the larger MW contributes to longer tissue retention in the inflamed footpad over small molecule Tempol. Inflamed tissues encourage passive targeting and retention of therapeutics via the extravasation through leaky vasculature and the subsequent inflammatory cell-mediated sequestration (ELVIS) effect[121,122]. Similar to the enhanced permeation and retention (EPR) effect in tumors, many drugs naturally accumulate in inflammatory tissues, a phenomenon which has been shown to

correlate with increasing polymer drug conjugate molecular weight or nanoparticle packaging[121-125] The ability for our polymers to reduce ROS levels in this aggressive model where inflammation has developed for 6 hours is encouraging for treatment of more established disease.

Antioxidant therapy has been investigated previously in the carrageenan footpad model, with most treatments administered prophylactically (similar to the air pouch model). For example, Chedid et al. demonstrated the ability of vasoactive intestinal peptide (VIP) to reduce cellular ROS production *in vitro* and ameliorate footpad edema *in vivo* when administered 1 day and 1 hour prior to carrageenan injection[126]. Similarly, antioxidant fullerenol nanoparticles[127] and *Ficus exasperata* bark extract[128] significantly reduced edema as a prophylactic treatment. These results support systemic antioxidant treatment for aggressively inflammatory conditions. Notably, our polymers were able to reduce ROS after 6 hours of inflammation, though we did not measure the functional outcome of edema. Additionally, our effect was seen after i.v. administration as opposed to i.p. or oral administration utilized in other studies[126-128].

Others have demonstrated the beneficial effects of polymeric TEMPO formulations in oxidative stress-driven diseases. Much of this work has been pursued by the Nagasaki group, who have formulated TEMPO polymers into nanoparticles, hydrogels, and device coatings[36,96,97,102,129]. These studies have demonstrated the efficacy of TEMPO polymer formulations in cerebral ischemia-reperfusion injury and inflammatory arthritis, among other disease models. Hydrogel and nanoparticle preparations have demonstrated significant improvements in TEMPO retention upon hind paw injection[129] and increased $t_{1/2}$ upon i.v. injection[36], similar to our finding of improved retention in the air pouch and increased systemic $t_{1/2}$ for the polymerized form of TEMPO. Others have investigated TEMPO conjugation to poly(ethylene glycol) (PEG) [25], hemoglobin[130], and β-cyclodextran nanoparticles[20] to improve delivery and efficacy. TEMPO-PEG improved outcomes in a rat ischemia-reperfusion model;

however, pharmacokinetics and therapeutic response was not compared to the free drug[25]. A recent study of a hemoglobin-Tempol polymer demonstrated ability to protect endothelial cells from $O_2^{\bullet-}$-induced cell death, indicating that this system could be promising *in vivo*[130]. Tempol conjugated to β-cyclodextran nanoparticles, in combination with a H_2O_2-scavenging PBAP moiety, significantly improved atherosclerosis outcomes in mice over free Tempol with i.v. injections twice per week[20]. Taken together, these results demonstrate the promise of TEMPO polymers in a variety of disease conditions. However, these preparations (besides TEMPO-PEG) require more complex formulation techniques than our free polymer, which is advantageous formulaically and because advanced carriers, particularly nanocarriers, have been shown to incur off-target effects[131,132]. An additional benefit of our system over a TEMPO-PEG or similar conjugate is the high density of active TEMPO on the polymer backbone, which demonstrated a clear benefit over lower densities (i.e. 10%) and required a lower overall polymer mass *in vivo* (i.e. 40T vs. 30T). Overall, our results demonstrate a simple formulation of TEMPO which has been optimized for therapeutic benefit in inflammation.

2.3. Conclusions

This work provides a structure-function analysis of a series of DMA-co-TEMPO copolymers for aqueous parenteral/local and i.v. administration to treat inflammatory diseases. The balance between hydrophilic character and ROS scavenging potential proved essential to therapeutic outcomes *in vitro* and *in vivo*. Specifically, 40% TEMPO backbone density appears to be a threshold above which increased TEMPO density reduced activity. The 40T composition demonstrated improved local retention in the air pouch model of inflammation, leading to reduced TNFα and ROS levels, while both the 30T and 40T compositions reduced ROS levels in inflammatory footpads with i.v. administration. In both models, the polymer formulations

outperformed free Tempol. The optimized random copolymer is promising to pursue for future testing in more physiologically relevant disease models and as a component of more advanced drug delivery systems such as particulate or bulk biomaterials.

2.4. Materials and Methods

2.4.i. Materials

All reagents were purchased from Sigma Aldrich unless otherwise stated. PFPA, 4-amino-TEMPO, and λ-carrageenan were purchased from TCI America. Cy5 amine was purchased from Lumiprobe. The FRAP kit was purchased from Cell BioLabs, and the Cell TiterGlo kit was purchased from Promega. TNFα enzyme-linked immunosorbent assay (ELISA) kit was purchased from PeproTech Inc.

2.4.ii. Polymer synthesis

Polymers were synthesized by RAFT polymerization. DMA monomer was filtered through basic alumina columns to remove radical inhibitor and stored at -20°C for up to one month before use. DMA, PFPA, 4-cyano-4-(ethylsulfanylthiocarbonyl) sulfanylpentanoic acid (ECT, chain transfer agent (CTA)), 2,2'-azobis(isobutyronitrile) (AIBN, initiator), and trioxane (inert NMR standard) were dissolved in anhydrous dioxane. Each component was added to a flame-dried round bottom flask under constant nitrogen stream at a final concentration of 20% (w/w) reactants. The molar ratio of monomer:CTA:initiator was 100:1:0.5. The reaction mixture was purged with nitrogen for 30 minutes and allowed to react for 18-24 hours at 65°C. The following day, the reaction was cooled to room temperature. 4-amino-TEMPO (1.5 molar excess relative to PFPA units) and dipyridyldisulfide (DPDS) (1.5 molar excess relative to polymer units, added to cap the reduced trithiocarbonate CTA expected to occur upon exposure to primary amine of amino-TEMPO) were dissolved in anhydrous dimethylformamide (DMF) and added to

the reaction under constant nitrogen stream. The resulting mixture was allowed to react overnight at room temperature protected from light. Polymers were purified by dialysis in methanol for 2 days (sink changed 3x/day) followed by 2 days in water (sink changed 3x/day). The resulting product was lyophilized and stored at 4°C protected from light. Fluorescently labeled polymers were prepared as above with the inclusion of Cy5 amine (0.5 molar equivalents relative to polymer units) in DMF at the TEMPO addition step.

2.4.iii. Polymer characterization

^{1}H and ^{19}F NMR

Samples were analyzed by NMR (Bruker) at ~1% (w/v) in deuterated chloroform ($CDCl_3$). Conversion of the DMA and PFPA monomers was confirmed by integrating the ^{1}H NMR (400 MHz) peaks associated with acrylic protons (δ= 5.7 and 6.18 ppm for DMA and PFPA, respectively) for t=0 and t=24h. Disappearance of these peaks was quantified relative to trioxane (δ= 5.1 ppm). ^{19}F NMR (376 MHz) was performed on the unreacted monomer mixture, the crude RAFT product, and the purified TEMPO-functionalized polymer to confirm presence of the PFP group on the parent polymers and loss of the leaving group upon TEMPO conjugation.

GPC

Polymer polydispersity and MW were characterized using GPC (Agilent Technologies). Polymers were dissolved at 10 mg/ml in DMF + 0.1 M LiBr mobile phase and run through three serial Tosoh Biosciences TSKGel Alpha columns at 60°C. A Wyatt miniDAWN TREOS light scattering (Wyatt Technology Co.) and Agilent refractive index detector were used to calculate absolute number and weight average MW based on dn/dc values determined on an offline refractometer (Anton Paar).

ESR

ESR was used to quantify the presence of active TEMPO on each polymer backbone. Polymers were dissolved at 2 mg/ml in dimethylsulfoxide (DMSO), and 50 µl of each sample was loaded into a glass microcapillary tube. ESR measurements were performed at room temperature using a Bruker EMXplus spectrometer (Bruker Biospin Corp. Billerica, MA). Spectrometer settings were as follows: field sweep, 120 G; center field, 3508 G; microwave frequency, 9.85 GHz; microwave power, 20 mW; modulation amplitude, 1 G; time constant 655 ms; sweep time, 121 s; receiver gain, 40 db. To quantify the nitroxide concentration ESR spectra of the copolymers were double integrated to determine the intensity of the radical signal. Total TEMPO residue content was calculated from a standard curve of TEMPO in DMSO.

HPLC

Reverse phase HPLC (Waters) was used to determine the relative polarity of the polymers. Polymers were dissolved in a 50:50 water:acetonitrile mixture at 1 mg/ml, and 100 µl was injected utilizing a 200 µl sample loop. Samples were run through a Phenomenex C18 column (250x10 mm, 5µm particle size) using a 10-minute gradient from 95:5 to 0:100 water:acetonitrile, followed by 3 minutes at 0:100 water:acetonitrile. The retention time was recorded for each polymer using the peak UV absorbance at 310 nm.

Octanol/water partition coefficient

To determine the partition coefficient, 10 mg of copolymer was added to a round bottom flask containing 5 ml each of octanol and water. The emulsion was stirred vigorously overnight and then added to a separatory funnel to collect the organic and aqueous phases. An aliquot from each phase was run on HPLC as described above, and peaks were integrated and compared to a standard to quantify the concentration of polymer in each phase. The logP value was calculated as the logarithm of the ratio of organic to aqueous phase polymer concentration.

2.4.iv. Cell-free antioxidant activity

General reducing power

A commercial FRAP kit was used to determine the general antioxidant capabilities of the polymers according to the manufacturer's protocol. First, polymers were dissolved or resuspended in deionized water, and 100 µl of each sample was dispensed into a black-walled 96-well plate in triplicate. The FRAP agent was prepared by combining a 1:5 dilution of buffer, 1:10 dilution of the colorimetric probe, and a 1:10 dilution of the oxidized iron substrate with the appropriate volume of DI water. 100 µl of FRAP agent was added to each well, and the samples were incubated at room temperature for 1 hour. Absorbance at 590 nm was measured on a Tecan plate reader, and background absorbance from each polymer (with no FRAP reagent added) was subtracted from the respective experimental wells. The assay was run both in a polymer mass-matched and TEMPO dose-matched format. For the former, all polymers were dissolved or resuspended at 0.4 mg/ml in DI water and plated. For the latter, all polymers and a Tempol control were dissolved or resuspended at 339 µM TEMPO in DI water and plated. Experiments were completed in triplicate.

$O_2^{\bullet-}$ scavenging

$O_2^{\bullet-}$ was generated enzymatically using the HX/XO system and detected colorimetrically using partially acetylated cytochrome C[88]. The following components were combined in the wells of a black-walled 96-well plate: 10 µl XO (0.2 U/ml), 10 ul CAT (50 µg/ml), 50 µl cytochrome C (2.4 mg/ml), and 10 µl polymers. Polymers were used at the same mass-matched and dose-matched concentrations as for the FRAP assay. SOD (final concentration 200 U/ml) and 1X phosphate buffered saline (PBS) were used as negative and positive controls, respectively. CAT was included to scavenge H_2O_2 generated in the reaction[133]. HX was dissolved

at 6.80 mg/ml in 1 M sodium hydroxide (NaOH) and diluted 1:100 in PBS. To initiate the enzymatic reaction, 20 µl HX was added to each well, and absorbance was measured immediately and every 10 minutes thereafter for 60 minutes on a Tecan plate reader at 550 nm. Background absorbance from the polymers was measured from non-$O_2^{\bullet-}$ containing wells and subtracted from the experimental data for each respective polymer.

2.4.v. In vitro *activity*

Cell culture

ATDC5 chondrogenic cells were maintained in Dulbecco's Modified Eagles Medium (DMEM)/F12 supplemented with 10% fetal bovine serum (FBS) and 1% penicillin/streptomycin (P/S) at 37°C, 5% CO_2. Sub-confluent (80%) cultures were passaged using 0.25% trypsin to detach cells at a seeding ratio of 1:10.

Cytocompatibility

ATDC5 chondrocyte-like cells were seeded at 10,000 cells/well in black-walled 96-well plates in dye-free DMEM +1% FBS and 1% P/S. After adhering overnight, the cells were washed with 1X PBS and treated with 100 µl polymers at 0.1, 1, and 5 mg/ml. After 24 hours, treatments were removed, and viability was assessed using a commercial CellTiter-Glo kit (Promega) according to the manufacturer's directions. Briefly, the substrate was reconstituted in assay buffer, and 100 µl was added to each well. After a 10-minute incubation at room temperature, luminescence was imaged on an *In Vivo* Imaging System (IVIS). Signal was normalized to media-treated cells.

Polymer Cell Uptake Visualization by Confocal Microscopy

ATDC5 cells (20,000) were seeded onto an 8-well chambered coverglass (#1 German borosilicate, Nunc™ Lab-Tek™) and allowed to adhere overnight. Cells were washed with PBS and then treated for 24 hours with 250 µg/mL Cy5-labeled polymers dissolved in DMEM + 1%

FBS + 1% P/S. After incubation, cells were washed with PBS, fixed with 4% paraformaldehyde in PBS (Alfa Aesar™) for 25 minutes, washed again with PBS, stained with DAPI (NucBlue™ Fixed Cell Stain ReadyProbes™, Invitrogen) based upon manufacturer directions, washed again with PBS, and overlaid with 25 mM tris(2-carboxyethyl)phosphine-supplemented PBS to reduce extracellular fluorescence of Cy5 as previously described[134]. Finally, cells were imaged with a confocal scanning laser microscope (Nikon Eclipse Ti Microscope with D-Eclipse C1 laser, Nikon Instruments, Inc.) using a 405 nm (blue) and 640 nm (red) laser line. Resulting images were processed by splitting the blue and red channels and merging images.

Polymer Cell Uptake Quantification by ESR

ATDC5 cells were seeded at 1×10^6 cells/flask in T75 flasks and allowed to adhere overnight. Polymers or Tempol were dissolved at 0.4 mg/ml in phenol red-free, supplement-free DMEM, and 10 ml treatments were applied to the flasks. After 24 hours, cells were lifted by scraping and collected in 15-ml centrifuge tubes. Cells were pelleted at 500xg for 5 minutes, and supernatant was removed by aspiration. To lyse cells and release polymers, pellets were suspended in 200 µl DMSO. Samples were frozen at -80°C until analysis. For analysis of uptake, samples were thawed, vortexed, and scanned by ESR as described above. Signals were normalized to inherent ESR signal of each polymer to quantify uptake. Polymers with TEMPO content >40% could not be evaluated for cell uptake because they were insoluble in cell culture media, precipitating to form insoluble aggregates that could not be separated from cells prior to measurement.

Protection from ROS-induced cell death

ATDC5 were seeded at 10,000 cells/well and allowed to adhere overnight. Cells were co-treated with polymers and 1 mM SIN-1 in dye-free DMEM +1% FBS and 1% P/S for 24 hours. SIN-1 was used to induce ROS toxicity, as it spontaneously decomposes to $O_2^{\bullet-}$ and $NO^{\bullet}$ in

aqueous media[110]. Polymer treatments were matched to polymer mass at 0.2 mg/ml or TEMPO dose at 170 μM as described above. Cell viability was measured using the CellTiter-Glo kit on the IVIS as described above and normalized to cells treated with media containing neither SIN-1 nor polymers.

2.4.vi. In vivo *anti-inflammatory activity*

Inflammatory air pouch procedure

All protocols were approved by the Institutional Animal Care and Use Committee of Vanderbilt University and done in accordance with the National Institutes of Health Guide for the Care and Use of Laboratory Animals. The anti-inflammatory effect of the polymers was tested in the murine air pouch model of inflammation[39] with slight modifications. Ten-week-old C57Bl/6 mice were obtained and allowed to acclimate for 3 days. Animals were kept on a 12-hour light/dark cycle and allowed free access to food and water. All experiments were performed under isoflurane anesthesia. On day 0 of the experiment, mice received a subcutaneous injection of 5 ml sterile air on the dorsal region. On day 3, mice were reinjected with 3 ml sterile air. On day 5, 0.5% λ-carrageenan was prepared by dissolving 500 mg carrageenan in 100 ml 0.9% sterile saline with vigorous stirring and heating to 90°C. The solution was sterilized by autoclaving. On day 6 of the experiment, mice received a 1 ml injection into the pouch of carrageenan ± treatments (5-6 mice per group). Five treatment groups were compared: saline, 0.5% carrageenan, 0.5% carrageenan + 40T, 0.5% carrageenan + 100T, and 0.5% carrageenan + Tempol. All TEMPO treatments were dissolved in carrageenan at 8.48 mM TEMPO (40T, 100T, and Tempol at 5.0, 2.7, and 1.46 mg/ml, respectively). Treatments were prepared immediately prior to injection.

Retention and anti-inflammatory effects after air pouch inflammation

Mice were sacrificed at 6 or 24 hours after carrageenan ± treatment injection by CO_2 inhalation. The pouch was rinsed with 1 ml sterile 5.4 mM ethylenediaminetetraacetic acid (EDTA) to collect the inflammatory exudate. A 100 µl aliquot was collected and frozen at -20°C for ESR measurement of polymer retention. Cells were pelleted with centrifugation at 500xg for 5 minutes, and a 100 µl aliquot of the supernatant was frozen at -80°C for ELISA. Fresh supernatant was plated at 50 µl/well in a black-walled 96-well plate. Cytochrome C (50 µl, 2.4 mg/ml) was added and absorbance at 550 nm was measured every 10 minutes for 60 minutes. For ELISAs, TNFα was measured in the supernatant using a commercial sandwich ELISA kit (PeproTech) according to the manufacturer's directions. Briefly, capture antibody was applied to the plate, followed by sample, biotinylated detection antibody, avidin-horseradish peroxidase (HRP), and finally 2,2'-Azinobis[3-ethylbenzothiazoline-6-sulfonic acid]-diammonium salt liquid substrate. Absorbance at 405 nm with correction at 650 nm was measured every 5 minutes for 45 minutes.

Intravital microscopy and biodistribution with intravenous delivery

IVM was used to measure the distribution $t_{1/2}$ of the hydrophilic copolymers (40, 30, 20, and 10T) as described previously[135]. Briefly, male C57Bl/6 mice (n=3 per group) were anesthetized with isoflurane and placed on the heated stage of a confocal microscope (Nikon). The ear was cleaned, and the microscope was focused on the veins in the ear. The mouse was injected with 100 µl Cy5-labeled copolymer solution in saline (10 mg/kg) and Cy5 fluorescence was monitored continuously. To measure $t_{1/2}$, a circular region of interest was highlighted within the vessel and signal intensity was measured within the region. The PKSolver plugin within Microsoft Excel software was used to calculate $t_{1/2}$ using a nonlinear regression one-compartment model[136]. To investigate biodistribution, polymers were injected i.v. at 10 mg/kg, and animals were sacrificed after 10 minutes. Heart, lungs, kidneys, liver, and spleen were

removed to a petri dish and imaged for Cy5 fluorescence by IVIS. Signal was measured by drawing a region of interest around each organ and measuring the total radiant efficiency. The signal for each organ was normalized to the total signal from all organs.

Footpad inflammation model

Female and male C57BL/6 mice were used for development of footpad inflammation to study systemic administration of DMA-co-TEMPO copolymers. A 1% λ-carrageenan solution was prepared by mixing 10 mg powder with 1 ml 0.9% saline in a sterile vial. After gentle swirling, the vial was left uninterrupted for 16 hours at room temperature. The resultant carrageenan solution (50 µl) was injected into the rear right footpad under isoflurane anesthesia. Control animals received no injection. After 6 hours to establish inflammation, animals received an i.v. injection of saline or treatment. Five treatment groups were compared (n=5-7 mice per group): no injection, carrageenan + saline, carrageenan + Tempol, carrageenan + 40T, and carrageenan + 30T. All TEMPO treatments were dissolved at 3.77 mM TEMPO (0.65, 2.0, and 2.63 mg/ml for Tempol, 40T, and 30T, respectively), and the injection volume was 100 µl.

In vivo measurement of ROS

Luminol sodium salt was used to measure ROS levels in the inflamed footpad[137]. The probe was dissolved at 50 mg/ml in sterile saline and protected from light throughout the experiment. Fifteen minutes after i.v. treatment administration, 100 µl of luminol was injected subcutaneously in the dorsal region. Signal was allowed to develop for 15 minutes, and bioluminescence was imaged by IVIS.

2.4.vii. Statistical analysis

All data are reported as mean ± standard deviation. Student's t-test was used to determine statistical significance between two groups. Analysis of variance (ANOVA) with a Tukey post-hoc test for multiple comparisons was used to compare three or more groups. $p<0.05$ was

considered significant. For the inflammatory footpad procedure, a Grubb's test was performed to identify statistical outliers, and one outlier was removed from the 30T group for the luminol measurement. All statistical analysis was performed in GraphPad Prism.

Chapter 3: Optimization of new polysulfide chemistries and formulation approaches to enable production of large, ROS scavenging MPs with high biologic drug loading

3.1. Background

Bioactive proteins and siRNAs are limited in their application as therapeutics, particularly locally, due to their fast clearance from tissues[138,139]. Polymeric MPs provide a mechanism for sustained local release of these cargos. However, care must be taken during formulation to protect the biomolecule from harsh solvents such as dichloromethane (DCM) and ethyl acetate[140,141]. The most common formulation technique for this purpose is the water-in-oil-in-water (W/O/W) process, in which the protein or nucleic acid (often in the form of a polyplex for nucleic acids[142,143]) is suspended in an aqueous phase, termed the primary aqueous (W1) phase. The cargo is vigorously mixed with an organic polymer solution oil (O) phase, followed by emulsification in a secondary aqueous (W2) phase, usually containing a stabilizing surfactant. This process is quick and simple, but can result in cargo degradation, poor encapsulation efficiency, burst release, and porous morphology due to internal water channels[141]. Alternative formulations include solid-in-oil-in-water (S/O/W) emulsions, in which the drug is formulated into a solid phase[144], or coacervation, in which the polymer is gradually enriched in an antisolvent before hardening[145]. These techniques can better stabilize the loaded drug and tend to achieve superior encapsulation and release profiles[141]. Regardless of strategy, polymeric MPs for drug delivery are versatile, with a nearly infinite variable space; by adjusting polymer species or molecular weight[146], concentration[147], emulsification technique[148], surfactant species, or other parameters, a vast range of target sizes, release profiles, degradation rates, or other goals can be achieved.

The gold standard for biomolecule MP delivery is PLGA, which has been used for protein delivery[138,144], siRNA delivery[143], and many other applications. The degradation rate for

PLGA can be adjusted by varying the lactide:glycolide ratio, with higher glycolide content resulting in faster degradation[149]. Additionally, lower molecular weight PLGA degrades faster than higher molecular weight[146]. This material has also been shown to be compatible with a variety of formulation techniques, including drug delivery particles ranging from 10s of nm[150] to 10s of μm[151], porous MPs[152], and micro-templating for novel architectures[153,154]. However, PLGA MPs exhibit foreign body response *in vivo*[40], and have recently shown to promote an inflammatory immune reaction via metabolic reprogramming by degradation fragments[41]. Therefore, our lab and others have pursued alternatives to PLGA which can maintain formulation versatility while mitigating adverse effects. Our lab has pioneered the use of the ROS-scavenging polymer PPS beyond NPs and polymersomes to the microscale for sustained drug delivery[18,29,30]. However, these formulations have been limited to MPs ~2 μm in diameter, making them susceptible to macrophage uptake and faster *in vivo* degradation[31]. In this work, we sought to formulate polysulfide-based MPs which can achieve larger size than PPS, resulting in high loading and sustained release of protein and siRNA drugs.

3.2. Results & Discussion

3.2.i. Incorporation of ES monomer increases crystallinity of polysulfides

Clinically-available MP products typically range in size from 10-100 μm[38]. This size range maintains injectability while allowing for diverse drug loading approaches and resistance to mechanical clearance from tissues. Historical PPS MPs exhibited a mean size of ~2 μm (ref). We attempted to change formulation parameters to increase PPS MP size; however, the larger polymer oily droplets tended to coalesce upon processing into large polymer aggregates instead of distinct MPs. We hypothesized that the challenges in formulating large MPs with PPS were due in part to the amorphous nature of PPS[155], and proceeded to synthesize a series of copolymers incorporating ethylene sulfide (ES), which is highly crystalline{Takahashi, 1968

#934. Poly(propylene sulfide-co-ethylene sulfide) (PPSES) copolymers were synthesized according to **Scheme 3.1** with ES content ranging from 0 (PPS) to 50 mol%. At higher percentages, polymers became insufficiently soluble in MP formulation solvents.

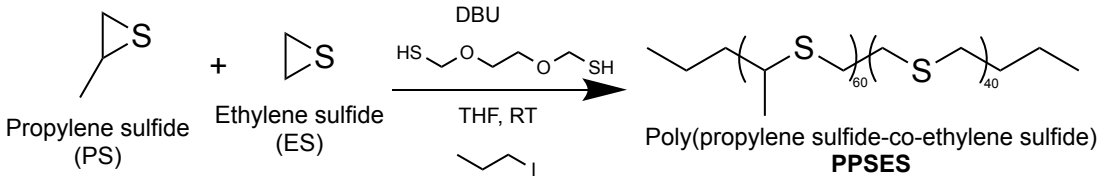

Scheme 3.1: Anionic ring opening polymerization for synthesis of PPSES polymer series.
PS and ES monomers are mixed and added to stirred initiator and base (DBU, 1,8-diazobicyclo(5.4.0)undec-7-ene) in eight equal portions, followed by end capping (1-iodopropane).

Polymers were characterized for composition by NMR (**Supplementary Figure B.1-B.6)** and GPC (**Supplementary Figure B.7**). Using differential scanning calorimetry (DSC), we confirmed that incorporating ES increased crystallinity of the polymers, notably above 40 mol%. Polymers were heated to 140°C to erase thermal history, cooled to -80°C to promote crystallization, and finally, heated to 140°C to promote melting of crystallites. As demonstrated in **Figure 3.1A**, both PS_{60}-co-ES_{40} and PS_{50}-co-ES_{50} exhibit broad exothermic crystallization peaks upon cooling from the melt. The onset temperature for crystallization ($T_{c,onset}$) is strongly dependent on ES percentage, where PS_{50}-co-ES_{50} demonstrating $T_{c,onset}$ of 51°C compared to PS_{60}-co-ES_{40} at 18°C. The remaining polymers, including PPS (PS_{100}-co-ES_0) do not exhibit appreciable crystallization. The broadness of the crystallization peaks is likely due to the heterogeneity of ES regions within a given polymer chain, due to the difference in reactivity of the two monomers[156,157]. We expect that chains containing longer ES oligomers exhibit crystallinity at higher temperatures, which has been shown when varying the architecture of PS-co-ES copolymers[155]. **Figure 3.1B** demonstrates the melting data for each polymer in the series, with melting events exhibited as broad endothermic shifts and corresponding with crystalline regions **Figure 3.1A**. Notably, the end temperature of the melt ($T_{m,end}$) is higher than $T_{c,onset}$,

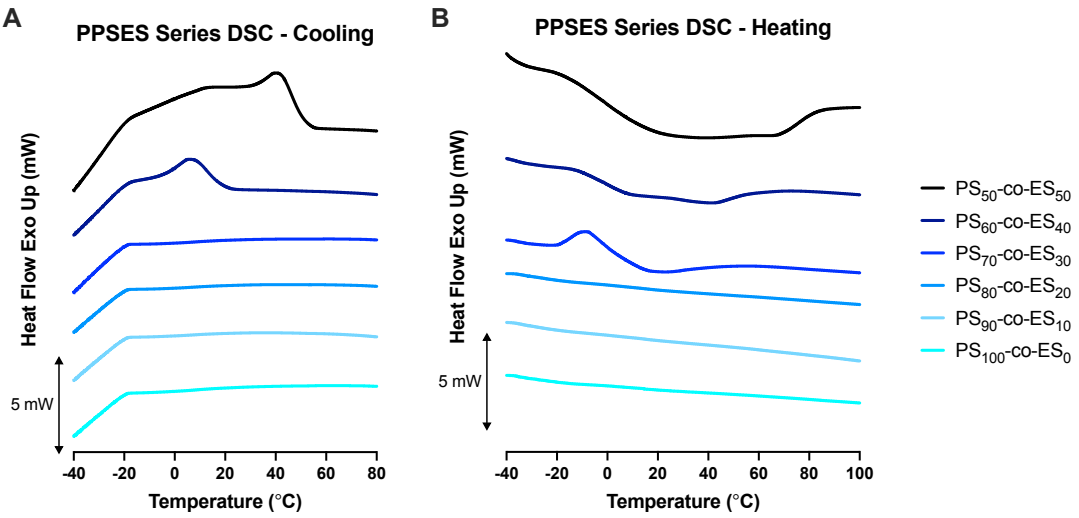

Figure 3.1: Differential scanning calorimetry (DSC) of PPSES polymer series. (**A**) Polymers were heated to 140°C to erase thermal history and achieve full melt, followed by cooling at 10°C/minute. Broad peaks represent exothermic crystallization. (**B**) Polymers were heated from -80°C at 10°C/minute to induce melting. Broad troughs represent endothermic melting of crystals formed in (**A**). Exo: exothermic.

reflecting the higher enthalpic cost to melt crystallites[158]. Additionally, as expected, $T_{m,end}$ is higher for PS_{50}-co-ES_{50} than for PS_{60}-co-ES_{40} (82.3°C vs. 55.1°C, respectively).

To further investigate crystal structure of the PPSES series, we utilized x-ray diffractive spectroscopy (XRD). Utilizing standard 2θ scans at room temperature, we detected a main peak at ~20°, typical of amorphous polymer compounds[159] and a secondary peak/shoulder at ~24° corresponding with the unit cell of ES[160] (**Figure 3.2**). Notably, the 24° peak was only detectable in the two highest ES compositions, indicating that 40 mol% ES represents a threshold for crystallization in these polymers. By measuring the area under the crystallization peak, we roughly determined the percent crystallinity ($X_{c,\%}$) of PS_{50}-co-ES_{50} and PS_{60}-co-ES_{40} as 13.0 and 7.1%, respectively. Notably, the $X_{c\%}$ of PS_{50}-co-ES_{50} matches that found for similar polymers[155].

Our results agree with those of Pérez-Camargo et al., who performed similar studies on PS-co-ES copolymers at 50/50 ratios with varying molecular weights and architectures[155]. Their

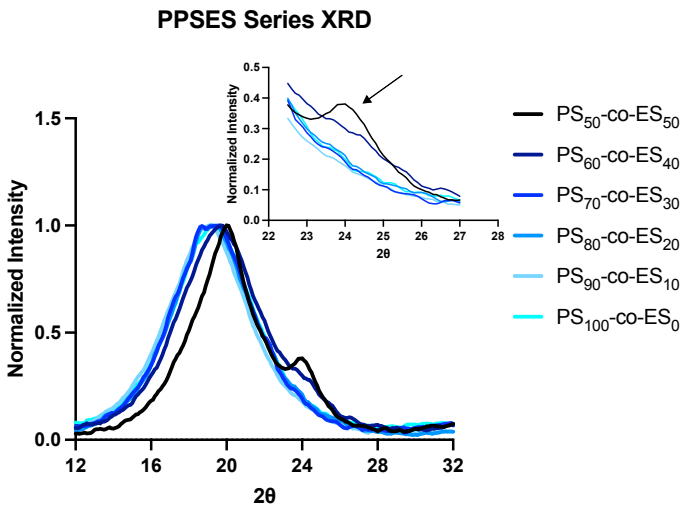

Figure 3.2: X-ray diffractive spectroscopy (XRD) pattern of PS-co-ES series.
Demonstrates crystallinity at room temperature.

results also demonstrated broad crystallization and melting peaks in DSC due to heterogeneity in ES distribution across polymer chains. Through successive self-nucleation and annealing, these authors further demonstrate the temperature-dependency of lamellae melting, with the thickest lamellae presenting the highest melting temperatures and corresponding with the longest uninterrupted regions of ES. Roggero et al. varied the PS:ES ratio from 10:90 to 45:55, similar to our studies here. The authors report detectable traces of ES crystal by x-ray analysis for 40% ES polymers, similar to our XRD result. Another important consideration for this series is the differential ROS scavenging rates for PS and ES. ES is more hydrophilic and less sterically hindered; therefore, all else being equal, materials with higher ES% will scavenge more rapidly[156]. The temperature dependency of the crystallization and melting of the series is also notable, where the most relevant temperature for injectable MPs is 37°C. Though $T_{m,onset}$ is similar for PS_{50}-co-ES_{50} and PS_{60}-co-ES_{40}, the higher $T_{m,end}$ for PS_{50}-co-ES_{50} indicates that a larger fraction will be crystallized at 37°C, helping to maintain structure after injection.

The thermal properties of PLGA are very different from our series, ranging from completely amorphous to highly crystalline. However, almost all PLGA copolymers exhibit a

glass transition temperature (T_g) above body temperature (37°C), which means that PLGA materials are in a glassy state unless heated significantly [161]. In contrast, the T_g of our series is approximately -55°C (**Supplementary Figure B.8**), far below a physiologically relevant value, with the PS-co-ES series existing in a viscous/rubbery state for all formulations. Therefore, crystallinity is a much more important property for our series than for PLGA, which can form MPs when either crystalline or amorphous.

3.2.ii.Polymer crystallinity influences microparticle fabrication

The molecular dynamics of the polymers directly influenced the stability of large MPs formulated with the series. Using a standard bulk oil-in-water (O/W) emulsion for MP fabrication (**Figure 3.3A**), we targeted a maximum size of ~100 μm using the following parameters. MP morphology was visualized by SEM, and qualitative resuspension capability after lyophilization was also assessed. **Figure 3.3B** demonstrates that only PS_{60}-co-ES_{40} and PS_{50}-co-ES_{50} maintained large, stable MPs, while the remaining polymers in the series generally coalesced on the SEM stub. This result agrees with qualitative observations of the processed MPs, which formed viscous aggregates as opposed to a MP suspension.

For the remainder of this thesis, we will refer to PS_{50}-co-ES_{50} as "PPSES" because this polymer exhibited the most consistent and predictable MP formulations. To demonstrate the versatility of PPSES MP formulations, we adjusted the fabrication parameters to produce batches of varying sizes. As demonstrated in **Figure 3.4,** there is a clear effect of emulsion technique and speed on MP size, with more aggressive techniques (faster stirring or homogenization) resulting in smaller MPs. This suggests that PPSES MPs are adaptable to various drug delivery applications, and further formulation processes including microfluidics, templating, and electrospray should be tested.

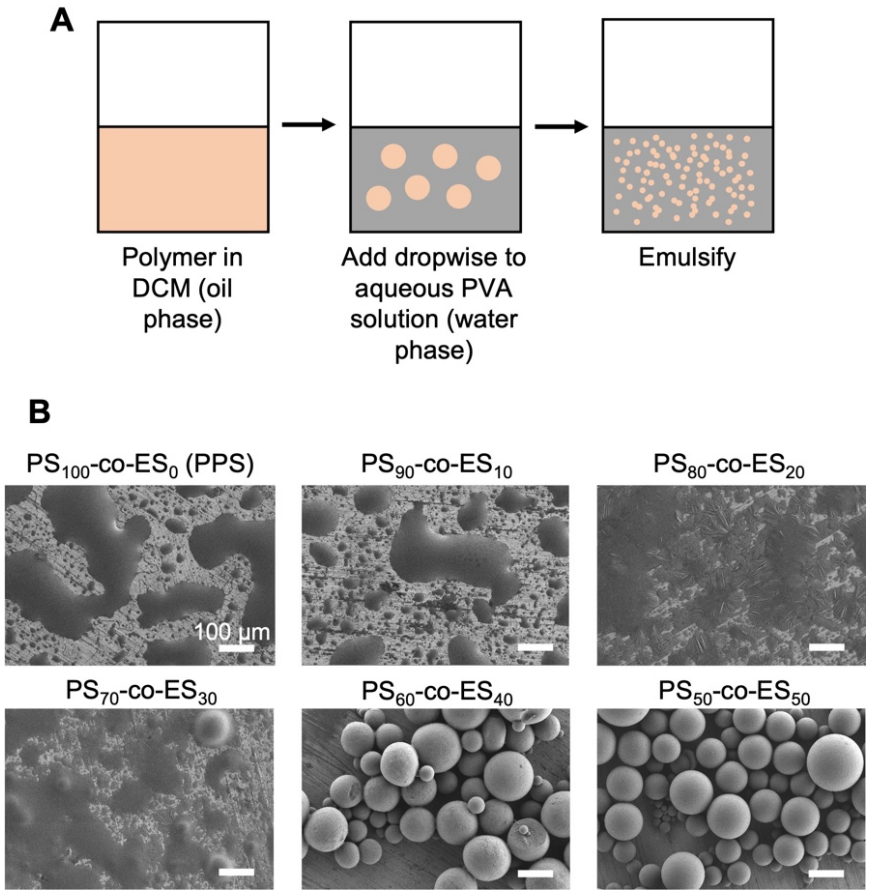

Figure 3.3: Oil-in-water (O/W) emulsion for microparticle (MP) formulation.
(**A**) Cartoon depiction of O/W process. (**B**) Morphology of resulting MPs. Scale bar = 100 µm.

Next, we investigated the degradation of MPs in varying concentrations of H_2O_2. MPs were incubated at 37°C on a shaker for the entirety of the experiment, suspended in 0, 10, 25, 50, or 100 mM H_2O_2. H_2O_2 was replenished at each collection time point. SEM was used to visualize degradation. As demonstrated in **Figure 3.5** and **Figure 3.6**, MPs are extraordinarily stable in aqueous conditions absent ROS, with the morphology virtually unchanged at day 81 of incubation. There is a clear dose response to H_2O_2, with higher concentrations prompting more rapid degradation. The results suggest that MPs hydrophilize as they oxidize, partially dissolving and coalescing on the imaging stub. This mechanism is in line with published results for PPS[29]. The stark morphology change, as opposed to gradual breakdown, suggests an oxidation threshold

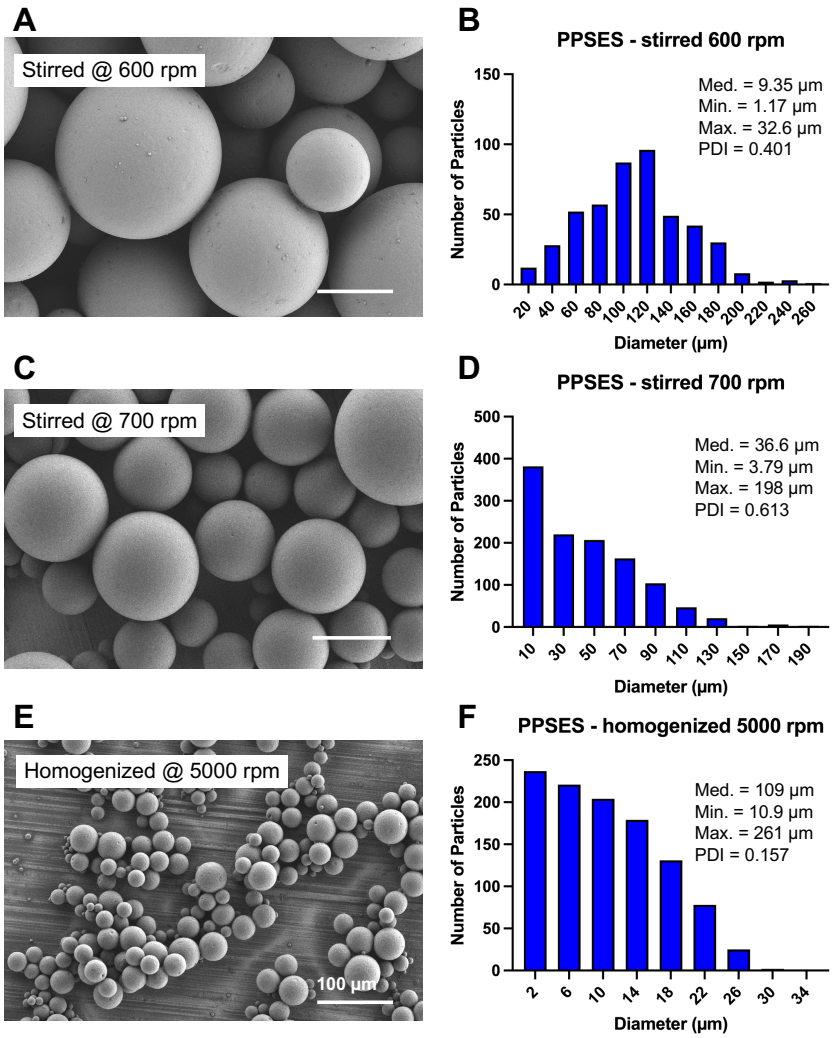

Figure 3.4: Effect of emulsion technique on microparticle (MP) size.
(**A, B**) Scanning electron microscopy (SEM, **A**) and size quantification (**B**) of MPs homogenized at 5000 rpm. (**C,D**) SEM (**C**) and size quantification (**D**) of MPs stirred at 700 rpm. (**E,F**) SEM (**E**) and size quantification (**F**) of MPs stirred at 600 rpm. Scale bar = 100 µm. PDI: polydispersity index.

which is reached, leading to rapid dissolution. For example, comparing the morphology of MPs exposed to 25 mM H_2O_2 at days 25 and 30 demonstrates the switch from spherical, distinct MPs to partially dissolved and flattened discs.

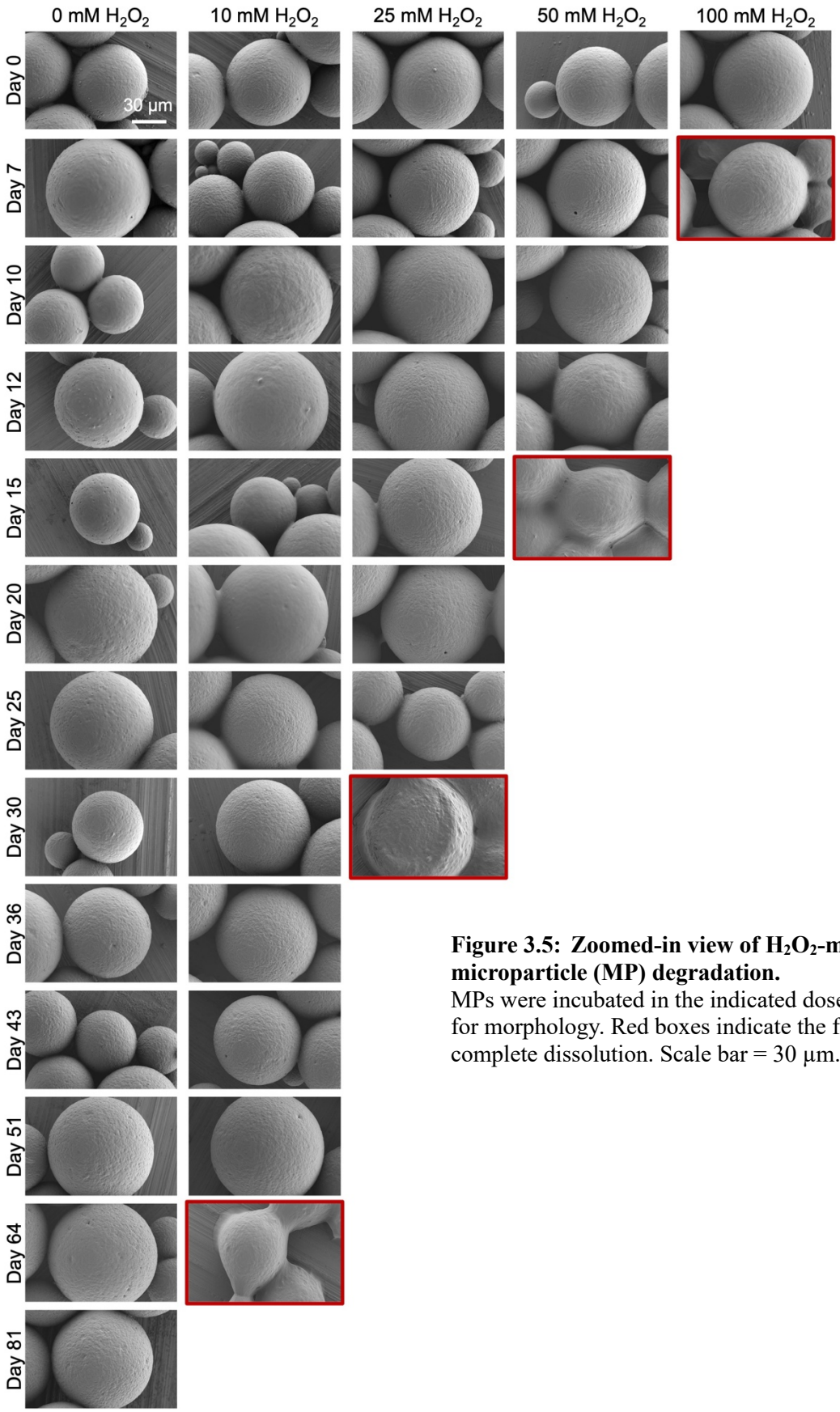

Figure 3.5: Zoomed-in view of H_2O_2-mediated PPSES microparticle (MP) degradation.
MPs were incubated in the indicated dose of H_2O_2 and imaged for morphology. Red boxes indicate the final time point before complete dissolution. Scale bar = 30 µm.

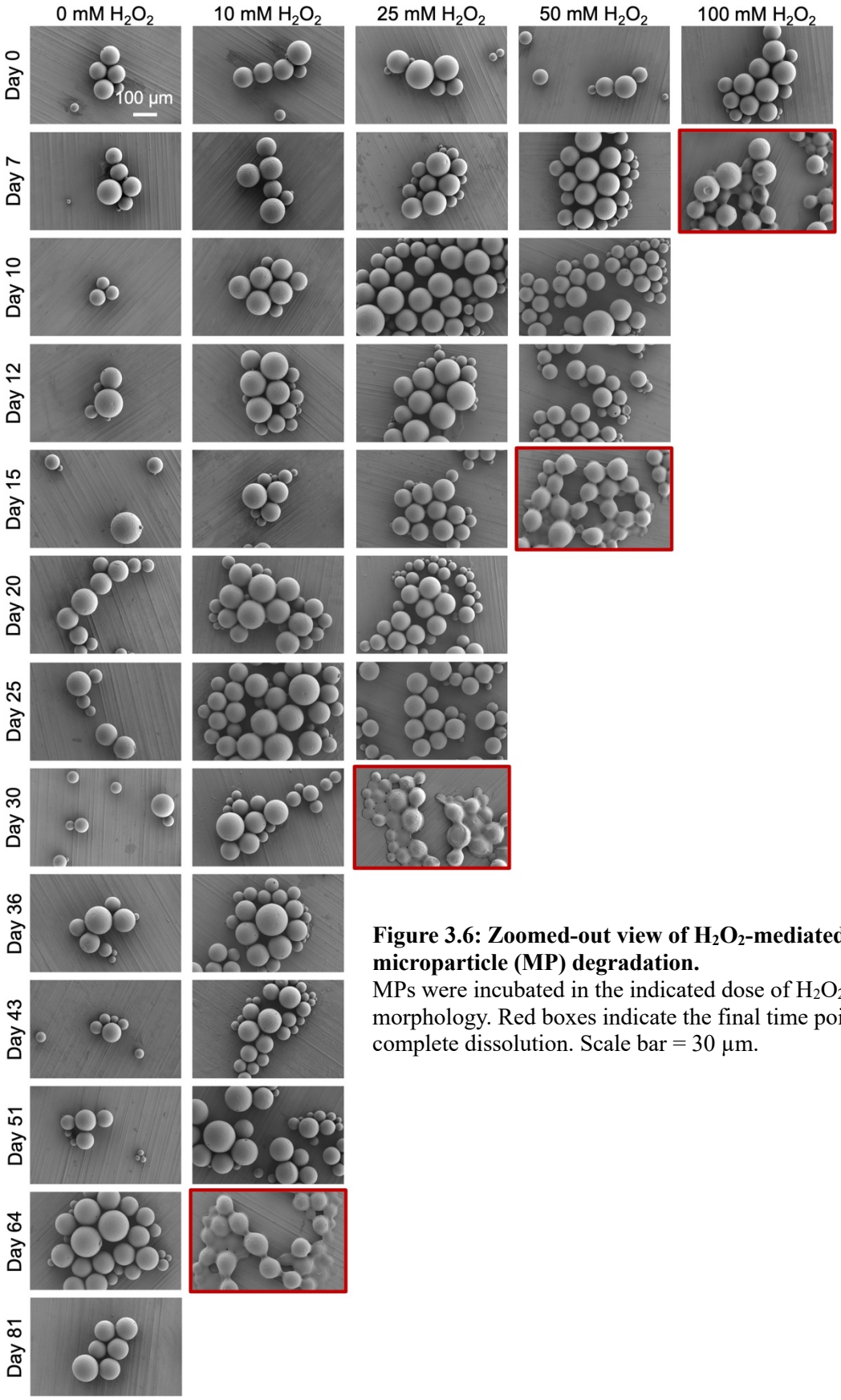

Figure 3.6: Zoomed-out view of H_2O_2-mediated PPSES microparticle (MP) degradation.
MPs were incubated in the indicated dose of H_2O_2 and imaged for morphology. Red boxes indicate the final time point before complete dissolution. Scale bar = 30 µm.

To further probe the dynamics of MP oxidation, we used energy dispersive x-ray spectroscopy (EDS) on the SEM. We scanned MPs <50 µm ("small") and >50 µm ("large") since the populations were very polydisperse. Using this technique, we measured the major constitutive elements of the particles, carbon, oxygen, and sulfur, at each time point (**Figure 3.7A** and **B**). We detected an increase in oxygen percentage before noticeable morphology changes are seen at lower H_2O_2 doses. The maximum oxidation occurred at the last time point, and MPs generally fully degraded after reaching 15-20% oxidation. There was no significant difference between small and large MPs in this experiment, though this comparison would be more robust on two distinct batches of differing median size, instead of a polydisperse population as was done here. Elemental mapping demonstrates localization of the sulfur, carbon, and oxygen signal to the MPs, with brighter oxygen signal for the oxidized MPs (**Figure 3.8**).

These data clearly demonstrate the oxidation-responsive character of PPSES MPs. This has been shown for NPs in the past[156] and for PPS MPs[18,29,30], and is now confirmed in our system. To our knowledge, this is the first demonstration of MPs formulated from PPSES polysulfides. The stability of our system in non-oxidative media is a stark contrast to PLGA, which degrades by hydrolysis at its ester

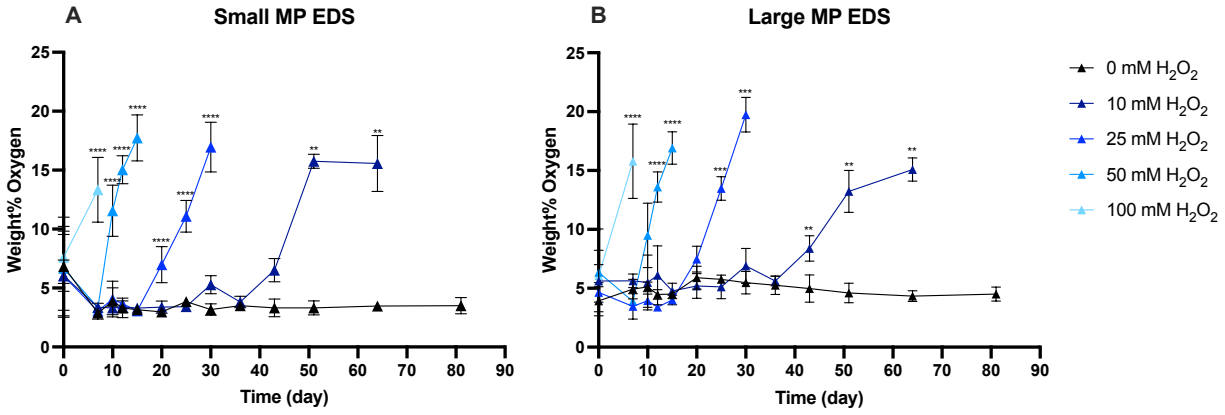

Figure 3.7: Energy dispersive x-ray spectroscopy (EDS) of degraded microparticle (MP) samples. Particles were scanned after incubation in the noted doses of H_2O_2 to collect atomic spectra, and relative oxygen percentage was quantified. N=5 particles/ time point/ condition. Small MP (**A**) were <50 µm, and large MP (**B**) were >50 µm. **p<0.01, ***p<0.001, ****p<0.0001 compared to 0 mM H_2O_2 at the matched time point.

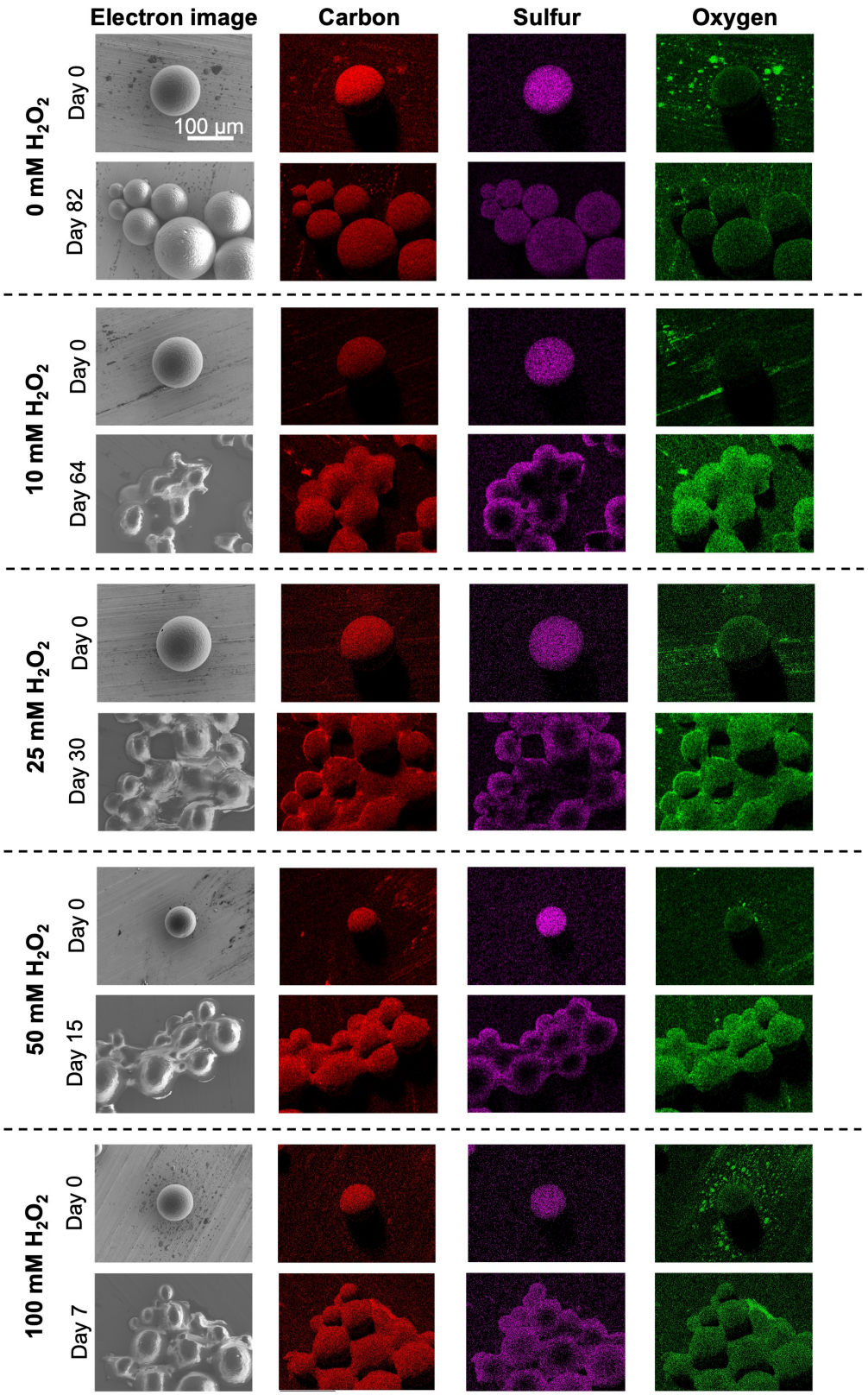

Figure 3.8: Elemental mapping of partially oxidized microparticles (MPs). Localization of the elements quantified by energy dispersive x-ray spectroscopy (EDS). Red = carbon, purple = sulfur, and green = oxygen. Scale bar = 100 µm.

linkages[162]. PLGA MP of similar size have shown degradation in PBS as early as 7 days incubation[163], and as mentioned above, the acidic degradation products mediate local inflammation[41]. We expect that our polymer stays intact upon degradation, since chain scission only occurs at high concentrations of hypochlorite[22], resulting in nontoxic, water-soluble polysulfoxide chains which are cleared from tissue. Multiple studies have demonstrated that PPS degradation products by H_2O_2 are nontoxic in vitro[21,164]. It is possible that the oxidative milieu *in vivo* could produce polysulfones, sulfur dioxide, and olefins, the products of chain scission which have been shown to be more toxic[164]; because of the difficulty dissecting oxidative species *in vivo*, the presence or absence of a foreign body response or other signs of toxicity could be the best way to determine MP degradation toxicity. Ntably, PPS has been shown to inhibit myofibroblastic transition and could be anti-fibrotic[165].

A material that has gained interest for ROS scavenging MP formulation is poly(vanillyl alcohol-co-oxalate) (PVAX), pioneered by the Lee laboratory[166]. This polymer contains H_2O_2-sensitive peroxalate ester bonds, and releases antioxidant vanillin upon degradation. MPs formulated from PVAX have shown drug-free activity in a mouse model of allergic asthma[167] and reduced liver damage when used to deliver manganese porphyrin[168]. Notably, PVAX MP demonstrated less inflammatory response than PLGA in the lung, supporting the use of ROS-scavenging biomaterials for a variety of applications. However, these MPs are also hydrolytically degradable, exhibiting 100% release of loaded drug in 24 hours for porous MPs[167] and 48 hours for 2 μm MPs[168]. Others have formulated ~5 μm MPs from curcuminoid extracts with polyvinylpyrrolidone (PVP) as a stabilizer, which demonstrated antioxidant activity by DPPH scavenging[169]. This agrees with the well-recognized antioxidant properties of curcumin[18].

Overall, we have formulated large MPs by increasing the crystallinity of the parent polymer. PPSES MPs can be formulated at clinically-relevant sizes while maintaining ROS scavenging character.

3.2.iii.MPs for EPO delivery

We were motivated to load proteins and siRNAs into PPSES MPs for local sustained release of these cargos. In the first application, previous work with PPS-EPO MPs demonstrated potent antioxidant and neuroprotective effects in a mouse model of traumatic optic neuropathy[30]. We hypothesized that the larger size and greater stability of PPSES MPs would allow for higher levels of EPO loading and more flexibility in dosing.

First, we formulated PPS-EPO and PPSES-EPO MPs using a standard W/O/W process. Both PPS-EPO and PPSES-EPO MP exhibited 39% encapsulation efficiency, resulting in EPO loading of 0.85 and 0.77 μg EPO per mg MP[30] (the difference in loading is due to slightly different EPO input between formulations). **Figure 3.9** demonstrates that PPS-EPO MP exhibit spherical morphology (**Figure 3.9A** and **B**) with a relatively small median diameter of 1.7 μm with a range of 0.6-4.4 μm (**Figure 3.9C**). PPS-EPO also exhibit sustained EPO release in an oxidation-responsive manner (**Figure 3.9D**). In contrast, PPSES-EPO MP exhibited an approximate size of 30-80 μm (**Figure 3.10A** and **B**). Notably, these MPs showed appreciable porosity and dimpling, due to the W/O/W formulation process. Moving forward, this PPSES-EPO MP formulation will be referred to as "PPSES-EPO Gen1" (generation 1).

To improve MP morphology and EPO loading, while better protecting the protein[140], we pursued the S/O/W strategy. The first step was to formulated protein-loaded, hydrophilic particles using the aqueous two-phase system technique with dextran and PEG[170,171] (**Figure 3.11**). BSA was used as an affordable model protein for optimization due to its similar mass and charge to EPO[172,173]. First, we studied the effect of freezing speed on particle size and protein encapsulation. As shown in **Figure 3.12A** and **B**, particles flash-frozen in liquid nitrogen (LN2) demonstrated smaller size and generally spherical morphology, whereas particles frozen more slowly (-20°C) exhibited more heterogeneity, including particles >10 μm. Controlling size of

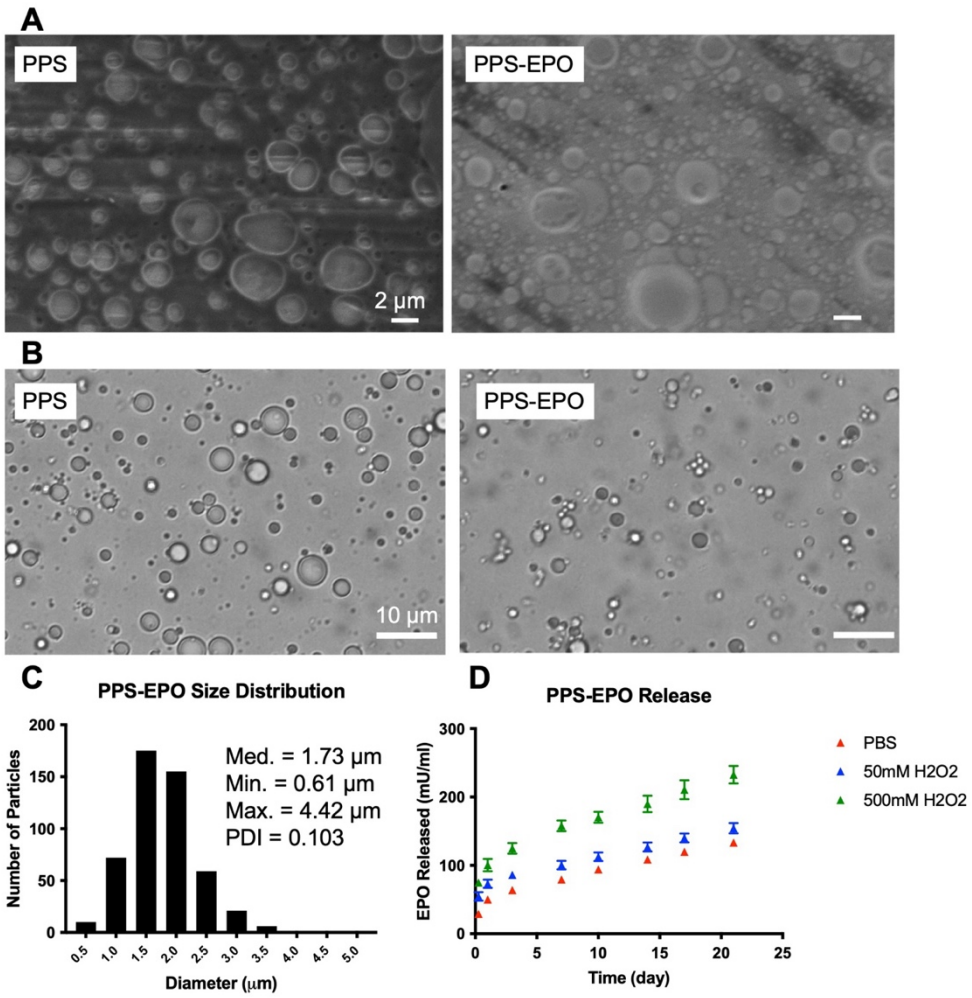

Figure 3.9: PPS-EPO microparticle (MP) characterization.
(**A**) Scanning electron microscopy (SEM) of PPS and PPS-EPO MP. Scale bar = 2 µm. (**B**) Brightfield microscopy of PPS and PPS-EPO MP in solution. Scale bar = 10 µm. (**C**) Size quantification histogram for PPS-EPO MP. (**D**) Cumulative release of EPO from PPS-EPO MP. N = 3 aliquots. "R76E" refers to the point mutation converting arginine-76 to glutamate. PDI: polydispersity index. Data from[30].

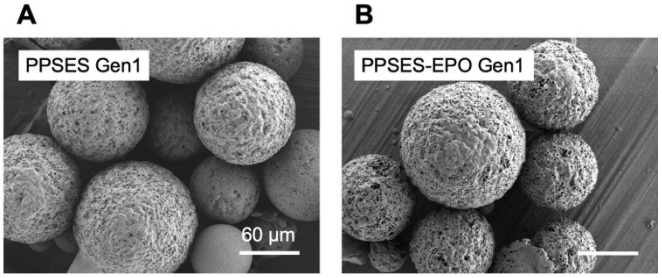

Figure 3.10: PPSES-EPO Gen1 microparticles (MPs).
Formulated using a water-in-oil-in-water (W/O/W) emulsion. Control MPs (**A**) were formulated with PBS as the primary water phase, and EPO MPs (**B**) were formulated with EPO dissolved in PBS as the primary water phase. Scale bar = 60 µm. Gen1: first generation.

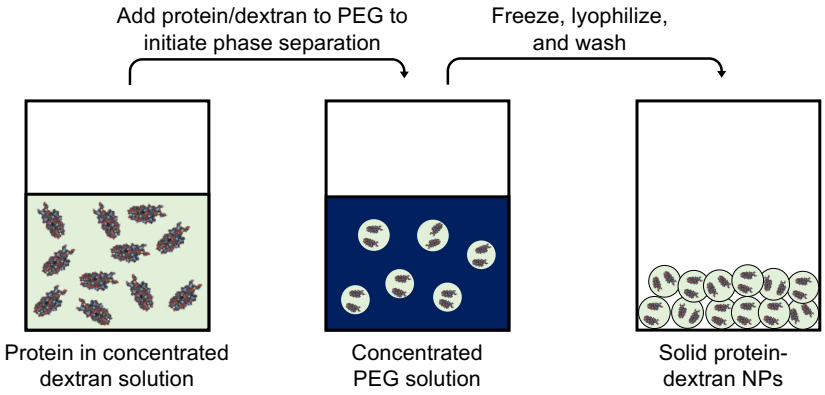

Figure 3.11: Cartoon depiction of dextran-protein particle formulation.
PEG: polyethylene glycol; NPs: nanoparticles.

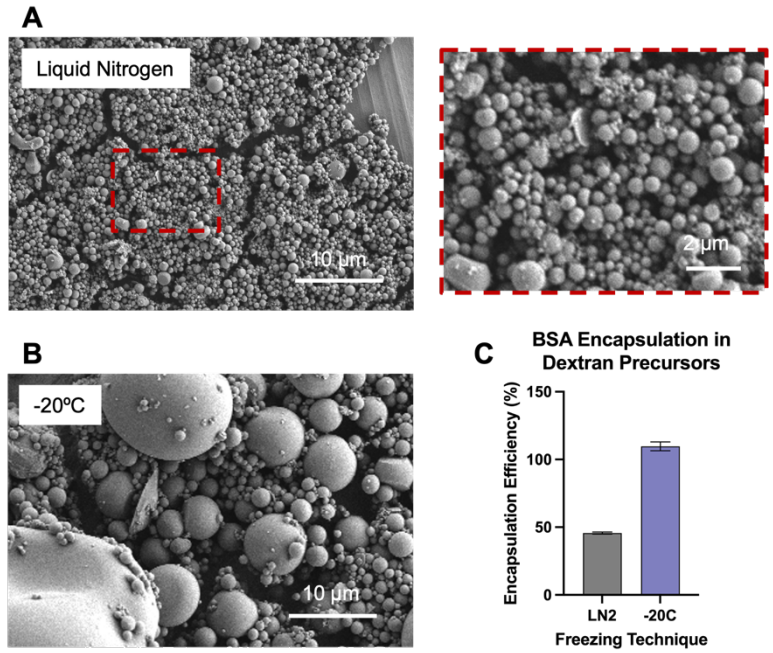

Figure 3.12: Effect of freezing technique on dextran precursor particles.
Bovine serum albumin (BSA), dextran, and polyethylene glycol (PEG) were vigorously mixed and either frozen in liquid nitrogen or at -20°C to promote particle formation. (**A**) Dextran particles formulated via freezing in liquid nitrogen (rapid) exhibited sub-micron diameter and generally spherical morphology. Scale bar = 10 µm for main image and 2 µm for blowout. (**B**) Freezing at -20°C exhibited particles with more variance in size, from <1 µm to >10 µm. (**C**) Slower freezing (-20°C) resulted in improved encapsulation of BSA. N=1 batch run in triplicate.

precursors is important because the ratio of internal:external particle diameter should be at least 1:20 to improve loading and prevent burst release[174]. However, rapid freezing in LN2 reduced protein loading in the resulting particles, likely due to the shorter time for protein to partition into the dextran phase.

Next, we tested if incubating the sample for a longer amount of time between mixing and snap-freezing would maintain small size while improving encapsulation. We repeated the formulation, and varied an incubation time of 0-60 minutes after mixing before freezing in LN2. **Figure 3.13A** demonstrates that particle morphology is largely maintained from 0-10 minutes, and some aggregates appear at 20 and 30 minutes. Particles incubated for 60 minutes

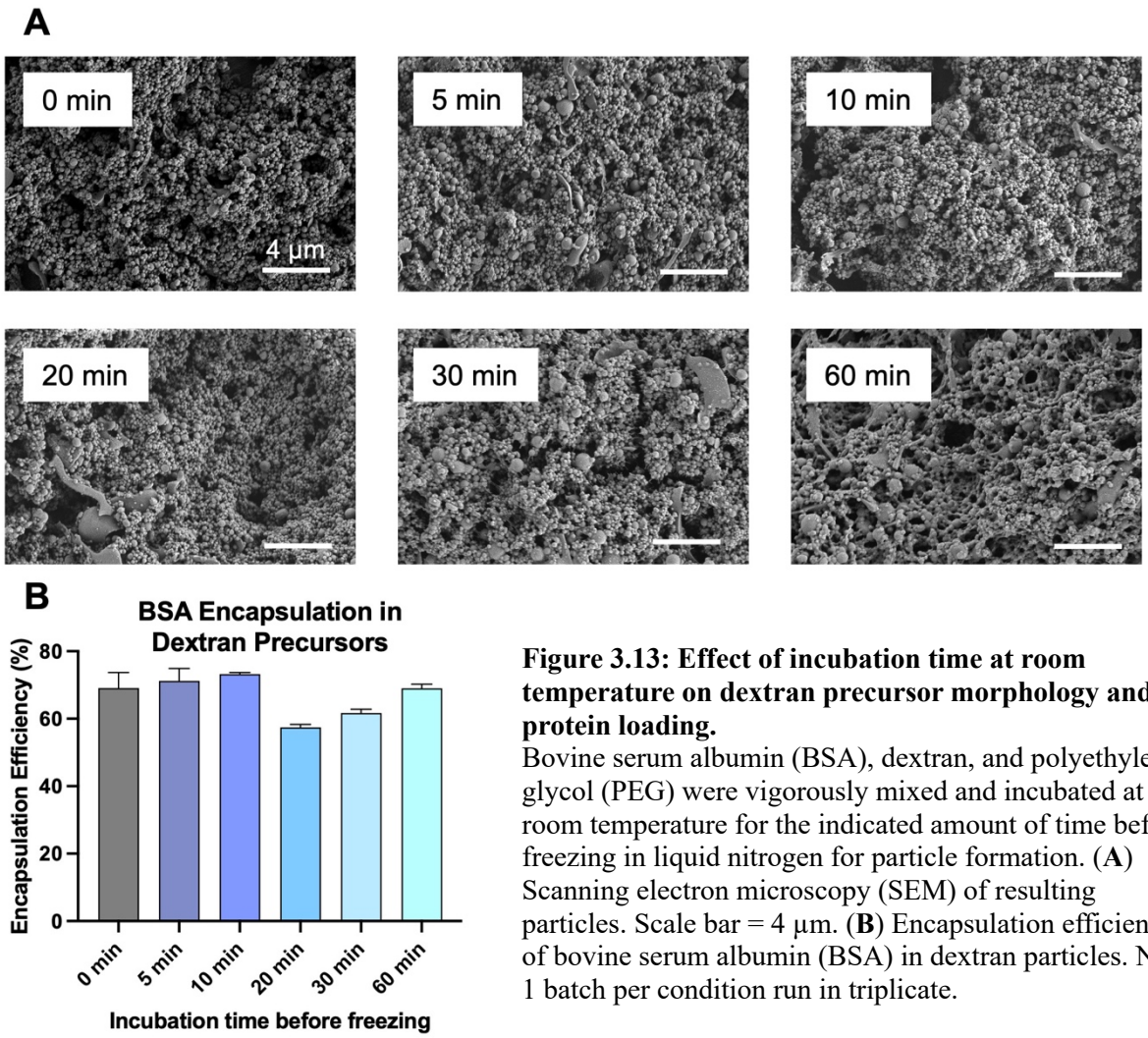

Figure 3.13: Effect of incubation time at room temperature on dextran precursor morphology and protein loading.
Bovine serum albumin (BSA), dextran, and polyethylene glycol (PEG) were vigorously mixed and incubated at room temperature for the indicated amount of time before freezing in liquid nitrogen for particle formation. (**A**) Scanning electron microscopy (SEM) of resulting particles. Scale bar = 4 µm. (**B**) Encapsulation efficiency of bovine serum albumin (BSA) in dextran particles. N = 1 batch per condition run in triplicate.

demonstrated a partially annealed morphology. Protein encapsulation was similar across incubation times, though notably, encapsulation in this experiment was higher than earlier LN2 data (**Figure 3.13B**).

To further increase protein loading, we investigated the effect of cationic dextran. BSA, esterase, and EPO possess a net negative charge at physiologic pH, so we hypothesized that cationic diethylamino-dextran (DEAE-dextran) could increase partition into the dextran phase. **Figure 3.14** demonstrates that 15 wt% DEAE dextran increases protein encapsulation compared to 0%.

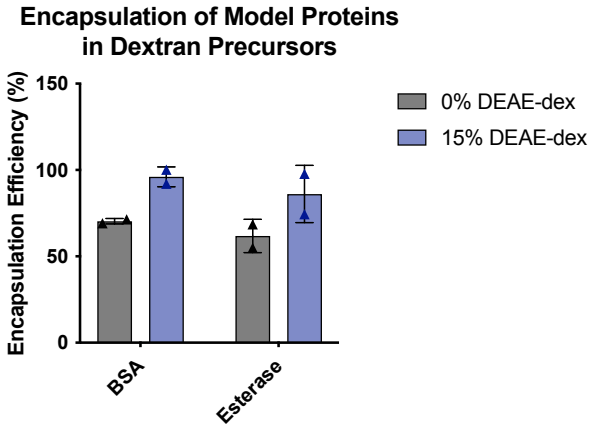

Figure 3.14: Effect of cationic dextran additive on bovine serum albumin (BSA) and esterase encapsulation.
Protein and diethylaminoethyl (DEAE) dextran were mixed, followed by addition of dextran and polyethylene glycol (PEG), vigorous mixing, and freezing in liquid nitrogen. N = 2 batches per protein per condition.

Based on the preceding studies, we formulated EPO-loaded dextran precursor particles as follows: 100 µg EPO (Prospec) was reconstituted in DEAE-dextran and incubated on ice for 5 minutes, followed by addition of uncharged dextran and PEG. The ATPS was vortexed at max speed for 45 seconds, snap frozen, and lyophilized. The dextran phase consisted of 20% protein, 15% DEAE-dextran, and 65% uncharged dextran by weight. Further formulation details can be found in the Methods section.

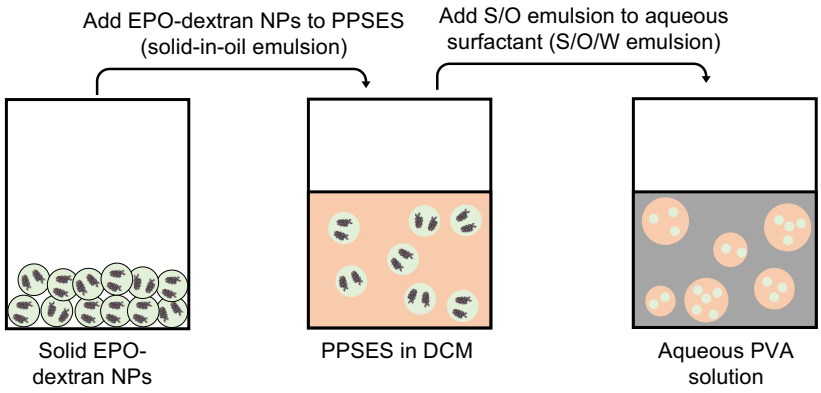

Figure 3.15: Cartoon of solid-in-oil-in-water (S/O/W) formulation process for EPO microparticles (MPs).
NPs: nanoparticles, DCM: dichloromethane, PVA: polyvinyl alcohol.

We formulated PPSES-EPO MPs using the previously-described solid-in-oil-in-water (S/O/W) formulation process[175] (**Figure 3.15**). The lyophilized EPO NPs were washed 3x with DCM to remove PEG, suspended in 200 µl PPSES, and emulsified in 6 ml 1% PVA. Notably, the EPO NPs exhibited unexpected aggregation during washing and S/O suspension, possibly due to additives to the EPO that were not present in the model proteins. This aggregation resulted in suboptimal MP morphology. **Figure 3.16A** shows the MPs exhibited some porosity and shell-like appearance in some instances. The MP exhibited a median diameter of 50.1 µm and range of 10.2-170 µm (**Figure 3.16B**), on par with other MP systems for ocular delivery[174,175], and relatively high PDI of 0.35, similar to previous batches. The suboptimal formulation parameters yielded low encapsulation (7.3% EE, 0.73 µg EPO per mg MP) and significant burst release (**Figure 3.16C**). For best performance *in vivo*, we expected that improved EPO loading and a more extended release profile would be necessary, so we returned to optimizing the formulation for EPO, as opposed to model proteins. For the remainder of this thesis, this batch will be referenced as "PPSES-EPO Gen2" (second-generation).

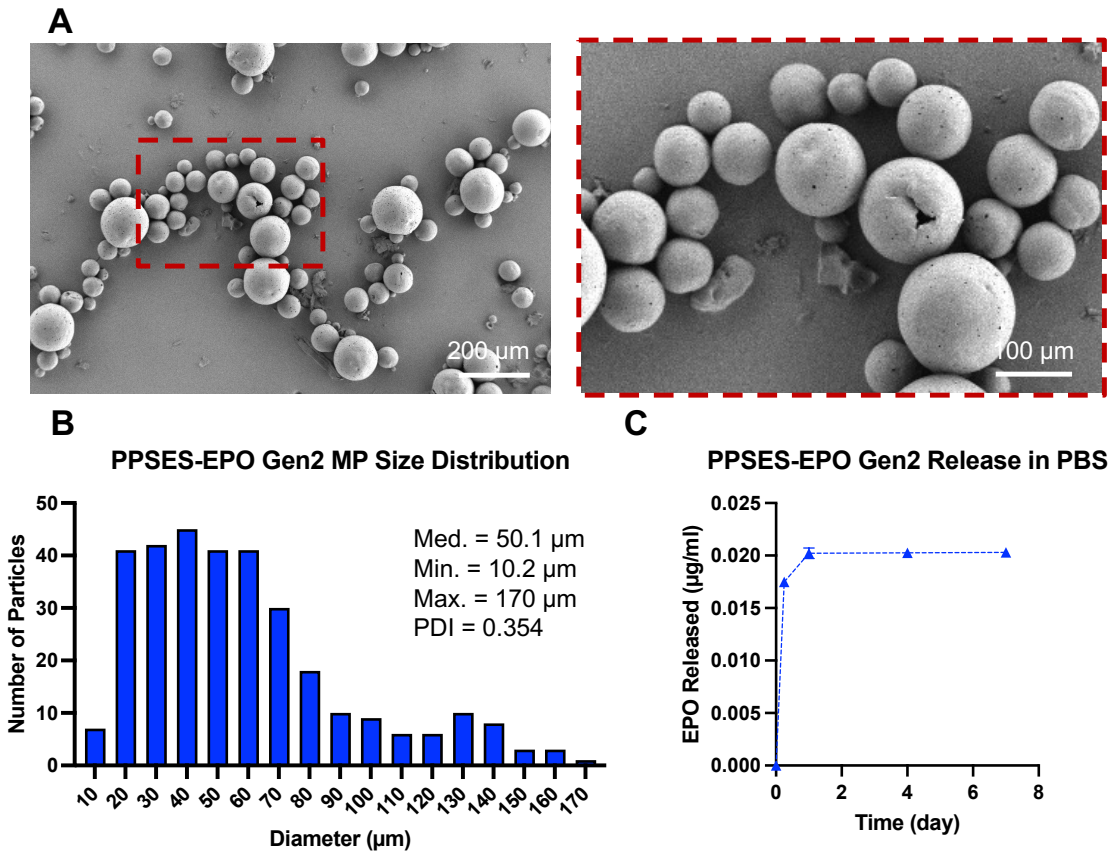

Figure 3.16: PPSES-EPO Gen2 microparticles (MPs).
MPs were formulated using the solid-in-oil-in-water (S/O/W) technique utilizing dextran precursors containing 15% diethylaminoethyl (DEAE) dextran. (**A**) Scanning electron microscopy (SEM) of resulting MPs. Scale bar = 200 µm for main image and 100 µm for blowout. (**B**) Size quantification histogram of PPSES-EPO MPs. (**C**) PPSES-EPO MP release in PBS. N = 1-2 aliquots. Gen2: second-generation; PDI: polydispersity index.

The following conditions were used to compare EPO loading in 0% vs. 15% DEAE-dextran NPs: EPO and DEAE-dextran were combined and incubated for 30 minutes on ice, uncharged dextran and PEG were added, the sample was vortexed for 60 seconds and incubated on ice for 10 minutes, and finally, snap frozen and lyophilized. **Figure 3.17A** demonstrates that 15% DEAE-dextran drastically increased EPO loading in the dextran NPs from 15.4% to 96.8% and maintained sub-1 µm size (**Figure 3.17B**).

We hypothesized that the suboptimal morphology of the PPSES-EPO Gen2 MPs was due in part to the high salt concentration in the starting protein, creating an osmotic gradient out of

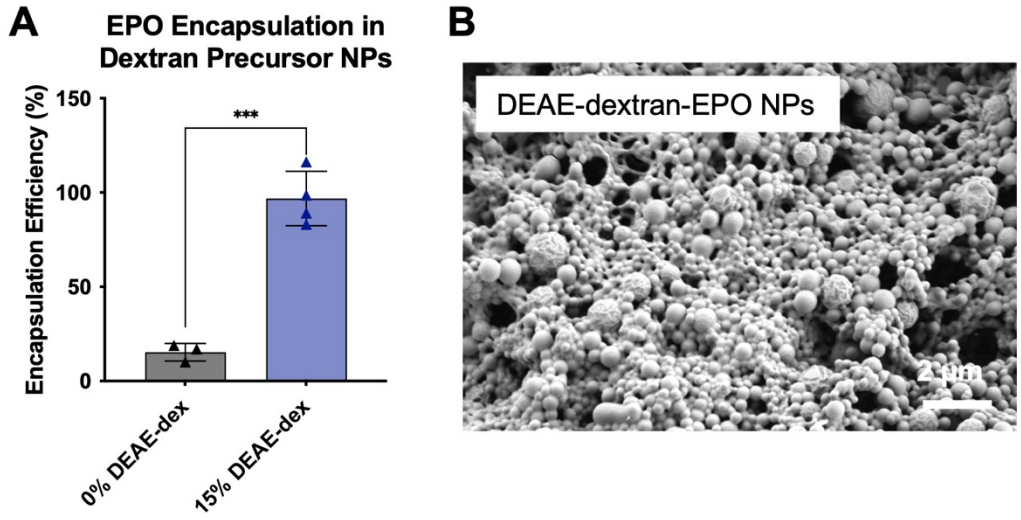

Figure 3.17: EPO formulation in diethylaminoethyl (DEAE)-dextran nanoparticles (NPs). EPO was mixed with DEAE-dextran, followed by dextran and polyethylene glycol (PEG), mixed vigorously, and frozen in liquid nitrogen for NP formulation. (**A**) EPO encapsulation in NPs. N = 3-4 batches. (**B**) Scanning electron microscopy (SEM) of EPO NPs. Scale bar = 2 µm. ***p<0.001.

the S/O phase during formulation[141]. To mitigate this, we made two changes to the formulation parameters: (1) the EPO protein was spin-filtered to flush out salts and achieve normosmolarity, and (2) 5% NaCl was included in the aqueous phases of the S/O/W procedure to produce a strong osmotic gradient into the S/O phase during hardening. These changes produced a stark improvement in MP morphology; as shown in **Figure 3.18A-B**, PPSES-EPO MPs exhibited smooth surfaces and lack of porosity when the osmotic pressure was directed into the S/O phase utilizing normosmotic EPO and NaCl in the W phases. These MPs also exhibited EPO encapsulation efficiency of 92.5±2.5% (9.6±0.76 µg EPO per mg MP). The size distribution was similar to PPSES-EPO Gen2, with a median diameter of 56 µm and range of 6.7-137 µm (**Figure 3.18C**). Finally, sustained release in PBS and 10 mM H_2O_2 was demonstrated using rhodamine-tagged EPO, where burst release was mitigated PBS and release was steady over time (**Figure 3.18D** and **E**). Notably, EPO release was more rapid upon exposure to ROS, indicating ROS-responsive cargo release.

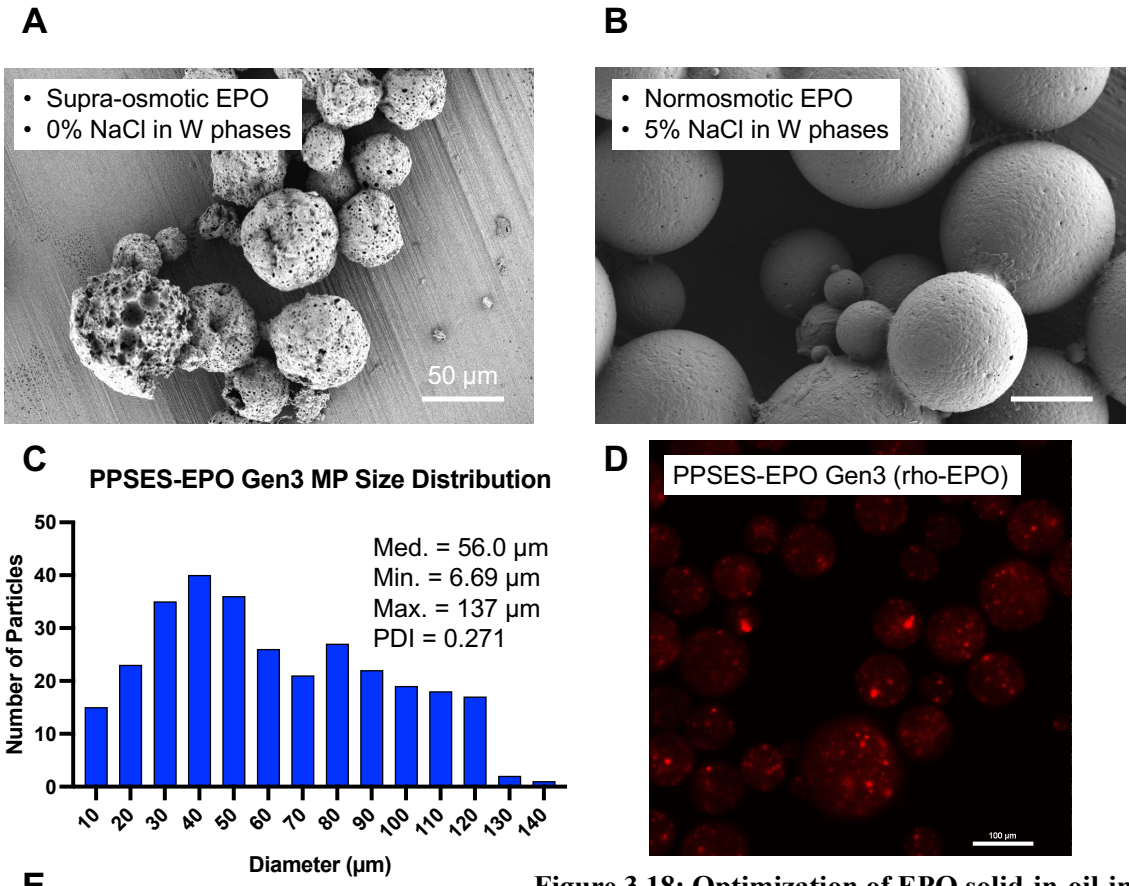

Figure 3.18: Optimization of EPO solid-in-oil-in-water (S/O/W) formulation.
EPO nanoparticles (NPs) were formulated with 15% diethylaminoethyl (DEAE) dextran and loaded in microparticles (MPs). (**A**) Formulations containing high salt concentration in the S phase and low salt concentration in the W phases resulted in MPs with porous morphology. (**B**) Formulations containing low salt concentration in the S phase and high salt concentration in the W phases resulted in MPs with smooth surfaces. Scale bar = 50 µm. (**C**) Size quantification histogram of MPs in (**B**). (**D**) MPs formulated with rhodamine (rho)-EPO imaged by confocal microscopy demonstrate signal distributed throughout MP with some denser pockets. Scale bar = 100 µm. (**E**) Cumulative release of rho-EPO from MPs. N = 3 aliquots. Gen3: third-generation; PDI: polydispersity index.

The S/O/W formulation technique has been pursued in many instances of EPO delivery from PLGA MPs[175169]. This process is attractive for protein delivery because the all-aqueous environment is preferable to exposing EPO to solvents like DCM. However, these dextran-EPO preparations have a size ranging from ~1-10 µm[174], as opposed to the nanoscale preparation we

have optimized. These particles are larger because they are prepared at -20°C, like our formulation in **Figure 3.12B**, which results in excellent EPO loading. We reduced the size while maintaining the high loading by incorporating cationic dextran, a strategy which has not been pursued for this application before. Electrostatic interactions have been leveraged to control protein release from alginate microgels[176] and PLGA NPs[177] and for loading of proteins in layer-by-layer microcapsules[178]. Here, we took advantage of DEAE dextran, a polymer commonly used for transfection of nucleic acids[179], to promote EPO loading in the dextran phase of the ATPS without necessitating slow freezing. This small size makes the EPO NPs amenable to small MP formulations while maintaining the 1:20 diamter ratio, where MPs as small as ~4 μm could load EPO NPs efficiently.

We progressively optimized the formulation paramaters for the EPO MPs to maximize EPO loading and release in the PPSES-EPO Gen3 MPs (**Figure 3.18**). The morphology and release rate of the MPs is superior to Gen1 and 2, minimizing burst release and presenting smooth surfaces. The sustained release over 80 days is comparable to PLGA-EPO MPs{Rong, 2012 #950}[175], though we see less burst in the early time points, which could be due to DEAE-dextran. We did not directly measure the effect of DEAE-dextran on EPO release, though it would be interesting to determine empirically if the electrostatic interaction can slow release as has been seen for other proteins[177].

3.2.iv. MPs for siRNA delivery

We also formulated MPs for sustained release of siRNA. The siRNA utilized was our laboratory's previously-optimized "zipper EG18" siRNA, in which "zipper" refers to backbone stabilization chemistries and "EG18" refers to PEG-diacyl tails[180] (**Supplementary Figure B.10**). First, we tested the optimized DEAE-dextran formulation for siRNA. This procedure produced siRNA NPs and MPs with smooth, spherical morphology (**Figure 3.19A** and **B**,

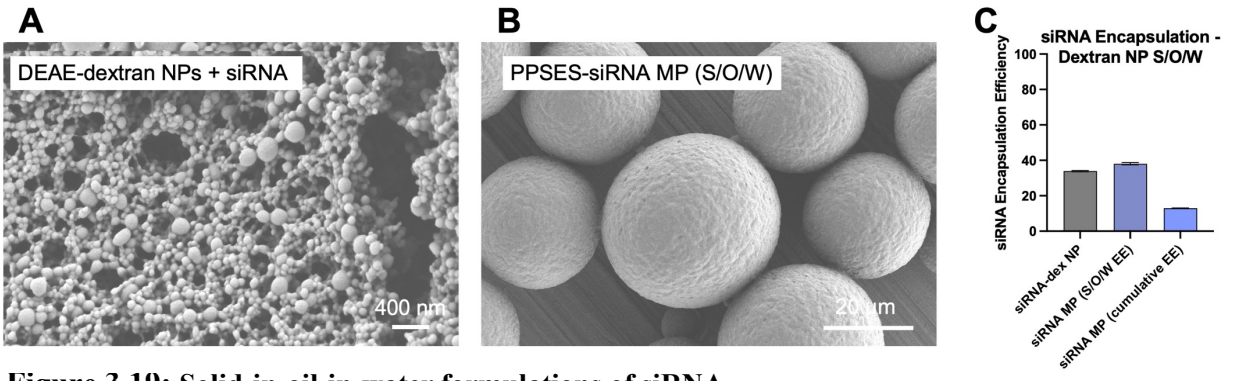

Figure 3.19: Solid-in-oil-in-water formulations of siRNA.
(**A**) siRNA-EG18 was mixed with diethylaminoethyl (DEAE) dextran, uncharged dextran, and polyethylene glycol (PEG) to promote particle formulation as optimized for EPO. Scanning electron microscopy (SEM) reveals sub-micron size and spherical morphology of precursor particles. Scale bar = 400 nm. (**B**) DEAE-dextran siRNA nanoparticles (NPs) were formulated in PPSES microparticles (MPs) via solid-in-oil-in-water (S/O/W) formulation. Scale bar = 20 µm. (**C**) Encapsulation efficiency in siRNA NPs (gray) and MPs (dark and light blue). S/O/W EE refers to EE based on siRNA feed from NP precursors, whereas cumulative EE reflects loss at both the NP step and MP step. N = 1 batch run in duplicate.

respectively). However, these formulations exhibited low siRNA encapsulation efficiencies (34% for NPs and 38% for S/O/W MPs), resulting in a total loss of ~80% of the input siRNA (**Figure 3.19C**). Therefore, we attempted a standard W/O/W formulation. Though the Cy5-tagged siRNA could be visualized throughout the MP matrix (**Figure 3.20A**), the MPs exhibited similar morpohological challenges as W/O/W protein MPs, including dimpling and porosity (**Figure 3.20B**).

Next, we formulated MPs with siRNA-EG18 using a S/O/W emulsion where the siRNA was lyophilized to form the solid phase (**Figure 3.21**). The surface of the MPs was smoother than the W/O/W formulation and lacked porosity (**Figure 3.22A**), and the formulation exhibited a median diameter of 18.3 µm (**Figure 3.22B**). To ensure that exposure to organic DCM was compatible with siRNA cargo, we ran gel electrophoresis after DCM exposure (**Figure 3.22C**), which demonstrated that the siRNA exhibited a single band which ran at the same position as the

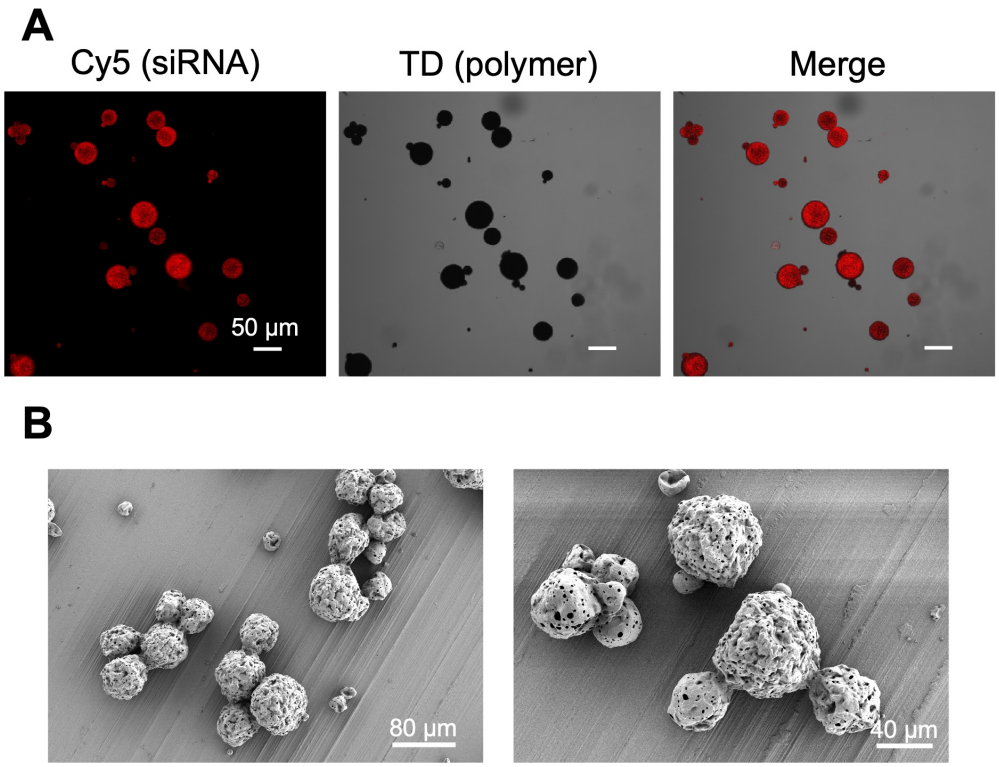

Figure 3.20: siRNA-PPSES MPs formulated using the water-in-oil-in-water (W/O/W) formulation. Cy5-tagged siRNA-cholesterol conjugate was the primary W phase and PPSES in dichloromethane (DCM) was the O phase. (A) Confocal microscopy demonstrates localization of Cy5 signal with MPs distributed through the polymer matrix. Scale bar = 50 µm. (B) Scanning electron microscopy (SEM) demonstrates porosity and dimpling of MP surface. Scale bar, left = 80 µm; right = 40 µm.

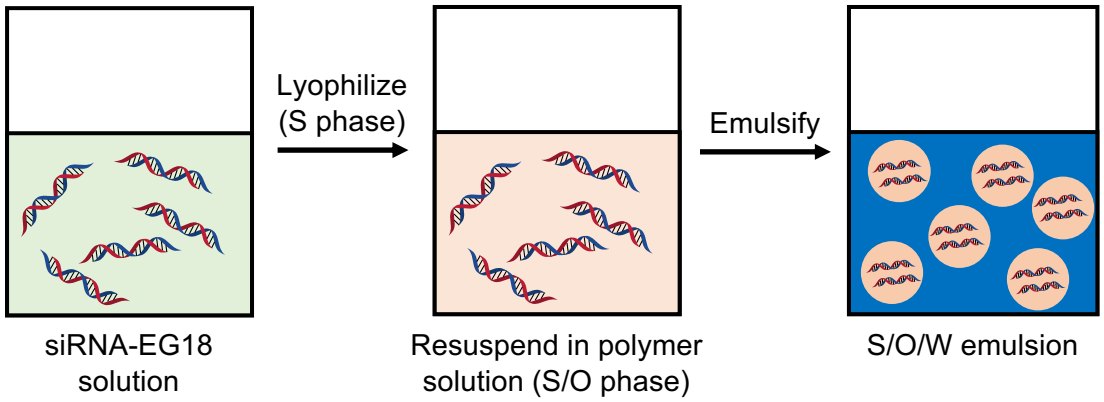

Figure 3.21: Cartoon depiction of solid-in-oil-in-water (S/O/W) microparticle (MP) formulation with lyophilized siRNA-EG18.

control sample. By loading MPs with Cy5-tagged siRNA, encapsulation efficiency was estimated at 56.5% (5.65 µg siRNA per mg MP).

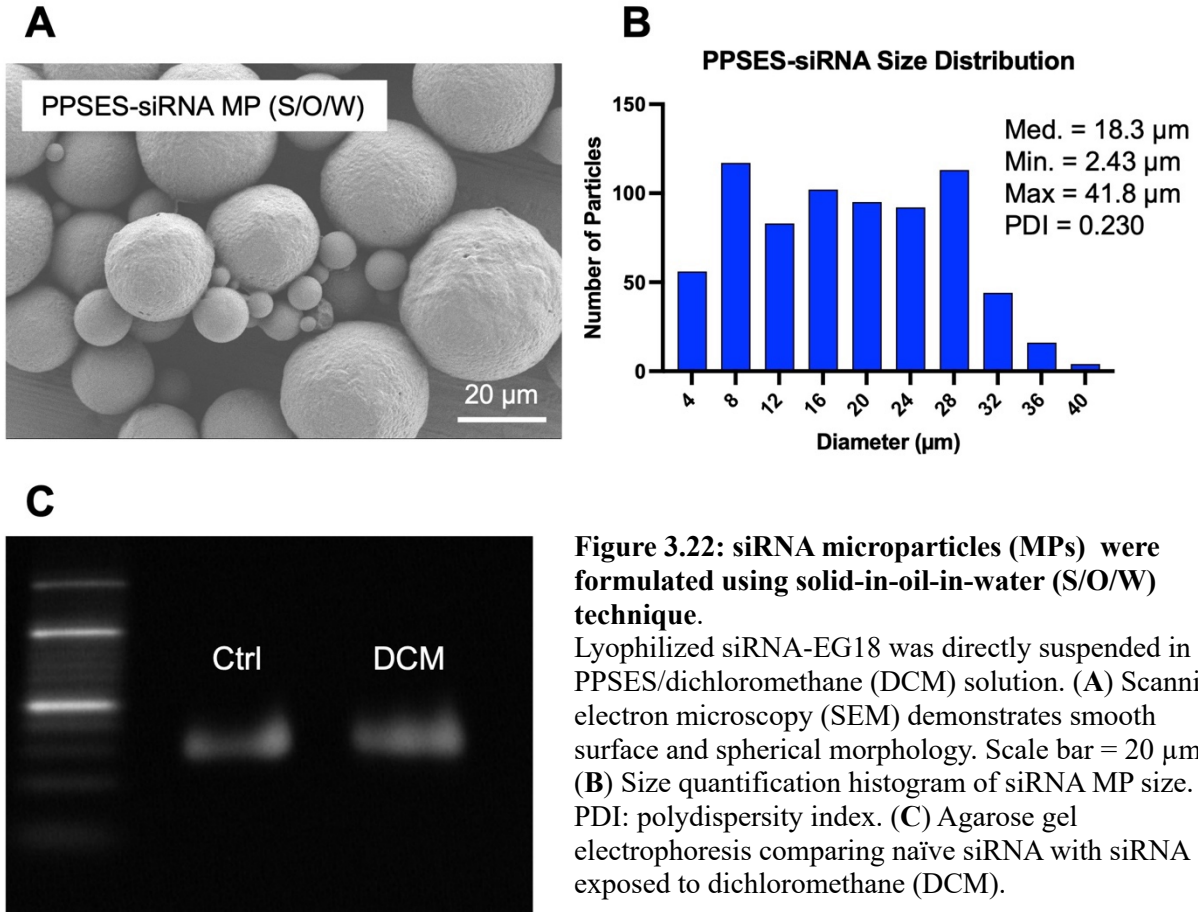

Figure 3.22: siRNA microparticles (MPs) were formulated using solid-in-oil-in-water (S/O/W) technique.
Lyophilized siRNA-EG18 was directly suspended in PPSES/dichloromethane (DCM) solution. (**A**) Scanning electron microscopy (SEM) demonstrates smooth surface and spherical morphology. Scale bar = 20 µm. (**B**) Size quantification histogram of siRNA MP size. PDI: polydispersity index. (**C**) Agarose gel electrophoresis comparing naïve siRNA with siRNA exposed to dichloromethane (DCM).

Sustained release of siRNA is advantageous to extend the effect of knockdown without repeat dosing, especially in the context of expanding cells, in which the dose can be "diluted" [181]. However, the field of siRNA delivery is dominated by NPs, due to their ability for efficient loading and transfection efficiency[182]. Despite their small size, some nanoformulations have demonstrated sustained local knockdown *in vivo*. Solid lipid NPs were retained in the mouse hindpaw for 11 days and exhibited a larger area under the curve (AUC) compared to free siRNA[183]. In another study, intradermal injection of PLGA-siRNA NPs were retained in the skin for >80 days, though repeat injections were needed to demonstrate target knockdown[184].

A common strategy for MP siRNA delivery is encapsulation of siRNA nanopolyplexes[143,153,185] for sustained local delivery, since naked, unconjugated siRNA suffers

from poor transfection and instability *in vivo*[186]. Bedingfield et al. demonstrated that loading siRNA polyplexes in PLGA microplates significantly improved retention and target gene knockdown compared to polyplexes alone[153]. In a similar application, Mountziaris et al. demonstrated efficacy of PLGA MPs loaded with siRNA polyplexes in the rat temporomandibular joint, though they were not compare to polyplexes alone[142]. Chitosan NPs have also been used for nano-in-micro formulations of siRNA due to chitosan's strong positive charge[187]. Bulk hydrogels provide another strategy for sustained local delivery of siRNA polyplexes; for example, poly(β-aminoester)-siRNA polyplexes delivered in a PAMAM-dextran hydrogel significantly improved knockdown over polyplex alone after intratumoral injection[188].

There is strong evidence for sustained siRNA release in many contexts; however, nano-in-micro formulations can be complicated, presenting a barrier to translation, and incorporate positively-charged moieties which can cause toxicity *in vivo*[189]. Additionally, W/O/W formulations with polyplexes can present similar encapsulation and morphology challenges as discussed for proteins. Here, we have utilized a stabilized lipophilic conjugate for direct suspension in the O phase to improve morphology and increase siRNA loading. The incorporation of lipid tails is essential for increased cell uptake and carrier-free activity after release from the MP, forgoing the need for cationic polymers[180,190]. Gel electrophoresis demonstrates that the siRNA does not degrade upon exposure to DCM. We hypothesize that this is due to the backbone stabilization chemistries utilized as well as the solid formulation, where the siRNA is merely suspended in the O phase instead of solubilized in an emulsion with W/O interfaces. Overall, this formulation represents a simplified formulation for local sustained release of siRNA.

3.3. Conclusions

In this work, we have demonstrated the necessity of crystallinity for fabrication of large polysulfide MPs. These MPs maintained their ROS scavenging, with a clear dose dependence to H_2O_2. The oxidation profile exhibited a long delay in oxidation, followed by a sharp increase in oxygen signal. We also optimized loading protocols for EPO protein and siRNA lipophilic conjugates. For EPO, S/O/W formulation was optimized for the inclusion of cationic dextran for nearly 100% EPO encapsulation. This resulted in MPs with >90% encapsulation and sustained release over nearly 3 months. siRNA formulation was also optimized for loading of lipophilic siRNA conjugates in a simplified formulation procedure.

3.4. Materials and Methods

3.4.i. Materials

Unless otherwise stated, all materials were purchased from Sigma Aldrich and used as is. EPO ELISA was purchased from Boster Bio. EPO was purchased from Prospec or Antibodies-online.com.

3.4.ii.Microparticle synthesis and characterization

Polymer synthesis

Propylene sulfide (PS) was distilled to remove inhibitor and stored at -20C until use. 2,2'-(ethylenedioxy)diethanethiol was used as initiator. Initiator (0.17 mmol), 1,8-diazabicyclo(5.4.0)undec-7-ene (DBU, 0.67 mmol), and tributylphosphine (TBP, 1.7 mmol) were mixed in 10 ml degassed THF at room temperature. PS and ethylene sulfide (ES) were combined in a single vial at molar ratios varying from 100:0 to 50:50 PS:ES, with a total monomer amount of 36.9 mmol. The monomer mixture was added to the reaction in 8 equal portions, with 15 minutes between additions, followed by an additional 45 minutes of reaction time. 1-iodopropane (0.50 mmol) was added to end cap the polymer and reacted for 1-3 hours. THF was removed by

rotary evaporation, crude product was redissolved in DCM and extracted 3x against brine. DCM was removed by rotary evaporation, and the concentrated polymer was precipitated 3x in MeOH. The purified polymer was redissolved in ~40 ml DCM, and insoluble fragments were removed via filtration through coarse filter paper. Excess DCM was removed by rotary evaporation and dried in a vacuum oven. Samples were analyzed by NMR (Bruker) at ~1% (w/v) in deuterated chloroform ($CDCl_3$). Conversion of the PS and ES monomers was confirmed by integrating the ^1H NMR (400 MHz), δ = 2.9, 2, CH_2; 2.8, 4, CH_2; 2.6, 1, CH; 1.4, 3, CH_3; 3.6, CH_2, 3.7, CH_2. The relative molecular weight of the series was determined via GPC as described in Section 2.4.iii.

Differential scanning calorimetry

Approximately 10 mg polymer was weighed into an aluminum Tzero pan, crimped, and loaded into the calorimeter (TA Instruments). Air was used as a reference sample. The sample was stabilized at 140°C for 3 minutes to erase thermal history. Next, the sample was cooled at 20°C/min to -80°C to promote crystallization and glass transition. After 3 minutes to stabilize, the sample was heated to 140°C at 20°C/min to capture melting events.

X-ray diffractive spectroscopy

Polymer samples were deposited onto a glass sample holder and placed in the vacuum chamber of the XRD instrument scanner (Rigaku). Reflections were captured at 2θ = 10-30 at 9°/min with a step size of 0.1°. Data was smoothed and normalized to peak intensity for sample comparison. The $X_{c\%}$ was determined by measuring the AUC at 2θ = 24° and comparing to the total AUC.

Microparticle fabrication

Polymers were dissolved in organic phase comprising of DCM or 50:50 DCM:$CHCl_3$ at 50 mg/ml w/v. Oil phase was added to water phase comprising 10-15 mg/ml PVA (w/v), with or without 50 mg/ml NaCl (w/v). The O/W emulsion was prepared either via homogenization or stirring at various speeds to control MP size. Polymer/oil droplets were hardened to MPs either via rotary evaporation (10-60 min) or gentle stirring in a hardening solution composed of 1 mg/ml PVA (w/v) with or without 50 mg/ml NaCl (/wv) and 0.5% Tween-20 (v/v) (10-60 min). MPs were centrifuged at 300xg for 3 minutes and rinsed with DI water 1-2x. Samples were resuspended in water or a lyoprotectant solution of 6.67 mM sucrose and 0.5% Tween-20, snap frozen in liquid nitrogen, and lyophilized.

Scanning electron microscopy

Samples were suspended in DI water and deposited onto steel stubs coated with copper tape. Dextran NPs were suspended in DCM instead of water to maintain morphology. After air drying, the sample was sputter coated with gold. MPs were imaged on a Nikon SEM with Gemini column.

Oxidation-dependent degradation of MPs

MPs were prepared using the following conditions: PPSES was dissolved at 50 mg/ml in DCM/$CHCl_3$ (50:50). 1000 µl was added dropwise to 6 ml 1% PVA + 5% NaCl, and the emulsion was stirred at 1000 rpm for 60 seconds. The MPs were hardened via gentle stirring in 200 ml 0.1% PVA + 5% NaCl + 0.5% Tween-20 (60 min). Aliquots were rinsed twice with DI water, resuspended in DI water, snap frozen in liquid nitrogen, and lyophilized for storage at -20°C. MPs were resuspended at 10 mg/ml in 0.25% Pluronic F-127 + 0.25% carboxymethylcellulose. H_2O_2 was added for final concentrations of 0, 10, 25, 50, and 100 mM H_2O_2 and 2.5 mg/ml MP. Samples were agitated at 37°C for the duration of the experiment. At pre-determined time points, 60 µl samples were collected, resuspended in water, and deposited

onto SEM stubs for morphological and elemental analysis. Stock tubes were centrifuged at 300 rcf, and supernatant was replaced with fresh H2O2 at each collection time point. 0.5% Tween-20 was incorporated into all solutions to prevent MP adherence to tube and pipette tip walls. Morphology was visualized via SEM as above.

Energy dispersive x-ray spectroscopy

At each time point, samples were analyzed for elemental composition via EDS on the Nikon SEM. Applied voltage and current were 10 kV and 1 nA, respectively, and collection time was 20 seconds. Weight percentage of the three major elements, C, O, and S, were calculated from the resulting spectra. MPs were categorized as "small" (<50 µm) and "large" (>50 µm), and five spectra per size per sample were collected.

3.4.iii. Fabrication of drug-loaded microparticles

W/O/W emulsion for EPO MPs

PPSES-EPO Gen1 MPs were formulated with the following conditions: 50 µl EPO-R76E (450 µg/ml) was added to 1 ml PPSES in DCM (11.25 mg/ml). The W/O emulsion was homogenized at 20,000 rpm for 30 seconds, then added dropwise to 6 ml 1% PVA +10% NaCl. The W/O/W emulsion was stirred at 800 rpm for 60 seconds and hardened in 200 ml 0.1% PVA + 10% NaCl for 4 hours on ice. The MPs were collected and rinsed 1x with water. The hardened MPs were resuspended in 1 ml 6.67 mM sucrose + 0.5% Tween-20, frozen in liquid nitrogen, and lyophilized. Control MPs were formulated with 50 µl PBS as the internal W phase. EPO encapsulation was determined by degrading the MPs in 1000 mM H_2O_2 for 48 hours and measuring EPO concentration by ELISA.

Protein-loaded dextran particle fabrication

For all-aqueous particle fabrication, proteins (BSA, esterase, or EPO) were dissolved in DI water. Concentrated dextran (40,000 Da) was added to the protein, followed by concentrated

PEG8000. The sample was vortexed aggressively and frozen, followed by lyophilization. PEG was removed by rinsing 3x with DCM. To investigate influence of cationic dextran, DEAE-dextran (70,000 Da) at varying ratios was complexed with protein for 30 minutes before proceeding with formulation. To investigate freezing speed, formulations were frozen at -20C or with liquid nitrogen. Finally, some EPO preparations compared high protein salt concentrations to approximately normosmotic preparations. To prepare "low-salt" EPO, commercial EPO was reconstituted at 100 mg/ml in 1X PBS and concentrated via centrifugation at 4°C through a 10 kDa spin filter to ~20 mg/ml. EPO was aliquoted, and final concentration was determined by ELISA. After dextran-protein particle fabrication, rinsed samples were imaged using SEM as above, and the protein loading was measured by dissolving samples in water and running BCA assay or EPO ELISA.

S/O/W emulsion for EPO MPs

PPSES-EPO Gen2 MPs: 100 µg EPO (Prospec) was reconstituted in ~200 µl DI water, transferred to a PCR tube, and lyophilized. The protein was reconstituted in 10 µl DEAE-dextran (6 mg/ml) and incubated for 5 minutes on ice. 10 µl dextran (34 mg/ml) was added, followed by 20 µl PEG (160 mg/ml). The suspension was vortexed at max speed for 45 seconds and snap-frozen in liquid nitrogen for lyophilization. The lyophilized NPs were washed 3x with DCM to remove PEG, suspended in 200 µl PPSES (50 mg/ml in DCM), and added dropwise to 6 ml 1% PVA. The sample was stirred for 60 seconds at 1000 rpm, rinsed 1x with DI water and resuspended in 0.5% Tween-20 + 6.67 mM sucrose. MPs were flash-frozen in liquid nitrogen and lyophilized. Control MPs were formulated with blank DEAE-dextran NPs. EPO loading was determined by dissolving MPs in DCM, collecting dextran MPs by centrifugation, and rinsing twice more with DCM before lyophilization. Dextran/EPO pellet was dissolved in DI water, and EPO concentration was determined by ELISA.

PPSES-EPO Gen3 MPs: “Low-salt” EPO was prepared and stored in single-use aliquots as above. 18 µl DEAE-dextran (4.69 mg/ml) was added to 2 µl EPO (562 µg/µl) and incubated for 30 minutes on ice. 10 µl dextran (36.59 mg/ml) was added, followed by 15 µl PEG8000 (240 mg/ml). The solution was vortexed at max speed for 60 seconds, incubated on ice for 10 minutes, and frozen in liquid nitrogen for lyophilization. The lyophilized NPs were washed 3x with DCM to remove PEG, suspended in 200 µl PPSES (50 mg/ml, $CHCl_3$/DCM), and added dropwise to 1 ml 1% PVA + 5% NaCl. MP droplets were hardened for 15 minutes in 200 ml 0.1% PVA + 5% NaCl + 0.5% Tween-20. Hardened MPs were collected and rinsed twice with DI water, resuspended in DI water, snap frozen, and lyophilized. Control MPs were formulated with blank DEAE-dextran NPs. EPO encapsulation was determined by measuring EPO concentration in each wash step by ELISA. Control samples were prepared by suspending dextran-EPO particles in a DCM/$CHCl_3$ oil phase, emulsified, and processed as MPs above. Encapsulation efficiency in EPO MPs was determined by comparing EPO concentration (ELISA) in the supernatants of control and MP samples.

DEAE-dextran S/O/W for siRNA MPs

siRNA-dextran NPs were fabricated as follows: 10 µl uncharged dextran was added to 10 µl siRNA-EG18 (10 µg/µl), followed by 10 µl DEAE-dextran (7.5 mg/ml). The solution was incubated on ice for 30 minutes, followed by the addition of PEG (10 µl, 320 mg/ml). The solution was vortexed for 60 seconds, incubated on ice for 10 minutes, and flash frozen for lyophilization. Lyophilized siRNA-dextran NPs were rinsed 3x with DCM and resuspended in 200 µl PPSES (50 mg/ml, $CHCl_3$/DCM). The S/O suspension was added dropwise to 6 ml 1% PVA + 5% NaCl and homogenized at 3000 rpm for 30 seconds. MPs were hardened for 15 minutes in 200 ml 0.1% PVA + 5% NaCl, rinsed twice with DI water, flash frozen and lyophilized. To measure siRNA loading, MPs were dissolved in DCM and centrifuged to pellet

dextran-siRNA NPs. Samples were washed twice more, dried, and measured for RNA concentration by Ribogreen.

W/O/W for siRNA MPs

Zipper-stabilized, cholesterol-conjugated siRNA (31.2 µg/ml, 50 µl) was suspended in 1 ml PPSES (3.12 mg/ml, DCM). The W/O emulsion was homogenized at 20,000 rpm for 30 seconds and added dropwise to 6 ml 1% PVA + 5% NaCl. The W/O/W emulsion was homogenized at 3000 rpm for 30 seconds and hardened for 15 minutes in 200 ml 0.1% PVA + 5% NaCl + 0.5% Tween-20. MPs were rinsed twice, frozen, and lyophilized.

S/O/W with lyophilized siRNA conjugates for PPSES-siRNA MPs

Stabilized lipid conjugate siRNA was prepared as described previously[180]. Annealed samples were desalted (Glen), quantified via A260, aliquoted to 100 µg aliquots, and lyophilized for storage at -20°C. 400 µl PPSES (50 mg/ml, DCM) was added to 200 siRNA, sample was vortex and sonicated briefly to disperse siRNA, and the suspension was added to 6 ml 1% PVA + 5% NaCl. The S/O/W emulsion was homogenized at 3000 rpm for 30 seconds, hardened for 30 minutes in 200 ml 0.1% PVA + 5% NaCl. + 0.5% Tween-20, rinsed twice with DI water, frozen, and lyophilized. siRNA loading was measured by dissolving MPs in DCM and running UV-VIS on the sample. Absorbance at 559 nm (Cy5) was quantified against a standard curve.

Measurement of EPO Release

PPSES-EPO Gen2 MP: 15 µg MP were transferred to 0.6-ml microcentrifuge tubes. 300 µl PBS was added, and samples were agitated at 37°C for the duration of the experiment. At pre-determined time points, samples were centrifuged at 300 rcf for 3 minutes to pellet MPs, supernatant was collected and stored at -20°C, and MPs were resuspended in fresh PBS. EPO concentration in releasate was measured by ELISA.

PPSES-EPO Gen3 MP: EPO (1 mg) was reconstituted in 1 ml POPSO buffer at pH 7.9. 50 µg rhodamine isothiocyanate (RITC) in 125 µl dry DMF was added, and the reaction was allowed to proceed for 5 hours at room temperature with gentle agitation. The sample was spin filtered to concentrate and remove DMF, POPSO, and unreacted RITC, and purified rho-EPO was aliquoted and stored at -20°C. EPO concentration was quantified by ELISA. Dextran particles were formulated as follows: RITC-EPO (144 µg, 4.5 µl) and DEAE-dextran (108 µg, 13.12 µl) were combined and incubated on ice for 30 min. Dextran (468 µg, 10 µl) was added, followed by PEG8000 (4.6 mg, 30 µl). The samples was vortexed at max speed for 60 seconds, incubated on ice for 10 minutes, snap frozen, and lyophilized.

RITC-EPO particles were rinsed 3x with DCM and suspended in 288 µl PPSES in DCM/$CHCl_3$ (50 mg/ml). The suspension was added dropwise to 6 ml 1% PVA+ 5% NaCl, stirred at 1000 rpm for 60 seconds, hardened for 15 minutes in 200 ml 0.1% PVA+ 5% NaCl+ 0.5% Tween-20, and rinsed twice with DI water before lyophilization and storage. For release experiments, MPs were resuspended at 10 mg/ml in 0.25% Pluronic F-127 (PF127)+ 0.25% carboxymethylcellulose (CMC). 3 mg was deposited in microcentrifuge tubes in triplicate, and PBS or H_2O_2 (final concentration 10 mM) were added. At predetermined time points, supernatants were collected and stored at -20°C until analysis, and fresh release buffer was added. 100 µl releasate was plated in duplicate in a black-walled 96-well plate, and RITC-EPO signal was measured at ex/em 570/585 and quantified from a standard curve.

3.4.iv.Statistical analysis

All data is presented as mean ± standard deviation unless otherwise stated. Statistical significance for MP oxidation was determined by 2-way ANOVA with Šídák's multiple comparisons test and for EPO loading in dex vs. DEAE dex NP by unpaired two-tailed t test.

Chapter 4: Test efficacy of ROS scavenging for local therapeutic delivery to reduce tissue damage in models of glaucoma and post-traumatic osteoarthritis

4.1. Background

4.1.i. EPO delivery for glaucoma

Glaucoma is a leading cause of blindness worldwide, with treatments largely focusing on lowering IOP, either by drug treatment or surgical means[77]. Because the eye is difficult to access systemically, local delivery of therapeutics is preferable[43]; however, eye drops are inefficient for delivery to posterior tissues, and repeated intravitreal injections are highly risky. Therefore, potent therapeutics for long-term neuroprotection are needed. EPO has been shown to be neuroprotective in many models[191]. The mechanism of neuroprotection has been attributed to EPO's ability to activate the antioxidant response element by increasing Nrf2 phosphorylation, which was recently shown to be MAP kinase-dependent[192] (**Figure 4.1**). We have previously

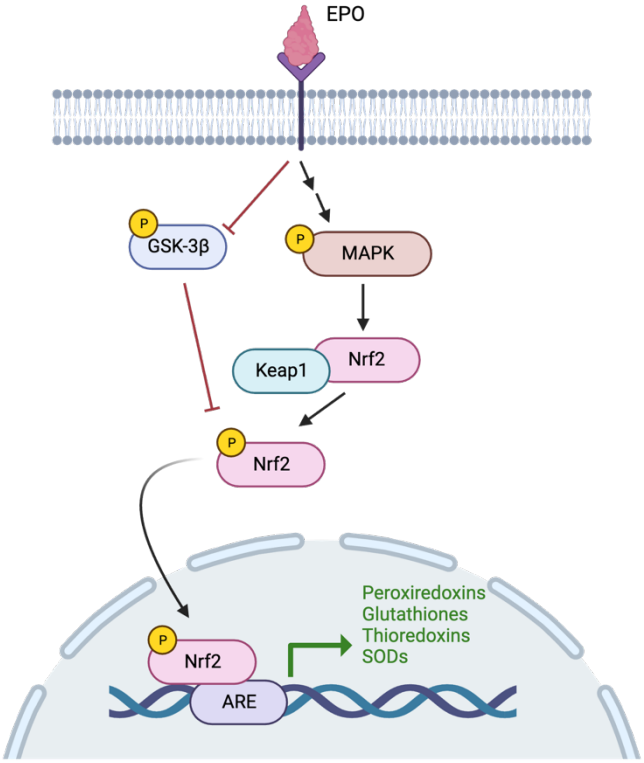

Figure 4.1: Mechanism by which EPO activates antioxidant protein production.
EPO activates phosphorylation of MAPK, phosphorylating Nrf2 to liberate Nrf2 from Keap1. Nrf2 translocates to the nucleus and activates the antioxidant response element (ARE). Schematic created in Biorender.

demonstrated that the antioxidant activity of EPO can synergize with ROS scavenging by PPS when PPS-EPO MPs were injected intravitreally in a mouse model of traumatic optic neuropathy[30]. PPS-EPO significantly reduced cytokine production and optic nerve damage in these mice, resulting in improved visual function. Notably, PPS alone exhibited intermediate or similar effects to PPS-EPO, whereas control PLGA MPs worsened most outcomes. Therefore, we were interested in testing our PPSES-EPO MPs in a more challenging model of glaucoma and comparing activity to PPS-EPO.

4.1.ii. MPs delivering siRNA targeting senescence and catabolism for post-traumatic osteoarthritis

Idiopathic OA and PTOA are leading causes of disability worldwide, which require innovative new treatments. Two major contributors to joint damage and inflammation in PTOA are the overproduction of proteases, including MMP13[193], and premature senescence[194]. MMP13 plays a major role in breaking down articular cartilage in the OA joint, and suppression of this protease significantly improves joint scores, bone morphology, and inflammatory signaling in PTOA mice[153,195,196]. The role of senescence in PTOA is more nuanced, and many research questions remain. It is clear that senescence markers increase in aged and injured cartilage[197], and senescent cells secrete the senescence-associated secretory phenotype (SASP), which includes cytokines and proteases that can influence activity of adjacent cells and tissues[198]. Targeting senescent cells using small-molecule senolytic drugs improves PTOA in mice[49]. However, a senolytic drug candidate did not meet primary endpoint in a Phase II clinical trial of OA[199], though this could be due to poor drug retention after intra-articular injection. A major target of interest in the field is *Cdkn2a*, the gene which encodes cell cycle inhibitor proteins $p16^{INK4a}$ and $p19^{ARF200}$ (**Figure 4.2**). We hypothesized that knockdown of Cdkn2a in PTOA via

siRNA-eluting MPs could mitigate OA by suppressing injury-induced senescent switch, thereby reducing SASP and cartilage damage.

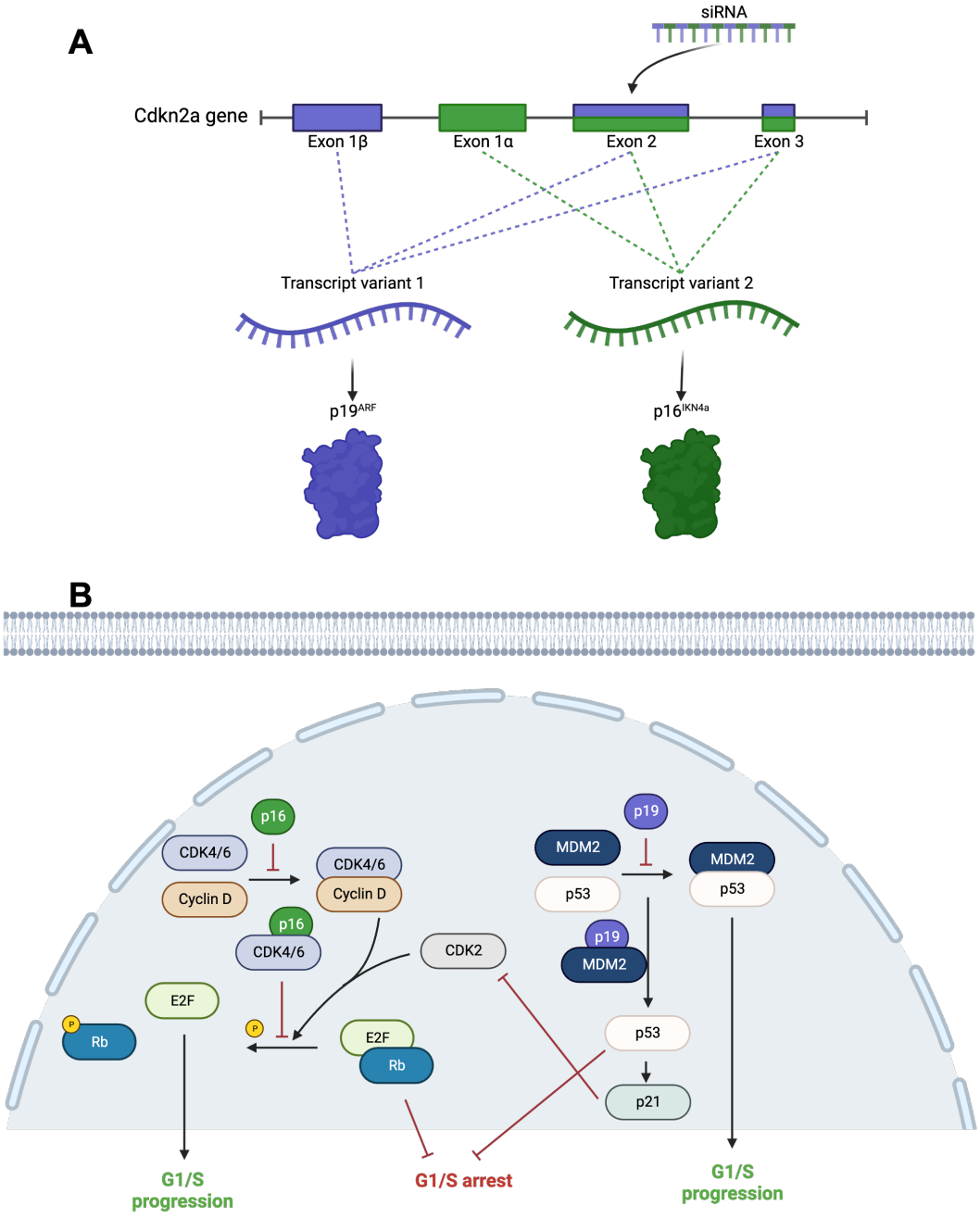

Figure 4.2: Biology of *Cdkn2a* signaling.
(**A**) The transcript variants of *Cdkn2a* vary at their first axon, with transcript variants 1 and 2 encoding $p19^{ARF}$ and $p16^{INK4a}$. siRNA can be designed to target an overlapping exon for simultaneous knockdown. (**B**) Both transcripts of *Cdkn2a* result in cell cycle arrest by different pathways. $P16^{INK4a}$ inhibits cyclin-dependent kinase 4/6 (CDK4/6), whereas $p19^{ARF}$ inhibits MDM2 to activate p53. Figure created in Biorender.

4.2. Results and Discussion

4.2.i. Low-dose EPO delivery by PPSES MPs in mouse model of glaucoma

As described in Section 0, we formulated EPO MPs using the standard W/O/W formulations using PPS and PPSES. PPS-EPO MPs previously exhibited promising results in a mouse model of blast-induced traumatic optic neuropathy (bITON) [30], so this system was used as our benchmark to test the first-generation PPSES-EPO MP in the mouse microbead occlusion model (MOM) of glaucoma[201]. All the studies in this section follow the outline in **Figure 4.3** with MPs injected intravitreally 1 week after initial IOP elevation.

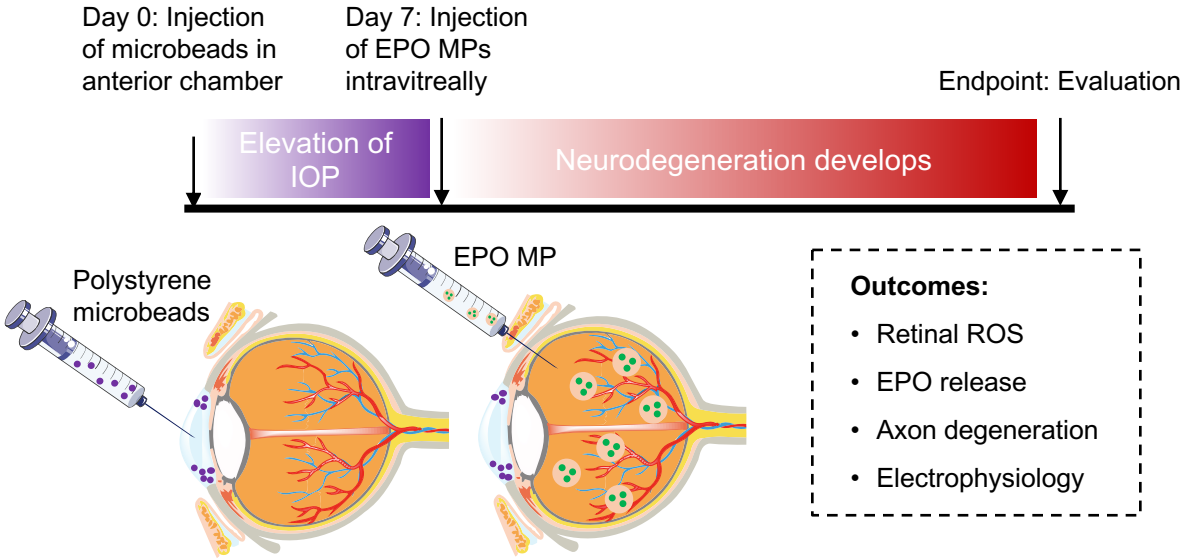

Figure 4.3: Schematic of microbead occlusion model (MOM) time course for EPO MP studies. Endpoint varies depending on study. IOP: intraocular pressure; MP: microparticles; ROS: reactive oxygen species. Adapted from Servier Medical Art.

In the first study, we compared PPS-EPO MPs with the PPSES-EPO Gen1 MPs formulated via W/O/W emulsion (Error! Reference source not found. and Error! Reference source not found.). The particle dose was matched at 10 µg PPSES, delivering 8.5 and 7.7 ng EPO for PPS and PPSES, respectively. Controls included mice receiving no MOM, PBS, 85 ng free EPO (10x dose), and polymer-matched unloaded PPS and PPSES MPs. 2 weeks after

injection (3 weeks after initial IOP elevation), we measured photopic negative response (PhNR) from electroretinograms to quantify retinal ganglion cell (RGC) function. **Figure 4.4** demonstrates that PhNR was significantly preserved in both EPO MP groups compared to free EPO, indicating that even at this intermediate time point, MP delivery is advantageous. This is

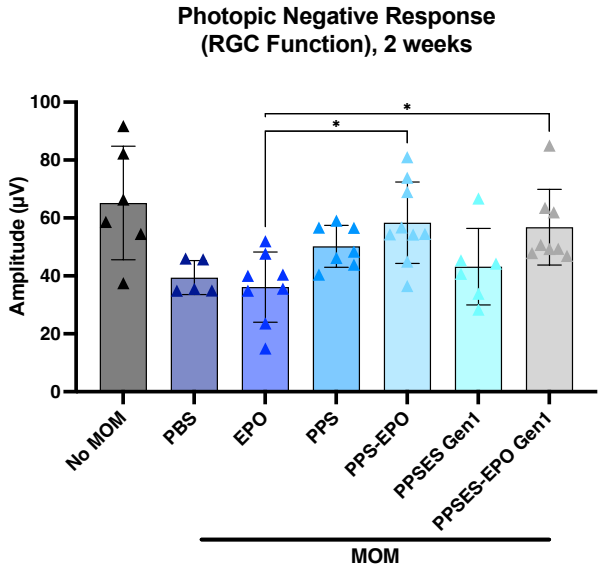

Figure 4.4: Photopic negative response (PhNR) 2 weeks after injection of treatments in glaucomatous mice.
MOM: microbead occlusion model; Gen1: first-generation. N = 5-9 eyes/group. *p<0.05.

likely due to fast clearance of the protein from the vitreous.

The mice were sacrificed at 5 weeks after MP injection (6 weeks after initial IOP elevation) for assessment of EPO delivery, retinal H_2O_2, and histological assessment of the optic nerve. PPSES-EPO Gen1 MP significantly retained EPO in the retina at this time point (**Figure 4.5A**), confirming sustained release from the MP. PPS-EPO MP trended upwards compared to free EPO. Amplex Red demonstrated an increase in retinal H_2O_2 with MOM, which was significantly reduced with all treatments except PPSES Gen1 blank MP (**Figure 4.5B**). Notably, EPO also exhibited reduction in H_2O_2, likely due to the higher injected dose and the elevation of downstream signaling networks to activate Nrf2 and expression of antioxidant proteins. The

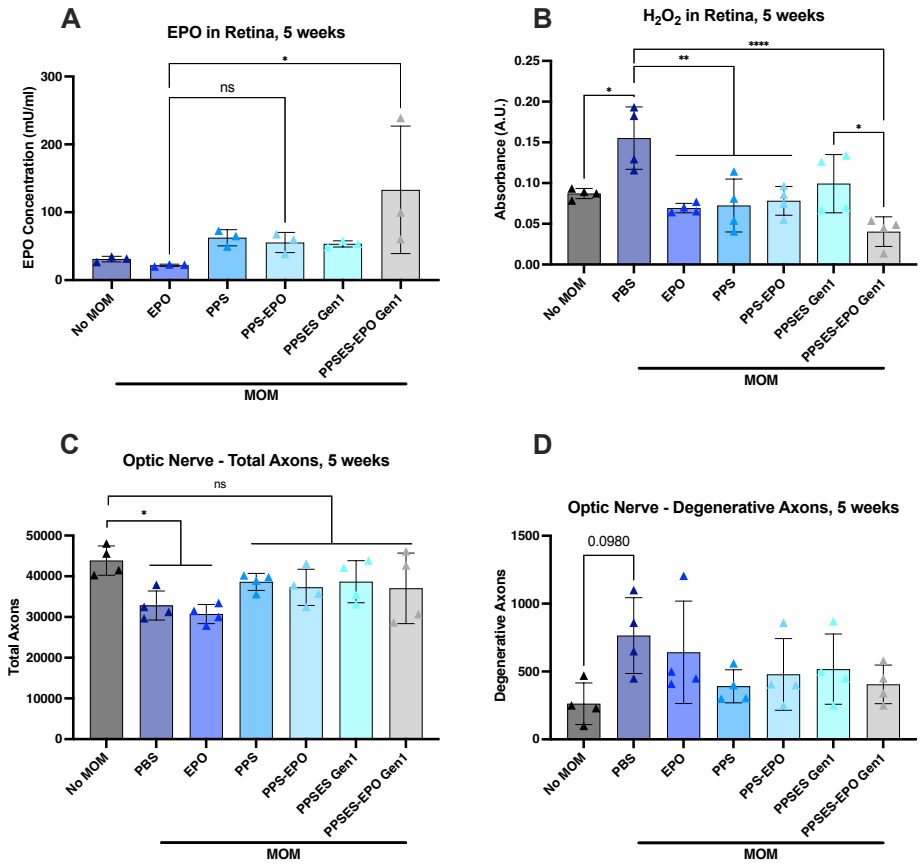

Figure 4.5: Evaluation of PPSES-EPO Gen1 MP 5 weeks after injection in mouse microbead occlusion model (MOM).
(**A**) EPO levels in mouse retina determined by ELISA. (**B**) Retina H_2O_2 levels determine by Amplex Red. (**C**) Total axon counts and (**D**) degenerative axons from histological sections of optic nerves. N = 4 eyes/group for all data. *p<0.05, **p<0.01, ****p<0.0001, ns=not significant. Gen1: first-generation.

scavenging of H_2O_2 resulted in promising improvements in both optic nerve total axons and degenerative axons. Total axons were significantly reduced in both PBS and EPO-injected eyes, whereas total axon counts were not significantly different from healthy controls in any of the MP-treated groups (**Figure 4.5C**). Degenerative axon counts were not significantly different across groups, likely due to relatively low n (4 eyes/group) and variability in the measurement (**Figure 4.5D**). Regardless, degenerative axon profiles trended upwards with PBS treatment, in line with previous results[30,192], and trended downwards with MP treatment.

Next, we evaluated PPSES-EPO Gen2 in the mouse MOM model compared to PPS-EPO according to the treatment timeline in Figure 4.3. The dose was matched to the previous study: 10 µg MP delivering 8.5 ng for PPS-EPO and 7.3 ng for PPES-EPO Gen2. Controls included no MOM, PBS, 8.5 ng free EPO, and unloaded MPs. At sacrifice, EPO ELISA demonstrated significant elevation of EPO in retinal tissues with MP delivery compared to free EPO injection, indicating that MP delivery with either PPS or PPSES achieved sustained release of cargo (**Figure 4.6A**). Utilizing the Amplex Red H_2O_2 assay, we demonstrated that PPS and PPSES MPs reduced retinal levels of H_2O_2, and this reduction was compounded with EPO delivery

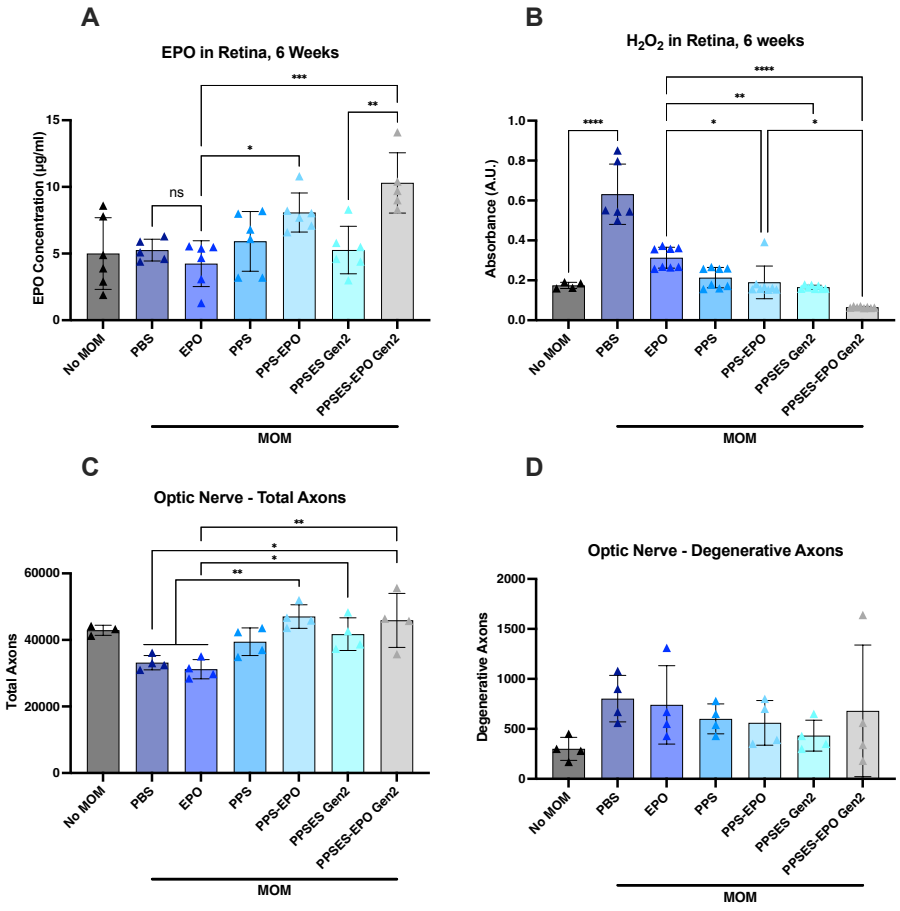

Figure 4.6: Evaluation of PPSES-EPO Gen2 MP 6 weeks after injection in mouse microbead occlusion model (MOM).
(**A**) EPO levels in mouse retina determined by ELISA. (**B**) Retina H_2O_2 levels determined by Amplex Red. (**C**) Total axon counts and (**D**) degenerative axons from histological sections of optic nerves. N = 3-6 eyes/group for all data. *p<0.05, **p<0.001 ***p<0.001, ****p<0.0001. Gen2: second-generation.

(Figure 4.6B). Notably, the largest reduction was demonstrated with PPSES-EPO MPs, which we attribute to the larger size and higher stability of these MPs, which should result in longer-term scavenging. The sustained release of EPO and antioxidant activity of EPO MPs combined to significantly protect the optic nerves of MOM mice, demonstrated by elevated counts of axons in histological sections compared to both PBS and free EPO treatment (**Figure 4.6C**). Degenerative axon profiles trended upwards with MOM and down to healthy levels with MP treatment, but these changes did not reach statistical significance due to variability in the measurement (**Figure 4.6D**).

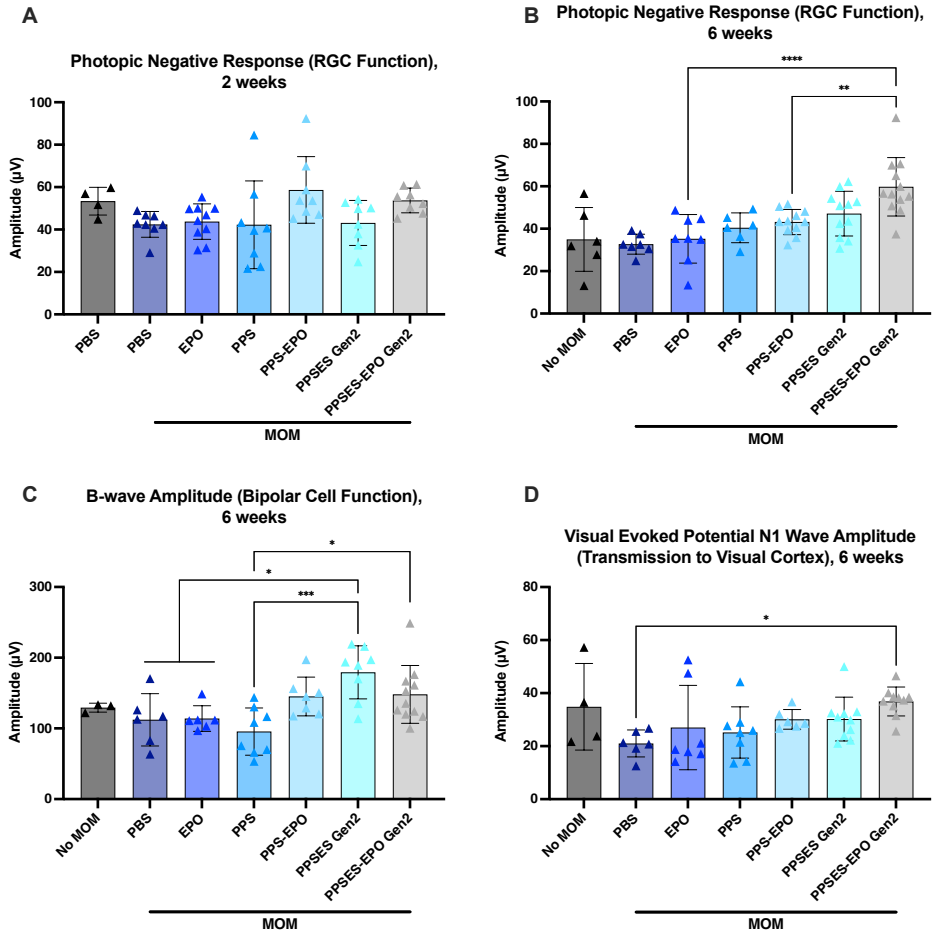

Figure 4.7: Electrophysiology of microbead occlusion model (MOM) mice treated with PPSES-EPO Gen2 at 6 weeks post-injection.
(**A**) Photopic negative response (PhNR) from electroretinogram (ERG) 2 weeks after treatment. (**B**) PhNR 6 weeks after treatment. (**C**) ERG B-wave amplitude 6 weeks after treatment. (**D**) Visual evoked potential (VEP) N1 wave amplitude. N = 3-12 eyes/group for all tests. *p<0.05, **p<0.01, ***p<0.001. Gen2: second-generation.

To test the efficacy of PPSES-EPO Gen2 in preserving retinal and optic nerve function, the Rex laboratory performed ERGs and VEP tests. Two weeks after treatment, PhNR changes were not significant across groups, though PBS and EPO groups trended downward, while EPO MP groups trended towards increased amplitude (**Figure 4.7A**). At 6 weeks, PPSES-EPO Gen2 significantly improved PhNR compared to EPO and PPS-EPO (**Figure 4.7B**). This effect held for the other electrophysiology readouts, ERG B-wave (**Figure 4.7C**) and VEP N1 wave (**Figure 4.7D**) amplitudes. ERG B-wave measures bipolar cell function, while VEP N1 measures signal transmission to the visual cortex. Taken together, these results indicate that PPSES-EPO Gen2 significantly preserves visual function, due to a combination of ROS scavenging and sustained EPO delivery, even at relatively low doses of EPO. The Gen1 and Gen2 studies strongly support the use of PPSES for EPO delivery in this model, so we pursued a more challenging time point with optimized EPO loading.

4.2.ii. High dose EPO delivery in mouse microbead occlusion model and optimization for non-human primates

With the optimized EPO loading and morphology of PPSES-EPO-Gen3 MPs, we targeted an 8-week time point. The injected dose was 102 ng EPO in 10 µg MP. Throughout the study, we measured EPO release in the retinas of mice injected with blank and EPO-loaded MPs (**Figure 4.8A**). EPO concentration peaked at day 14 and remained elevated out to 42 days post-injection, returning to baseline at day 56. At this time point, there was no significant difference between groups in the Amplex Red H_2O_2 assay (**Figure 4.8B**), which is likely due to the late time point and loss of EPO.

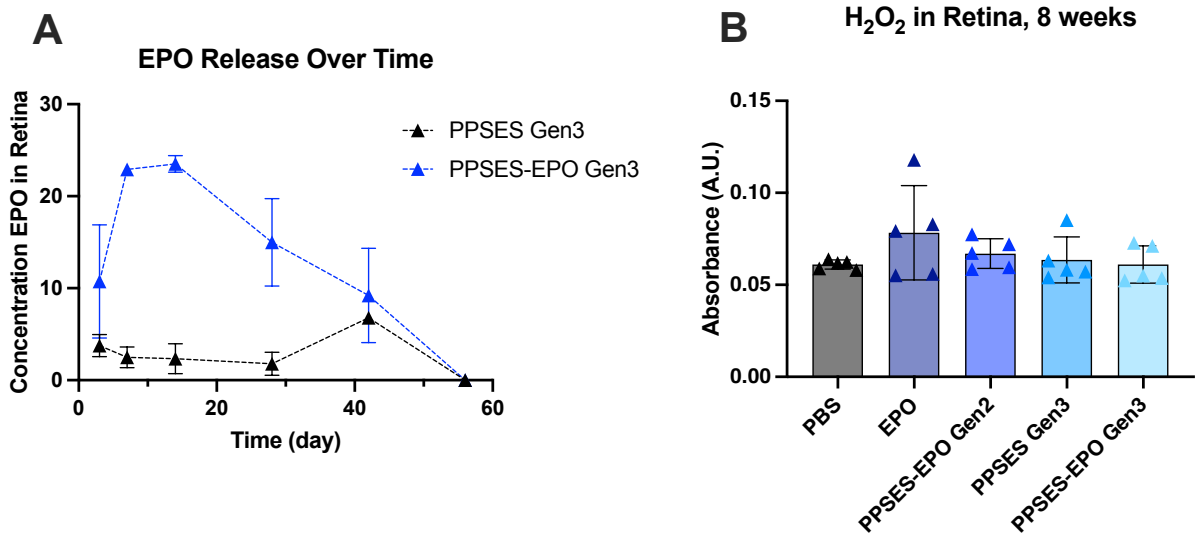

Figure 4.8: Evaluation of PPSES-EPO Gen3 MPs in mouse microbead occlusion model (MOM) at 8 weeks.
(**A**) EPO in retina measured in homogenized tissues at the indicated time point. (**B**) Retinal H_2O_2 measured by Amplex Red. N = 3-5 eyes per group per time point. Gen2: second generation; Gen3: third generation.

The electrophysiology at 6 weeks demonstrated excellent preservation of visual function (**Figure 4.9A-C**), with significant improvement in PhNR, B-wave, and VEP N1 for PPSES-EPO Gen3. The unloaded control PPSES MP also exhibited significant effects in PhNR and B-wave, but not VEP. However, these effects were not seen at 8 weeks (**Figure 4.9D-F**), which is likely due to the drop in EPO levels at this time point. Therefore, these data demonstrate that beneficial effects of PPSES-EPO MP in mouse MOM is dependent on released EPO, and provides a time frame of efficacy for larger animal models.

Our results demonstrate that sustained release of EPO offers significant benefits in the mouse MOM model, with efficacy out to 6 weeks after initial injection. The ability of PPSES-EPO MP to protect the optic nerve and retina over this time represents a possibility to reduce intravitreal injection frequency while preserving tissue function. EPO has demonstrated efficacy in neurodegenerations in our work and others. Intraperitoneal injection of EPO in rats significantly improved outcomes in a model of traumatic brain injury[202], and a similar treatment

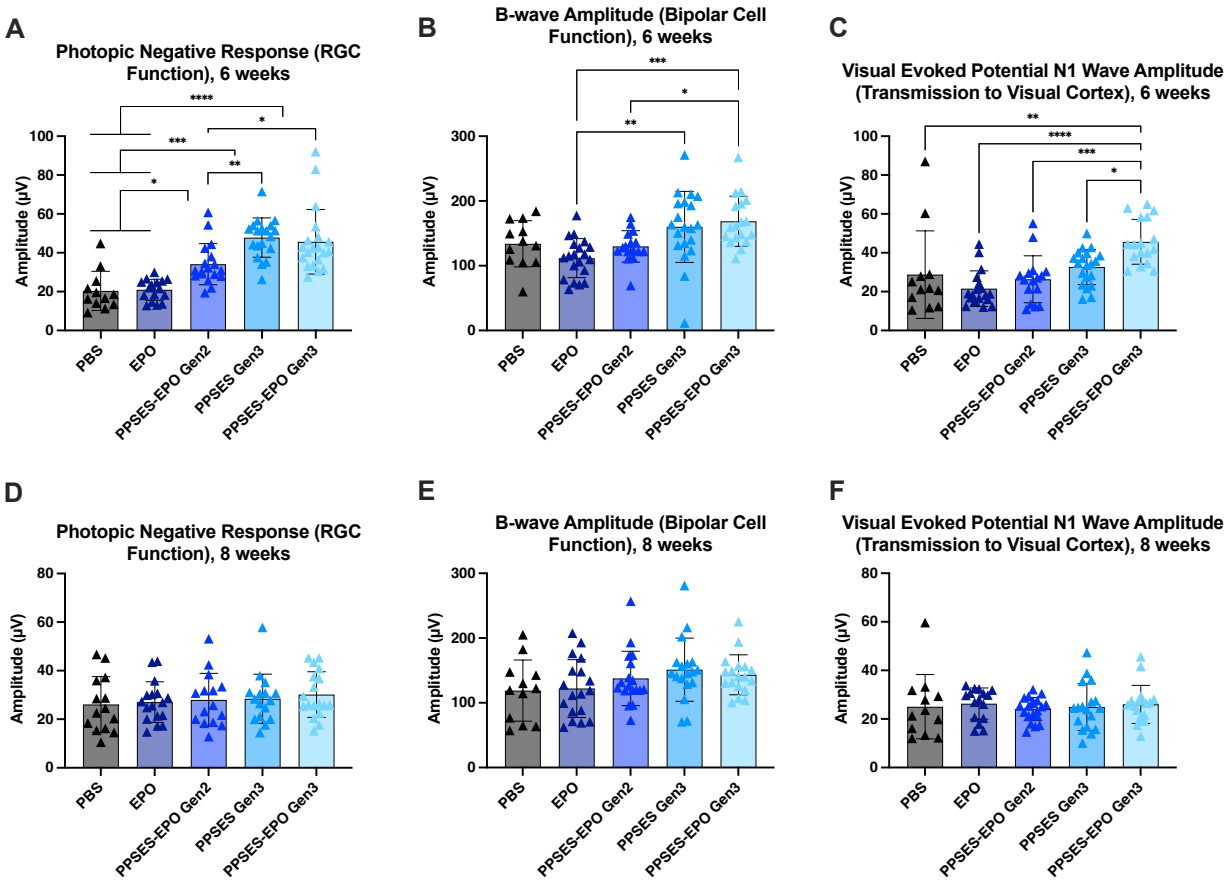

Figure 4.9: Electrophysiology for PPSES-EPO Gen3 MPs at 6 and 8 weeks.
(**A**) Photopic negative response (PhNR) from electroretinogram (ERG) 6 weeks after treatment. (**B**) ERG B-wave amplitude 6 weeks after treatment. (**C**) Visual evoked potential (VEP) N1 wave 6 weeks after treatment. (**D**) PhNR 8 weeks after treatment. (**E**) ERG B-wave amplitude 8 weeks after treatment. (**F**) VEP N1 wave 8 weeks after treatment. N = 12-18 eyes per group for all tests. *p<0.05, **p<0.01, ***p<0.001, ****p<0.0001.

regimen preserved RGCs in a transgenic mouse model of glaucoma[203]. These studies demonstrate the potential of EPO as a neuroprotective agent, though repeat intraperitoneal injections are not translatable.

Multiple studies have investigated the effect of locally-injected PLGA-EPO MPs for treating various neuropathologies. In a rat model of optic nerve crush, PLGA-EPO MP significantly protected RGCs 4 and 8 weeks post-injury compared to unloaded PLGA MP, and performed similarly to free EPO injected every other week[175]. Additionally, a single injection of PLGA-EPO MP in two models of peripheral nerve injury significantly preserved axon count

even 8 weeks after injection[204,205]. EPO delivery exhibits beneficial effects in the context of neurodegeneration, including reduction of glial fibrillary acidic protein (GFAP) in the retina[175] and an increase in protein gene product 9.5 (PGP 9.5) in the optic nerve[205]. These studies did not measure ROS levels in their models, though the Rex laboratory has previously shown activation of Nrf2 by EPO to increase antioxidant expression, including SOD2 and glutathione[192]. Additionally, PLGA alone did not have any effect on pathology, indicating that it serves only as a delivery vehicle. This is in agreement with our previous results, which demonstrated worsened inflammation and degeneration with alone[30]. The is in stark contrast to PPSES, which demonstrates ROS scavenging and neuroprotection in multiple studies. Therefore, we propose that PPSES could represent a new biomaterial for sustained cargo release intravitreally for a variety of applications.

We proceeded to test PPSES-EPO Gen3 in a non-human primate (NHP) MOM model of glaucoma[206]. Early tests indicated that the injection buffer for Gen2, ~0.5% Tween-20 + 6.67 mM sucrose, was not compatible with injection in NHP vitreous, with animals exhibiting behavior suggesting impaired vision (**Supplementary Table C.1**). We determined that Tween-20 was likely causing the issue, and formulated a new buffer utilizing Pluronic F-127 as a surfactant and carboxymethylcellulose as a bulking agent to keep MPs suspended[207]. This allowed for resuspension of MPs after lyophilization in water, whereas in previous batches the MPs would aggregate upon resuspension without Tween-20 and sucrose lyoprotection. This change gives much more dose control and adaptability when administering MPs, as well as improving safety. We utilized brightfield imaging to qualitatively demonstrate improved injectability in our resuspension buffer compared to PBS (**Figure 4.10**). This formulation improved MP transmission through the 29g needle used for NHP intravitreal injections compared to PBS while

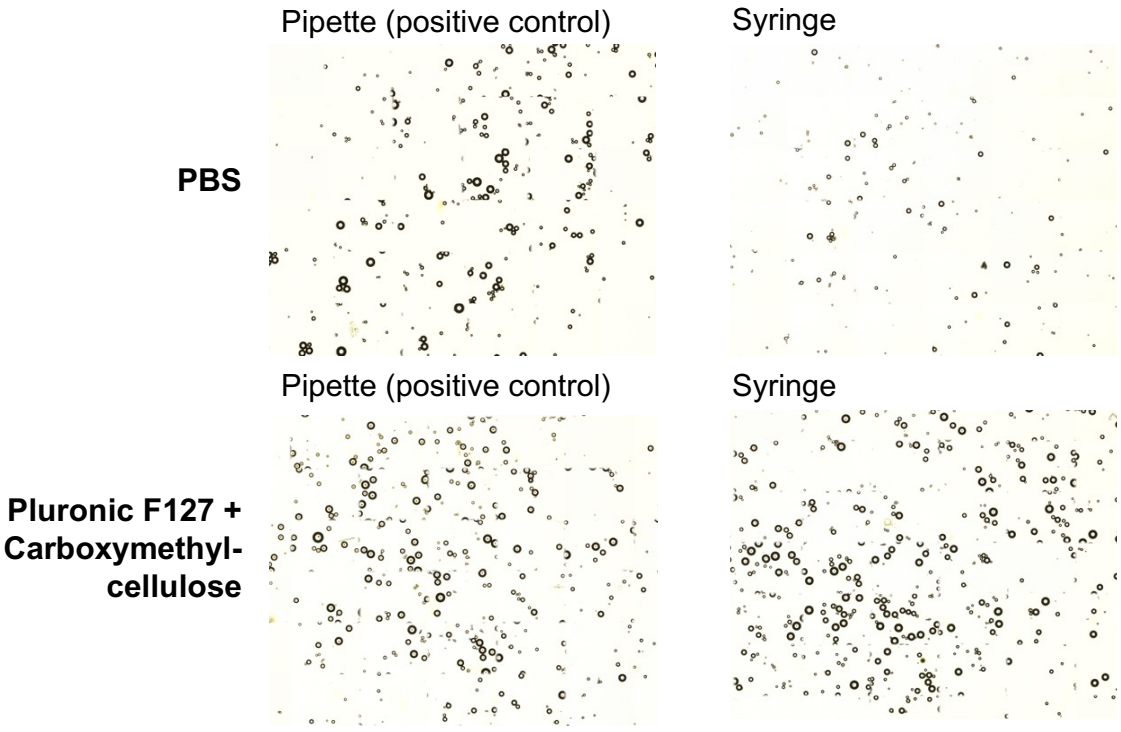

Figure 4.10: PPSES MP injectability.
Microparticles suspended in PBS or injection buffer formulated from 0.25% Pluronic F127 + 0.25% carboxymethylcellulose.

exhibiting no impairment of visual function. Efficient MP injectability is essential for dose control.

We were also interested in reducing endotoxin levels in the MPs to <0.5 EU/ml, the International Standards Organization (ISO) recommendation for intraocular use[208]. Thorough cleaning of glassware by soaking in sodium hydroxide and sterile filtration of all formulation buffers improved endotoxin levels in the EPO MPs (**Figure 4.11A** and **B**). Notably, the FDA guideline for intraocular devices is lower than ISO (0.2 mU/ml vs. 0.5 mU/ml) [208], so further optimization could be necessary for translation. To date, we have not noted any adverse events in the NHPs that indicated toxic anterior segment syndrome (TASS), the most common endotoxin-related complication after intravitreal injection[209].

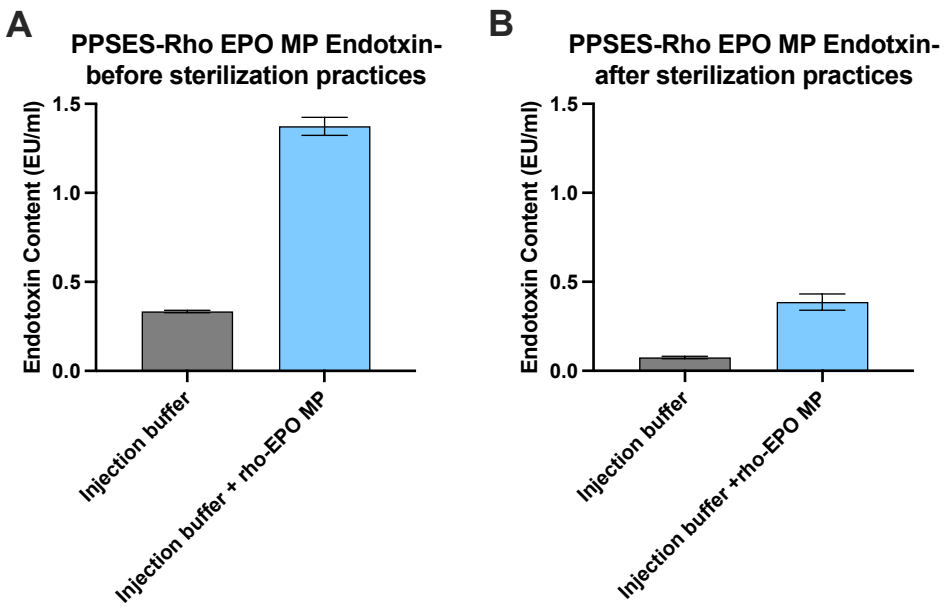

Figure 4.11: Endotoxin levels in PPSES MP loaded with rhodamine-tagged EPO.
Before extensive sterilization practices, endotoxin content was above acceptable levels (**A**). After implementing sterilization practices, endotoxin was reduced (**B**). N = 1 batch per group run in duplicate.

Overall, PPSES-EPO MPs are a promising candidate for intravitreal treatment of glaucoma. This system exhibits potent ROS scavenging and neuroprotection and has been adapted to a translatable animal model. Rescue of retina and optic nerve is extremely challenging clinically, necessitating innovative therapies.

4.2.iii. H_2O_2 elevation in mouse models of PTOA

Because of the ROS-responsive character of PPSES MPs and their potent H_2O_2 scavenging in mouse MOM, we tested whether MPs would provide ROS scavenging after intra-articular injection in PTOA mice. First, we utilized the noninvasive ACL rupture model of PTOA[210]. MPs were formulated with mean diameter ~20 µm and injected intra-articularly (~1 mg MP in 20 µl). PPSES was compared to similarly-formulated PLA MPs. The next day, mice underwent the ACL rupture procedure unilaterally to induce PTOA. Mice were sacrificed 7 days post-rupture, and whole joint H_2O_2 was measured via Amplex Red. As shown in **Figure 4.12A**, H_2O_2 signal significantly increased with rupture, but there was no difference in signal between PLA and PPSES. Therefore, we hypothesized that smaller particles would have higher reactivity to ROS in the joint, and performed a similar experiment comparing MPs (~20 µm) with NPs (~100 nm, **Supplementary Figure C.1**) 1 week after ACLR. Neither group was significantly different from buffer-treated limbs (**Figure 4.12B**).

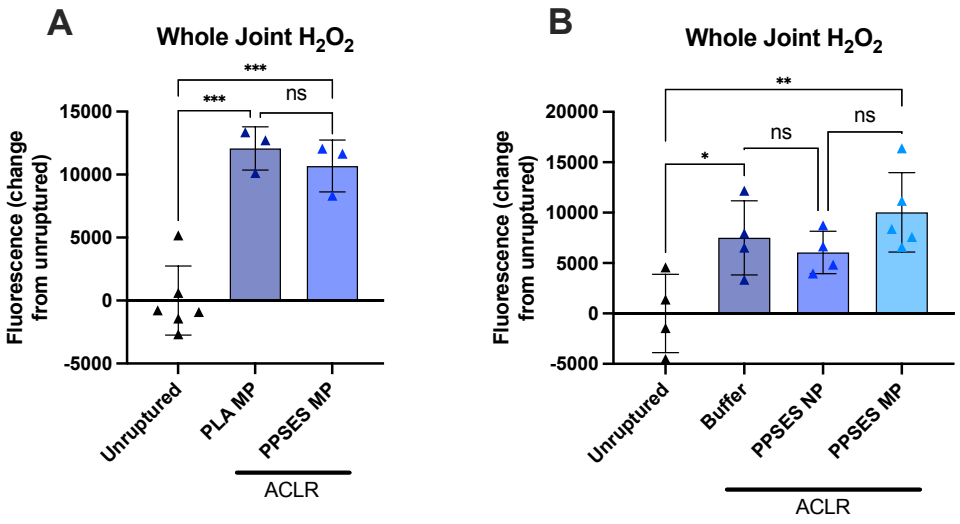

Figure 4.12: Amplex Red signal in whole joint samples 1 week after ACL rupture (ACLR). Mice were injected with 1 mg MP, and rupture occurred the following day. Amplex red was measured in whole joints. (**A**) PPSES MP were compared to size-matched PLA MPs. (**B**) PPSES MP (~20 µm) were compared to PPSES NP (~100 nm). N = 3-6 knees per group. *p<0.05, **p<0.01, ***p<0.001., ns=not significant.

Next, we investigated later time points in PTOA with the rationale that PPSES MP exhibit a lag phase in oxidation *in vitro* (**Figure 3.7**) suggesting a similar lag *in vivo*. We pivoted to the repeat loading model of PTOA due to our lab's experience with this model[153,154,195,196] and the ability to load bilaterally, as opposed to unilateral ACLR. Mice were injected with 1 mg PPSES MP (**Figure 4.13A**) the day before loading began, and mice were loaded bilaterally 3x/week for 3 weeks before sacrifice and joint Amplex Red as above. We included PPS MPs (**Figure 4.13B**) as a historical control based on the ability of these MPs to protect joints from cartilage damage and reduce MMP activity in this model[29]. H_2O_2 signal trended downward with

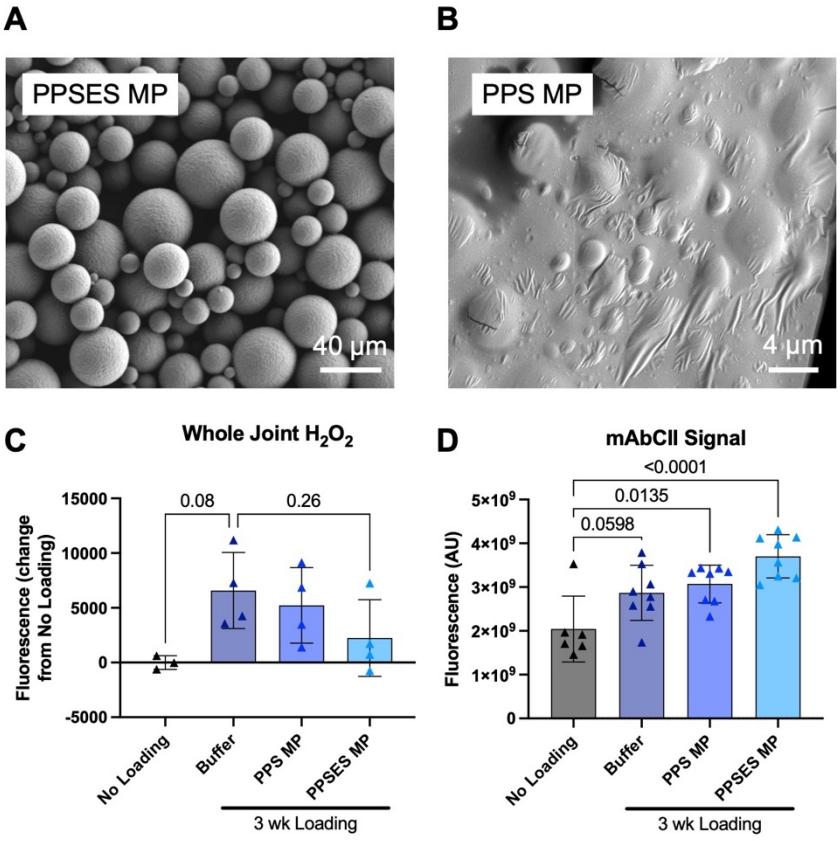

Figure 4.13: PPSES and PPS MP for PTOA.
Mice were injected intra-articularly with 1 mg MP, and compressive mechanical loading began the next day. Joints were loaded 3x/week for 3 weeks before evaluation. (**A**) Scanning electron microscopy (SEM) of PPSES microparticles (MPs) injected in this study. Scale bar = 40 µm. (**B**) SEM of PPS MPs injected in this study. Scale bar = 4 µm. (**C**) Amplex Red assay for joint H_2O_2. N = 3-4 joints/group. P values reported on graph. (**D**) Fluorescent signal of mAbCII in explanted joints with skin removed. N = 6-8 joints/group. P values reported on graph.

PPSES treatment, but the change was not significant compared to buffer treated limbs (**Figure 4.13C**). PPS did not reduce H_2O_2 signal. We also utilized the fluorescently-labeled mAbCII to visualize cartilage damage at sacrifice and saw no reduction with either MP treatment (**Figure 4.13D**). This is contradictory to previously-published results for PPS[29], which could be due to the longer timecourse of this experiment (3 weeks vs. 2 weeks), increased number of loading cycles (250 vs. 40) and potential PPS MP batch differences. Finally, we investigated scavenging in the same model 4 weeks after treatment, comparing standard PPSES MP (~20 µm, **Figure 4.14A**)

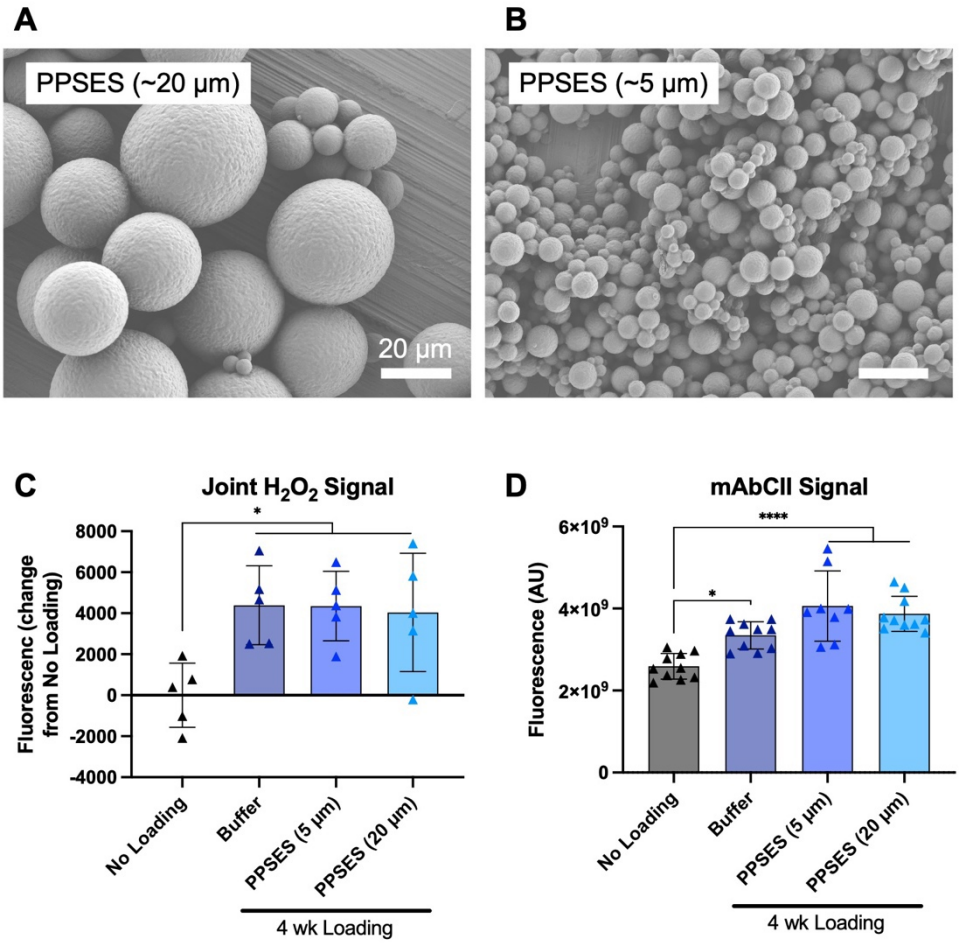

Figure 4.14: PPSES MP of varying sizes for PTOA.
Mice were injected intra-articularly with 1 mg MP, and compressive mechanical loading began the next day. Joints were loaded 3x/week for 3 weeks before evaluation. (**A**) Scanning electron microscopy (SEM) of standard PPSES microparticles (MPs) injected in this study. Scale bar = 20 µm. (**B**) SEM of "small" PPSES MPs injected in this study. Scale bar = 20 µm. (**C**) Amplex Red assay for joint H_2O_2. N = 5 joints/group. (**D**) Fluorescent signal of mAbCII in explanted joints with skin removed. N = 10 joints/group. *p<0.05, ****p<0.0001.

with smaller MPs (~5μm, **Figure 4.14B**), with the hypothesis that 5 μm MP would provide more potent scavenging while also lasting longer in the joint than NPs. However, there was no significant reduction in Amplex Red signal or mAbCII fluorescence with either treatment (**Figure 4.14C-D**). Taken together, these data indicate that PPSES MP of various sizes do not scavenge H_2O_2 in the mouse PTOA joint as measured by Amplex Red.

As mentioned above, PPS MPs have demonstrated efficacy in a short-term, mild PTOA mechanical loading model, where a single dose of PPS MP reduced mAbCII signal and MMP activity at 2 weeks[29]. Others have investigated ROS scavenging biomaterials for PTOA treatment, including poly(thioketal) (PTK) NPs[211,212] and curcumin NPs[213]. Similar to our PPSES-EPO results, PTK NPs demonstrated synergistic activity with loaded anti-inflammatory drugs to mitigate disease progression, providing evidence for joint drug delivery with antioxidant polymers. It is possible that the crystallinity of PPSES renders these particles too stable for oxidation *in vivo* at the time points we studied, supported by the remarkably similar morphology when incubated in aqueous environment for 81 days (**Figure 3.5**, **Figure 3.6**, and **Figure 3.8**). The lowest H_2O_2 concentration used in the degradation study, 10 mM, is still ~3-6 orders of magnitude higher than estimated *in vivo* concentrations[214]. Of course, the oxidative milieu *in vivo* is more complex and dynamic than a homogenous H_2O_2 dose, therefore, degradation could be expected to accelerate after injection. It is also notable to compare the difference in efficacy of PPSES MPs in the intravitreal space and the joint, particularly in terms of Amplex Red. There are a few key differences in these studies which could help to explain the discrepancy. First, the time point in the glaucoma studies was slightly longer (6 vs. 4 weeks), allowing more time to reach the exponential oxidation phase seen at the end of the *in vitro* degradation studies. Additionally, the MP dose was very different- mouse eyes received 10 μg MP injected into an approximate vitreous humor volume of 5 μl[215], whereas mouse knees received ~1000 μg MP

injected into an approximate synovial fluid volume of 3 µl[215]. This required a large injection volume (20 µl), and it is possible that the introduction of a large mass of our relatively crystalline caused mechanical damage to the mouse knee. Because decreasing MP size did not improve scavenging, we believe that strategies to make the MPs more reactive *in vivo* would improve biocompatibility and antioxidant effect.

4.2.iv.Efficacy of siRNA-loaded MPs in the PTOA joint

PPSES MPs (~20 µm) were loaded with stabilized, amphiphilic siRNA PEG-lipid conjugate (EG18) as described in Section 3.2.iv. The siRNA was tagged with Cy5 for tracking *in vivo*. Mice were injected with 1 mg siRNA-MP intra-articularly, and knee joints were imaged over the course of 4 weeks by IVIS. **Figure 4.15A** demonstrates that siRNA was still detected at day 28 intravitally, indicating sustained release of the cargo over the course of the study. The variability in the measurement is likely due to variable injection, and self-quenching of the fluorophore resulting in difficulty quantifying absolute retention[216] (**Supplementary Figure C.2**). **Figure 4.15B** demonstrates strong extravital signal with no appreciable signal in clearance organs, indicating the advantages of sustained local release to minimize off-target effects.

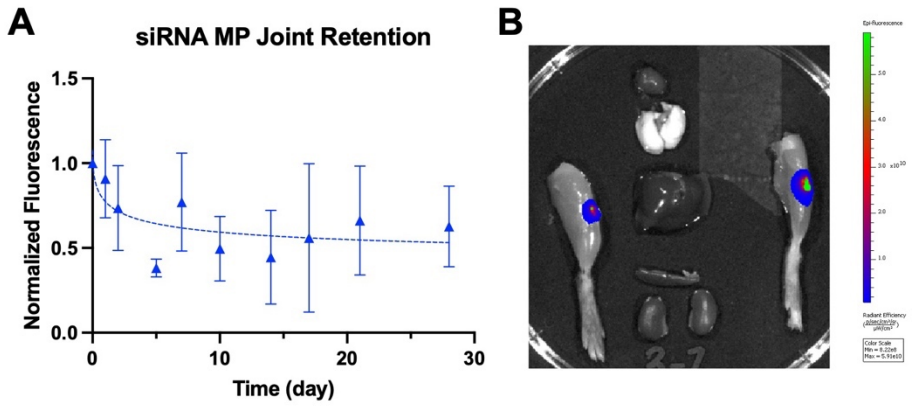

Figure 4.15: siRNA-EG18 MP joint retention.
(A) Intravital fluorescence of Cy5-tagged siRNA conjugate normalized to day 0. N = 4 knees. Dashed line represents sigmoidal fit. (B) Mouse knees and major clearance organs imaged extravitally for Cy5 signal.

We also harvested knee joints once per week to determine MP localization by cryohistology. Samples were sectioned and imaged for Cy5 fluorescence by confocal microscopy. Large MP depots were visualized in the synovium and fat pad of the knees, in agreement with other drug delivery MP systems[153,217] (**Figure 4.16, Figure 4.17, Figure 4.18**). It is not surprising for micromaterials to embed in the synovium due to the dynamic joint environment continuously cyclically compressing the intra-articular space. We expect that MPs release siRNA over time into adjacent tissues to potentiate target knockdown. SiRNA signal was detected at the articular surface on day 1 after injection (**Supplementary Figure C.3**), but not at later time points; however, diffuse signal could be seen distributed throughout the synovium at later time points. We also noted partially degraded particles at each time point in the synovium/ fat pad (**Figure 4.18**).

To investigate the efficacy of our MP platform in the context of intra-articular siRNA delivery, we loaded MPs with a previously-validated siRNA-EG18 against MMP13 (siMMP13) [196]. These MPs were injected on day 0 (1 mg MP/ 5.65 μg siRNA), and mice were loaded 3x per week for four weeks. The following tissues were harvested for total joint qPCR: synovium, patellar tendon, infrapatellar fat pad, meniscus, and cartilage. We assessed *Mmp13* target knockdown compared to MPs loaded with a control sequence, and saw a trend towards silencing (~60% knockdown, p=0.074, **Figure 4.19**). These results supported pursual of a more robust cohort with siMmp13 MPs and our new target of interest, *Cdkn2a*.

Four candidate sequences were screened for *Cdkn2a* knockdown, three of which achieved potent silencing (**Figure 4.20A** and **B**). siRNA and qPCR primer sequences are listed in **Supplementary Table C.2** and **Supplementary Table** C.3**,** respectively. Two lead candidate sequences were synthesized in-house with 2'OMe and 2'F "zipper" backbone stabilization, which has been shown to prevent endonuclease degradation[218], as well as phosphorothioate

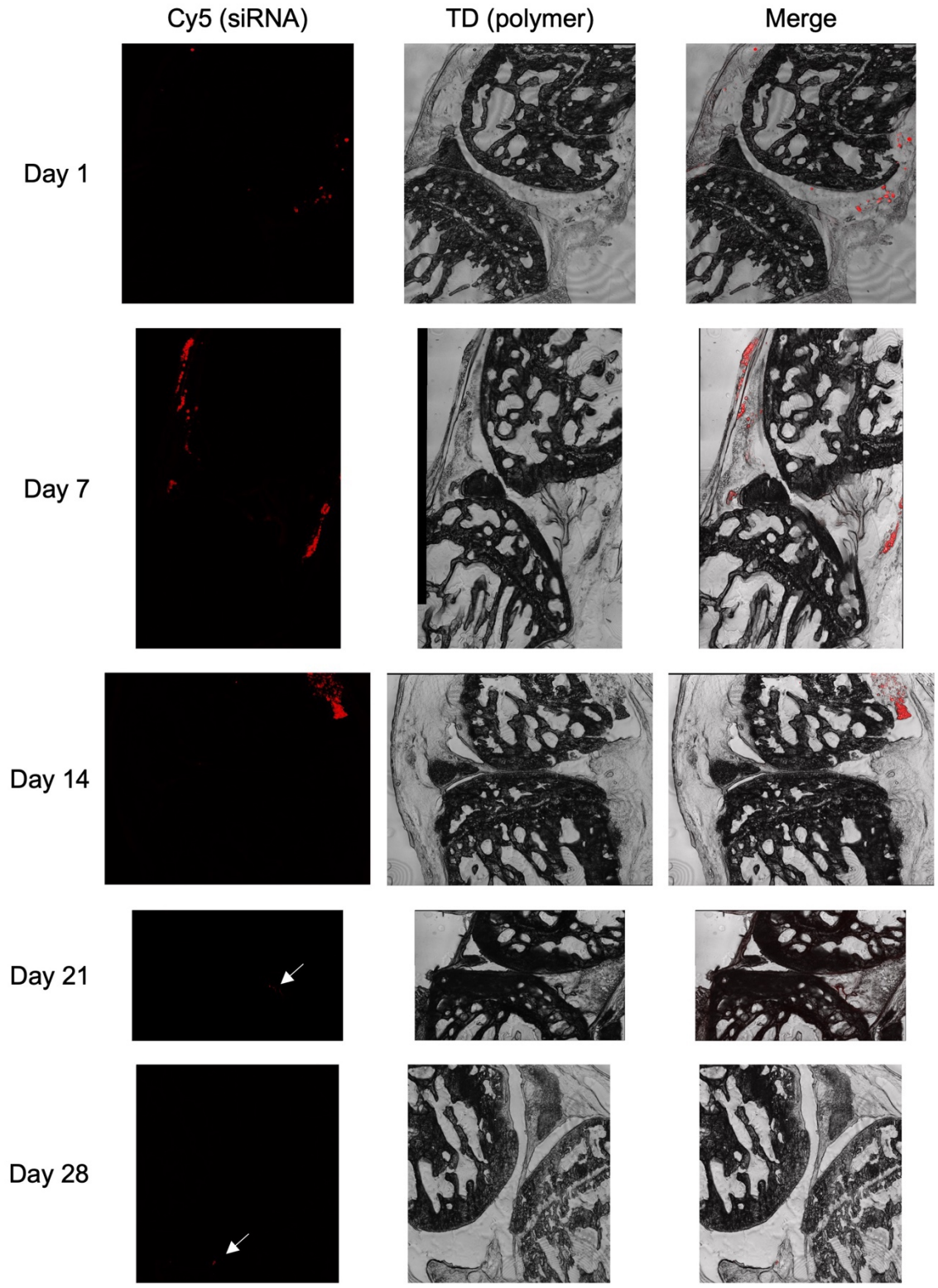

Figure 4.16: Whole joint cryohistology.
Mice were injected with 1 mg MP loaded with siRNA-EG18 tagged with Cy5 on day 0 and loaded 3x/ week until takedown. White arrows indicate Cy5 signal.

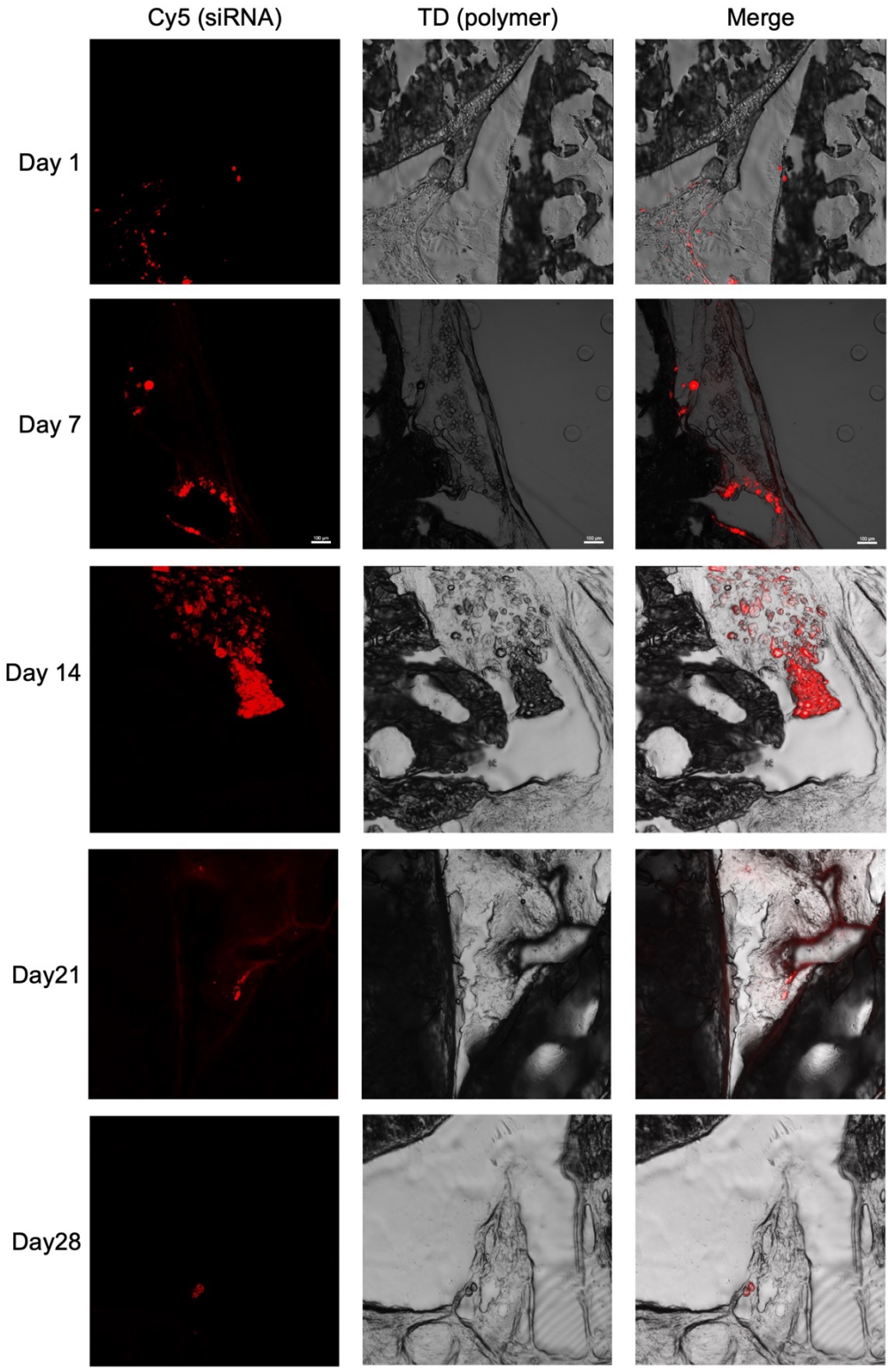

Figure 4.17: Cryohistology of MP localization in synovium/ infrapatellar fat pad.
Mice were injected with 1 mg MP loaded with siRNA-EG18 tagged with Cy5 on day 0 and loaded 3x/ week until takedown.

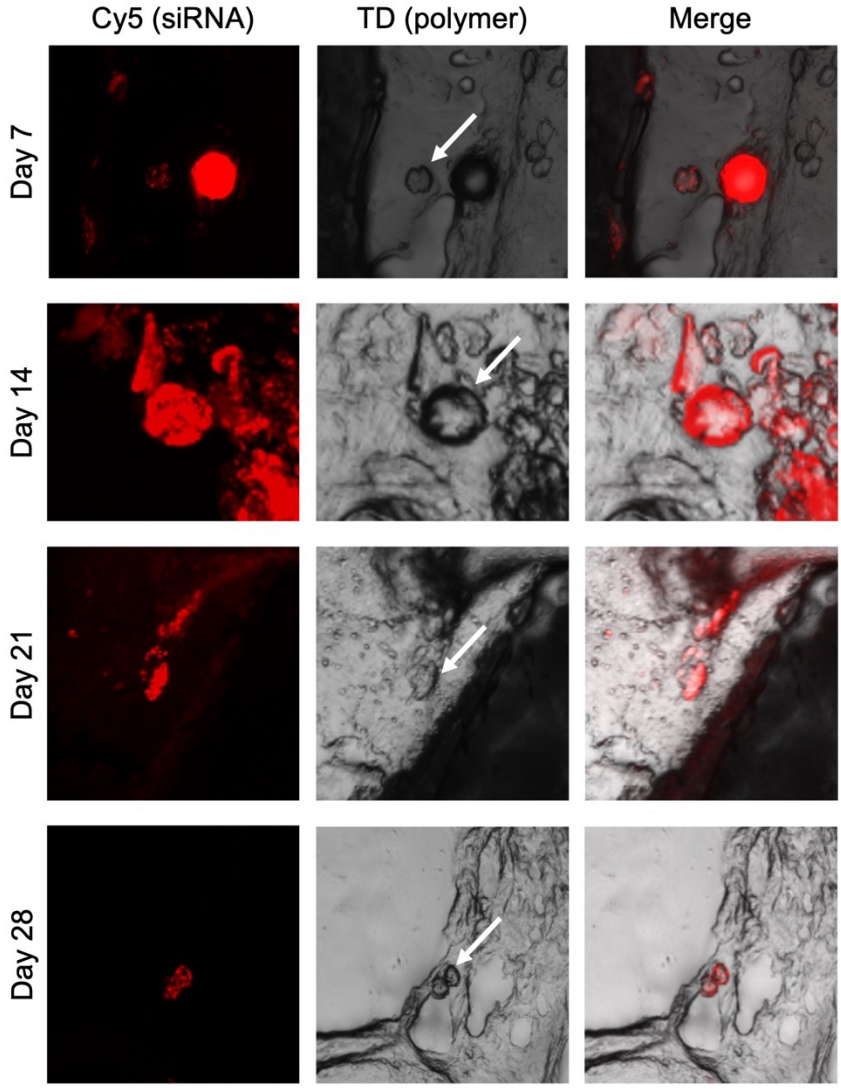

Figure 4.18: Cryohistology showing partially degraded MPs in the joint.

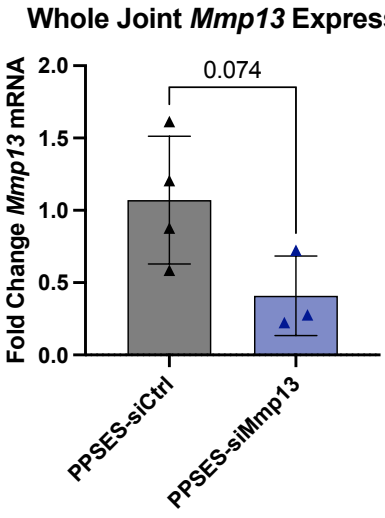

Figure 4.19: Knockdown of Mmp13 in whole joint samples.
Mice received a single injection of siMmp13 MP and 4 weeks of cyclic mechanical loading (3x/week). N = 3-4.

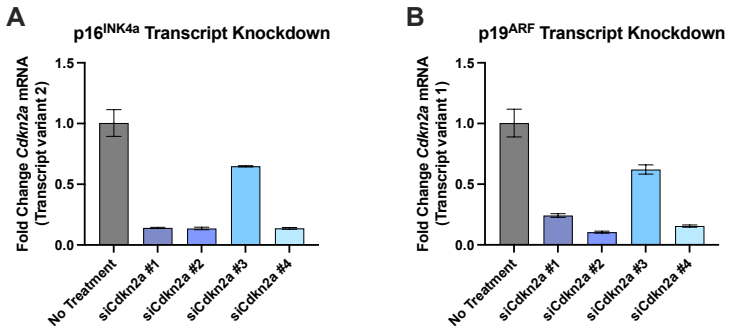

Figure 4.20: Screening commercially-available sequences of siRNA against *Cdkn2a*.
ATDC5 cells were treated in a reverse transfection with 25 nM siRNA for 48 hours. (**A**) $p16^{INK4a}$ transcript and (**B**) $p19^{ARF}$ transcript. N = 3 wells per group.

bonds to prevent exonuclease degradation[219]. Additionally, sense strands for two lead candidate sequences were synthesized with the above stabilization and the previously-described 5' PEG-diacyl lipid conjugate to promote albumin association and interaction with the cell membrane for carrier-free activity[180]. The conjugates exhibited both carrier-mediated (**Figure 4.21A** and **B**) and carrier-free (**Figure 4.21C** and **D**) target knockdown of both transcripts, resulting in a stabilized

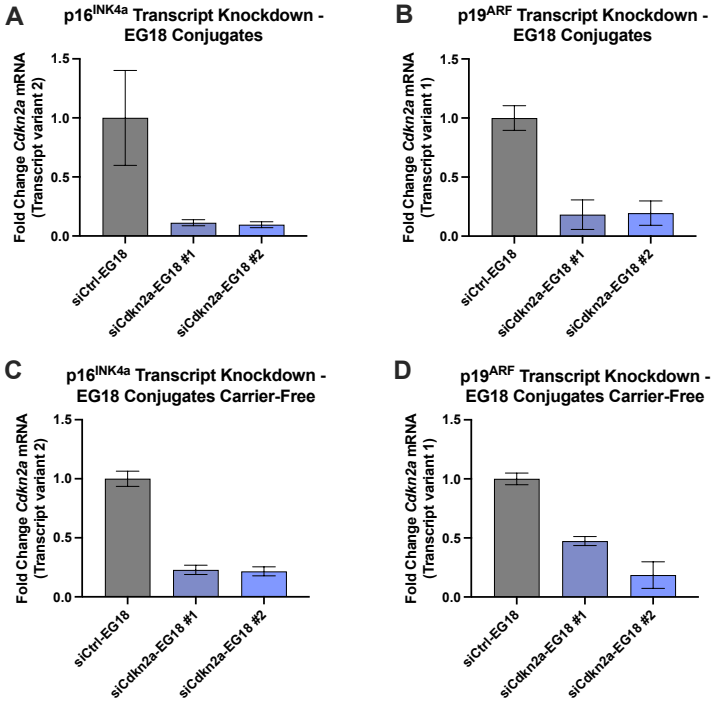

Figure 4.21: Activity of stabilized EG18 conjugates.
(**A, B**) ATDC5 cells were treated with 25 nM siRNA-EG18 in a reverse transfection for 48 hours. (**C, D**) ATDC5 cells were treated with 1 µM siRNA-EG18 in a forward transfection for 72 hours. N = 3 wells per group.

siRNA conjugate with potent activity which could be loaded into sustained-release MPs for target knockdown *in vivo*.

MPs were loaded with lead candidate siCdkn2a (sequence #2) as determined above, siCtrl, or siMmp13 (**Supplementary Figure C.4**). Mice were treated as described for siMMP13 MPs and loaded 3x per week for 4 weeks. The following groups were included in the study: siCtrl, siCdkn2a, siMmp13, siCtrl MP, siCdkn2a MP, and siMmp13 MP. The dose of free siRNA was 10 µg/knee, while MP groups received 1 mg MP loaded with 5.5 µg siRNA/knee.

After 4 weeks, limbs were harvested, and the following tissues were dissected for qPCR: (1) cartilage, meniscus, and IPFP; (2) patellar tendon; (3) synovium. As demonstrated in **Figure 4.22**, the three targets of interest ($p16^{INK4a}$, $p19^{ARF}$, and Mmp13) were highly upregulated in the

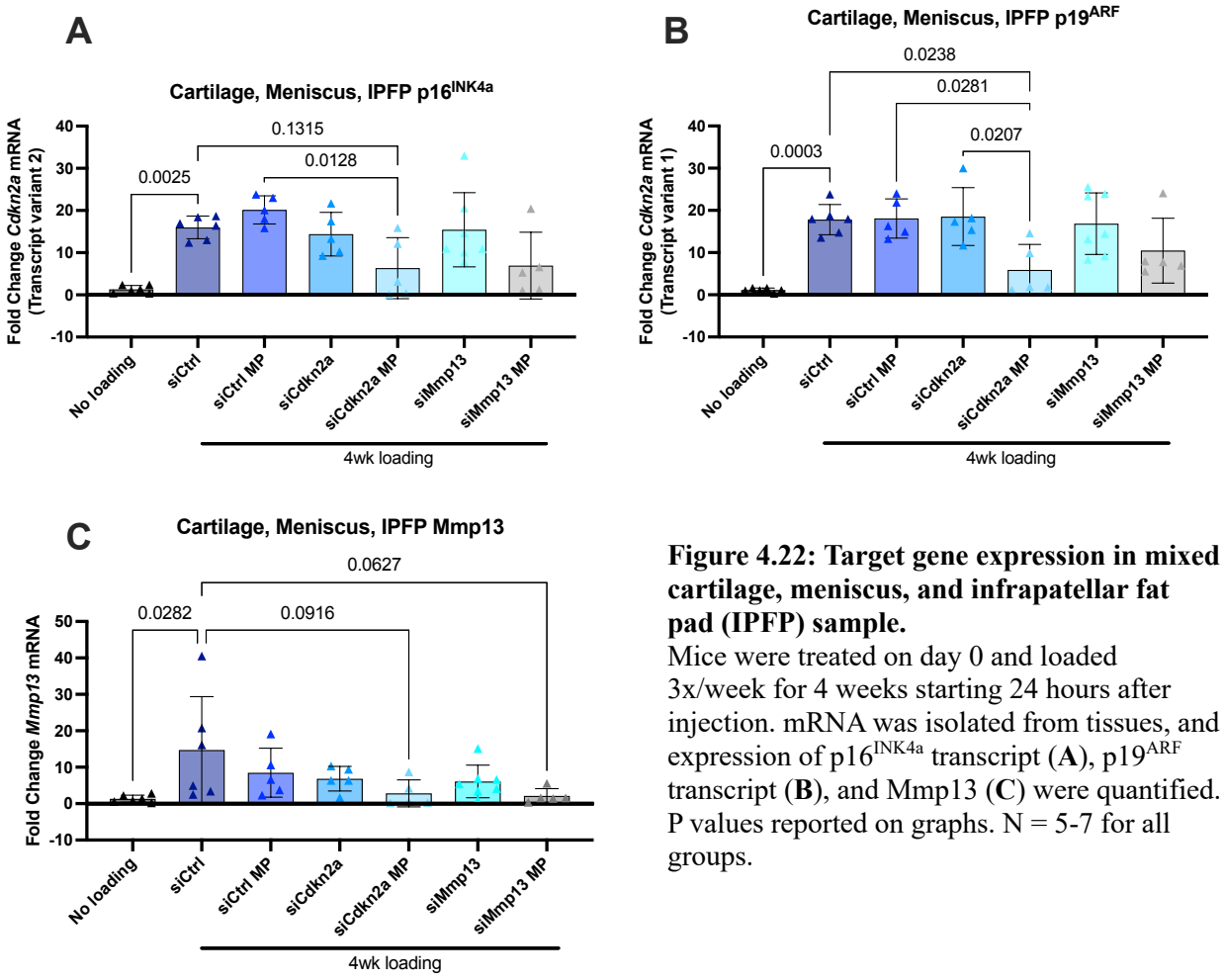

Figure 4.22: Target gene expression in mixed cartilage, meniscus, and infrapatellar fat pad (IPFP) sample.
Mice were treated on day 0 and loaded 3x/week for 4 weeks starting 24 hours after injection. mRNA was isolated from tissues, and expression of $p16^{INK4a}$ transcript (**A**), $p19^{ARF}$ transcript (**B**), and Mmp13 (**C**) were quantified. P values reported on graphs. N = 5-7 for all groups.

cartilage+ meniscus+ IPFP sample, in agreement with published results in PTOA models[49,195]. For $p16^{INK4a}$ and $p19^{ARF}$ transcripts, siCdkn2a MP achieved ~68% knockdown of each transcript compared to siCtrl MP and was the only treatment to achieve significant silencing (**Figure 4.22A** and **B**). siMmp13 MPs achieved ~86% knockdown compared to siCtrl treatment, though this result did not achieve statistical significance, likely due to variability in the siCtrl group (**Figure 4.22C**). The results were more mixed in the patellar tendons (**Figure 4.23**). Both transcripts of *Cdkn2a* were significantly increased with loading 10 and 20-fold, respectively (**Figure 4.23A** and **B**). siCdkn2a MP achieved 80 and 70% knockdown of $p16^{INK4a}$ and $p19^{ARF}$, respectively, compared to siCtrl. Interestingly, siMmp13 MP significantly silenced $p16^{INK4a}$ transcript (79% knockdown compared to siCtrl). However, *Mmp13* was not significantly increased with loading in patellar tendons, though the siCdkn2a and siMmp13 MP groups trended upwards (**Figure**

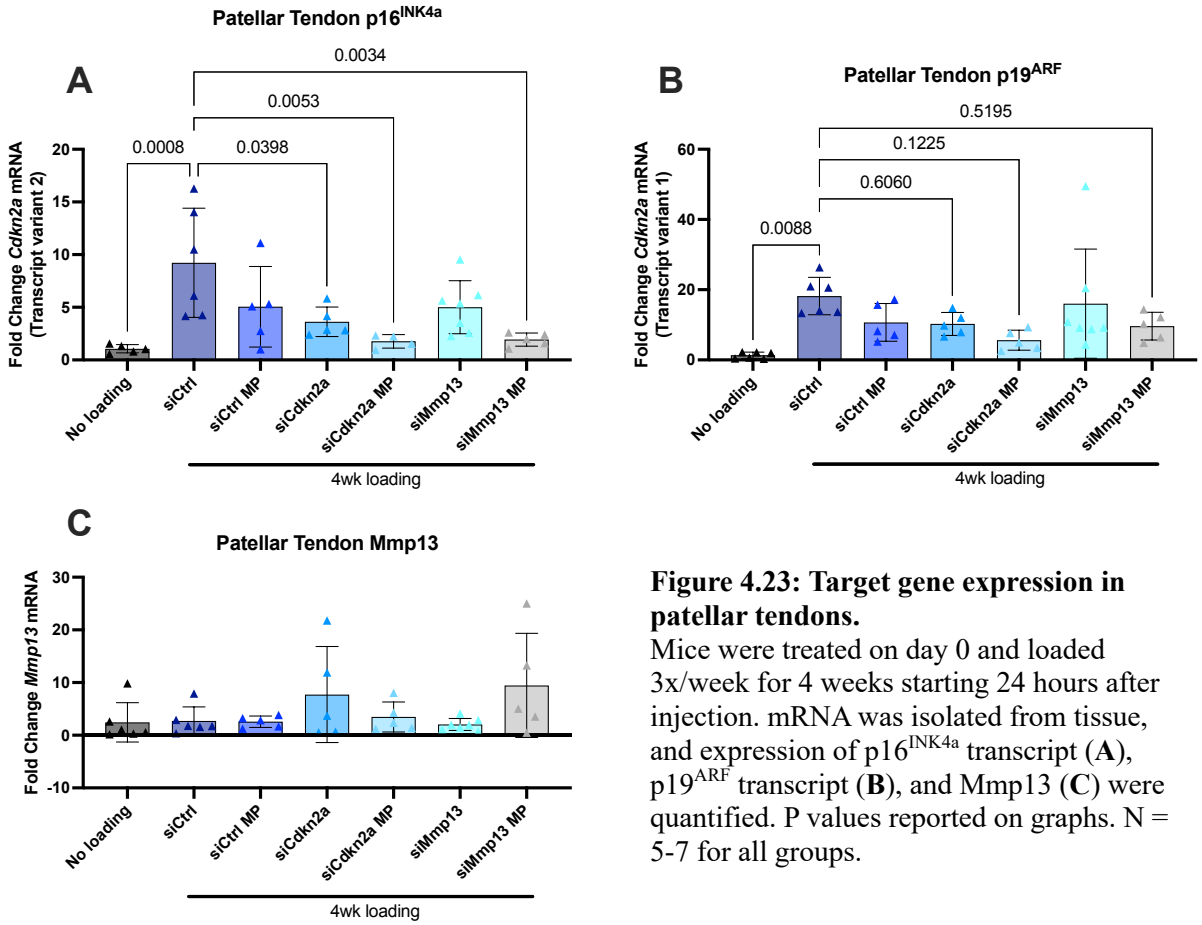

Figure 4.23: Target gene expression in patellar tendons.
Mice were treated on day 0 and loaded 3x/week for 4 weeks starting 24 hours after injection. mRNA was isolated from tissue, and expression of $p16^{INK4a}$ transcript (**A**), $p19^{ARF}$ transcript (**B**), and Mmp13 (**C**) were quantified. P values reported on graphs. N = 5-7 for all groups.

4.23C). In synovium, both p16^{INK4a} and p19^{ARF} were upregulated, but there were no significant differences between other groups (**Figure 4.24A** and **B**). However, Mmp13 in the synovium was strongly upregulated with siCdkn2a and siMmp13 MP treatment, though this data is highly variable (**Figure 4.24C**).

Determining the tissue-specific effects of novel therapeutics is essential for understanding treatment mechanism. The knockdown data demonstrated here is apparently contradictory when taken together with cryohistology, which demonstrates strong localization and release of siRNA in the synovium with little signal in the cartilage. Therefore, we would expect the strongest silencing to occur in the synovial tissues. However, the opposite occurred, with the strongest effects in the mixed cartilage/meniscus/IPFP, which exhibited promising activity of both siRNAs. Notably, patellar tendon knockdown of *Cdkn2a* transcripts was strong with siCdkn2a

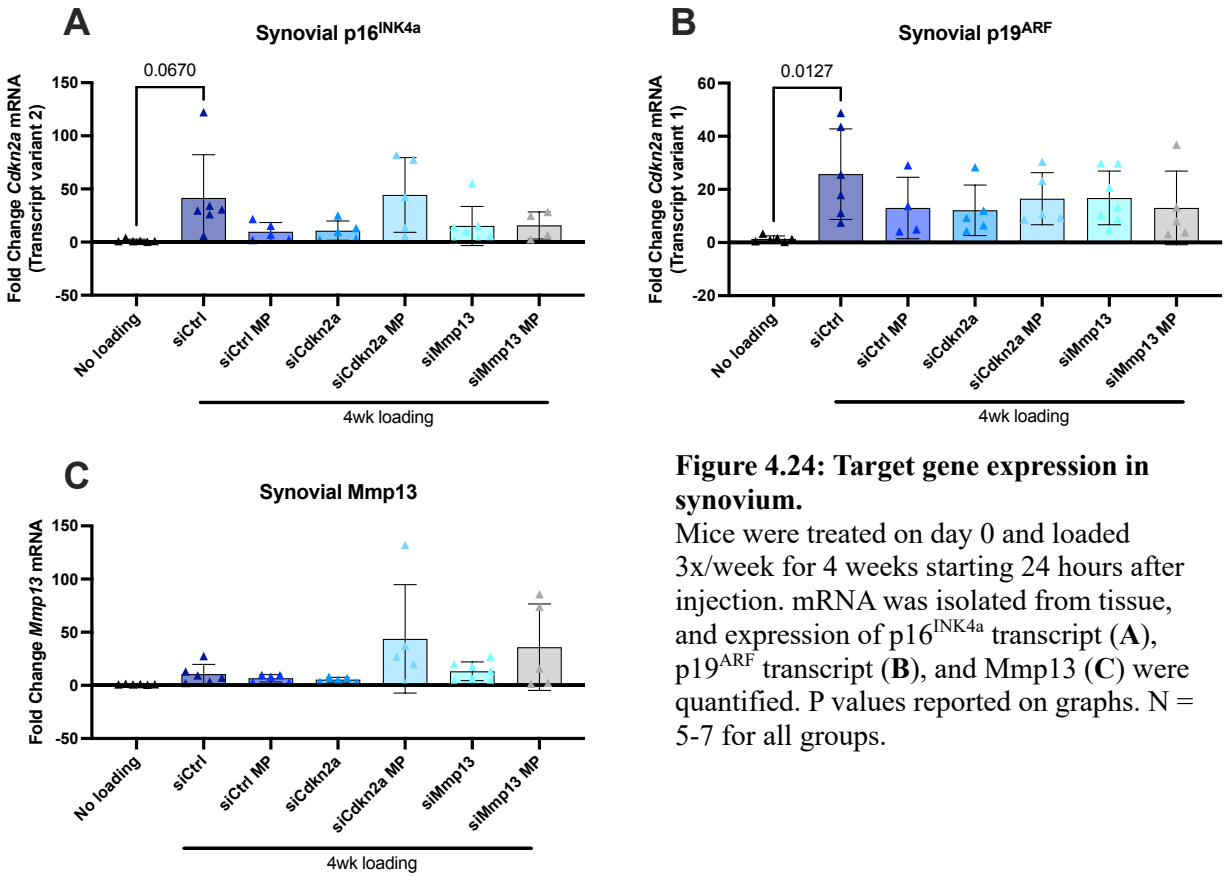

Figure 4.24: Target gene expression in synovium.
Mice were treated on day 0 and loaded 3x/week for 4 weeks starting 24 hours after injection. mRNA was isolated from tissue, and expression of p16^{INK4a} transcript (**A**), p19^{ARF} transcript (**B**), and Mmp13 (**C**) were quantified. P values reported on graphs. N = 5-7 for all groups.

MP, and we did note MP deposition adjacent to the patellar tendon. It is possible that the strong Mmp13 response to MPs is due to a broader tissue rejection of the biomaterial, though the lack of response to siCtrl MPs confounds this conclusion. The free siRNA conjugates did not exhibit significant knockdown in any tissue despite treating at ~2x the dose compared to MPs, highlighting the necessity of sustained delivery for long-term knockdown. To further probe the localization effects of MPs, we examined bone by microcomputed tomography (μCT) and tissue phenotype by histology.

Cortical bone and osteophytes were evaluated by μCT (**Figure 4.25** and **Supplementary Figure C.5**).Qualitative analysis of bone morphology reveals osteophyte formation and meniscal ectopic mineralization, typical of moderate PTOA. These changes appear markedly reduced in

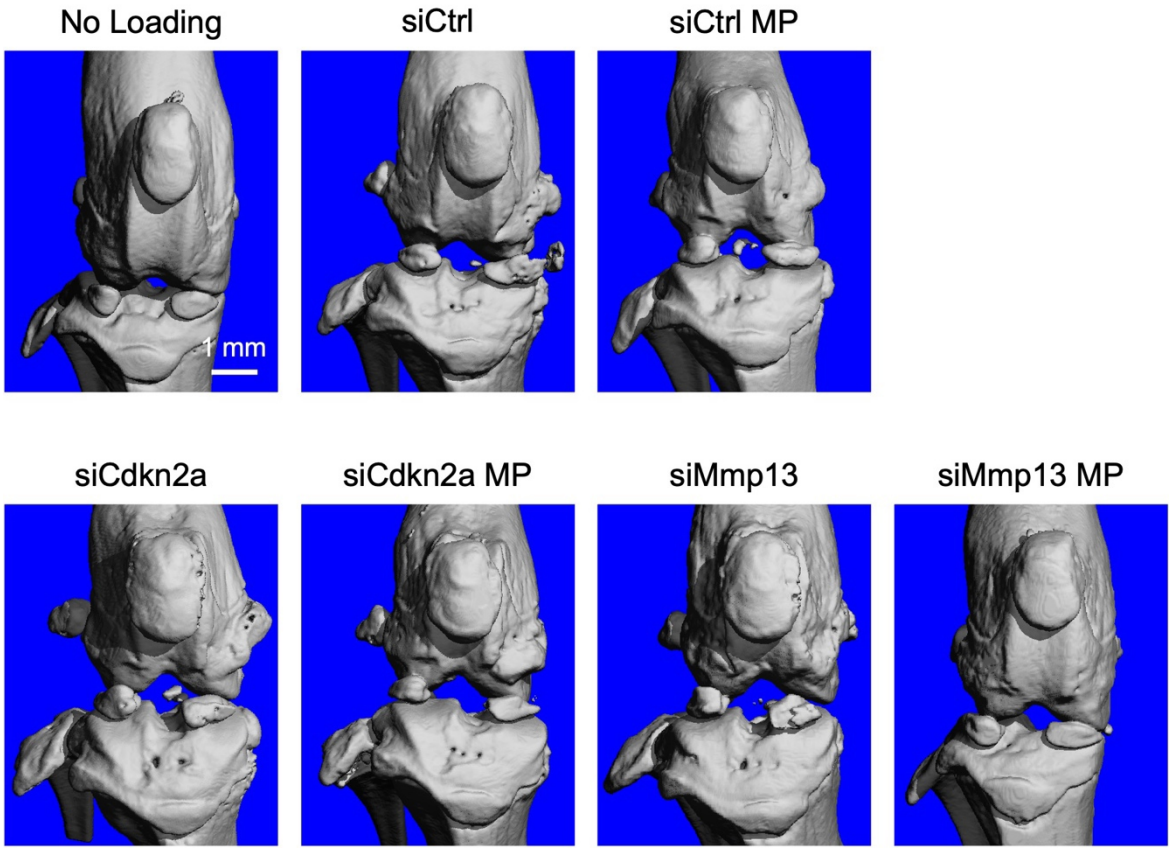

Figure 4.25: Representative μCT reconstructions of mouse knee joints.
Mice were treated on day 0 and loaded 3x/week for 4 weeks starting 24 hours after injection. Scale bar = 1 mm.

siMmp13 MP-treated knees, an indication that Mmp13 knockdown demonstrated in the cartilaginous tissues helped to preserve bone as well. All other treatments demonstrated similar bone morphology to siCtrl, though quantitative analysis will be essential to draw firm conclusions. We also demonstrated joint tissue structure histologically. By toluidine blue (**Figure 4.26**) and hematoxylin and eosin (**Figure 4.27**) staining, we saw marked synovial hyperplasia (thickening) and meniscal calcification (**Figure 4.26A** and **Figure 4.27A**), which is strikingly mitigated with siMmp13 delivery from MPs. In toluidine blue-stained cartilage, fainter staining

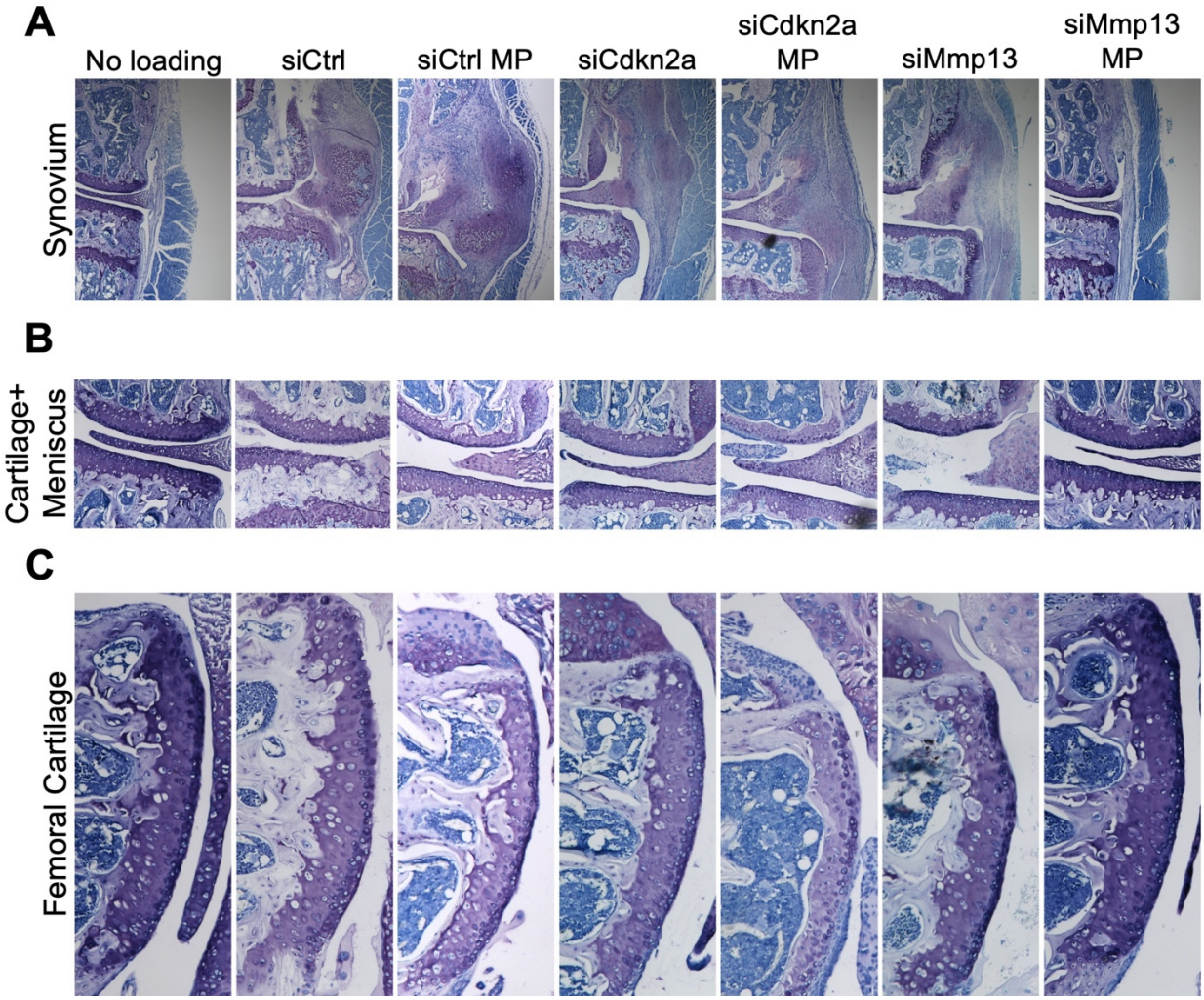

Figure 4.26: Toluidine blue staining for evaluation of medial joint structural damage.
Mice were treated on day 0 and loaded 3x/week for 4 weeks starting 24 hours after injection. (**A**) Medial synovium, (**B**) medial cartilage and meniscus, (**C**) medial femoral cartilage.

in the PTOA groups indicates loss of extracellular matrix (**Figure 4.26B** and **C**). The exception is limbs treated with siMmp13 MP, in which the staining intensity was comparable to the unloaded group. Clonal expansion of chondrocytes was also evident in diseased cartilage (**Figure 4.27 B** and **C**), a sign of diseased or aging tissue[220]. Notably, we did not see significant loss of articular surface in any groups, in line with the moderate loading regimen (3x/wk). Lateral synovium, meniscus, and cartilage demonstrate similar trends seen in the medial tissues (**Supplementary Figure C.6** and **Supplementary Figure C.7**). However, similar to the µCT results, increased n

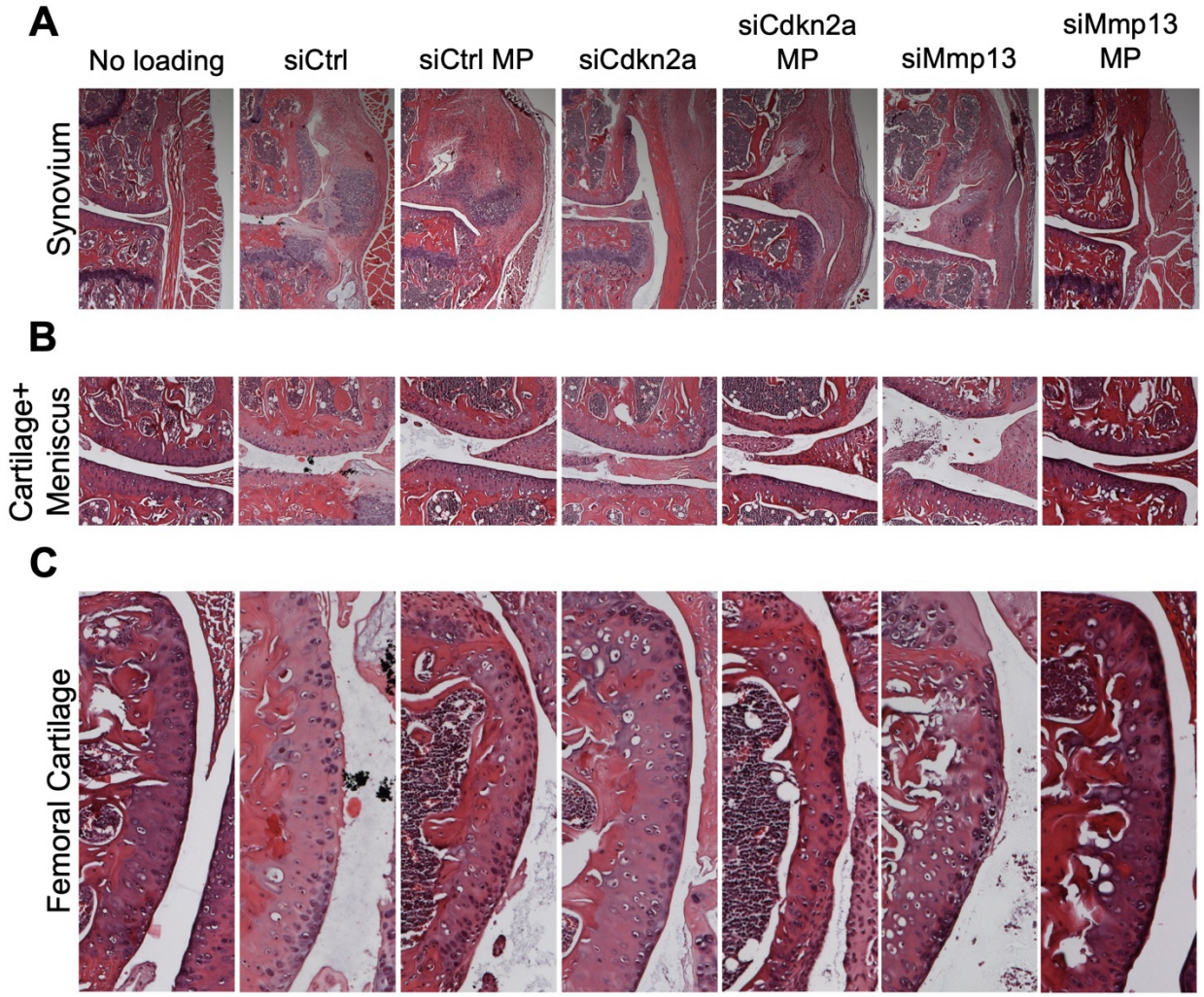

Figure 4.27: Hematoxylin & eosin staining for evaluation of medial joint structural damage. Mice were treated on day 0 and loaded 3x/week for 4 weeks starting 24 hours after injection. (**A**) Medial synovium, (**B**) medial cartilage and meniscus, (**C**) medial femoral cartilage.

and quantitative analysis, including scoring for total joint and cartilage health, will be necessary to draw conclusions about the efficacy of the siRNA-MP treatments in this study.

Sustained intra-articular release of siRNA has been efficacious in various disease contexts. Bedingfield et al. loaded siMMP13 polyplexes in PLGA microplates for PTOA treatment, which potentiated knockdown out to 28 days and significantly preserved bone and joint tissue morphology[153]. In a similar system, siRNA targeting FcγRIII complexed with PEI was loaded in PLGA MPs, which exhibited target knockdown and therapeutic effects in a rat model of inflamed TMJ[142]. However, nano-in-micro formulations are more complex and potentially face regulatory challenges. To our knowledge, this is the first report of sustained knockdown via loading lipophilic siRNA conjugates in polymeric MPs. Local injection of conjugates has demonstrated efficacy[196,221], though up to 10x higher doses have been used.

ROS have been shown to drive both senescence[222] and MMP13 overexpression[223], which was one motivation to combine a ROS-scavenging material with sustained knockdown of these targets. Chin et al. recently demonstrated that senolytic treatment can reduce oxidation of cartilage proteins in PTOA mice, more evidence for crosstalk between ROS and senescent cells[224]. Due to our finding and others'[48] that Cdkn2a increases significantly in PTOA synovium, a similar proteomics analysis would be informative in the synovium. Since our MPs did not demonstrate antioxidant behavior via Amplex Red assay, we could not determine the effect of combined ROS scavenging/target knockdown in these studies. Oher avenues including histological staining for oxidized DNA or nitrotyrosine could be alternative methods to study oxidative environment after MP delivery.

Another important observation is the synovial Mmp13 response to MPs by qPCR (**Figure 4.24C**). As noted above, this is in contrast to siRNA imaging in joint tissues, which demonstrated

diffuse signal throughout the synovium at later time points. Other techniques for local activity of siRNA, especially immunohistochemistry for MMP13, $p16^{INK4a}$, and $p19^{ARF}$, should be pursued.

The efficacy of knocking down Cdkn2a transcripts, especially silencing of $p16^{INK4a}$ activity, is disputed in PTOA. Park and colleagues injected NPs loaded with siRNA against $p16^{INK4a}$, which accumulated in the synovium and reduced $p16^{INK4a}$ staining in this tissue[225]. NP treatment reduced pain behavior and inflammation in PTOA mice. However, Diekman et al. report that ablation of chondrocyte $p16^{INK4a}$ in chondrocytes is not sufficient to prevent PTOA[197]. The discrepancy between these studies could be due to differential tissue localization (ie synovium vs. cartilage); taken together, these results could suggest that silencing $p16^{INK4a}$ is only effective against PTOA in synovial cells. This is plausible due to the strong secretion of proteases and cytokines from the proliferating synovium in PTOA[226], many of which are SASP factors. This could also explain why, despite strong knockdown by siCdkn2a MPs in the cartilage and meniscus (and not in synovium, **Figure 4.24**), this treatment does not appear to reduce disease progression at the bone and tissue level.

4.3. Conclusions

In this work, we have tested optimized PPSES MPs for biologic drug delivery in multiple local degeration models. In mouse glaucoma studies, PPSES-EPO significantly attenuated tissue degeneration and improved visual function. These effects were due to extended release of EPO in the retina, as well as ROS scavenging by the polymer to reduce oxidative stress. We also demonstrate potent knockdown of siRNA targets by loading lipophilic siRNA constructs in our MPs. siRNA MPs outperform the free siRNA alone, and by knocking down *Mmp13*, we see promising preliminary effects on joint structure and tissue health. Taken together, these studies demonstrate the benefits of local sustained release in challenging-to-treat, degenerative diseases.

4.4. Materials and Methods

4.4.i. Materials

All reagents were purchased from Sigma Aldrich and used as received unless otherwise stated. EPO ELISA kits were purchased from R&D Systems and Boster Bio.

4.4.ii. Mouse microbead occlusion model and treatments

MOM

Pathological elevation of intraocular pressure (IOP) was induced in the Rex lab in male C57/Bl6 mice (8-10 wk) via the microbead occlusion model (MOM) as previously described[201]. Polystyrene microbeads were injected in the anterior chamber, and IOP elevation was confirmed using an Icare Tonolab rebound tonometer. IOP was tracked biweekly through the course of the study, and microbeads were reinjected when IOP returned to baseline (approximately every 2-3 weeks).

PPSES-EPO Gen1 5wk study treatment

One week after initial microbead injection, MPs were injected intravitreally (1 µl at 10 mg/ml). The following groups were investigated: no MOM + saline injection, MOM + saline injection, MOM + free EPO (85 ng), MOM + PPS MP, MOM + PPS-EPO MP, MOM + PPSES Gen1 MP, and MOM + PPSES-EPO Gen1 MP. PPS and PPS-EPO MPs were prepared as previously described[30]. PPSES Gen1 MPs were formulated according to Section 3.4.iii. PPS-EPO MP delivered 8.5 ng EPO, whereas PPSES-EPO Gen1 delivered 7.7 µg. For injection, MPs were resuspended in sterile PBS. In this study, mice were sacrificed 5 weeks after MP treatment.

PPSES-EPO Gen2 6wk study treatment

One week after initial microbead injection, MPs were injected intravitreally (1 µl at 10 mg/ml). The following groups were investigated: no MOM + saline injection, MOM + saline injection, MOM + free EPO (8.5 ng), MOM + PPS MP, MOM + PPS-EPO MP, MOM + PPSES

Gen2 MP, and MOM + PPSES-EPO Gen2 MP. PPS groups were prepared as above and delivered 8.5 ng EPO as above. PPSES-EPO Gen2 MPs were formulated as described in Section 3.4.iii, which delivered 7.3 ng EPO. In this study, mice were sacrificed 6 weeks after MP treatment. For injection, MPs were resuspended in sterile PBS.

PPSES-EPO Gen3 8wk study treatment

One week after initial microbead injection, MPs were injected intravitreally (1 µl at 10 mg/ml). The following groups were investigated: MOM + saline, MOM + free EPO (100 ng), MOM + PPSES-EPO Gen2, MOM + PPSES Gen3, and MOM + PPSES-EPO Gen3. PPSES-EPO Gen2 and Gen3 were prepared as described in Section 3.4.iii. PPSES-EPO Gen2 delivered 7.3 ng EPO, and Gen3 delivered 102 ng. PPSES Gen3 MP were resuspended in autoclaved 0.25% Pluronic F127 + 0.25% carboxymethylcellulose for injection. In this study, mice were sacrificed 8 weeks after MP treatment.

4.4.iii. Efficacy of PPSES-EPO MP in mouse MOM model

In vivo *electrophysiology*

ERGs and VEP measurements were performed in the Rex laboratory at 2 weeks and endpoint as previously described[30,192]. Briefly, mice were dark-adapted overnight before being anesthetized for electrode placement at the cornea, snout, and back of the head (visual cortex). For the VEPs, mice were exposed to 50 flashes of 1 Hz of 0.05 cd.s/m^2 white light. For the ERGs, mice were exposed to flashes of 1 Hz of 1 cd.s/m^2 white light. For the photopic negative ERGs (PhNR), mice were exposed to 20 flashes of white light on a green background.

Amplex Red assay

6 weeks after MP injection, mice were sacrificed and retinas were harvested. Fresh retinas were placed on ice until Amplex Red assay according to the manufacturer's protocol with the following adaptations: Assay reagent was prepared by combining 11.82 ml Kreb's buffer (pH

7.4), 120 µl HRP, and 60 µl Amplex Red dye. Retinas were suspended in 500 µl reagent and homogenized by hand. Samples were incubated at 37°C, centrifuged at max speed for 5 minutes, and the supernatant was plated in duplicate. Absorbance was measured at 570 nm.

Retinal EPO ELISA

For ELISA, retinas were flash frozen until analysis. Samples were sonicated, and supernatant was diluted in ELISA buffer (R&D Systems) for analysis according to manufacturer's directions.

Optic nerve histology

Optic nerves were post-fixed in glutaraldehyde and 4% paraformaldehyde and embedded in Resin 812 and Araldite 512 (Electron Microscopy Sciences). Sections were stained with 1% paraphenylenediamine and 1% toluidine blue. Axons and degenerative axon profiles were counted via ImageJ.

4.4.iv. MP preparations for NHP injections

Preparation of low-endotoxin MPs

For preparation of "low-endotoxin" MP, the following sterilization protocol was followed: all aqueous solutions were prepared in sterile DEPC-treated water and sterile filtered prior to use. All glassware and stir bars were soaked in freshly-prepared 0.2 M NaOH overnight, rinsed twice with sterile saline, rinsed twice with sterile DEPC-treated water, and allowed to dry in a laminar flow hood. The samples were exclusively handled in laminar flow hoods except during the use and evaporation of volatile solvents DCM and CHCl3 (S/O/W and hardening steps), which was done in a chemical fume hood.

Testing injectability in NHP-compatible buffers

100 ml sterile 1x PBS (pH 7.4) was heated in a laboratory oven to 55-65°C. To warmed, stirring PBS, 250 mg Pluronic F127 and 250 mg carboxymethylcellulose sodium salt (medium

viscosity) was added and stirred until full dissolution. The pH was confirmed to be 7.2-7.4, and the solution was autoclaved and stored at 4°C for up to 3 months. Lyophilized MPs were resuspended at 5 mg/ml in PBS or prepared buffer, and 50 µl was deposited onto a glass slide using a pipette (positive control) or syringe fitted with a 29g needle. The transferred MPs were imaged by tiled brightfield imaging to capture the heterogeneity of the MP droplet.

Endotoxin measurement

MPs were resuspended in injection buffer, and 50 µl were plated in a 96-well plate. Endotoxin was measured using the Pierce Chromogenic Endotoxin Quant Kit based on limulus amebocyte lysate (LAL) according to manufacturer's directions with the following adjustment: after stop solution was added and absorbance was measured, a second measurement was taken on reaction supernatants. This helped to correct for absorbance interference from sedimented MPs in the wells.

4.4.v. siRNA MP preparation and treatment in PTOA

siRNA sequence screening

Four siRNA sequences against mouse *Cdkn2a* were purchased from Dharmacon (**Supplementary Table C.2**). siRNA was complexed with Lipofectamine-2000 reagent, and 25 nM was applied to ATDC5 cells on the day of plating (reverse transfection, 100,000 cells/well in a 12-well plate). Media was changed after 24 hours, and cells were assayed for knockdown 48 hours after plating.

The two lead candidates were synthesized in-house on a MerMade RNA synthesizer as previously described using a "zipper" stabilization pattern of modifications, phosphodiester bonds, and the EG18 PEG-diacyl 5' conjugation (sense strand) [180] (**Supplementary Table C.2**). These sequences were applied to ATDC5 cells in a reverse transfection as described above. Finally, carrier-free knockdown of the conjugates was confirmed as follows: 10,000 ATDC5 cells

were plated in collagen-coated 12-well plates. 1 μM siRNA was applied in Opti-MEM for 72 hours before assessment of target knockdown.

Quantitative PCR

Total RNA was isolated from cells or tissues using a Qiagen RNEasy kit with on-column DNAse digestion. Up to 1000 ng RNA was reverse transcribed to cDNA (iScript kit). Quantitative PCR was performed using SYBR green assay (12.5 ng cDNA and 300 nM forward and reverse primer per reaction). *Rpl4* was used as housekeeping gene (**Supplementary Table C.3**).

PTOA model and treatment

The knee joints of male C57/Bl6 mice were subjected to 250 cycles of bilateral compressive mechanical loading (9N/cycle) 3 times per week to induce PTOA. Treatments (20 μl) were injected intra-articularly on day 0 of the study, one day before loading began. Loading continued for 4 weeks. Treatment groups included: siScr, siCdkn2a, siMmp13, PPSES-siScr, PPSES-siCdkn2a, and PPSES-siMmp13. An additional group of unloaded mice was included as a non-diseased control. For free siRNA groups, siRNA was dissolved in 0.25% PF127 + 0.25% CMC + 0.5% Tween-20 at 0.4 mg/kg/knee. For siRNA PPSES MP groups, 1 mg MP containing ~5.5μg siRNA (2.2 mg/kg/knee) was suspended in the same buffer for injection. MPs were continuously resuspended to ensure homogeneous injection.

Amplex Red assay

Amplex Red reagent was prepared as above. Freshly harvested limbs were cleaned of muscle, disarticulated at the knee joint, and the tibial plateau and distal femur were cut from the remaining bone with a razor blade. Samples were homogenized in 500 μl Amplex Red reagent using a bead homogenizer at 50,000 Hz for 5 minutes, incubated at 37°C for 1 hour, and

centrifuged for 5 minutes at max speed. The supernatant was plated in a black-walled 96 well plate in duplicate for fluorescence measurement at 570/585 nm ex/em.

MP joint retention

MPs were loaded with siRNA labeled with Cy5 (10% of total siRNA, Luc sequence (**Supplementary Table C.2**). 1 mg MP was injected per knee, and mice were imaged intravitally via IVIS for Cy5 fluorescence in the knee over 28 days. Mice were sacrificed at 1, 7, 14, 21, and 28 days, limbs were harvested and cleaned of excess muscle, and snap-frozen in liquid nitrogen for storage at -20°C for cryosectioning.

Cryohistology and confocal microscopy

Frozen limbs were embedded in OCT on dry ice. Saggital sections (20 μm) were cut into the medial side of the joint. Cryofilm tape (Section-Labs) was used to maintain structure of the calcified joints. Slides were imaged on a confocal microscope (Nikon) for Cy5 signal after thresholding on control joint slides. For whole-joint images, tiled images were stitched.

4.4.vi. Evaluation of siRNA MP treatment in PTOA

Joint dissection for RNA isolation

After sacrifice, mouse limbs were cleaned of posterior muscle and placed in RNALater solution at 4°C until dissection (within 2 weeks). The quadriceps muscle was separated from the femur, and excess muscle was trimmed. The joint cavity was carefully opened using a scalpel blade, and medial and lateral synovium was cut from the femur. Medial and lateral synovium was harvested by carefully trimming from the patellar tendon, excess muscle was removed if necessary, and tissue was stored in RNALater at 4°C until RNA harvest.

After synovial collection, the patellar tendon was cut from the joint cavity and stored as above. Finally, the femur and tibia were separated and cleaned of excess muscle. The meniscus

and infrapatellar fat pad were gently separated from the tibial plateau, and cartilage was scraped from both articular surfaces. These tissues were collected together in a mixed sample and stored as above. RNA was harvested from all three tissues by homogenizing in 500 µl TRIzol using a bead homogenizer (30,000 rpm for 5 mintues). After addition of 100 µl chloroform and centrifugation (12,000 xg for 15 minutes), the aqueous layer was collected and purified via Qiagen RNEasy kit. Reverse transcription and qPCR were performed as above.

Microcomputed tomography and histology

Mouse knees were cleaned of excess muscle and fixed in 10% neutral buffered formalin for 72 hours, with formalin changed every day. Samples were stored in 70% ethanol at 4°C until micro-computed tomography (µCT). Samples were scanned using a ScanCo µCT-50 with 15 µm-thick slices, a 15 µm isotropic voxel size, a current/voltage of 109 µA/55kVp, and a 900 ms integration time. Contouring was then performed to generate 3D renderings of the mouse knees using a threshold of 303.

After µCT, limbs were decalcified in 20% disodium EDTA (pH 7.4) for five days, with the solution changed after 48 hours. Samples were weighed once per day to confirm full decalcification, then post-fixed overnight in 10% neutral buffered formalin. Samples were embedded in paraffin, sectioned at 5 µm, and stained with hematoxylin and eosin or toluidine blue for whole joint and cartilage evaluation.

4.4.vii. Statistical analysis

All data are presented as mean ± standard devUnless otherwise stated, all statistical comparisons were performed via one-way ANOVA with Tukey's post-hoc comparison. Knockdown of Mmp13 was compared to siCtrl MP with a two-tailed t test.

Chapter 5: Conclusions

5.1. Chapter summaries and impact

In the first aim of this work (Chapter 2), we investigated the structure-function relationship between the antioxidant drug TEMPO and the hydrophilic spacer DMA. Using RAFT polymerization, we had precise control of TEMPO backbone density, which directly influenced the water solubility of the resulting polymers. When polymers exhibited a high TEMPO density, they had poor water solubility, resulting in worse antioxidant activity. However, when TEMPO density was too low, antioxidant activity was also impaired due to low TEMPO concentration. We found an optimal ratio of the two monomers, and demonstrated its efficacy in a mouse model of inflammation. Our polymer system outperformed the free drug, indicating the benefit of increasing overall molecular weight for *in vivo* administration. This work contributes to the field of polymer science and redox biology by demonstrating a new application for RAFT polymerization, highlighting the benefits of producing monodisperse polymers for antioxidant applications.

The second aim of this work (Chapter 3) was focused on designing an antioxidant microparticle system for sustained drug release of proteins and nucleic acids. We generated a new series of materials which exhibited crystalline character at an optimized monomer concentration. Crystallinity directly influenced the stability of large microparticle formulation, overcoming a major hurdle for previous versions of this material. We carefully dissected the oxidation profiles of the resulting microparticles. Through formulation optimization, we demonstrated high encapsulation efficiency and sustained release of an exciting drug candidate for neuroprotection, erythropoietin. We also achieved efficient loading of small interfering RNA, another therapeutic transforming treatment for many diseases. This work represents a new biomaterial candidate for biomedical applications, for which clinically-approved polyesters have

been the gold standard. The goal of these materials is to form injectable drug depots which expose diseased tissues to sustained, high drug concentrations for prolonged therapy. The hydrolytic stability and redox-responsiveness of our system lends a new release and breakdown mechanism to the field. Expanding both materials and encapsulated drugs will continue to push the boundaries of drug development.

In the third aim of this work, (Chapter 4), we tested our EPO and siRNA-loaded MPs in glaucoma and post-traumatic osteoarthritis mouse models. EPO delivery in ROS-scavenging MPs significantly preserved visual axis function through antioxidant signaling and chemical reaction. Additionally, we further optimized the formulation for testing in non-human primates, which is a key step towards clinical implementation of new drugs. MP-mediated delivery of siRNA in the joint significantly improved siRNA function at a lower overall dose due to the strong retention in the tissue. Reducing effective drug dose, especially for biologics, is key to making them more affordable and widely available.

5.2. Shortcomings

There are some shortcomings to the work presented here. For example, the DMA-co-TEMPO series was structured to jump from 50% TEMPO to 100% TEMPO with no intermediates. The conclusions drawn from the work would have had stronger support if a few more intermediate compositions were included, to ensure that the 50% composition was not an outlier masking a more optimal formulation. Additionally, inclusion of a previously-reported TEMPO-PEG[25] or TEMPO NP[36] would position our study more firmly in the broader field.

For the PS-co-ES series, we utilized DSC to demonstrate crystallinity at a standard temperature sweep of 10°C/min. However, for heterogeneous materials like polymers, characteristic broad peaks are expected and can be difficult to characterize. More precise techniques, such as successive self-nucleation and annealing[155] can detect lamellae of different

thickness corresponding to different ES oligomer lengths, providing more robust characterization of the material. The same is true for XRD, in which implementation of wide-angle x-ray diffraction (WAXS) is more appropriate for semicrystalline materials[227].

MP degradation and cargo release was studied in pure H_2O_2 at supraphysiologic concentrations, which does not recapitulate the *in vivo* environment. Because of downstream applications, it would be advantageous to study degradation and release in vitreous humor and/or synovial fluid. Alternatively, we could compare degradation in a mixed milieu of ROS, such as H_2O_2/hypochlorite. Also, for the EPO work, differential degradation for the different MP formulations should be compared. The high surface area: volume ratio in the first-generation particles formulated by W/O/W will significantly increase ROS ingress into the polymer matrix to accelerate degradation.

In this work, we targeted *Cdkn2a* in PTOA due to the high association of $p16^{INK4a}$-positive cells with PTOA. We designed an siRNA knocking down both transcripts with the rationale that inhibiting two mechanisms of senescence would be more potent as a potential disease-modifying agent. However, there is some evidence that $p19^{ARF}$ activity can suppress senescence in certain contexts[200]. A stronger comparison would be the design of siRNAs targeting each transcript separately, along with the dual-silencing version we have presented here.

The lack of H_2O_2 scavenging in the joint was also an unexpected shortcoming. We had determined the maximum dose which was injectable into the mouse joint with the rationale that we would want the highest dose of siRNA and polymer for potent gene knockdown. However, a dose-finding study with H_2O_2 scavenging as the primary outcome would be informative for this context. It is possible that the optimal doses for siRNA knockdown and for antioxidant activity are different, which would present a challenge moving forward.

5.3. Future work and potential applications

There are many exciting avenues for continuation of these aims. A major opportunity is to increase the reactivity of the PPSES polymer to ROS, particularly in the joint. Ideally, the MPs would oxidize steadily over time, as opposed to quickly in a delayed fashion, to act as a continuous sink for produced ROS. By further optimizing the structure of the polymer with this goal, we believe that antioxidant activity would be disease modifying in PTOA. For example, hydrophilic monomers could be incorporated into the PPSES chain to hydrophilize the matrix and promote oxidation. Alternatively, TEMPO could be loaded or conjugated to the MP to diversify the species which can be scavenged.

The PPSES-EPO MPs are currently being tested in a primate model of glaucoma, representing an exciting translational avenue for this system. A great deal of characterization, including batch-to-batch variability, MP size dispersity, and endotoxin <0.2 EU/ml represent formulation challenges which could be addressed. Additionally, intravital tracking of the MPs and their degradation products after intravitreal injection should be completed. Clinical products have failed due to blocking the visual axis; therefore, engineering the particles to avoid this issue could also be necessary.

Another interesting avenue is to expand the materials formulated with PPSES. We have demonstrated MP and NP formulations; but many biomaterials including porous MPs, scaffolds, micropatterned particles, or nanofibers could be pursued. By further diversifying the formulation capabilities of this polymer, we can continue to make head-to-head comparisons to PLGA, demonstrating the advantage of incorporating ROS scavenging. This would also increase the applications for PPSES.

In sum, we have demonstrated the importance of optimizing antioxidant polymer structure for desired application. Antioxidant materials exhibit a vast field of opportunities to

treat inflammatory and degenerative disease, especially in combination with proteins, nucleic acids, or small molecule drugs.

Appendix A: Supplementary Information for Chapter 2

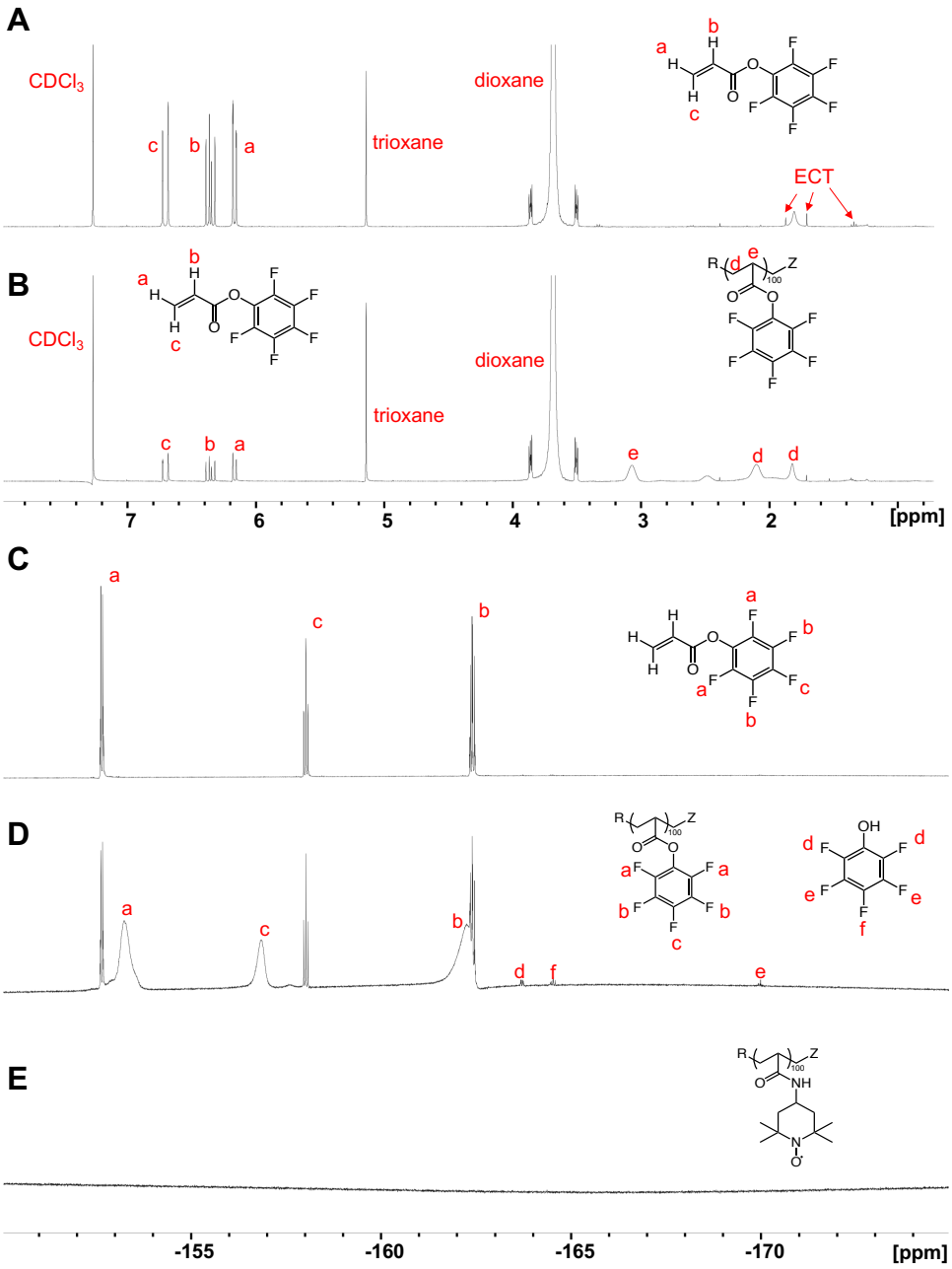

Supplementary Figure A.1: NMR characterization of DMA0-co-TEMPO100 synthesis.
(**A**) T0 RAFT mixture, 1H, CDCl3. (**B**) T24 RAFT mixture, 1H, CDCl3. (**C**) T0 RAFT mixture, 19F, CDCl3. (**D**) T24 RAFT mixture, 19F, CDCl3. (**E**) Purified DMA0-co-TEMPO100 polymer, 19F, CDCl3. Data from[24].

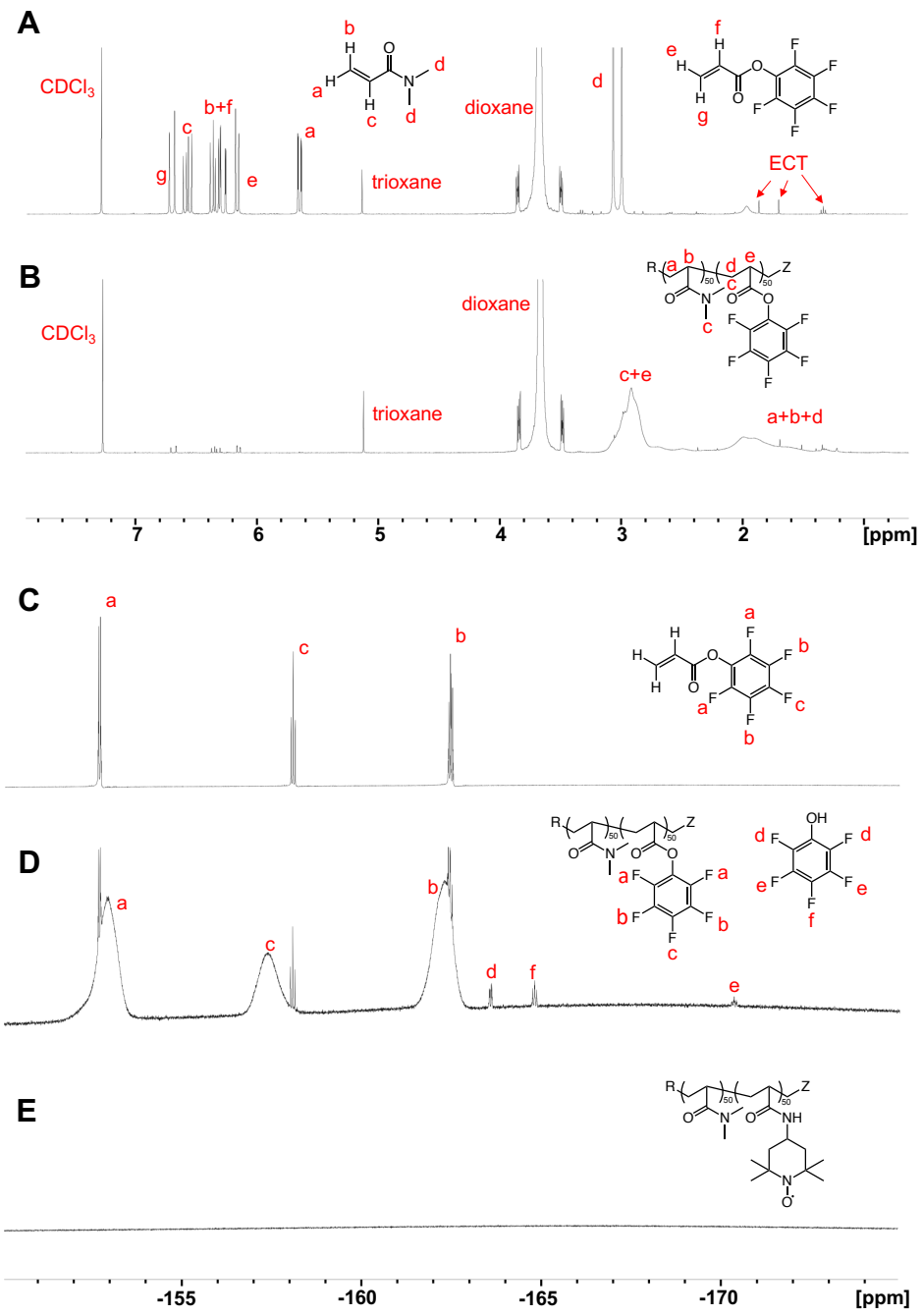

Supplementary Figure A.2: NMR characterization of DMA50-co-TEMPO50 synthesis.
(**A**) T0 RAFT mixture, 1H, CDCl3. (**B**) T24 RAFT mixture, 1H, CDCl3. (**C**) T0 RAFT mixture, 19F, CDCl3. (**D**) T24 RAFT mixture, 19F, CDCl3. (**E**) Purified DMA50-co-TEMPO50 copolymer, 19F, CDCl3. Data from[24].

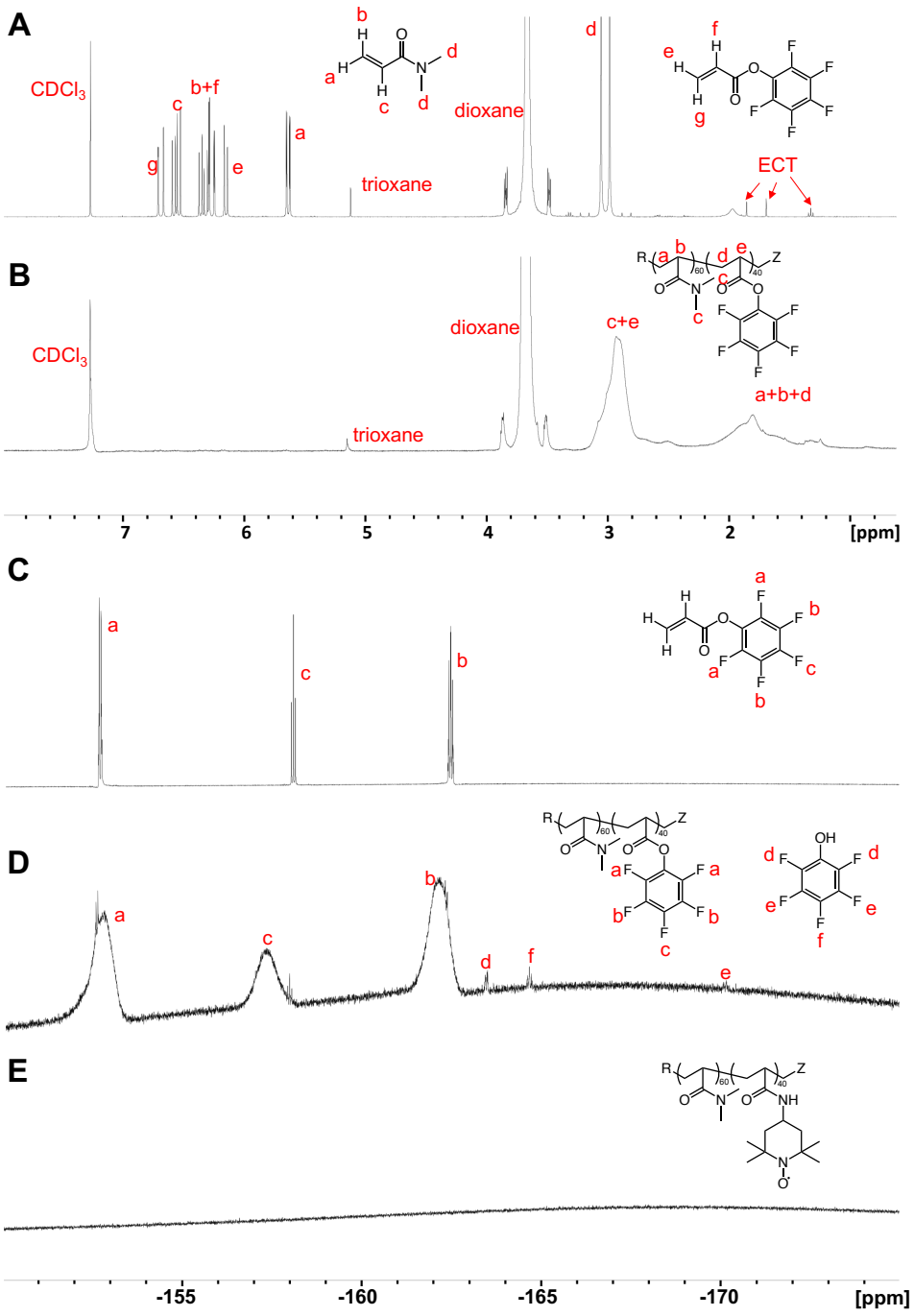

Supplementary Figure A.3: NMR characterization of DMA60-co-TEMPO40 synthesis.
(**A**) T0 RAFT mixture, 1H, CDCl3. (**B**) T24 RAFT mixture, 1H, CDCl3. (**C**) T0 RAFT mixture, 19F, CDCl3. (**D**) T24 RAFT mixture, 19F, CDCl3. (**E**) Purified DMA60-co-TEMPO40 copolymer, 19F, CDCl3. Data from[24].

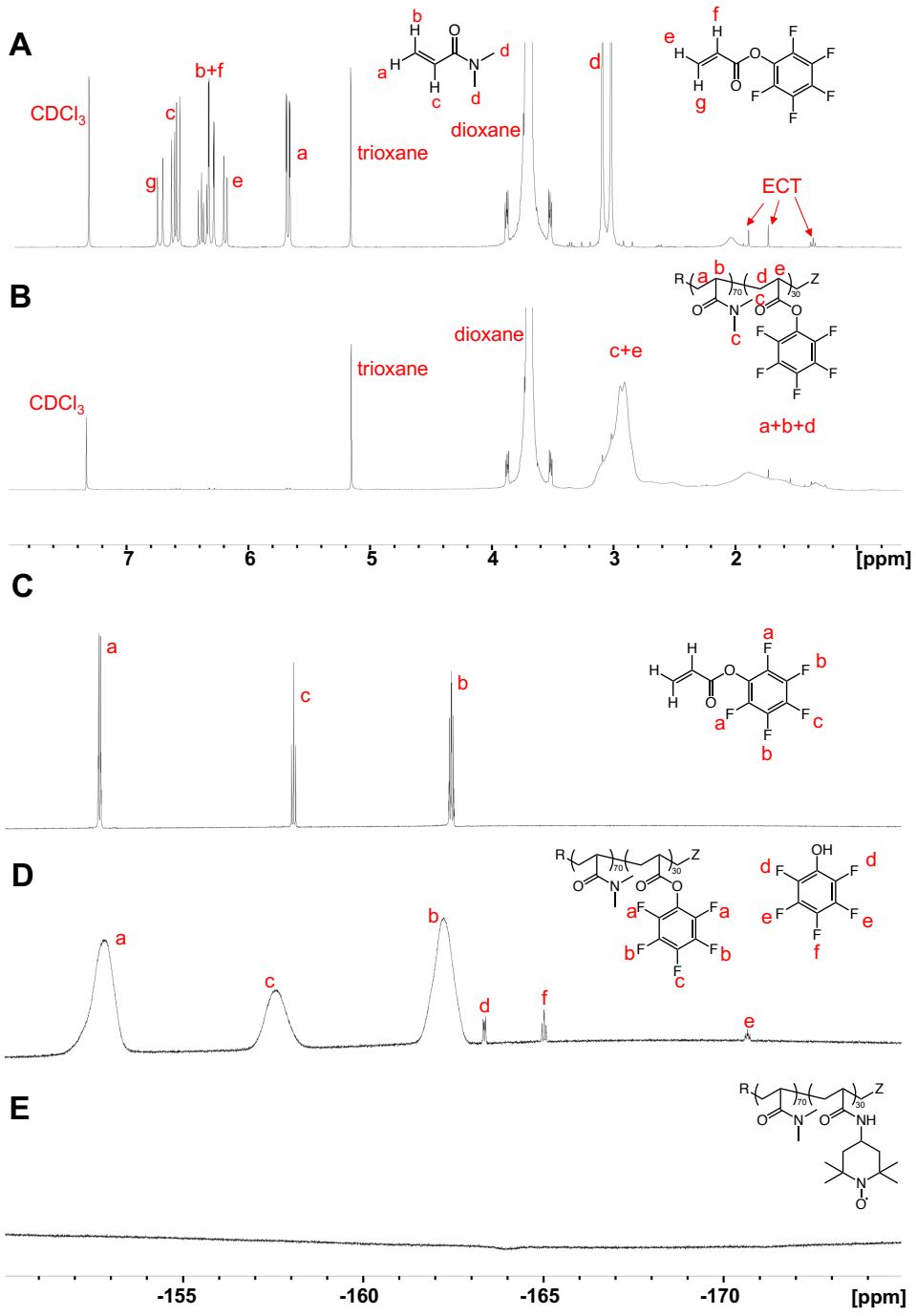

Supplementary Figure A.4: NMR characterization of DMA70-co-TEMPO30 synthesis.
(**A**) T0 RAFT mixture, 1H, CDCl3. (**B**) T24 RAFT mixture, 1H, CDCl3. (**C**) T0 RAFT mixture, 19F, CDCl3. (**D**) T24 RAFT mixture, 19F, CDCl3. (**E**) Purified DMA70-co-TEMPO30 copolymer, 19F, CDCl3. Data from[24].

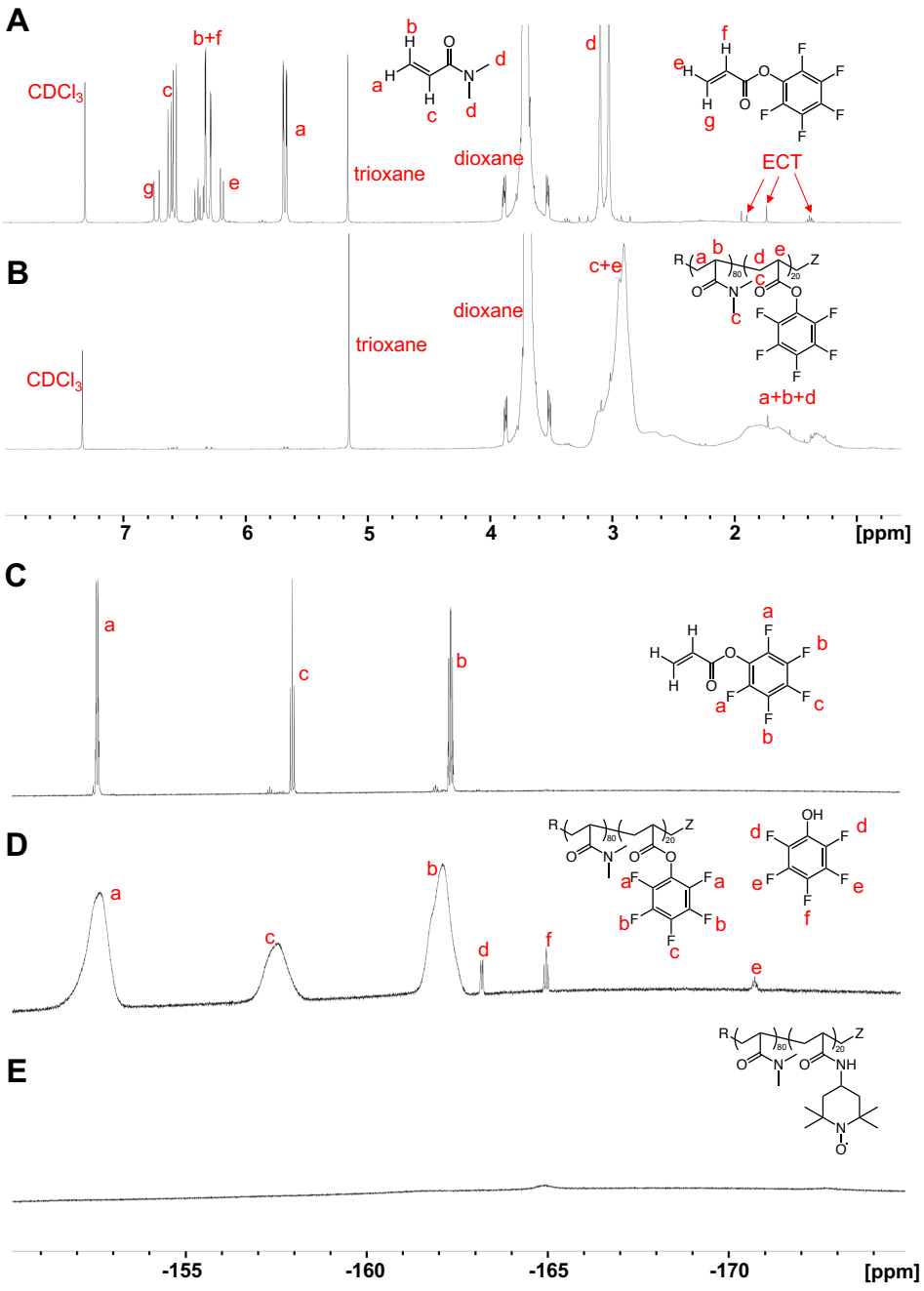

Supplementary Figure A.5: NMR characterization of DMA80-co-TEMPO20 synthesis.
(**A**) T0 RAFT mixture, 1H, CDCl3. (**B**) T24 RAFT mixture, 1H, CDCl3. (**C**) T0 RAFT mixture, 19F, CDCl3. (**D**) T24 RAFT mixture, 19F, CDCl3. (**E**) Purified DMA80-co-TEMPO20 copolymer, 19F, CDCl3. Data from[24].

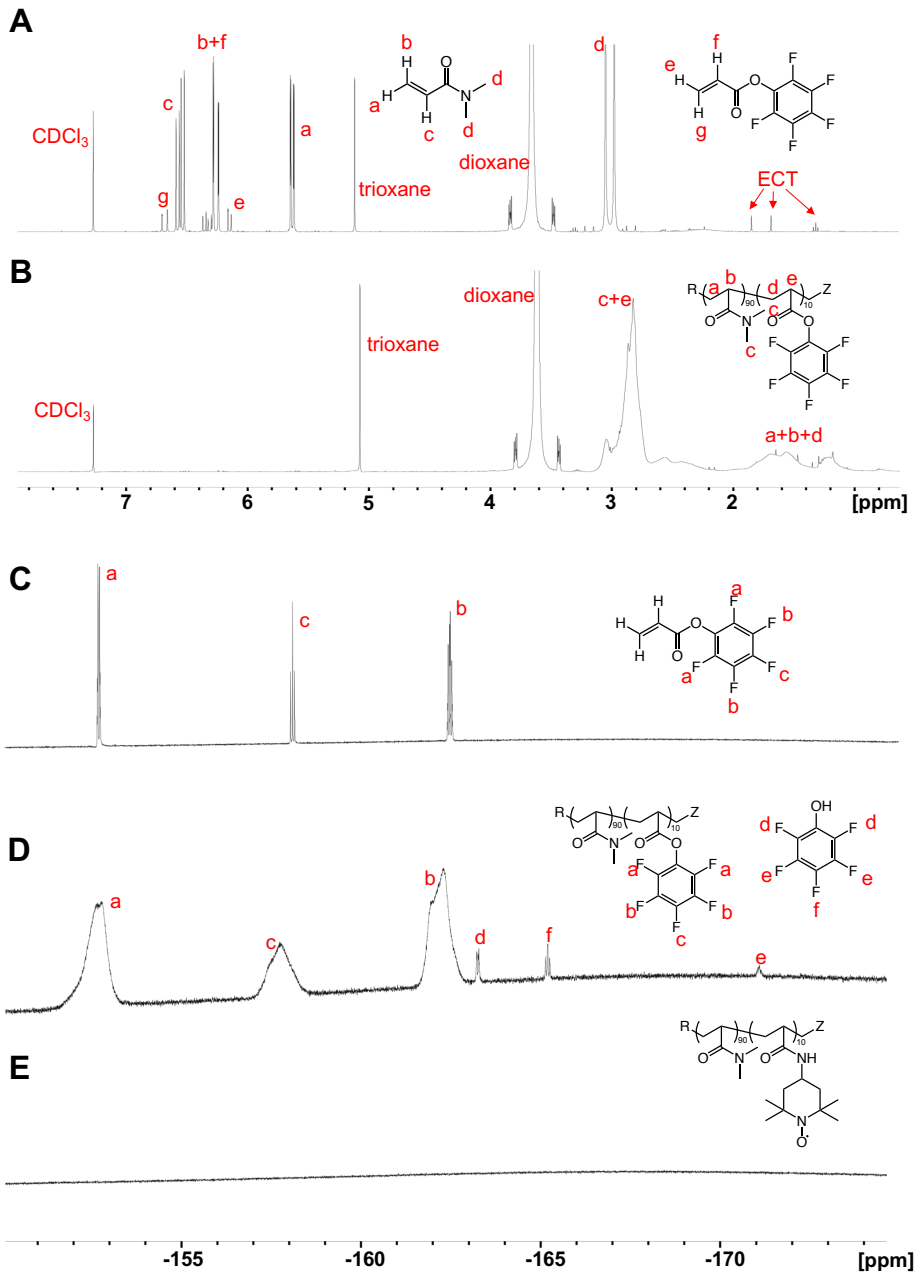

Supplementary Figure A.6: NMR characterization of DMA$_{90}$-co-TEMPO$_{10}$ synthesis.
(**A**) T$_0$ RAFT mixture, ^{1}H, CDCl$_3$. (**B**) T$_{24}$ RAFT mixture, ^{1}H, CDCl$_3$. (**C**) T$_0$ RAFT mixture, ^{19}F, CDCl$_3$. (**D**) T$_{24}$ RAFT mixture, ^{19}F, CDCl$_3$. (**E**) Purified DMA$_{90}$-co-TEMPO$_{10}$ copolymer, ^{19}F, CDCl$_3$. Data from[24].

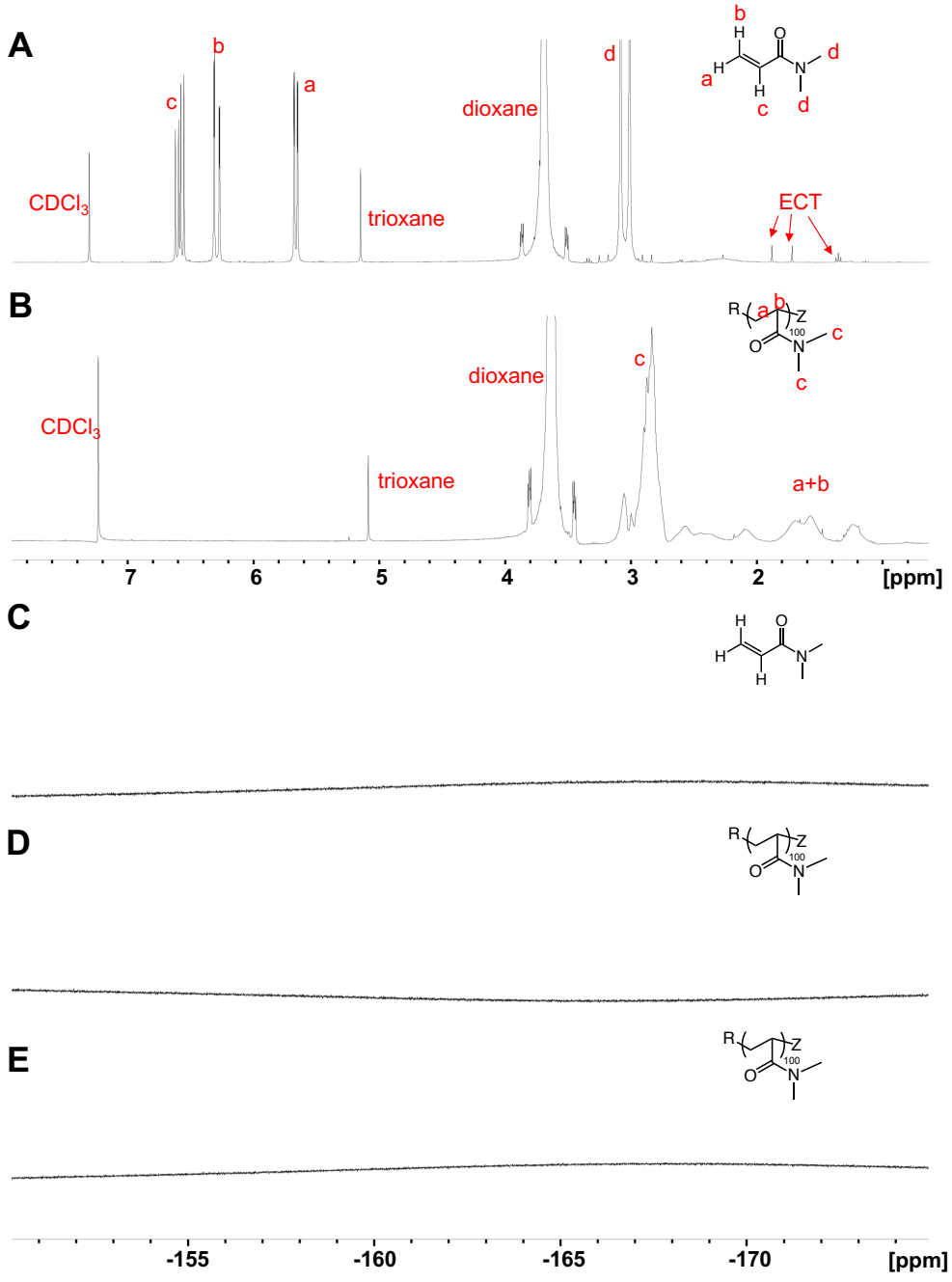

Supplementary Figure A.7: NMR characterization of DMA$_{100}$-co-TEMPO$_0$ synthesis.
(**A**) T$_0$ RAFT mixture, ^{1}H, $CDCl_3$. (**B**) T$_{24}$ RAFT mixture, ^{1}H, $CDCl_3$. (**C**) T$_0$ RAFT mixture, ^{19}F, $CDCl_3$. (**D**) T$_{24}$ RAFT mixture, ^{19}F, $CDCl_3$. (**E**) Purified DMA$_{100}$-co-TEMPO$_0$ polymer, ^{19}F, $CDCl_3$. Data from[24].

A

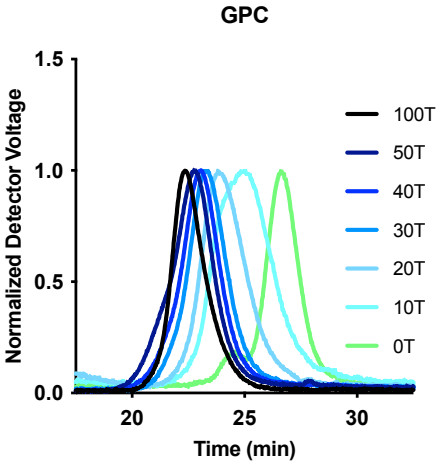

B

Target DMA: TEMPO	% DMA	% PFPA	Mn (kDa)	Mw (kDa)	Mw/ Mn
0:100	0	100	13.30	16.19	1.21
50:50	50	50	16.60	18.45	1.11
60:40	59	41	15.13	17.10	1.13
70:30	69	31	15.44	16.13	1.04
80:20	80	20	12.84	13.63	1.06
90:10	90	10	11.90	12.10	1.02
100:0	100	0	9.81	1.00	1.02

Supplementary Figure A.8: DMA-co-TEMPO characterization by GPC and NMR.
(**A**) Light scattering detector traces from GPC indicate monodisperse populations with increasing molecular weight as TEMPO content increases. (**B**) Table of characterization of DMA and PFPA composition of the parent copolymers, M_n and M_w of final polymers, and polydispersity of final polymers. Data from[24].

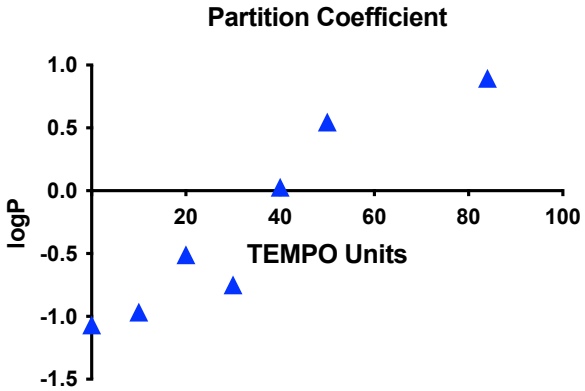

Supplementary Figure A.9: Octanol-water partition coefficient for DMA-co-TEMPO series.
Data from[24].

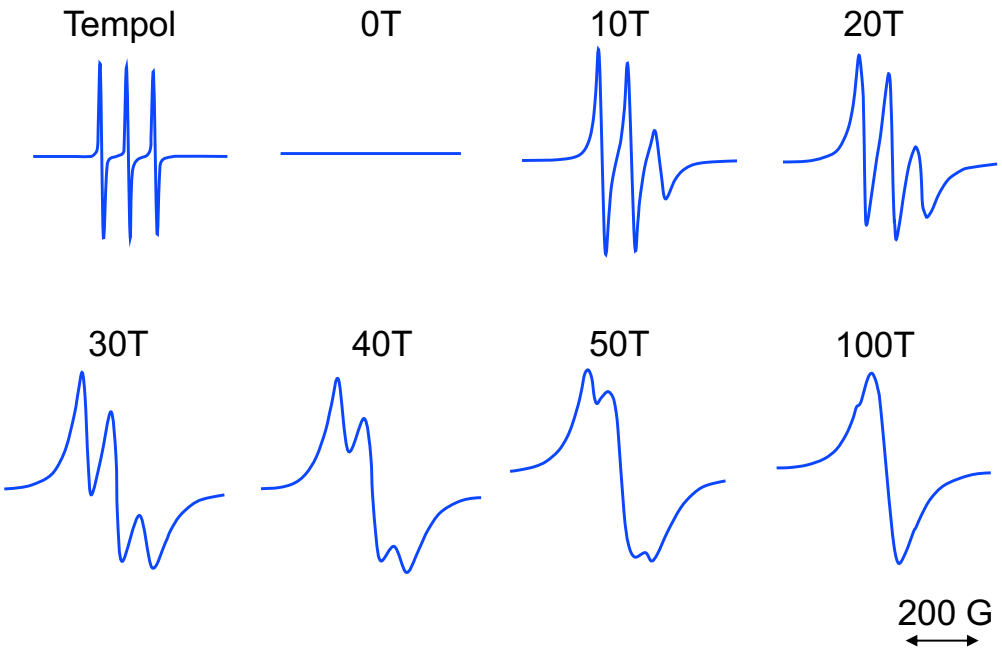

Supplementary Figure A.10: ESR shows gradual broadening of spectra as TEMPO packing increases in DMA-co-TEMPO series.
Data from[24].

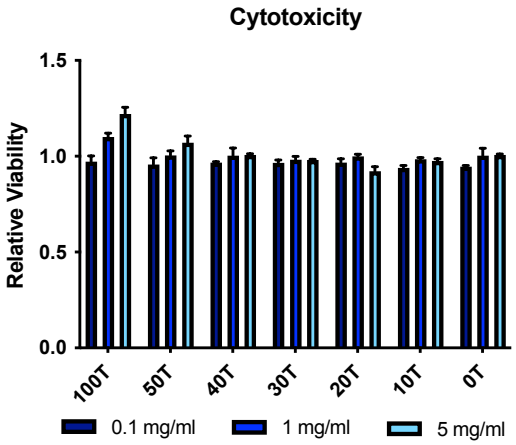

Supplementary Figure A.11: Cytocompatibility of DMA-co-TEMPO series in ATDC5 cells.
Data from[24].

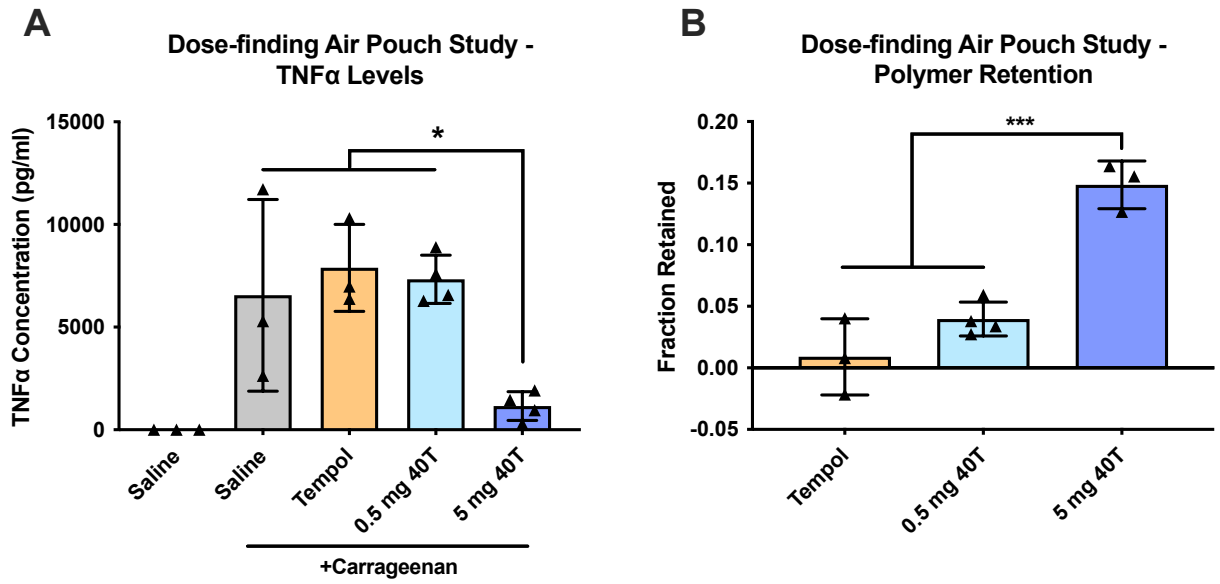

Supplementary Figure A.12: Dose-finding study in the air pouch model.
(**A**) TNFa levels in air pouch exudate. (**B**) Polymer retention measured by ESR in the air pouch exudate. *p<0.05, ***p<0.001. Data from[24].

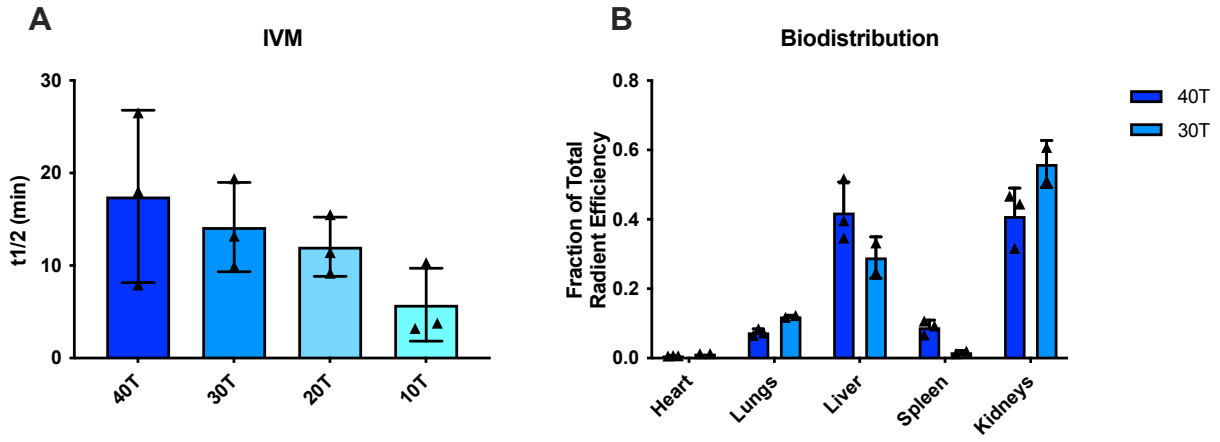

Supplementary Figure A.13: DMA-co-TEMPO copolymers circulate systemically and are cleared by the liver and kidneys.
(**A**) T1/2 of water-soluble DMA-co-TEMPO copolymers measured by IVM. (**B**) Organ biodistribution of lead candidate copolymers 10 minutes after i.v. injection (n=2-3). Data from[24].

Appendix B: Supplementary information for Chapter 3

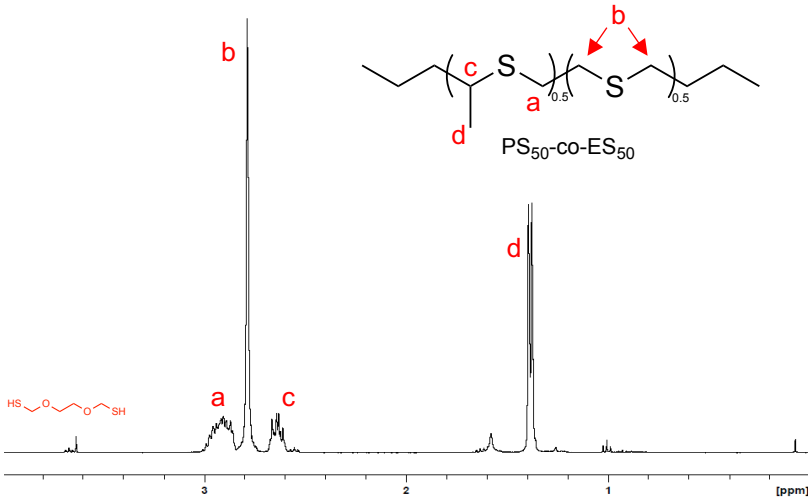

Supplementary Figure B.1: NMR spectra for PS_{50}-co-ES_{50}. ^1H, $CDCl_3$.

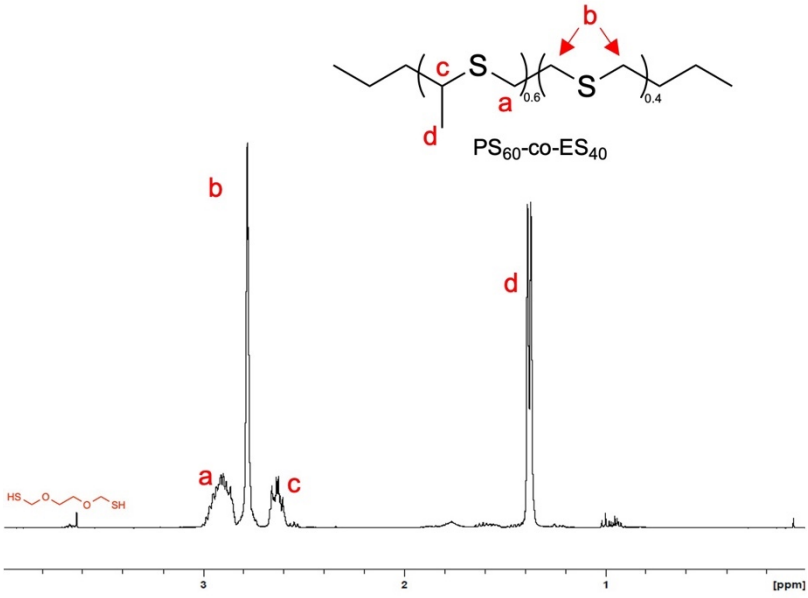

Supplementary Figure B.2: NMR spectra for PS_{60}-co-ES_{40}. ^1H, $CDCl_3$.

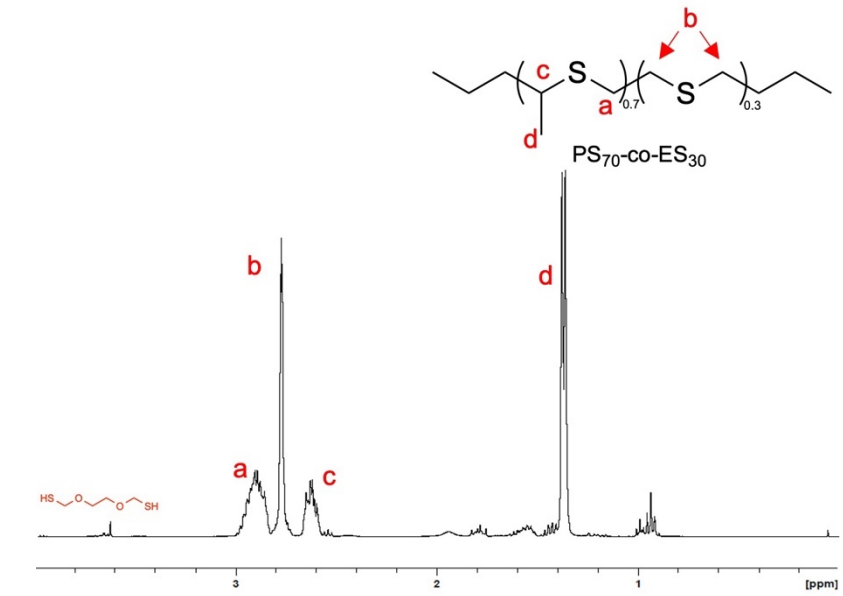

Supplementary Figure B.3: NMR spectra for PS_{70}-co-ES_{30}. ^{1}H, $CDCl_3$.

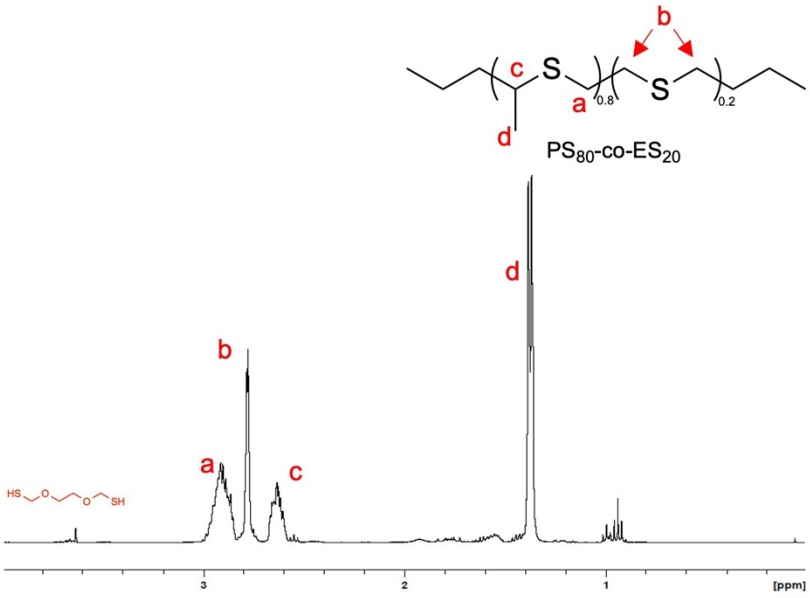

Supplementary Figure B.4: NMR spectra for PS_{80}-co-ES_{20}. ^{1}H, $CDCl_3$.

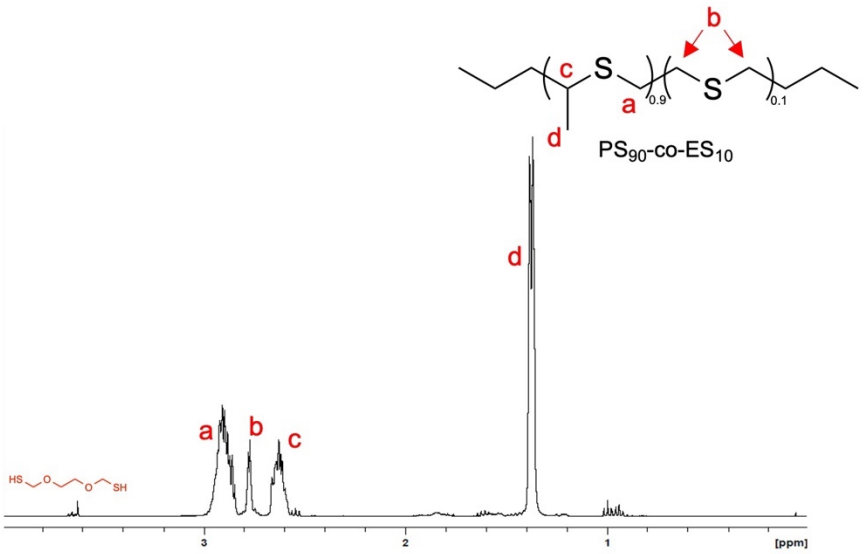

Supplementary Figure B.5: NMR spectra for PS_{90}-co-ES_{10}. ^1H, $CDCl_3$.

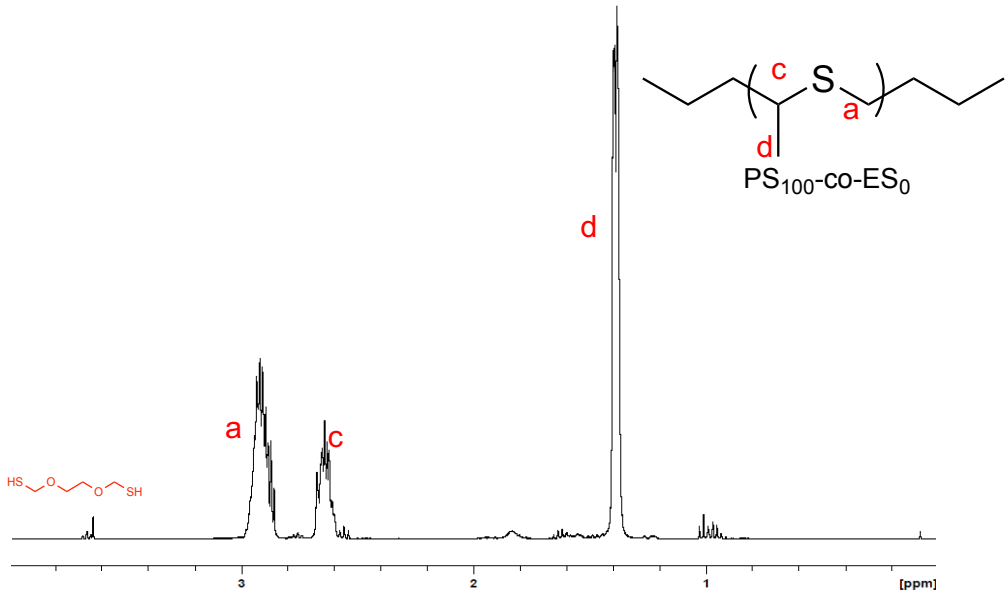

Supplementary Figure B.6: NMR spectra for PS_{100}-co-ES_0. ^1H, $CDCl_3$.

Supplementary Table B.1: NMR Characterization of PS-co-ES series

Target PS:ES	Actual PS:ES (NMR)	Target MW (kDa)	Actual MW (kDa, NMR)
50:50	51:49	14.8	11.7
60:40	60:40	15.1	14.4
70:30	66:34	15.4	14.3
80:20	75:25	15.7	14.6
90:10	90:10	16.0	16.6
100:0	100:0	16.3	16.3

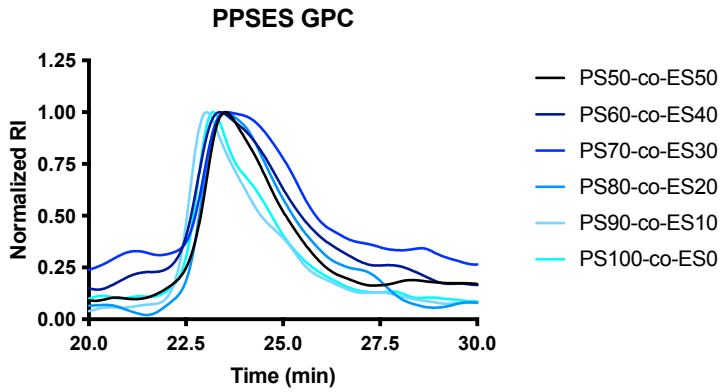

Supplementary Figure B.7: GPC light scattering detector data of PS-co-ES series.

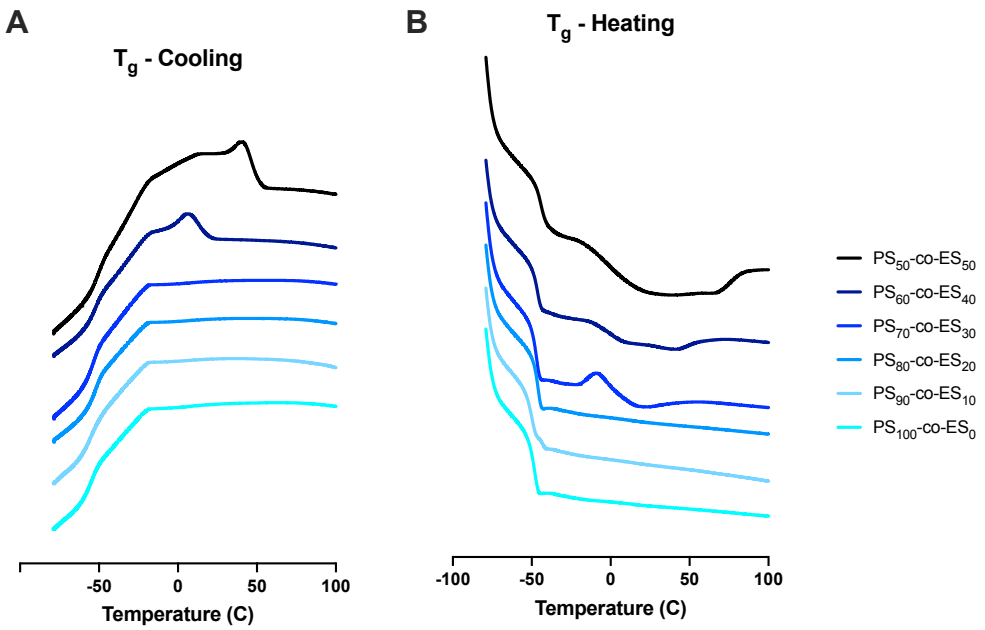

Supplementary Figure B.8: DSC scans showing glass transition temperature (T_g) for the PS-co-ES series.
(A) Cooling scans and (B) heating scans.

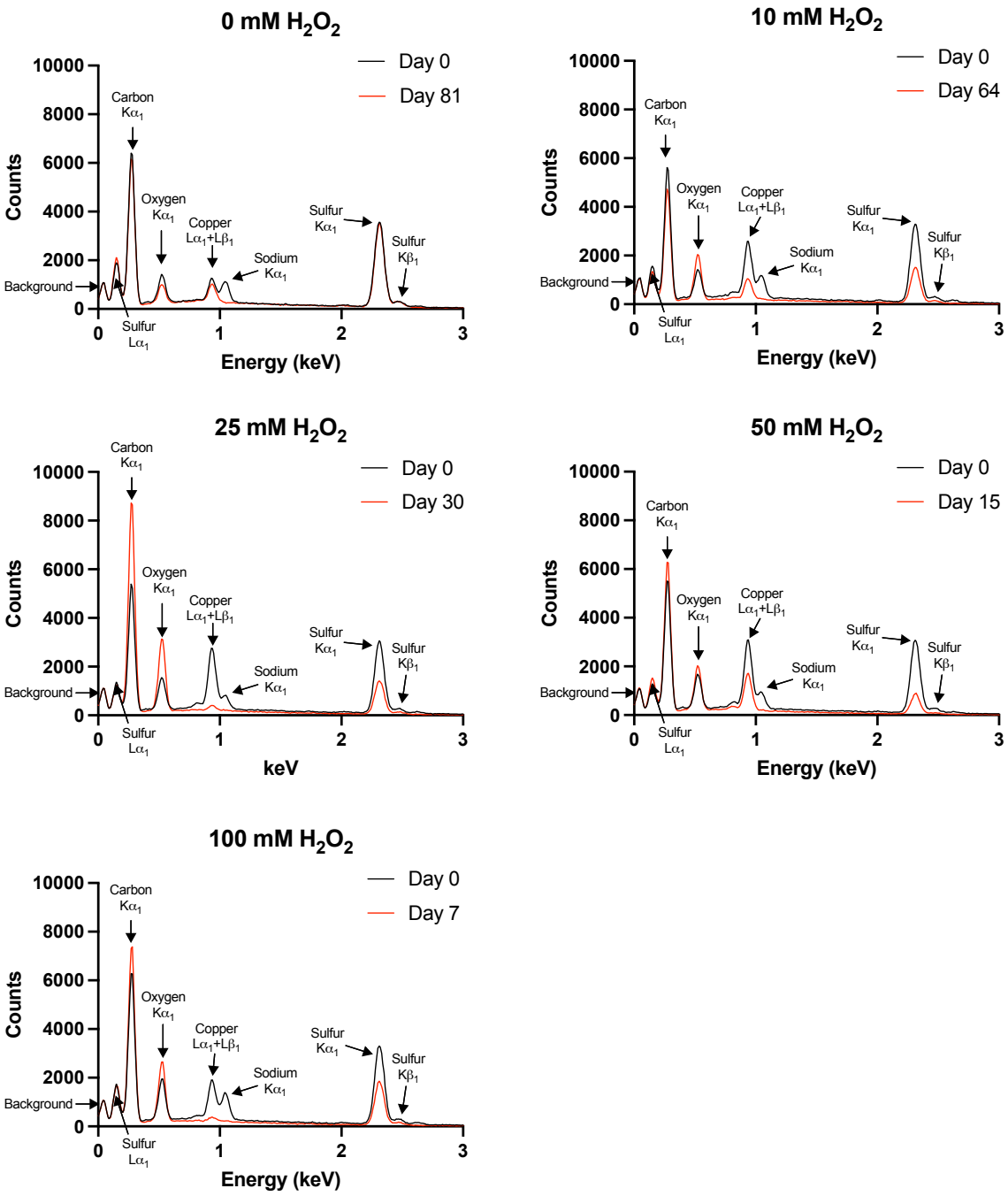

Supplementary Figure B.9: Example energy dispersive x-ray spectroscopy (EDS) spectra for PPSES MP oxidation.

(**A**) Days 0 and 82 for 0 mM H_2O_2; (**B**) days 0 and 64 for 10 mM H_2O_2; (**C**) days 0 and 30 for 25 mM H_2O_2; (**D**) days 0 and 15 for 50 mM H_2O_2; (**E**) days 0 and 7 for 100 mM H_2O_2. $K\alpha_1$, $K\beta_1$, $L\alpha_1$, and $L\beta_1$ refer to the peaks generated from migration of electrons to the vacancy formed in the denoted energy shell upon excitation by x-rays.

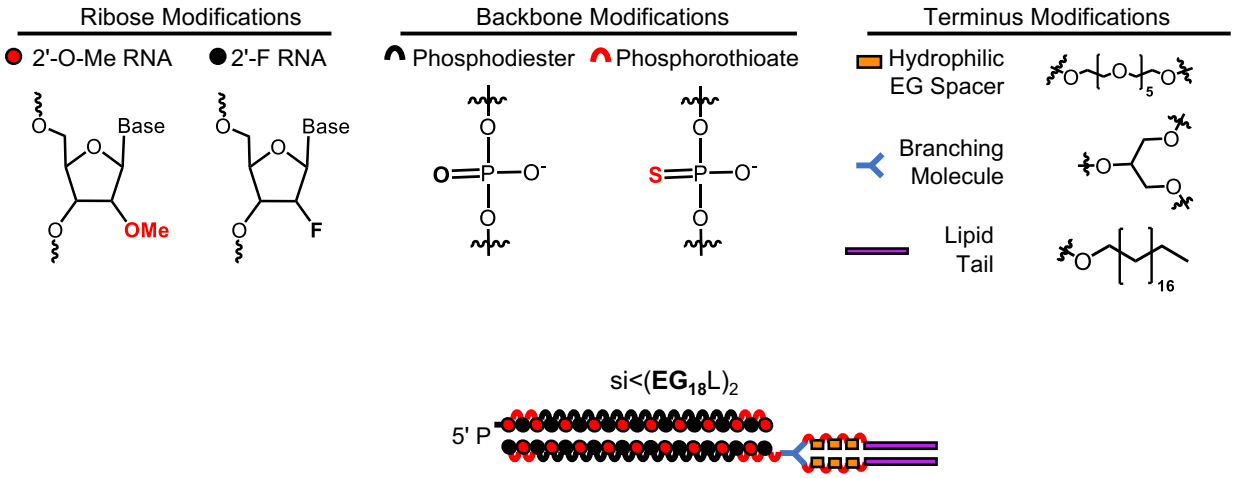

Supplementary Figure B.10: Structure of stabilized, albumin-binding amphiphilic siRNA conjugate, referred to as "siRNA-EG18".

Appendix C: Supplementary information for Chapter 4

Supplementary Table C.1: Documentation of formulation details and adverse events in non-human primates treated with PPSES Gen3 MP.

Animal ID: NHP 6352 [euthanized 11/9/21]				
Date	July 20, 2021	August 30, 2021	September 27, 2021	
Treatment	LE: 100 µg of unloaded MP (40 µl) RE: buffer (40 µl)	LE: 100 µg of unloaded MP (40 µl) RE: PBS (40 µl)	LE: 100 µg unloaded MP (40 µl) RE: buffer (40 µl)	
Buffer ingredients	Sample contained ~0.5% Tween-20 and 6.67 mM sucrose	Sample was washed 1x with PBS to remove Tween-20 and sucrose	0.02% Tween-80, 5% sucrose, 10 mM sodium citrate (pH 7.2-7.4)	
Impact on vision	Significant visual impairment	Minimal visual impairment	Significant visual impairment	
Particle injectability	Good	Poor (MPs aggregated and adhered to tube)	Moderate (some MP aggregation)	
Animal ID: NHP 6350 [euthanized 2/1/22]				
Date	September 27, 2021	November 9, 2021	December 15, 2021	January 18, 2022
Treatment	LE: 100 µg unloaded MP (40 µl) RE: buffer (40 µl)	LE: 100 µg of unloaded MP* (20 µl) RE: buffer (20 µl)	LE: 100 µg of unloaded MP (20 µl) RE: buffer (20 µl)	LE: 100 µg of unloaded MP (20 µl) RE: buffer (20 µl)
Buffer ingredients	0.02% Tween-80, 5% sucrose, 10 mM sodium citrate (pH 7.2-7.4)	0.25% Pluronic F-127 + 0.25% carboxymethyl-cellulose in sterile PBS (pH 7.2-7.4)	0.25% Pluronic F-127 + 0.25% carboxymethyl-cellulose in sterile PBS (pH 7.2-7.4)	0.25% Pluronic F-127 + 0.25% carboxymethyl-cellulose in sterile PBS (pH 7.2-7.4)
Impact on vision	Significant visual impairment	No visual impairment	No visual impairment	No visual impairment
Particle injectability	Moderate (some MP aggregation)	Good	Good	Good
Animal ID: NHP 6543 [euthanized 3/29/23][$,^]				
Date	November 8, 2022	December 13, 2022	January 17, 2023	February 21, 2023
Treatment	LE: 100 µg EPO MP (20 µl) RE: buffer (20 µl)	LE: 100 µg EPO MP (20 µl) RE: buffer (20 µl)	LE: 100 µg EPO MP[#] (20 µl) RE: buffer (20 µl)	LE: 100 µg EPO MP[#] (20 µl) RE: buffer (20 µl)
Animal ID: NHP 6527 [euthanized 9/18/23] [$,^]				
Date	May 1, 2023	June 13, 2023	July 17, 2023	August 15, 2023
Treatment	Bilateral: rhodamine-EPO MP	Bilateral: rhodamine-EPO MP	Bilateral: rhodamine-EPO MP	Bilateral: rhodamine-EPO MP

*MP mean diameter 21.4 µm. All other injections formulated at mean diameter 44.5 µm
[#]MP was thawed from storage at -20ºC from a previous injection. All other samples were freshly resuspended from lyophilized MPs.
[$]No visual impairment or injection issues
[^]All injections in buffer of 0.25% Pluronic F-127 + 0.25% carboxymethylcellulose in sterile PBS (pH 7.2-7.4)

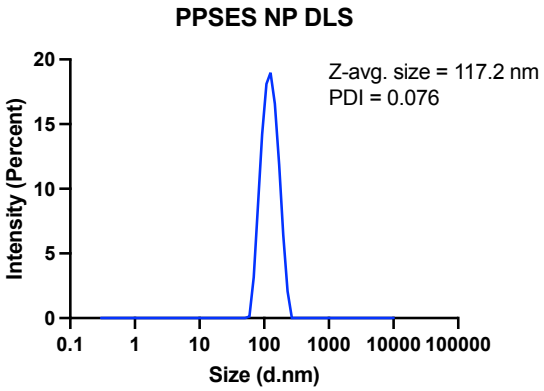

Supplementary Figure C.1: Dynamic light scattering of PPSES NP for ACL rupture Amplex Red study.

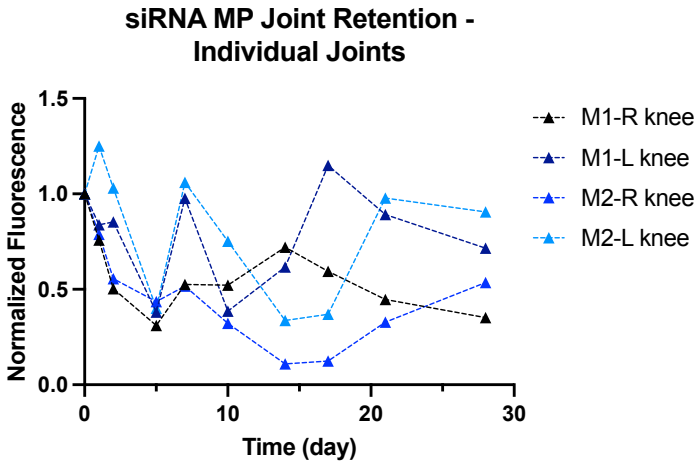

Supplementary Figure C.2: IVIS tracking of siRNA-Cy5 MPs plotting individual mice.

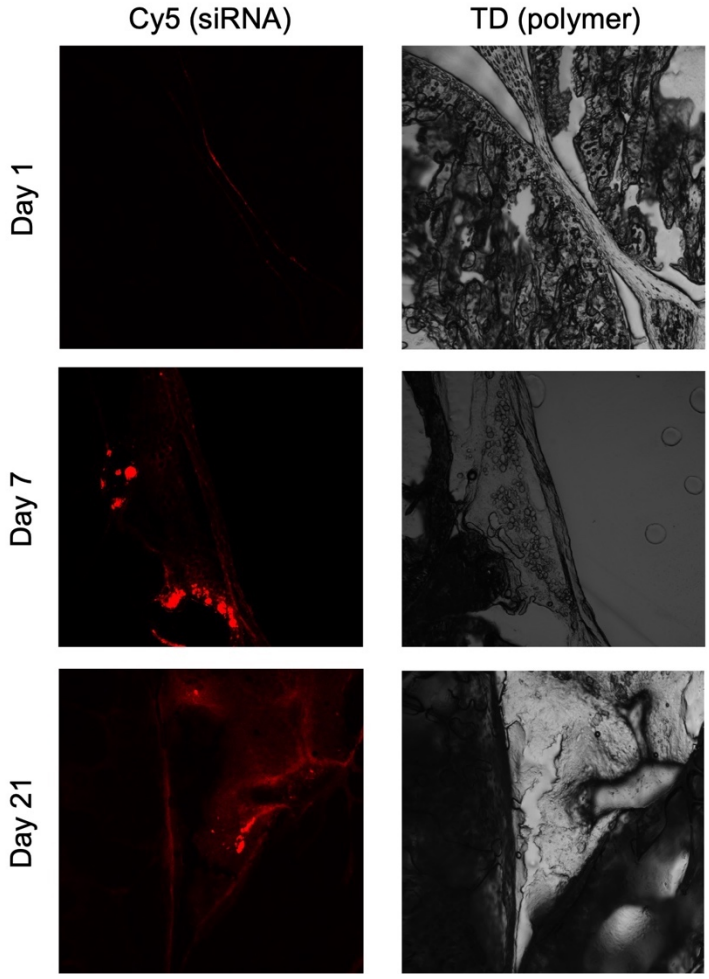

Supplementary Figure C.3: Confocal images of cryosectioned mouse knees.
Thresholded to highlight weaker, more diffuse signal at the joint interface (day 1) and through the synovium (days 7 and 21).

Supplementary Table C.2: siRNA Sequences

	Sequence 5' to 3'
Nontargeted control (Ctrl) sense, zipper	(fU)*(MeU)*(fC)(MeU)(fC)(MeC)(fG)(MeA)(fA)(MeC)(fG)(MeU)(fG)(MeU)(fC)(MeA)(fC)*(MeG)*(fU)
Ctrl antisense, zipper	(PHO)(MeA)*(fC)*(MeG)(fU)(MeG)(fA)(MeC)(fA)(MeC)(fG)(MeU)(fU)(MeC)(fG)(MeG)(fA)(MeG)*(fA)*(MeA)
Cyclin-dependent kinase sequence #1 (Cdkn2a #1) sense	A.C.A.U.C.A.A.G.A.C.A.U.C.G.U.G.C.G.A.U.U
Cdkn2a #1 antisense	P.U.C.G.C.A.C.G.A.U.G.U.C.U.U.G.A.U.G.U.U.U
Cdkn2a #2 sense	A.G.G.U.G.A.U.G.A.U.G.A.U.G.G.G.C.A.A.U.U
Cdkn2a #2 antisense	U.U.G.C.C.C.A.U.C.A.U.C.A.U.C.A.C.C.U.U.U
Cdkn2a #3 sense	G.C.U.C.A.A.C.U.A.C.G.G.U.G.C.A.G.A.U.U.U
Cdkn2a #3 antisense	A.U.C.U.G.C.A.C.C.G.U.A.G.U.U.G.A.G.C.U.U
Cdkn2a #4 sense	G.C.U.G.G.G.U.G.G.U.C.U.U.U.G.U.G.U.A.U.U
Cdkn2a #4 antisense	U.A.C.A.C.A.A.A.G.A.C.C.A.C.C.C.A.G.C.U.U
Cdkn2a #1 sense, zipper	(fA)*(MeC)*(fA) (MeU) (fC) (MeA) (fA) (MeG) (fA) (MeC) (fA) (MeU) (fC) (MeG) (fU) (MeG) (fC)*(MeG)*(fA)
Cdkn2a #1 antisense, zipper	(MeU)*(fC)*(MeG) (fC) (MeA) (fC) (MeG) (fA) (MeU) (fG) (MeU) (fC) (MeU) (fU) (MeG) (fA) (MeU)*(fG)*(MeU)
Cdkn2a #2 sense, zipper	(fA)*(MeG)*(fG) (MeU) (fG) (MeA) (fU) (MeG) (fA) (MeU) (fG) (MeA) (fU) (MeG) (fG) (MeG) (fC)*(MeA)*(fA)
Cdkn2a #2 antisense, zipper	(MeU)*(fU)*(MeG) (fC) (MeC) (fC) (MeA) (fU) (MeC) (fA) (MeU) (fC) (MeA) (fU) (MeC) (fA) (MeC)*(fC)*(MeU)
Ckdkn2a #4 sense, zipper	(fG)*(MeC)*(fU) (MeG) (fG) (MeG) (fU) (MeG) (fG) (MeU) (fC) (MeU) (fU) (MeU) (fG) (MeU) (fG)*(MeU)*(fA)
Cdkn2a #4 antisense, zipper	(MeU)*(fA)*(MeC) (fA) (MeC) (fA) (MeA) (fA) (MeG) (fA) (MeC) (fC) (MeA) (fC) (MeC) (fC) (MeA)*(fG)*(MeC)
Luciferase (Luc) sense, zipper	(MeU)*(fU)*(MeC) (fA) (MeU) (fU) (MeA) (fU) (MeC) (fA) (MeG) (fU) (MeG) (fC) (MeA) (fA) (MeU)*(fU)*(MeG)
Luciferase (Luc) sense, zipper, Cy5	(Cy5) (MeU)*(fU)*(MeC) (fA) (MeU) (fU) (MeA) (fU) (MeC) (fA) (MeG) (fU) (MeG) (fC) (MeA) (fA) (MeU)*(fU)*(MeG)
Luc antisense, zipper	(PHO) (MeU)*(fU)*(MeC) (fA) (MeU) (fU) (MeA) (fU) (MeC) (fA) (MeG) (fU) (MeG) (fC) (MeA) (fA) (MeU)*(fU)*(MeG)
Phosphorothioate bone (X)*(X); phosphodiester bond (X) (X); 2'F substituted base (fX); 2'OMe substituted base (MeX)	

Supplementary Table C.3: qPCR Primer Sequences

	Sequence 5' to 3'
Rpl4 Forward	GCCAGGCCAGAAATCACAAA
Rpl4 Reverse	TCCTTTCTTGCCTACCGCTG
Cdkn2a, Transcript Variant 1, Forward	TCGCAGGTTCTTGGTCACTG
Cdkn2a, Transcript Variant 1, Reverse	CCCATCATCATCACCTGGTCC
Cdkn2a, Transcript Variant 2, Forward	TGAATCTCCGCGAGGAAAGC
Cdkn2a, Transcript Variant 2, Reverse	TGCCCATCATCATCACCTGAA
Mmp13 Forward	GGCCAGAACTTCCCAACCAT
Mmp13 Reverse	GAGCCCAGAATTTTCTCCCTCT

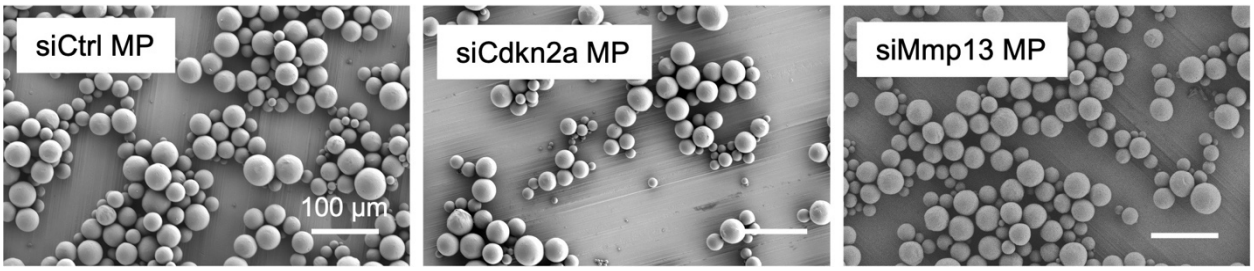

Supplementary Figure C.4: SEM of siRNA MPs injected in PTOA mice.
Scale bar = 100 µm.

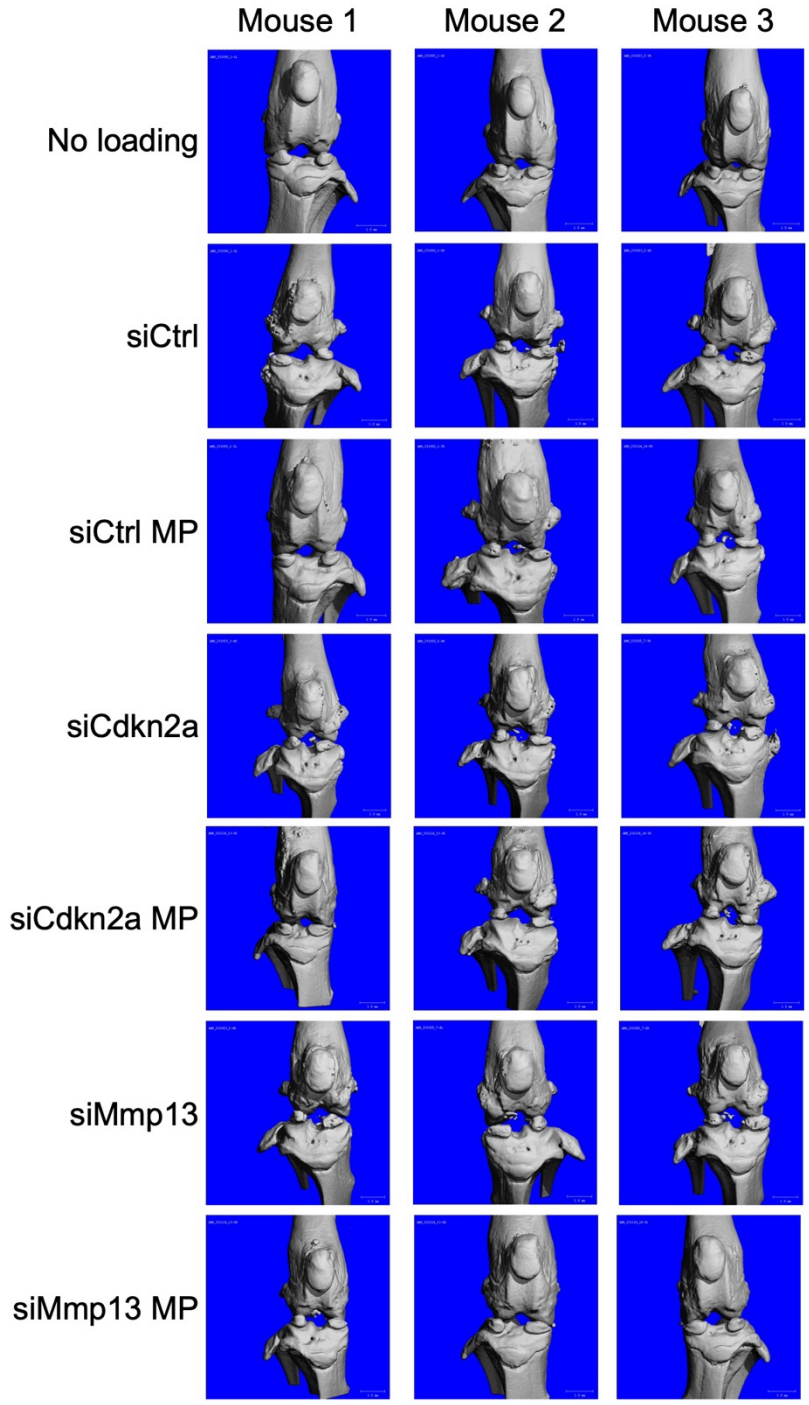

Supplementary Figure C.5: MicroCT reconstructions for siRNA-MP treated mice.
Demonstrates cortical bone and osteophyte remodeling for 3 mice per group treated with siRNA or siRNA MPs. Mice were treated with MPs on day 0, and loaded for 4 weeks (3x/wk) starting 24 hours after injection.

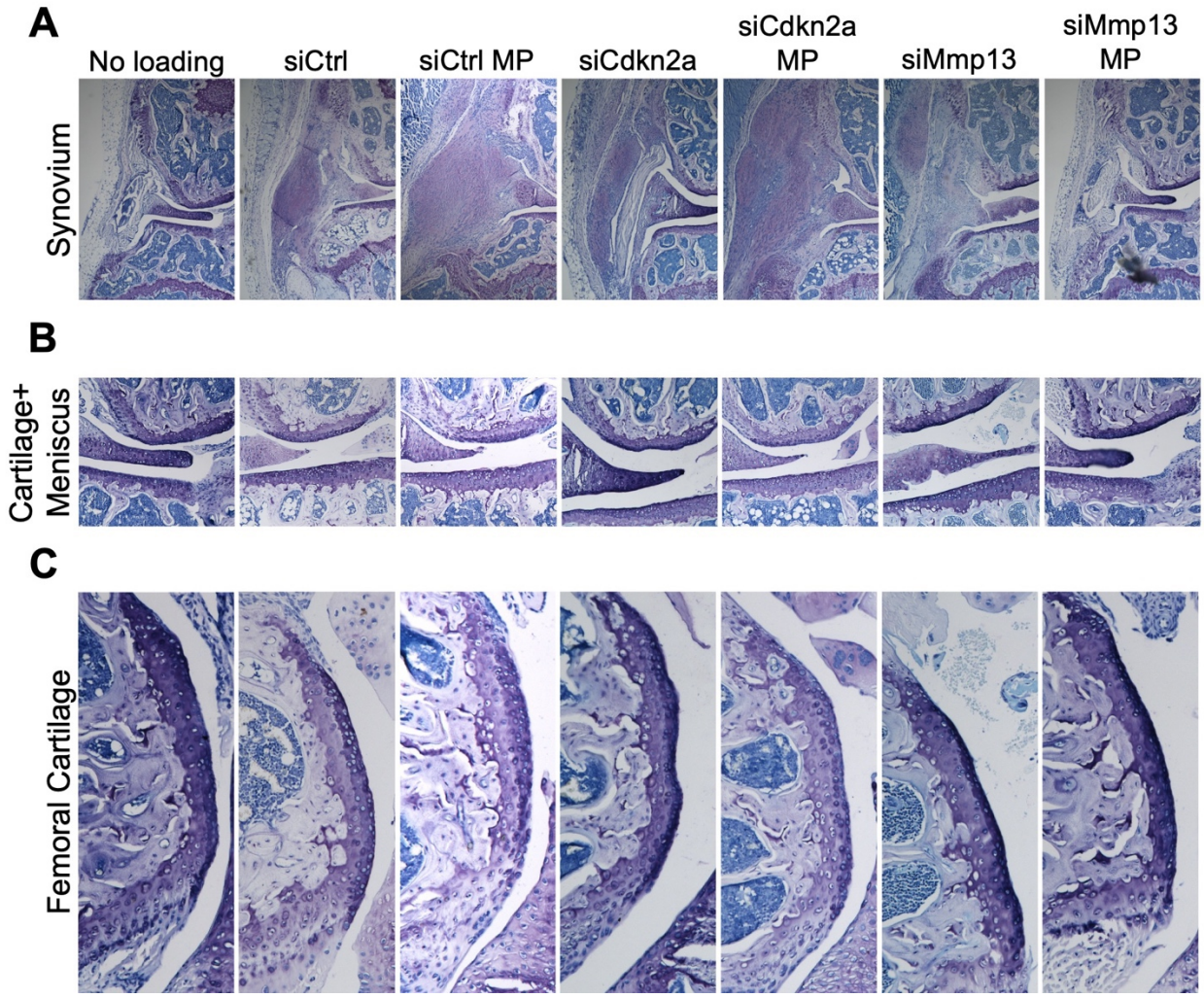

Supplementary Figure C.6: Toluidine blue staining for evaluation of lateral joint structural damage.
Mice were treated on day 0 and loaded 3x/week for 4 weeks starting 24 hours after injection. (**A**) Lateral synovium, (**B**) lateral cartilage and meniscus, (**C**) lateral femoral cartilage.
al cartilage.

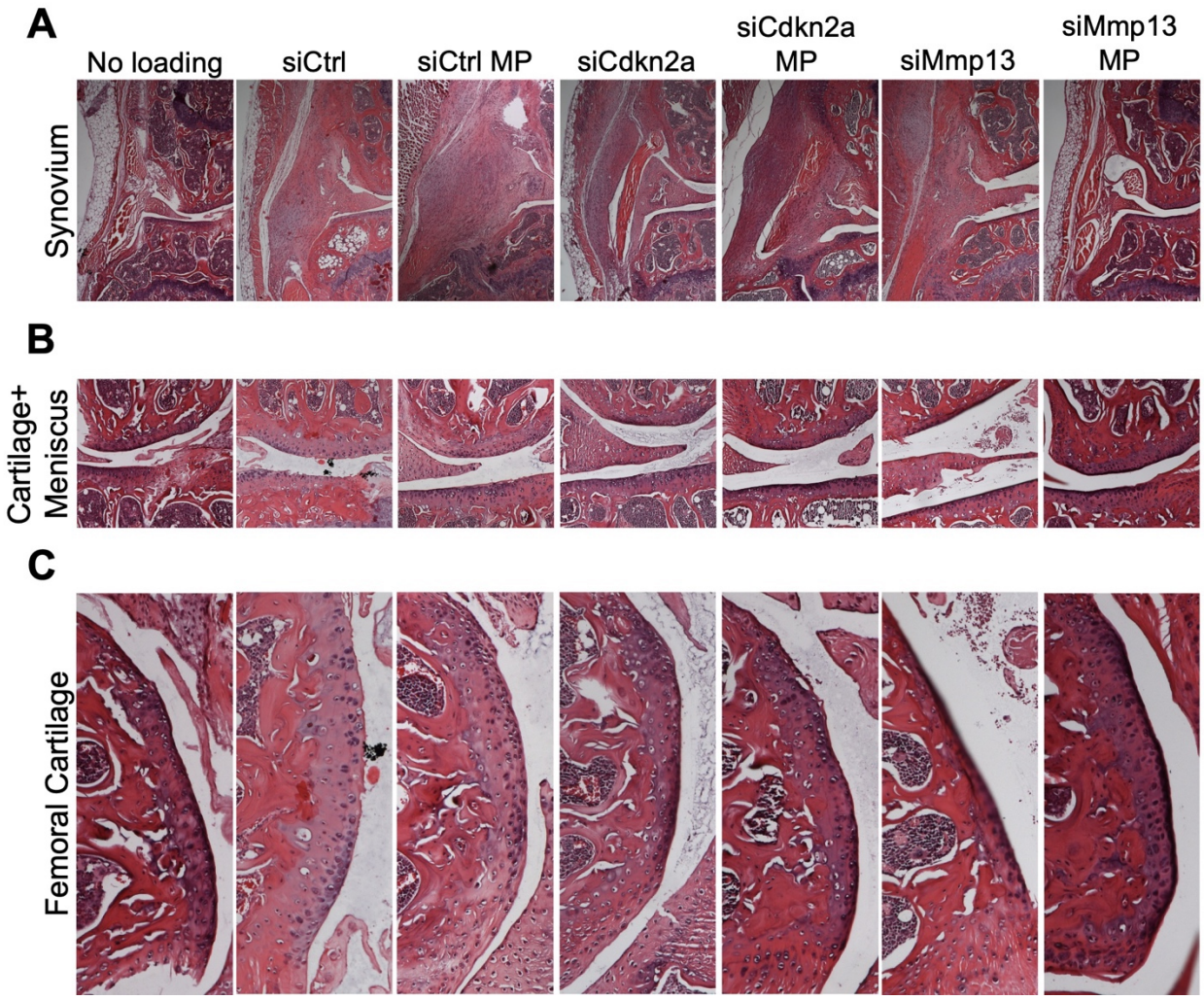

Supplementary Figure C.7: Hematoxylin and eosin staining for evaluation of lateral joint structural damage.
Mice were treated on day 0 and loaded 3x/week for 4 weeks starting 24 hours after injection. (**A**) Lateral synovium, (**B**) lateral cartilage and meniscus, (**C**) lateral femoral cartilage.

Appendix D: References

1. Zhang, J. *et al.* ROS and ROS-Mediated Cellular Signaling. *Oxidative Medicine and Cellular Longevity* (2016). https://doi.org:10.1155/2016/4350965
2. El-Benna, J. *et al.* Priming of the neutrophil respiratory burst: role in host defense and inflammation. *Immunological reviews* **273**, 180-193 (2016).
3. Halliwell, B. Reactive oxygen species in living systems: Source, biochemistry, and role in human disease. *The American Journal of Medicine* **91**, S14-S22 (1991). https://doi.org:https://doi.org/10.1016/0002-9343(91)90279-7
4. Chapple, I. L. C. Reactive oxygen species and antioxidants in inflammatory diseases. *Journal of Clinical Periodontology* **24**, 287-296 (1997). https://doi.org:10.1111/j.1600-051X.1997.tb00760.x
5. Blaser, H., Dostert, C., Mak, T. W. & Brenner, D. TNF and ROS Crosstalk in Inflammation. *Trends in Cell Biology* **26**, 249-261 (2016). https://doi.org:https://doi.org/10.1016/j.tcb.2015.12.002
6. Simon, H. U., Haj-Yehia, A. & Levi-Schaffer, F. Role of reactive oxygen species (ROS) in apoptosis induction. *Apoptosis* **5**, 415-418 (2000). https://doi.org:10.1023/A:1009616228304
7. Lo, Y. Y. C., Conquer, J. A., Grinstein, S. & Cruz, T. F. Interleukin-1β induction of c-fos and collagenase expression in articular chondrocytes: Involvement of reactive oxygen species. *Journal of cellular biochemistry* **69**, 19-29 (1998).
8. Lepetsos, P. & Papavassiliou, A. G. ROS/oxidative stress signaling in osteoarthritis. *Biochimica et Biophysica Acta (BBA) - Molecular Basis of Disease* **1862**, 576-591 (2016). https://doi.org:https://doi.org/10.1016/j.bbadis.2016.01.003
9. Loeser, R. F. Aging and osteoarthritis. *Current opinion in rheumatology* **23**, 492-496 (2011). https://doi.org:10.1097/BOR.0b013e3283494005
10. Izzotti, A., Bagnis, A. & Saccà, S. C. The role of oxidative stress in glaucoma. *Mutation Research/Reviews in Mutation Research* **612**, 105-114 (2006). https://doi.org:https://doi.org/10.1016/j.mrrev.2005.11.001
11. Tezel, G. Oxidative stress in glaucomatous neurodegeneration: Mechanisms and consequences. *Progress in Retinal and Eye Research* **25**, 490-513 (2006). https://doi.org:https://doi.org/10.1016/j.preteyeres.2006.07.003
12. Newsholme, P., Cruzat, V. F., Keane, K. N., Carlessi, R. & de Bittencourt, P. I. H., Jr. Molecular mechanisms of ROS production and oxidative stress in diabetes. *Biochemical Journal* **473**, 4527-4550 (2016). https://doi.org:10.1042/BCJ20160503C
13. Pelicano, H., Carney, D. & Huang, P. ROS stress in cancer cells and therapeutic implications. *Drug Resistance Updates* **7**, 97-110 (2004). https://doi.org:https://doi.org/10.1016/j.drup.2004.01.004
14. Bonomini, F., Tengattini, S., Fabiano, A., Bianchi, R. & Rezzani, R. (Murcia : F. Hernández, 2008).
15. Gordon, M. H. Dietary antioxidants in disease prevention. *Nat Prod Rep* **13**, 265-273 (1996).
16. Forman, H. J. & Zhang, H. Targeting oxidative stress in disease: promise and limitations of antioxidant therapy. *Nature Reviews Drug Discovery* **20**, 689-709 (2021). https://doi.org:10.1038/s41573-021-00233-1

17. Beckman, J. S. *et al.* Superoxide Dismutase and Catalase Conjugated to Polyethylene Glycol Increases Endothelial Enzyme Activity and Oxidant Resistance. *The Journal of Biological Chemistry* **263**, 6884-6892 (1987).
18. Poole, K. M. *et al.* ROS-responsive microspheres for on demand antioxidant therapy in a model of diabetic peripheral arterial disease. *Biomaterials* **41**, 166-175 (2015). https://doi.org:https://doi.org/10.1016/j.biomaterials.2014.11.016
19. Rajkovic, O. *et al.* Reactive Oxygen Species-Responsive Nanoparticles for the Treatment of Ischemic Stroke. *Advanced Therapeutics* **2**, 1900038 (2019). https://doi.org:https://doi.org/10.1002/adtp.201900038
20. Wang, Y. *et al.* Targeted Therapy of Atherosclerosis by a Broad-Spectrum Reactive Oxygen Species Scavenging Nanoparticle with Intrinsic Anti-inflammatory Activity. *ACS Nano* **12**, 8943-8960 (2018). https://doi.org:10.1021/acsnano.8b02037
21. Jeanmaire, D. *et al.* Chemical specificity in REDOX-responsive materials: the diverse effects of different Reactive Oxygen Species (ROS) on polysulfide nanoparticles. *Polymer Chemistry* **5**, 1393-1404 (2014).
22. Carampin, P. *et al.* Oxidant-Dependent REDOX Responsiveness of Polysulfides. *Macromolecular Chemistry and Physics* **213**, 2052-2061 (2012). https://doi.org:https://doi.org/10.1002/macp.201200264
23. Patil, P. *et al.* Reactive oxygen species–degradable polythioketal urethane foam dressings to promote porcine skin wound repair. *Science Translational Medicine* **14**, eabm6586 https://doi.org:10.1126/scitranslmed.abm6586
24. DeJulius, C. R. *et al.* Optimizing an Antioxidant TEMPO Copolymer for Reactive Oxygen Species Scavenging and Anti-Inflammatory Effects in Vivo. *Bioconjugate Chemistry* **32**, 928-941 (2021). https://doi.org:10.1021/acs.bioconjchem.1c00081
25. Bi, W. *et al.* Novel TEMPO-PEG-RGDs Conjugates Remediate Tissue Damage Induced by Acute Limb Ischemia/Reperfusion. *Journal of Medicinal Chemistry* **55**, 4501-4505 (2012). https://doi.org:10.1021/jm201381w
26. Napoli, A., Valentini, M., Tirelli, N., Müller, M. & Hubbell, J. A. Oxidation-responsive polymeric vesicles. *Nature Materials* **3**, 183-189 (2004). https://doi.org:10.1038/nmat1081
27. Velluto, D., Thomas, S. N., Simeoni, E., Swartz, M. A. & Hubbell, J. A. PEG-b-PPS-b-PEI micelles and PEG-b-PPS/PEG-b-PPS-b-PEI mixed micelles as non-viral vectors for plasmid DNA: Tumor immunotoxicity in B16F10 melanoma. *Biomaterials* **32**, 9839-9847 (2011). https://doi.org:https://doi.org/10.1016/j.biomaterials.2011.08.079
28. Burke, J. A. *et al.* Subcutaneous nanotherapy repurposes the immunosuppressive mechanism of rapamycin to enhance allogeneic islet graft viability. *Nature Nanotechnology* **17**, 319-330 (2022). https://doi.org:10.1038/s41565-021-01048-2
29. O'Grady, K. P. *et al.* Drug-Free ROS Sponge Polymeric Microspheres Reduce Tissue Damage from Ischemic and Mechanical Injury. *ACS Biomaterials Science & Engineering* **4**, 1251-1264 (2018). https://doi.org:10.1021/acsbiomaterials.6b00804
30. DeJulius, C. R. *et al.* Microsphere antioxidant and sustained erythropoietin-R76E release functions cooperate to reduce traumatic optic neuropathy. *Journal of Controlled Release* **329**, 762-773 (2021). https://doi.org:https://doi.org/10.1016/j.jconrel.2020.10.010
31. Champion, J. A., Walker, A. & Mitragotri, S. Role of particle size in phagocytosis of polymeric microspheres. *Pharmaceutical research* **25**, 1815-1821 (2008).
32. Arlington, T. U. o. T. a. (U.S. National Library of Medicine, 2018).
33. Arlington, T. U. o. T. a. (U.S. National Library of Medicine 2019).

34. Pharmaceuticals, M. (U.S. National Library of Medicine, 2008).
35. Matrix Biomed, I. (U.S. National Library of Medicine, 2019).
36. Yoshitomi, T. & Nagasaki, Y. Nitroxyl radical-containing nanoparticles for novel nanomedicine against oxidative stress injury. *Nanomedicine* **6**, 509-518 (2011). https://doi.org:10.2217/nnm.11.13
37. Hu, F., Qi, J., Lu, Y., He, H. & Wu, W. PLGA-based implants for sustained delivery of peptides/proteins: Current status, challenge and perspectives. *Chinese Chemical Letters* **34**, 108250 (2023). https://doi.org:https://doi.org/10.1016/j.cclet.2023.108250
38. Wan, B., Bao, Q. & Burgess, D. Long-acting PLGA microspheres: Advances in excipient and product analysis toward improved product understanding. *Advanced Drug Delivery Reviews* **198**, 114857 (2023). https://doi.org:https://doi.org/10.1016/j.addr.2023.114857
39. Duarte, D. B., Vasko, M. R. & Fehrenbacher, J. C. Models of Inflammation: Carrageenan Air Pouch. *Current Protocols in Pharmacology* **56**, 5.6.1-5.6.8 (2012). https://doi.org:10.1002/0471141755.ph0506s56
40. Zandstra, J. *et al.* Microsphere size influences the foreign body reaction. *Eur Cell Mater* **28**, 335-347 (2014).
41. Maduka, C. V. *et al.* Polylactide degradation activates immune cells by metabolic reprogramming. *Advanced Science* **10**, 2304632 (2023).
42. Maudens, P., Jordan, O. & Allémann, E. Recent advances in intra-articular drug delivery systems for osteoarthritis therapy. *Drug Discovery Today* **23**, 1761-1775 (2018). https://doi.org:10.1016/j.drudis.2018.05.023
43. Gaudana, R., Ananthula, H. K., Parenky, A. & Mitra, A. K. Ocular drug delivery. *The AAPS journal* **12**, 348-360 (2010).
44. Khella, C. M., Asgarian, R., Horvath, J. M., Rolauffs, B. & Hart, M. L. An Evidence-Based Systematic Review of Human Knee Post-Traumatic Osteoarthritis (PTOA): Timeline of Clinical Presentation and Disease Markers, Comparison of Knee Joint PTOA Models and Early Disease Implications. *Int J Mol Sci* **22** (2021).
45. Wojdasiewicz, P., Poniatowski, Ł. A. & Szukiewicz, D. The Role of Inflammatory and Anti-Inflammatory Cytokines in the Pathogenesis of Osteoarthritis. *Mediators of Inflammation* **2014**, 561459 (2014). https://doi.org:10.1155/2014/561459
46. Mitchell, P. G. *et al.* Cloning, expression, and type II collagenolytic activity of matrix metalloproteinase-13 from human osteoarthritic cartilage. *The Journal of Clinical Investigation* **97**, 761-768 (1996). https://doi.org:10.1172/JCI118475
47. Glasson, S. S. *et al.* Deletion of active ADAMTS5 prevents cartilage degradation in a murine model of osteoarthritis. *Nature* **434**, 644-648 (2005). https://doi.org:10.1038/nature03369
48. Knights, A. J. *et al.* Synovial fibroblasts assume distinct functional identities and secrete R-spondin 2 in osteoarthritis. *Annals of the Rheumatic Diseases* **82**, 272 (2023). https://doi.org:10.1136/ard-2022-222773
49. Jeon, O. H. *et al.* Local clearance of senescent cells attenuates the development of post-traumatic osteoarthritis and creates a pro-regenerative environment. *Nature Medicine* **23**, 775-781 (2017). https://doi.org:10.1038/nm.4324
50. Lanas, A., Tornero, J. & Zamorano, J. L. Assessment of gastrointestinal and cardiovascular risk in patients with osteoarthritis who require NSAIDs: the LOGICA study. *Annals of the Rheumatic Diseases* **69**, 1453 (2010). https://doi.org:10.1136/ard.2009.123166
51. Lu, Y. C. S., Evans, C. H. & Grodzinsky, A. J. Effects of short-term glucocorticoid treatment on changes in cartilage matrix degradation and chondrocyte gene expression induced by

mechanical injury and inflammatory cytokines. *Arthritis Research & Therapy* **13**, R142 (2011). https://doi.org:10.1186/ar3456
52. Bajpayee, A. G., Quadir, M. A., Hammond, P. T. & Grodzinsky, A. J. Charge based intra-cartilage delivery of single dose dexamethasone using Avidin nano-carriers suppresses cytokine-induced catabolism long term. *Osteoarthritis and Cartilage* **24**, 71-81 (2016). https://doi.org:https://doi.org/10.1016/j.joca.2015.07.010
53. Huebner, K. D., Shrive, N. G. & Frank, C. B. Dexamethasone inhibits inflammation and cartilage damage in a new model of post-traumatic osteoarthritis. *Journal of Orthopaedic Research* **32**, 566-572 (2014). https://doi.org:10.1002/jor.22568
54. Sinusas, K. Osteoarthritis: Diagnosis and Treatment. *American Family Physician* **85**, 49-56 (2012).
55. McAlindon, T. E. *et al.* Effect of Intra-articular Triamcinolone vs Saline on Knee Cartilage Volume and Pain in Patients With Knee Osteoarthritis: A Randomized Clinical Trial. *JAMA* **317**, 1967-1975 (2017). https://doi.org:10.1001/jama.2017.5283
56. Macfarlane, E. *et al.* Deletion of the chondrocyte glucocorticoid receptor attenuates cartilage degradation through suppression of early synovial activation in murine posttraumatic osteoarthritis. *Osteoarthritis and Cartilage* (2023).
57. Cooper, C. *et al.* Use of Intraarticular Hyaluronic Acid in the Management of Knee Osteoarthritis in Clinical Practice. *Arthritis Care & Research* **69**, 1287-1296 (2017). https://doi.org:https://doi.org/10.1002/acr.23204
58. O'Connell, B., Wragg, N. M. & Wilson, S. L. The use of PRP injections in the management of knee osteoarthritis. *Cell and Tissue Research* **376**, 143-152 (2019). https://doi.org:10.1007/s00441-019-02996-x
59. Shariatzadeh, M., Song, J. & Wilson, S. L. The efficacy of different sources of mesenchymal stem cells for the treatment of knee osteoarthritis. *Cell Tissue Res* **378**, 399-410 (2019). https://doi.org:10.1007/s00441-019-03069-9
60. Katz, J. N. Total joint replacement in osteoarthritis. *Best Practice & Research Clinical Rheumatology* **20**, 145-153 (2006). https://doi.org:https://doi.org/10.1016/j.berh.2005.09.003
61. Ong, K. L., Runa, M., Lau, E. & Altman, R. D. Cost-of-illness of knee osteoarthritis: potential cost savings by not undergoing arthroplasty within the first 2 years. *Clinicoecon Outcomes Res* **11**, 245-255 (2019). https://doi.org:10.2147/CEOR.S170119
62. Wrzaczek, M., Brosché, M. & Kangasjärvi, J. ROS signaling loops — production, perception, regulation. *Current Opinion in Plant Biology* **16**, 575-582 (2013). https://doi.org:https://doi.org/10.1016/j.pbi.2013.07.002
63. Yin, W., Park, J.-I. & Loeser, R. F. Oxidative stress inhibits insulin-like growth factor-I induction of chondrocyte proteoglycan synthesis through differential regulation of phosphatidylinositol 3-Kinase-Akt and MEK-ERK MAPK signaling pathways. *Journal of Biological Chemistry* **284**, 31972-31981 (2009).
64. Yu, S.-M. & Kim, S.-J. The thymoquinone-induced production of reactive oxygen species promotes dedifferentiation through the ERK pathway and inflammation through the p38 and PI3K pathways in rabbit articular chondrocytes. *Int J Mol Med* **35**, 325-332 (2015).
65. Lo, Y. Y. C., Wong, J. M. S. & Cruz, T. F. Reactive oxygen species mediate cytokine activation of c-Jun NH2-terminal kinases. *Journal of Biological Chemistry* **271**, 15703-15707 (1996).

66. Tham, Y.-C. *et al.* Global Prevalence of Glaucoma and Projections of Glaucoma Burden through 2040: A Systematic Review and Meta-Analysis. *Ophthalmology* **121**, 2081-2090 (2014). https://doi.org:https://doi.org/10.1016/j.ophtha.2014.05.013
67. Calkins, D. J. & Horner, P. J. The Cell and Molecular Biology of Glaucoma: Axonopathy and the Brain. *Investigative Ophthalmology & Visual Science* **53**, 2482-2484 (2012). https://doi.org:10.1167/iovs.12-9483i
68. Nuzzi, R. & Tridico, F. Glaucoma: biological trabecular and neuroretinal pathology with perspectives of therapy innovation and preventive diagnosis. *Frontiers in Neuroscience* **11**, 494 (2017).
69. Downs, J. C., Roberts, M. D. & Burgoyne, C. F. The mechanical environment of the optic nerve head in glaucoma. *Optometry and vision science: official publication of the American Academy of Optometry* **85**, 425 (2008).
70. Mozaffarieh, M. & Flammer, J. Is there more to glaucoma treatment than lowering IOP? *Survey of ophthalmology* **52**, S174-S179 (2007).
71. Weinreb, R. N. & Khaw, P. T. Primary open-angle glaucoma. *The Lancet* **363**, 1711-1720 (2004). https://doi.org:https://doi.org/10.1016/S0140-6736(04)16257-0
72. Wright, C., Tawfik, M. A., Waisbourd, M. & Katz, L. J. Primary angle-closure glaucoma: an update. *Acta Ophthalmologica* **94**, 217-225 (2016). https://doi.org:https://doi.org/10.1111/aos.12784
73. Weinreb, R. N., Aung, T. & Medeiros, F. A. The Pathophysiology and Treatment of Glaucoma: A Review. *JAMA* **311**, 1901-1911 (2014). https://doi.org:10.1001/jama.2014.3192
74. Denis, P., Lafuma, A., Khoshnood, B., Mimaud, V. & Berdeaux, G. A meta-analysis of topical prostaglandin analogues intra-ocular pressure lowering in glaucoma therapy. *Current Medical Research and Opinion* **23**, 601-608 (2007). https://doi.org:10.1185/030079907X178720
75. Odberg, T. & Sandvik, L. The medium and long-term efficacy of primary argon laser trabeculoplasty in avoiding topical medication in open angle glaucoma. *Acta Ophthalmologica Scandinavica* **77**, 176-181 (1999).
76. Mills, K. B. Trabeculectomy: a retrospective long-term follow-up of 444 cases. *British Journal of Ophthalmology* **65**, 790-795 (1981).
77. McKinnon, S. J., Goldberg, L. D., Peeples, P., Walt, J. G. & Bramley, T. J. Current management of glaucoma and the need for complete therapy. *Am J Manag Care* **14**, S20-S27 (2008).
78. Moreno, M. C. *et al.* Retinal oxidative stress induced by high intraocular pressure. *Free Radical Biology and Medicine* **37**, 803-812 (2004).
79. Ko, M.-L., Peng, P.-H., Ma, M.-C., Ritch, R. & Chen, C.-F. Dynamic changes in reactive oxygen species and antioxidant levels in retinas in experimental glaucoma. *Free Radical Biology and Medicine* **39**, 365-373 (2005).
80. Izzotti, A., Saccà, S. C., Cartiglia, C. & De Flora, S. Oxidative deoxyribonucleic acid damage in the eyes of glaucoma patients. *The American journal of medicine* **114**, 638-646 (2003).
81. Saccà, S. C., Pascotto, A., Camicione, P., Capris, P. & Izzotti, A. Oxidative DNA damage in human trabecular meshwork and its correlation with intraocular pressure and visual field in primary open angle glaucoma. *Arch Ophthalmol* **123**, 458-463 (2005).
82. Kahn, M. G., Giblin, F. J. & Epstein, D. L. Glutathione in calf trabecular meshwork and its relation to aqueous humor outflow facility. *Investigative ophthalmology & visual science* **24**, 1283-1287 (1983).

83. Luthra, A., Gupta, N., Kaufman, P. L., Weinreb, R. N. & Yücel, Y. H. Oxidative injury by peroxynitrite in neural and vascular tissue of the lateral geniculate nucleus in experimental glaucoma. *Experimental eye research* **80**, 43-49 (2005).
84. Tezel, G. l. n., Yang, X. & Cai, J. Proteomic identification of oxidatively modified retinal proteins in a chronic pressure-induced rat model of glaucoma. *Investigative ophthalmology & visual science* **46**, 3177-3187 (2005).
85. D'Autréaux, B. & Toledano, M. B. ROS as signalling molecules: mechanisms that generate specificity in ROS homeostasis. *Nature Reviews Molecular Cell Biology* **8**, 813-824 (2007). https://doi.org:10.1038/nrm2256
86. El-Mohtadi, F., d'Arcy, R. & Tirelli, N. Oxidation-Responsive Materials: Biological Rationale, State of the Art, Multiple Responsiveness, and Open Issues. *Macromolecular Rapid Communications* **40**, 1800699 (2019). https://doi.org:10.1002/marc.201800699
87. Bauerova, K. & Bezek, S. Role of reactive oxygen and nitrogen species in etiopathogenesis of rheumatoid arthritis. *General physiology and biophysics* **18**, 15-20 (2000).
88. McCord, J. M. & Fridovich, I. Superoxide Dismutase: An Enzymatic Function for Erythrocuprein (Hemocuprein). *The Journal of Biological Chemistry* **244**, 6049-6055 (1969).
89. Trnka, J., Blaikie, F. H., Smith, R. A. J. & Murphy, M. P. A mitochondria-targeted nitroxide is reduced to its hydroxylamine by ubiquinol in mitochondria. *Free Radical Biology and Medicine* **44**, 1406-1419 (2008). https://doi.org:https://doi.org/10.1016/j.freeradbiomed.2007.12.036
90. Ni, R. *et al.* Therapeutic inhibition of mitochondrial reactive oxygen species with mito-TEMPO reduces diabetic cardiomyopathy. *Free Radical Biology and Medicine* **90**, 12-23 (2016). https://doi.org:https://doi.org/10.1016/j.freeradbiomed.2015.11.013
91. Dikalova, A. E. *et al.* Therapeutic targeting of mitochondrial superoxide in hypertension. *Circ Res* **107**, 106-116 (2010). https://doi.org:10.1161/CIRCRESAHA.109.214601
92. Du, K., Farhood, A. & Jaeschke, H. Mitochondria-targeted antioxidant Mito-Tempo protects against acetaminophen hepatotoxicity. *Archives of Toxicology* **91**, 761-773 (2017). https://doi.org:10.1007/s00204-016-1692-0
93. Zhang, J. *et al.* MitoTEMPO Prevents Oxalate Induced Injury in NRK-52E Cells via Inhibiting Mitochondrial Dysfunction and Modulating Oxidative Stress. *Oxidative Medicine and Cellular Longevity* **2017**, 7528090 (2017). https://doi.org:10.1155/2017/7528090
94. Liu, Y., Wang, Y., Ding, W. & Wang, Y. Mito-TEMPO Alleviates Renal Fibrosis by Reducing Inflammation, Mitochondrial Dysfunction, and Endoplasmic Reticulum Stress. *Oxidative Medicine and Cellular Longevity* **2018**, 5828120 (2018). https://doi.org:10.1155/2018/5828120
95. Eberhardt, M., Mruk, R., Zentel, R. & Théato, P. Synthesis of pentafluorophenyl(meth)acrylate polymers: New precursor polymers for the synthesis of multifunctional materials. *European Polymer Journal* **41**, 1569-1575 (2005). https://doi.org:https://doi.org/10.1016/j.eurpolymj.2005.01.025
96. Yoshitomi, T., Kuramochi, K., Binh Vong, L. & Nagasaki, Y. Development of nitroxide radicals-containing polymer for scavenging reactive oxygen species from cigarette smoke. *Sci Technol Adv Mater* **15**, 035002-035002 (2014). https://doi.org:10.1088/1468-6996/15/3/035002

97. Yoshitomi, T., Miyamoto, D. & Nagasaki, Y. Design of Core−Shell-Type Nanoparticles Carrying Stable Radicals in the Core. *Biomacromolecules* **10**, 596-601 (2009). https://doi.org:10.1021/bm801278n
98. Voest, E. E., Faassen, E. v. & Marx, J. J. M. An electron paramagnetic resonance study of the antioxidant properties of the nitroxide free radical tempo. *Free Radical Biology and Medicine* **15**, 589-595 (1993). https://doi.org:https://doi.org/10.1016/0891-5849(93)90161-M
99. Berliner, L. J., Khramtsov, V., Fujii, H. & Clanton, T. L. Unique in vivo applications of spin traps. *Free Radical Biology and Medicine* **30**, 489-499 (2001). https://doi.org:https://doi.org/10.1016/S0891-5849(00)00491-3
100. Yoshida, E. & Tanaka, T. Oxidation-induced micellization of a diblock copolymer containing stable nitroxyl radicals. *Colloid and Polymer Science* **285**, 135-144 (2006). https://doi.org:10.1007/s00396-006-1529-0
101. Benzie, I. F. F. & Strain, J. J. The Ferric Reducing Ability of Plasma (FRAP) as a Measure of "Antioxidant Power": The FRAP Assay. *Analytical Biochemistry* **239**, 70-76 (1996). https://doi.org:https://doi.org/10.1006/abio.1996.0292
102. Yoshitomi, T., Yamaguchi, Y., Kikuchi, A. & Nagasaki, Y. Creation of a blood-compatible surface: A novel strategy for suppressing blood activation and coagulation using a nitroxide radical-containing polymer with reactive oxygen species scavenging activity. *Acta Biomaterialia* **8**, 1323-1329 (2012). https://doi.org:https://doi.org/10.1016/j.actbio.2011.11.029
103. Dikalov, S. I., Dikalova, A. E., Morozov, D. A. & Kirilyuk, I. A. Cellular accumulation and antioxidant activity of acetoxymethoxycarbonyl pyrrolidine nitroxides. *Free radical research* **52**, 339-350 (2018).
104. Luxenhofer, R. *et al.* Structure-property relationship in cytotoxicity and cell uptake of poly(2-oxazoline) amphiphiles. *Journal of Controlled Release* **153**, 73-82 (2011). https://doi.org:https://doi.org/10.1016/j.jconrel.2011.04.010
105. Batrakova, E. V., Li, S., Alakhov, V. Y., Miller, D. W. & Kabanov, A. V. Optimal Structure Requirements for Pluronic Block Copolymers in Modifying P-glycoprotein Drug Efflux Transporter Activity in Bovine Brain Microvessel Endothelial Cells. *Journal of Pharmacology and Experimental Therapeutics* **304**, 845 (2003). https://doi.org:10.1124/jpet.102.043307
106. Dailing, E. A. *et al.* Modifying Cell Membranes with Anionic Polymer Amphiphiles Potentiates Intracellular Delivery of Cationic Peptides. *ACS Appl. Mater. Interfaces* **12**, 50222-50235 (2020). https://doi.org:10.1021/acsami.0c13304
107. Swartz, H. M., Sentjurc, M. & Morse, P. D. Cellular metabolism of water-soluble nitroxides: Effect on rate of reduction of cell/nitroxide ratio, oxygen concentrations and permeability of nitroxides. *Biochimica et Biophysica Acta (BBA) - Molecular Cell Research* **888**, 82-90 (1986). https://doi.org:https://doi.org/10.1016/0167-4889(86)90073-X
108. Thirunavukkarasu, C., Watkins, S., Harvey, S. A. K. & Gandhi, C. R. Superoxide-induced apoptosis of activated rat hepatic stellate cells. *Journal of Hepatology* **41**, 567-575 (2004). https://doi.org:https://doi.org/10.1016/j.jhep.2004.06.023
109. Jameel, N. M. *et al.* p38-MAPK- and caspase-3-mediated superoxide-induced apoptosis of rat hepatic stellate cells: Reversal by retinoic acid. *Journal of Cellular Physiology* **218**, 157-166 (2009). https://doi.org:10.1002/jcp.21581

110. Gergel, D., Misik, V., Ondrias, K. & Cederbaum, A. I. Increased Cytotoxicity of 3-Morpholinosydnonimine to HepG2 Cells in the Presence of Superoxide Dismutase. *The Journal of Biological Chemistry* **270**, 20922-20929 (1995).
111. Martin-Romero, F. J., Gutiérrez-Martin, Y., Henao, F. & Gutiérrez-Merino, C. Fluorescence measurements of steady state peroxynitrite production upon SIN-1 decomposition: NADH versus dihydrodichlorofluorescein and dihydrorhodamine 123. *Journal of fluorescence* **14**, 17-23 (2004).
112. Kim, Y., Choi, Y., Ham, H., Jeong, H.-S. & Lee, J. Protective effects of oligomeric and polymeric procyanidin fractions from defatted grape seeds on tert-butyl hydroperoxide-induced oxidative damage in HepG2 cells. *Food Chemistry* **137**, 136-141 (2013). https://doi.org:https://doi.org/10.1016/j.foodchem.2012.10.006
113. Chen, H.-M. & Yan, X.-J. Antioxidant activities of agaro-oligosaccharides with different degrees of polymerization in cell-based system. *Biochimica et Biophysica Acta (BBA) - General Subjects* **1722**, 103-111 (2005). https://doi.org:https://doi.org/10.1016/j.bbagen.2004.11.016
114. Chelombitko, M. A. *et al.* Comparison of the Effects of Mitochondria-Targeted Antioxidant 10-(6'-Plastoquinonyl)Decyltriphenylphosphonium Bromide (SkQ1) and a Fragment of its Molecule Dodecyltriphenylphosphonium on Carrageenan-Induced Acute Inflammation in Mouse Model of Subcuteneous Air Pouch. *Bulletin of Experimental Biology and Medicine* **162**, 730-733 (2017). https://doi.org:10.1007/s10517-017-3699-9
115. Sunita, P., Jha, S. & Pattanayak, S. P. Anti-inflammatory and in-vivo Antioxidant activities of Cressa cretica Linn., a halophytic plant. *Middle-East Journal of Scientific Research* **8**, 129-140 (2011).
116. Menshchikova, E. B., Zenkov, N. K., Tkachev, V. O., Lemza, A. E. & Kandalintseva, N. V. Protective Effect of ARE-Inducing Phenol Antioxidant TS-13 in Chronic Inflammation. *Bulletin of Experimental Biology and Medicine* **155**, 330-334 (2013). https://doi.org:10.1007/s10517-013-2146-9
117. El-Achkar, G. A. *et al.* Heme oxygenase-1—Dependent anti-inflammatory effects of atorvastatin in zymosan-injected subcutaneous air pouch in mice. *PloS one* **14** (2019).
118. Mathew, G. *et al.* A novel synthetic small molecule DMFO targets Nrf2 in modulating proinflammatory/antioxidant mediators to ameliorate inflammation. *Free Radical Research* **52**, 1140-1157 (2018). https://doi.org:10.1080/10715762.2018.1533636
119. Komarov, A. M., Joseph, J. & Lai, C.-S. In vivo pharmacokinetics of nitroxides in mice. *Biochemical and biophysical research communications* **201**, 1035-1042 (1994).
120. Uddin, M. J. *et al.* Fluorocoxib A loaded nanoparticles enable targeted visualization of cyclooxygenase-2 in inflammation and cancer. *Biomaterials* **92**, 71-80 (2016). https://doi.org:https://doi.org/10.1016/j.biomaterials.2016.03.028
121. Tan, J., Deng, Z., Liu, G., Hu, J. & Liu, S. Anti-inflammatory polymersomes of redox-responsive polyprodrug amphiphiles with inflammation-triggered indomethacin release characteristics. *Biomaterials* **178**, 608-619 (2018). https://doi.org:https://doi.org/10.1016/j.biomaterials.2018.03.035
122. Koziolová, E., Venclíková, K. & Etrych, T. Polymer-drug conjugates in inflammation treatment. *Physiological research* **67** (2018).
123. Yuan, F., Quan, L.-d., Cui, L., Goldring, S. R. & Wang, D. Development of macromolecular prodrug for rheumatoid arthritis. *Advanced Drug Delivery Reviews* **64**, 1205-1219 (2012). https://doi.org:https://doi.org/10.1016/j.addr.2012.03.006

124. Maeda, H., Wu, J., Sawa, T., Matsumura, Y. & Hori, K. Tumor vascular permeability and the EPR effect in macromolecular therapeutics: a review. *Journal of Controlled Release* **65**, 271-284 (2000). https://doi.org:https://doi.org/10.1016/S0168-3659(99)00248-5
125. Maeda, H. Vascular permeability in cancer and infection as related to macromolecular drug delivery, with emphasis on the EPR effect for tumor-selective drug targeting. *Proceedings of the Japan Academy, Series B* **88**, 53-71 (2012).
126. Chedid, P. *et al.* Vasoactive intestinal peptide dampens formyl-peptide-induced ROS production and inflammation by targeting a MAPK-p47phox phosphorylation pathway in monocytes. *Mucosal Immunology* **10**, 332-340 (2017). https://doi.org:10.1038/mi.2016.51
127. Dragojevic-Simic, V. *et al.* ANTI-INFLAMMATORY ACTIVITY OF FULLERENOL C 60 (OH) 24 NANO-PARTICLES IN A MODEL OF ACUTE INFLAMMATION IN RATS. *Digest Journal of Nanomaterials & Biostructures (DJNB)* **6** (2011).
128. Ik, A. *et al.* Anti-inflammatory, antioxidant and antimicrobial activity of the stem bark extract and fractions of Ficus exasperata Vahl.(Moraceae). *Journal of Pharmacognosy and phytochemistry* **2**, 38-44 (2013).
129. Pua, M. L., Yoshitomi, T., Chonpathompikunlert, P., Hirayama, A. & Nagasaki, Y. Redox-active injectable gel using thermo-responsive nanoscale polyion complex flower micelle for noninvasive treatment of local inflammation. *Journal of Controlled Release* **172**, 914-920 (2013). https://doi.org:https://doi.org/10.1016/j.jconrel.2013.10.009
130. Wu, M. *et al.* Glutaraldehyde-polymerized hemoglobin and tempol (PolyHb-tempol) has superoxide dismutase activity that can attenuate oxidative stress on endothelial cells induced by superoxide anion. *Artificial Cells, Nanomedicine, and Biotechnology* **46**, 47-55 (2018). https://doi.org:10.1080/21691401.2017.1328685
131. Parhiz, H. *et al.* Unintended effects of drug carriers: Big issues of small particles. *Advanced drug delivery reviews* **130**, 90-112 (2018). https://doi.org:10.1016/j.addr.2018.06.023
132. Jackson, M. A. *et al.* Kupffer cell release of platelet activating factor drives dose limiting toxicities of nucleic acid nanocarriers. *Biomaterials* **268**, 120528 (2021). https://doi.org:https://doi.org/10.1016/j.biomaterials.2020.120528
133. Fridovich, I. Quantitative Aspects of the Production of Superoxide Anion Radical by Milk Xanthine Oxidase. *The Journal of Biological Chemistry* **245**, 4053-4057 (1970).
134. Vaughan, J. C., Dempsey, G. T., Sun, E. & Zhuang, X. Phosphine quenching of cyanine dyes as a versatile tool for fluorescence microscopy. *Journal of the American Chemical Society* **135**, 1197-1200 (2013).
135. Jackson, M. A. *et al.* Zwitterionic Nanocarrier Surface Chemistry Improves siRNA Tumor Delivery and Silencing Activity Relative to Polyethylene Glycol. *ACS Nano* **11**, 5680-5696 (2017). https://doi.org:10.1021/acsnano.7b01110
136. Zhang, Y., Huo, M., Zhou, J. & Xie, S. PKSolver: An add-in program for pharmacokinetic and pharmacodynamic data analysis in Microsoft Excel. *Computer Methods and Programs in Biomedicine* **99**, 306-314 (2010). https://doi.org:https://doi.org/10.1016/j.cmpb.2010.01.007
137. Liu, W. F. *et al.* Real-time in vivo detection of biomaterial-induced reactive oxygen species. *Biomaterials* **32**, 1796-1801 (2011). https://doi.org:https://doi.org/10.1016/j.biomaterials.2010.11.029
138. Langer, R. & Folkman, J. Polymers for the sustained release of proteins and other macromolecules. *Nature* **263**, 797-800 (1976). https://doi.org:10.1038/263797a0

139. Khan, A. *et al.* Sustained Polymeric Delivery of Gene Silencing Antisense ODNs, siRNA, DNAzymes and Ribozymes: In Vitro and In Vivo Studies. *Journal of Drug Targeting* **12**, 393-404 (2004). https://doi.org:10.1080/10611860400003858
140. Morlock, M., Koll, H., Winter, G. & Kissel, T. Microencapsulation of rh-erythropoietin, using biodegradable poly(d,l-lactide-co-glycolide): protein stability and the effects of stabilizing excipients. *European Journal of Pharmaceutics and Biopharmaceutics* **43**, 29-36 (1997). https://doi.org:https://doi.org/10.1016/S0939-6411(96)00017-3
141. Ye, M., Kim, S. & Park, K. Issues in long-term protein delivery using biodegradable microparticles. *Journal of Controlled Release* **146**, 241-260 (2010). https://doi.org:https://doi.org/10.1016/j.jconrel.2010.05.011
142. Mountziaris, P. M. *et al.* Intra-articular controlled release of anti-inflammatory siRNA with biodegradable polymer microparticles ameliorates temporomandibular joint inflammation. *Acta Biomaterialia* **8**, 3552-3560 (2012). https://doi.org:https://doi.org/10.1016/j.actbio.2012.06.031
143. Garland, K. M. *et al.* Microparticle Depots for Controlled and Sustained Release of Endosomolytic Nanoparticles. *Cellular and Molecular Bioengineering* **12**, 429-442 (2019). https://doi.org:10.1007/s12195-019-00571-6
144. Liu, C. D., Tu, X. F. & Chen, F. Neovascularization by Sustained Delivery of G-CSF, EPO and VEGF Using Dextran/PLGA Microspheres. *Annals of Vascular Surgery* **64**, 328-338 (2020). https://doi.org:https://doi.org/10.1016/j.avsg.2019.10.033
145. Ciombor, D. M. *et al.* Encapsulation of BSA using a modified W/O/O emulsion solvent removal method. *Journal of microencapsulation* **23**, 183-194 (2006).
146. Mylonaki, I., Allémann, E., Delie, F. & Jordan, O. Imaging the porous structure in the core of degrading PLGA microparticles: the effect of molecular weight. *Journal of Controlled Release* **286**, 231-239 (2018).
147. Bhaskar, S., Pollock, K. M., Yoshida, M. & Lahann, J. Towards Designer Microparticles: Simultaneous Control of Anisotropy, Shape, and Size. *Small* **6**, 404-411 (2010). https://doi.org:10.1002/smll.200901306
148. Baena-Aristizábal, C. M., Fessi, H., Elaissari, A. & Mora-Huertas, C. E. Biodegradable microparticles preparation by double emulsification—Solvent extraction method: A Systematic study. *Colloids and Surfaces A: Physicochemical and Engineering Aspects* **492**, 213-229 (2016). https://doi.org:https://doi.org/10.1016/j.colsurfa.2015.11.067
149. Spenlehauer, G., Vert, M., Benoit, J. P. & Boddaert, A. In vitro and In vivo degradation of poly(D,L lactide/glycolide) type microspheres made by solvent evaporation method. *Biomaterials* **10**, 557-563 (1989). https://doi.org:https://doi.org/10.1016/0142-9612(89)90063-X
150. Hernández-Giottonini, K. Y. *et al.* PLGA nanoparticle preparations by emulsification and nanoprecipitation techniques: Effects of formulation parameters. *Rsc Advances* **10**, 4218-4231 (2020).
151. Rapier, C. E., Shea, K. J. & Lee, A. P. Investigating PLGA microparticle swelling behavior reveals an interplay of expansive intermolecular forces. *Scientific Reports* **11**, 14512 (2021). https://doi.org:10.1038/s41598-021-93785-6
152. Yang, Y. *et al.* Development of highly porous large PLGA microparticles for pulmonary drug delivery. *Biomaterials* **30**, 1947-1953 (2009).
153. Bedingfield, S. K. *et al.* Top-Down Fabricated microPlates for Prolonged, Intra-articular Matrix Metalloproteinase 13 siRNA Nanocarrier Delivery to Reduce Post-traumatic

Osteoarthritis. *ACS Nano* **15**, 14475-14491 (2021). https://doi.org:10.1021/acsnano.1c04005
154. Di Francesco, M. *et al.* Shape-Defined microPlates for the Sustained Intra-articular Release of Dexamethasone in the Management of Overload-Induced Osteoarthritis. *ACS Appl. Mater. Interfaces* **13**, 31379-31392 (2021). https://doi.org:10.1021/acsami.1c02082
155. Pérez-Camargo, R. A. *et al.* Influence of Chain Primary Structure and Topology (Branching) on Crystallization and Thermal Properties: The Case of Polysulfides. *Macromolecules* **52**, 2093-2104 (2019). https://doi.org:10.1021/acs.macromol.8b02659
156. d'Arcy, R., Siani, A., Lallana, E. & Tirelli, N. Influence of Primary Structure on Responsiveness. Oxidative, Thermal, and Thermo-Oxidative Responses in Polysulfides. *Macromolecules* **48**, 8108-8120 (2015). https://doi.org:10.1021/acs.macromol.5b02007
157. Roggero, A., Zotteri, L., Proni, A., Gandini, A. & Mazzei, A. Syntheses and properties of ethylene sulphide-isobutylene sulphide copolymers and their unsaturated terpolymers. *European Polymer Journal* **12**, 837-842 (1976). https://doi.org:https://doi.org/10.1016/0014-3057(76)90127-0
158. Cheng, S. Z. D. & Lotz, B. Enthalpic and entropic origins of nucleation barriers during polymer crystallization: the Hoffman–Lauritzen theory and beyond. *Polymer* **46**, 8662-8681 (2005). https://doi.org:https://doi.org/10.1016/j.polymer.2005.03.125
159. Schliecker, G., Schmidt, C., Fuchs, S., Wombacher, R. & Kissel, T. Hydrolytic degradation of poly (lactide-co-glycolide) films: effect of oligomers on degradation rate and crystallinity. *International journal of pharmaceutics* **266**, 39-49 (2003).
160. Takahashi, Y., Tadokoro, H. & Chatani, Y. Structure of polyethylene sulfide. *Journal of Macromolecular Science, Part B: Physics* **2**, 361-367 (1968).
161. Makadia, H. K. & Siegel, S. J. Poly Lactic-co-Glycolic Acid (PLGA) as Biodegradable Controlled Drug Delivery Carrier. *Polymers* **3**, 1377-1397 (2011).
162. Yoo, J. Y. *et al.* Characterization of degradation behavior for PLGA in various pH condition by simple liquid chromatography method. *Bio-Medical Materials and Engineering* **15**, 279-288 (2005).
163. Siepmann, J., Elkharraz, K., Siepmann, F. & Klose, D. How Autocatalysis Accelerates Drug Release from PLGA-Based Microparticles: A Quantitative Treatment. *Biomacromolecules* **6**, 2312-2319 (2005). https://doi.org:10.1021/bm050228k
164. El Mohtadi, F. *et al.* Main Chain Polysulfoxides as Active 'Stealth' Polymers with Additional Antioxidant and Anti-Inflammatory Behaviour. *Int J Mol Sci* **20** (2019).
165. Siani, A. *et al.* Polysulfide nanoparticles inhibit fibroblast-to-myofibroblast transition via extracellular ROS scavenging and have potential anti-fibrotic properties. *Biomaterials Advances* **153**, 213537 (2023). https://doi.org:https://doi.org/10.1016/j.bioadv.2023.213537
166. Lee, D. *et al.* H2O2-responsive molecularly engineered polymer nanoparticles as ischemia/reperfusion-targeted nanotherapeutic agents. *Scientific Reports* **3**, 2233 (2013). https://doi.org:10.1038/srep02233
167. Jeong, D. *et al.* Porous antioxidant polymer microparticles as therapeutic systems for the airway inflammatory diseases. *Journal of Controlled Release* **233**, 72-80 (2016). https://doi.org:https://doi.org/10.1016/j.jconrel.2016.04.039
168. Ko, E. *et al.* Antioxidant polymeric prodrug microparticles as a therapeutic system for acute liver failure. *Biomaterials* **35**, 3895-3902 (2014). https://doi.org:https://doi.org/10.1016/j.biomaterials.2014.01.048

169. Martins, R. M., Pereira, S. V., Siqueira, S., Salomão, W. F. & Freitas, L. A. P. Curcuminoid content and antioxidant activity in spray dried microparticles containing turmeric extract. *Food Research International* **50**, 657-663 (2013). https://doi.org:https://doi.org/10.1016/j.foodres.2011.06.030
170. Chao, Y. & Shum, H. C. Emerging aqueous two-phase systems: from fundamentals of interfaces to biomedical applications. *Chemical Society Reviews* **49**, 114-142 (2020).
171. Yuan, W., Wu, F., Geng, Y., Xu, S. & Jin, T. Preparation of dextran glassy particles through freezing-induced phase separation. *International journal of pharmaceutics* **339**, 76-83 (2007).
172. Lasne, F., Martin, L., Crepin, N. & de Ceaurriz, J. Detection of isoelectric profiles of erythropoietin in urine: differentiation of natural and administered recombinant hormones. *Analytical Biochemistry* **311**, 119-126 (2002). https://doi.org:https://doi.org/10.1016/S0003-2697(02)00407-4
173. Peng, Z. G., Hidajat, K. & Uddin, M. S. Adsorption of bovine serum albumin on nanosized magnetic particles. *Journal of Colloid and Interface Science* **271**, 277-283 (2004). https://doi.org:https://doi.org/10.1016/j.jcis.2003.12.022
174. Geng, Y. *et al.* Formulating erythropoietin-loaded sustained-release PLGA microspheres without protein aggregation. *Journal of Controlled Release* **130**, 259-265 (2008). https://doi.org:https://doi.org/10.1016/j.jconrel.2008.06.011
175. Rong, X. *et al.* Effects of Erythropoietin-Dextran Microparticle-Based PLGA/PLA Microspheres on RGCs. *Investigative Ophthalmology & Visual Science* **53**, 6025-6034 (2012). https://doi.org:10.1167/iovs.12-9898
176. Rahmani, V., Elshereef, R. & Sheardown, H. Optimizing electrostatic interactions for controlling the release of proteins from anionic and cationically modified alginate. *European Journal of Pharmaceutics and Biopharmaceutics* **117**, 232-243 (2017). https://doi.org:https://doi.org/10.1016/j.ejpb.2017.04.025
177. Pakulska, M. M. *et al.* Encapsulation-free controlled release: Electrostatic adsorption eliminates the need for protein encapsulation in PLGA nanoparticles. *Science Advances* **2**, e1600519 https://doi.org:10.1126/sciadv.1600519
178. Tiourina, O. P. & Sukhorukov, G. B. Multilayer alginate/protamine microsized capsules: encapsulation of α-chymotrypsin and controlled release study. *International Journal of Pharmaceutics* **242**, 155-161 (2002). https://doi.org:https://doi.org/10.1016/S0378-5173(02)00140-0
179. Gulick, T. Transfection Using DEAE-Dextran. *Current Protocols in Molecular Biology* **40**, 9.2.1-9.2.10 (1997). https://doi.org:https://doi.org/10.1002/0471142727.mb0902s40
180. Hoogenboezem, E. N. *et al.* Structural Optimization of siRNA Conjugates for Albumin Binding Achieves Effective MCL1-Targeted Cancer Therapy. *bioRxiv*, 2023.2002.2014.528574 (2023). https://doi.org:10.1101/2023.02.14.528574
181. Raemdonck, K., Vandenbroucke, R. E., Demeester, J., Sanders, N. N. & De Smedt, S. C. Maintaining the silence: reflections on long-term RNAi. *Drug Discovery Today* **13**, 917-931 (2008). https://doi.org:https://doi.org/10.1016/j.drudis.2008.06.008
182. Williford, J.-M. *et al.* Recent Advances in Nanoparticle-Mediated siRNA Delivery. *Annual Review of Biomedical Engineering* **16**, 347-370 (2014). https://doi.org:10.1146/annurev-bioeng-071813-105119
183. Lobovkina, T. *et al.* In Vivo Sustained Release of siRNA from Solid Lipid Nanoparticles. *ACS Nano* **5**, 9977-9983 (2011). https://doi.org:10.1021/nn203745n

184. Jacobson, G. B. *et al.* Biodegradable nanoparticles with sustained release of functional siRNA in skin. *Journal of Pharmaceutical Sciences* **99**, 4261-4266 (2010). https://doi.org:https://doi.org/10.1002/jps.22147
185. Deng, J. *et al.* Anti-Inflammatory Therapy for Temporomandibular Joint Osteoarthritis Using mRNA Medicine Encoding Interleukin-1 Receptor Antagonist. *Pharmaceutics* **14** (2022).
186. Hickerson, R. P. *et al.* Stability study of unmodified siRNA and relevance to clinical use. *Oligonucleotides* **18**, 345-354 (2008).
187. Xu, P.-Y. *et al.* Overcoming multidrug resistance through inhalable siRNA nanoparticles-decorated porous microparticles based on supercritical fluid technology. *International Journal of Nanomedicine* **13**, 4685-4698 (2018). https://doi.org:10.2147/IJN.S169399
188. Segovia, N. *et al.* Hydrogel Doped with Nanoparticles for Local Sustained Release of siRNA in Breast Cancer. *Advanced Healthcare Materials* **4**, 271-280 (2015). https://doi.org:https://doi.org/10.1002/adhm.201400235
189. Shao, X.-R. *et al.* Independent effect of polymeric nanoparticle zeta potential/surface charge, on their cytotoxicity and affinity to cells. *Cell Proliferation* **48**, 465-474 (2015). https://doi.org:https://doi.org/10.1111/cpr.12192
190. Osborn, M. F. & Khvorova, A. Improving siRNA delivery in vivo through lipid conjugation. *Nucleic acid therapeutics* **28**, 128-136 (2018).
191. Lai, Y.-F. *et al.* Erythropoietin in Optic Neuropathies: Current Future Strategies for Optic Nerve Protection and Repair. *Int J Mol Sci* **23** (2022).
192. Naguib, S. *et al.* Intraocular Sustained Release of EPO-R76E Mitigates Glaucoma Pathogenesis by Activating the NRF2/ARE Pathway. *Antioxidants* **12** (2023).
193. Wang, M. *et al.* MMP13 is a critical target gene during the progression of osteoarthritis. *Arthritis Research & Therapy* **15**, R5 (2013). https://doi.org:10.1186/ar4133
194. Chen, Y. H., Chou, C. H., Haraden, C., Attarian, D. & Kraus, V. B. Senescence in osteoarthritis. *Osteoarthritis and Cartilage* **27**, S94 (2019).
195. Bedingfield, S. K. *et al.* Amelioration of post-traumatic osteoarthritis via nanoparticle depots delivering small interfering RNA to damaged cartilage. *Nature Biomedical Engineering* **5**, 1069-1083 (2021). https://doi.org:10.1038/s41551-021-00780-3
196. Colazo, J. M. *et al.* Albumin-binding RNAi Conjugate for Carrier Free Treatment of Arthritis. *bioRxiv*, 2023.2005.2031.542971 (2023). https://doi.org:10.1101/2023.05.31.542971
197. Diekman, B. O. *et al.* Expression of p16INK4a is a biomarker of chondrocyte aging but does not cause osteoarthritis. *Aging Cell* **17**, e12771 (2018). https://doi.org:https://doi.org/10.1111/acel.12771
198. Borodkina, A. V., Deryabin, P. I. & Nikolsky, N. N. "Social life" of senescent cells: what is SASP and why study it? *Acta Naturae (англоязычная версия)* **10**, 4-14 (2018).
199. Lane, N. *et al.* A phase 2, randomized, double-blind, placebo-controlled study of senolytic molecule UBX0101 in the treatment of painful knee osteoarthritis. *Osteoarthritis and Cartilage* **29**, S52-S53 (2021).
200. Baker, D. J., Jin, F. & Van Deursen, J. M. The yin and yang of the Cdkn2a locus in senescence and aging. *Cell cycle* **7**, 2795-2802 (2008).
201. Sappington, R. M., Carlson, B. J., Crish, S. D. & Calkins, D. J. The microbead occlusion model: a paradigm for induced ocular hypertension in rats and mice. *Investigative ophthalmology & visual science* **51**, 207-216 (2010).

202. Grasso, G. *et al.* Neuroprotection by erythropoietin administration after experimental traumatic brain injury. *Brain Research* **1182**, 99-105 (2007). https://doi.org:https://doi.org/10.1016/j.brainres.2007.08.078
203. Zhong, L. *et al.* Erythropoietin Promotes Survival of Retinal Ganglion Cells in DBA/2J Glaucoma Mice. *Investigative Ophthalmology & Visual Science* **48**, 1212-1218 (2007). https://doi.org:10.1167/iovs.06-0757
204. Zhang, W. *et al.* A sequential delivery system employing the synergism of EPO and NGF promotes sciatic nerve repair. *Colloids and Surfaces B: Biointerfaces* **159**, 327-336 (2017). https://doi.org:https://doi.org/10.1016/j.colsurfb.2017.07.088
205. Zhang, W. *et al.* Localized and Sustained Delivery of Erythropoietin from PLGA Microspheres Promotes Functional Recovery and Nerve Regeneration in Peripheral Nerve Injury. *BioMed Research International* **2015**, 478103 (2015). https://doi.org:10.1155/2015/478103
206. Lambert, W. S. *et al.* Towards A Microbead Occlusion Model of Glaucoma for a Non-Human Primate. *Scientific Reports* **9**, 11572 (2019). https://doi.org:10.1038/s41598-019-48054-y
207. Qutachi, O. *et al.* Improved delivery of PLGA microparticles and microparticle-cell scaffolds in clinical needle gauges using modified viscosity formulations. *International Journal of Pharmaceutics* **546**, 272-278 (2018). https://doi.org:https://doi.org/10.1016/j.ijpharm.2018.05.025
208. Vijayakumar, R., Aboody, M. S. A., Alturaiki, W. & Sandle, T. Review on endotoxin mediated toxic anterior segment syndrome (TASS) in ophthalmic products—outbreaks, product recall and testing limits. *EJPPS-Phss* **22**, 1-6 (2016).
209. Sharma, A., Kumar, N., Kuppermann, B. D., Bandello, F. & Loewenstein, A. Ophthalmic biosimilars and biologics—role of endotoxins. *Eye* **34**, 614-615 (2020). https://doi.org:10.1038/s41433-019-0636-3
210. Christiansen, B. A. *et al.* Musculoskeletal changes following non-invasive knee injury using a novel mouse model of post-traumatic osteoarthritis. *Osteoarthritis and Cartilage* **20**, 773-782 (2012). https://doi.org:https://doi.org/10.1016/j.joca.2012.04.014
211. Wang, Z. *et al.* Reactive oxygen species-scavenging nanoparticles coated with chondroitin sulfate protect cartilage against osteoarthritis in vivo. *Nano Research* **16**, 2786-2797 (2023). https://doi.org:10.1007/s12274-022-4934-x
212. Zhang, H. *et al.* Reactive oxygen species-responsive and scavenging polyurethane nanoparticles for treatment of osteoarthritis in vivo. *Chemical Engineering Journal* **409**, 128147 (2021). https://doi.org:https://doi.org/10.1016/j.cej.2020.128147
213. Crivelli, B. *et al.* Silk fibroin nanoparticles for celecoxib and curcumin delivery: ROS-scavenging and anti-inflammatory activities in an in vitro model of osteoarthritis. *European Journal of Pharmaceutics and Biopharmaceutics* **137**, 37-45 (2019). https://doi.org:https://doi.org/10.1016/j.ejpb.2019.02.008
214. Sies, H. Hydrogen peroxide as a central redox signaling molecule in physiological oxidative stress: Oxidative eustress. *Redox Biology* **11**, 613-619 (2017). https://doi.org:https://doi.org/10.1016/j.redox.2016.12.035
215. Lin, C.-H. *et al.* A protocol to inject ocular drug implants into mouse eyes. *STAR Protocols* **3**, 101143 (2022). https://doi.org:https://doi.org/10.1016/j.xpro.2022.101143
216. Kang, J., Kaczmarek, O., Liebscher, J. & Dähne, L. Prevention of H-Aggregates Formation in Cy5 Labeled Macromolecules. *International Journal of Polymer Science* **2010**, 264781 (2010). https://doi.org:10.1155/2010/264781

217. Pradal, J. *et al.* Intra-articular bioactivity of a p38 MAPK inhibitor and development of an extended-release system. *European Journal of Pharmaceutics and Biopharmaceutics* **93**, 110-117 (2015). https://doi.org:https://doi.org/10.1016/j.ejpb.2015.03.017
218. Chiu, Y.-L. & Rana, T. M. siRNA function in RNAi: a chemical modification analysis. *Rna* **9**, 1034-1048 (2003).
219. Shaw, J.-P., Kent, K., Bird, J., Fishback, J. & Froehler, B. Modified deoxyoligonucleotides stable to exonuclease degradation in serum. *Nucleic acids research* **19**, 747-750 (1991).
220. Rutgers, M., van Pelt, M. J. P., Dhert, W. J. A., Creemers, L. B. & Saris, D. B. F. Evaluation of histological scoring systems for tissue-engineered, repaired and osteoarthritic cartilage. *Osteoarthritis and Cartilage* **18**, 12-23 (2010). https://doi.org:https://doi.org/10.1016/j.joca.2009.08.009
221. Tang, Q. *et al.* RNAi-based modulation of IFN-γ signaling in skin. *Molecular Therapy* **30**, 2709-2721 (2022).
222. Shmulevich, R. & Krizhanovsky, V. Cell senescence, DNA damage, and metabolism. *Antioxidants & Redox Signaling* **34**, 324-334 (2021).
223. Waldron, A. L. *et al.* Oxidative stress-dependent MMP-13 activity underlies glucose neurotoxicity. *Journal of Diabetes and its Complications* **32**, 249-257 (2018). https://doi.org:https://doi.org/10.1016/j.jdiacomp.2017.11.012
224. Chin, A. F. *et al.* Senolytic treatment reduces oxidative protein stress in an aging male murine model of post-traumatic osteoarthritis. *Aging Cell* **22**, e13979 (2023). https://doi.org:https://doi.org/10.1111/acel.13979
225. Park, H. *et al.* p16INK4a-siRNA nanoparticles attenuate cartilage degeneration in osteoarthritis by inhibiting inflammation in fibroblast-like synoviocytes. *Biomaterials Science* **10**, 3223-3235 (2022).
226. De Lange-Brokaar, B. J. E. *et al.* Synovial inflammation, immune cells and their cytokines in osteoarthritis: a review. *Osteoarthritis and cartilage* **20**, 1484-1499 (2012).
227. Rabiej, S. & Wlochowicz, A. SAXS and WAXS investigations of the crystallinity in polymers. *Die Angewandte Makromolekulare Chemie* **175**, 81-97 (1990). https://doi.org:https://doi.org/10.1002/apmc.1990.051750107